Politecnico di Milano

Department of Civil & Environmental Engineering

School of Civil, Environmental and Land Management Engineering

Master Degree

Spatial variability of ground motions for seismic analysis of bridge structures: insights from recordings and physics-based numerical simulations

Marco Vittone

Supervisor:

Prof. Chiara Smerzini

Academic Year 2019/20

Abstract

The spatial variation of earthquake ground motion in near-fault region can significantly affect the dynamic response of large and extended engineered structures. In engineering practice, such a variation is considered in terms of coherency, as a function of frequency and separation distance, calibrated on an empirical basis, using sparse datasets of strong motion recordings provided by dense arrays. Despite the increasing availability of strong motion records, observations at dense arrays are still very scarce especially in near-source conditions and, therefore, available empirical models for spatial coherency may be hardly extrapolated for site-specific estimates. Hence, a good understanding of the physical factors underlying the SVEGM is fundamental for an accurate modelling of the spatially variable seismic action to be considered for engineering analyzes of large civil engineering constructions.

To this aim, spatial coherency estimates have been analyzed from a wide set of both dense arrays recordings and 3D physics-based numerical simulations (spectral element code, SPEED: `http://speed.mox.polimi.it/`). The results confirm the complex dependence of coherence on the specific site and source features. As a general comment, it was observed that spatial coherency decreases non-linearly with inter-station distance and frequency, with decreasing source-to-site distance and passing from rock to soil site conditions. Furthermore, it was found that fault rupture details, such as the slip distribution, the hypocenter location and relative position with respect to the causative fault, may have a strong impact on spatial coherency.

Finally, the effects of spatially variable ground motions on an idealized integral-abutment bridge has been assessed by using as seismic input broadband physics-based waveforms obtained at different pier supports. The results show that spatial variability of ground motion, obtained from physic-based numerical simulations, may present features that have a considerable impact even on a regular, 360-m long structure on homogenous soil conditions, leading to localized increase or decrease of engineering demands parameters up to a factor of about 50%.

Contents

List of Figures

v

List of Tables

Chapter 1

Introduction

Earthquake ground motion exhibits spatial variability effects not only at a regional scale but also at local scales, with potential impact for the class of spatially extended structures. As a matter of fact, the largest dimension of most structures is usually small enough that the ground motion can be reasonably assumed to be the same at each point of the structure itself. On the other hand, for structures which extend over significant distances, such as bridges, ground motions arriving at different points of the structure may vary significantly both in amplitude and phase. In such cases evaluation of spatial variability of earthquake ground motion (SVEGM) is crucial to accurately estimate the structural seismic response.

For this reason, for Eurocode 8, EC8 – Part 2 (CEN, 2005), as well as for the 2008 Italian Building Code, NTC18, a spatially varying seismic input has to be taken into account for the design of bridges. In particular, in EC8 spatial variability of seismic action is defined as the "situation in which the ground motion at different supports of the bridge differs and, hence, the seismic action cannot be based on the characterization of the motion at a single point". Furthermore, according to the same norm, the model describing the spatial variability of seismic actions should take into account, even if only in a simplified way, the propagative character of the seismic waves as well as the loss of correlation between motions at different points along the bridge owing to random heterogeneities of the soil and to differences in the mechanical properties of the involved media.

Therefore, a good understanding of the physical factors underlying the SVEGM is of paramount relevance for the definition of an appropriate model for the variability of seismic input to be applied for the structural analysis of bridges and extended structures in general.

1.1 Background and motivation

Engineering models of SVEGM are calibrated on the basis of strong motion recordings at dense seismic arrays during past earthquakes and usually neglect the aspects related to the proximity to the seismic source. In spite of the increasing availability of strong motion records, observations at dense arrays are still very scarce especially in near-source conditions even on a worldwide scale and further studies are needed. As an alternative powerful method, numerical simulations of earthquake ground, based on physical models of the seismic source, the propagation path from the source to the site and local geologic irregularities, can be used to simulate spatially variable ground motions when recorded data are lacking. This approach has been extensively used in this study (see Chapter 4), where 3D physics-based numerical simulations of earthquake ground motion play a key role. Note that the numerical approach has the advantage of allowing one to investigate the dependence of SVEGM on physical factors, such as magnitude, near-source effects, local site conditions, for a variety of "virtual", albeit realistic, conditions.

On the other hand, the main limitation of 3D physics-based simulated ground motions, which historically has prevented their use in the seismic analysis of structure, is the frequency limitation, typically at around 1.5-2 Hz (as seen later in this thesis), owing to the constraints in mesh size and limited knowledge at short wavelength on both the source and the medium. However, it is expected that in future years the increasing computational power will lead to the achievement of synthetics in a larger and larger frequency range.

After over three decades of studies, it is nowadays well recognized that SVEGM may have detrimental effects on the structural response, causing displacement patterns along the structure and/or strength/ductility demands which are almost unpredictable owing to the multi-parametric nature of wave propagation and of its interaction with different structural elements. After the first pioneering research studies in the middle 1960s, when structures were studied in the linear range and the SVEGM was considered only in terms of delay in the arrival time at the supports, the installation of dense instrument arrays and the development of spatial coherency models (see e.g. Harichandran and Vanmarcke (1986); Abrahamson et al. (1991);

Luco and Wong (1986); Der Kiureghian (1996)) gave rise to an increasing interest on the issues related to the effect of spatially variable excitations on the response of a large variety of structural systems (for a comprehensive overview see Zerva (2009)).

Only to cite few among the most important and recent contributions, the work of Monti et al. (1996), is one of the first extensive parametric numerical studies about the response of bridges undergoing asynchronous seismic motion. Authors found out that a spatial variable input motion reduces the ductility demand for central piers and increase it for lateral ones and finally that the uniform input motion results in a conservative design.

Saxena et al. (2000) reached different conclusions: they observed that the uniform support excitation assumption almost always is not conservative, especially in case of different soil conditions for different supports. In fact, while for the uniform soil type case the spatially variable input leads to a light increase in the demand with respect to the synchronous motion, in case of variable ground type at the support the peak pier ductility demand can increase up to twice with respect to the case of uniform soil.

Finally, two recent studies on the inelastic response of bridges, including structural irregularities, are conducted by Sextos et al. (2004) and Lupoi et al. (2005). Unlike the majority of authors, Sextos et al. (2004) pointed out that the response in terms of pier base bending moment in the transversal direction in almost unpredictable because, depending on the variable character of the motion, the asynchronous response leads from a reduction up to 70% to an increment exceeding the 100% with respect to the fully coherent case.

Based on the analysis of a wide set of 200-m long idealized bridges, Lupoi et al. (2005) found that the probability of failure systematically grows with the geometrical irregularity of the structures.

1.2 Aim and organization of the thesis

Stimulated by the considerations above, the aim of this Thesis is two-fold.

First, the aspects regarding the evaluation of the SVEGM in near source conditions will be addressed based on both earthquake recordings (Chapter 3) and numerically-based approaches (Chapter 4).

The second aim of this Thesis is to present a challenging application focused on the coupling of 3D physics-based numerical scenarios in near-fault region and structural

analysis of a bridge structure (Chapter 5).

Chapter 3 presents the results of the statistical analysis of spatial coherencies estimated from earthquakes signals recorded at four different world wide dense arrays: the ICEARRAY (Iceland), the UPSAR array (California), the L'Aquila array (Central Italy) and the Mirandola array (Northern Italy). A brief description of the dense arrays and events considered is presented. Some possible factors influencing the spatial coherency of seismic ground motions are analyzed and discussed by using those in-situ results. The coherencies estimated are then compared to the existing empirical coherency models to discuss on the limitations of those models and to conclude on the possibility of selecting a coherency model which can be conformed the most to the theoretical aspects as well as practical aspects.

Chapter 4 is focused on the estimation of spatial coherency from a rather wide set of 3D physics-based numerical simulations of near-source seismic ground motion in different areas of Italy. Since the numerical tests are realized with an high-performance computer code SPEED based on Discontinuous Galerkin Spectral Elements, the numerical method and software are briefly introduced in the beginning. Several numerical tests are realized to understand more precisely about how each physical parameters, such as magnitude, distance, rupture directivity, ground motion component and site conditions, affect the spatial variability of earthquake ground motions.

In Chapter 5 the impact of spatially variable motion on the response of a regular, idealized RC bridge, belonging to the class of the integral abutment bridges, is analyzed. Considering an integral abutment bridge is expected to increase the impact of SVEGM on its seismic response, because the lack of joints makes it more sensitive to differential movements of the ground. Furthermore, at variance with previous studies the results of which may be conditioned on the specific assumptions of the spatial coherency model, the effects of SVEGM on a bridge structure is studied by considering direct application at the different foundation points of earthquake ground motion obtained from 3D physics-based numerical models.

Before achieving this two goals, Chapter 2 presents the state-of-the-art on the spatial variability of seismic ground motions and on coherency functions which are proposed and used in the literature. The chapter is also dedicated to describe the methodology for estimating coherencies from seismic signals including the main theoretical

aspects aim at defining a coherency function of seismic wave propagating in random heterogeneous media

Chapter 2

Overview on spatial variability of seismic ground motion

The term "spatial variation of seismic ground motions" refers to the differences in the amplitude and phase of seismic motions recorded at two different locations of the ground. The Spatial Variability of Earthquake Ground Motion (SVEGM) is a consequence of the general transmission of the waves from the source through the different earth strata to the ground surface.

As sketched in Figure 2.1, typically, the spatial variation of ground motion is attributed to three different factors:

- **Wave passage effect**: arising from differences in the arrival times of seismic waves at separate stations.

- **Local site effects**: arising from the propagation of seismic waves from the bedrock level to the ground surface through local sub-surface soil condition which, in general, differs at each stations.

- **Scattering effects**: arising from differences in the amplitudes and phases of seismic waves due to reflections and refractions that occur as waves propagate in a heterogeneous medium.

- **Extended source effect** arising from differences in the manner of superposition of waves arriving from an extended source;
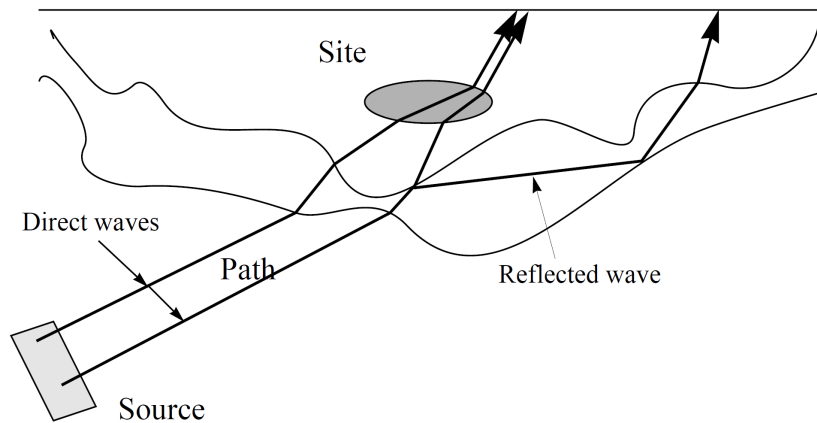
Figure 2.1: Sketch illustrating the main sources of spatial variability of earthquake ground motion. From Harichandran (1999).

Spatial variability of the ground motion due to attenuation of seismic waves, i.e., the decay of wave amplitudes due to geometric spreading and energy dissipation, is usually negligible on the local scale, typical of engineered structures.

In this chapter a general overview of spatial variability of SVEGM is provided. The theoretical background (Section 2.1) and and the main coherency models available in the literature (Section 2.3) are presented. Moreover, following the common approach to quantify SVEGM in engineering applications that consists on the estimation of the spatial coherency function, the procedure adopted to estimate coherency is illustrated (Section 2.2).

2.1 Stochastic estimation of spatial variability

Seismic data recorded or numerically simulated at dense instrument arrays permit the probabilistic (stochastic) estimation and modelling of the spatial variability of the ground motions. Signal processing techniques are first applied to the data to evaluate their stochastic estimators in the time or, more commonly, the frequency domain. These techniques are described in this section.

The procedure for the estimation of the stochastic spatial variation of seismic motions considers that the motions are realizations of space-time random field expressed

as a function of its position with respect to a selected origin, $\vec{p} = x, y, z^T$ and time, t. At each location, the acceleration time history in each direction $\vec{a}$ is a realization (a sample) of a stochastic process of time.

Some basic definitions for random variables are reported in Section 2.1.1. The concept of stochastic processes is then presented in Section 2.1.2. Finally, Section 2.1.3 introduces the concept of the complex-valued coherency in the frequency domain.

2.1.1 Basic Definitions

This section presents basic definitions for random variables, as an introduction to the description of stochastic process. Following Zerva (2009), let denote X a (continuous) random variable characterized by a cumulative density function (CDF) defined as follow:

$$F_X(x) = P(X \leq x) \tag{2.1}$$

where P means probability and x indicates the value of the random variable X. The respective probability density function (PDF) is provided by the following expression:

$$f_X(x) = \frac{dF_X(x)}{dx} \tag{2.2}$$

The mean, μ_X, and variance, σ_X^2, are, respectively:

$$\mu_X = E[X(t)] = \int_{-\infty}^{+\infty} x f_X(X) \tag{2.3}$$

$$\sigma_X^2 = \int_{-\infty}^{+\infty} (x - \mu_X)^2 f_X(x) dx = E(X^2) - \mu_X^2 \tag{2.4}$$

The joint probability distribution function of two random variables X and Y is defined as:

$$F_{X,Y}(x, y) = P(X \leq x, Y \leq y) \tag{2.5}$$

Thus, the joint probability density function is:

$$f_X(x) = \frac{\delta^2 F_{X,Y}(x, y)}{\delta x \delta y} \tag{2.6}$$

The covariance of X and Y is given by:

$$cov(X, Y) = E[(X - \mu_X)(Y - \mu_Y)] \tag{2.7}$$

The normalized covariance, or correlation coefficient, ρ_{XY} is defined as:

$$\rho_{XY} = \frac{cov(X,Y)}{\sigma_X \sigma Y} \tag{2.8}$$

which assumes values between -1 and +1: when $\rho_{XY} = \pm 1$, X and Y are linearly related, and the slope of the line is positive or negative, respectively; As $|\rho_{XY}|$ decreases the values of the X and Y pairs start "scattering" around the straight line, with the scatter increasing with decreasing of $|\rho_{XY}|$. $\rho_{XY} = 0$ indicates that X and Y are uncorrelated.

2.1.2 Stochastic Process

In general, a random phenomenon can depend on one or more deterministic parameters, such as the spatial coordinates and time. In the latter case, the random phenomenon is called stochastic (or random) process.

Stochastic processes dependent only on time t (continuous-state process) are considered herein. Therefore, the stochastic process is denoted as $X(t)$ and represents a sequence of an infinite number of random variables, $X_1, \ldots, X_n$, one for each time $t_1, \ldots, t_n$. The statistical properties of a real stochastic process $X(t)$ are completely determined from its n-th order joint probability distribution function:

$$F_{X_1,\ldots,X_n}(x_1,...,x_n;t_1,...,t_n) = P[X(t_1) \leq x_1, ..., X(t_n) \leq x_n] \tag{2.9}$$

To characterize a stochastic process, knowledge of the function is required for each x_i, t_i and n. However, for many applications, only certain statistical properties are used (e.g. mean, autocorrelation). The mean value of the process is defined by Eq. 2.3 while the autocorrelation function by Eq. 2.10:

$$R_{XX}(t_1, t_2) = E[X_1 X_2] = \int_{-\infty}^{+\infty} \int_{-\infty}^{+\infty} x_1 x_2 f_{X_1 X_2}(x_1, x_2; t_1, t_2) dx_1 dx_2 \tag{2.10}$$

Two hypothesis need to be made in order to extract valuable information from the limited amount of data available, such as the recorded time histories at the array stations during an earthquake. These are the assumptions of stationarity and ergodicity described in the following.

- **Stationarity**: implies that the stochastic descriptors of the motions do not depend on absolute time, but are functions of time differences (or time lag)

only.

In theory the time histories should have neither a beginning nor an end, and maintain the same stochastic characteristics throughout their (infinite) duration. This characteristic is unrealistic, as, obviously, seismic ground motions have an absolute starting and ending time. However, in engineering applications, if we consider only a portion of the actual seismic time history (strong motion window), which maintains the same properties throughout its duration, the assumption of stationarity became realistic (this window can be seen as a segment of an infinite series with uniform characteristics through time).

- **Ergodicity**: A stationary process is ergodic, if averages taken along any realization of the process over its infinite duration are identical to the ensemble averages, i.e., the information contained in each realization is sufficient for the full description of the process. This hypothesis is very powerful since, ideally, the characterization of the random processes and fields would require records at the same site from many earthquakes with similar characteristics while under the hypothesis of ergodicity a single realization is representative of the entire stochastic process (in reality only one time history at each recording station for an earthquake with specific characteristics is typically available).

2.1.3   Coherency

The coherency of the seismic motions is obtained from the cross spectral density of the time histories between two sites, normalized with respect to the corresponding power spectral density. More specifically, given a pair of motions recorded at two discrete locations j and k at a separation distance d, the coherency $\gamma_{jk}(\omega, d)$, function of both circular frequency ω (or frequency f, with $\omega = 2\pi f$) and distance (d), can be computed as follows:

$$\gamma_{jk}(\omega, d) = \frac{S_{jk}(\omega, d)}{\sqrt{S_{jj}(\omega) \cdot S_{kk}(\omega)}} \tag{2.11}$$

where:

- $S_{jj}(\omega)$ and $S_{kk}(\omega)$ are the smoothed power spectral density at stations j and k, respectively. For a generic station j, the power spectrum is defined as the Fourier transform of the autocorrelation function, $R_{jj}(\tau)$, of the strong motion S-wave window $(a(t))$ of duration T recorded at station j (Zerva, 2009):

$$R_{jj}(\tau) = \begin{cases} \frac{1}{T} \int_0^{T-|\tau|} a_j(t)a_j(t+\tau)dt & for |\tau| \leq T \\ 0 & for |\tau| > T \end{cases}$$

$$S_{jj}(\omega) = \frac{1}{2\pi} \int_{-\infty}^{+\infty} R_{jj}(\tau)e^{-i\omega\tau}d\tau \tag{2.12}$$

- $S_{jk}(\omega, d)$ is the smoothed cross spectrum between stations j and k, defined as the Fourier transform of the cross correlation function, $R_{jk}(\tau)$, between stations j and k:

$$R_{jk}(\tau) = \begin{cases} \frac{1}{T} \int_0^{T-|\tau|} a_j(t)a_k(t+\tau)dt & for |\tau| \leq T \\ 0 & for |\tau| > T \end{cases}$$

$$S_{jk}(\omega) = \frac{1}{2\pi} \int_{-\infty}^{+\infty} R_{jk}(\tau)e^{-i\omega\tau}d\tau \tag{2.13}$$

Note that, following the definitions above, the power spectral density (PSD) and cross-spectral density (CSD) are defined as the Fourier Transform of the autocorrelation and crosscorrelation, respectively, i.e. correlation and cross-correlation are related to PSD and CSD by the Fourier Transform operators (Wiener-Khintchine theorem). More details about smoothing of spectral densities and strong motion window evaluation can be found in Appendix A and Appendix B, respectively.

The coherency function is a complex-valued function, therefore it can be written in a exponential form as follows:

$$\gamma_{jk}(\omega, d) = |\gamma_{jk}(\omega, d)| \cdot \exp[i\theta(\omega, d)] \tag{2.14}$$

In this way two terms appear clearly: the lagged coherency and the phase spectrum.

Lagged coherency

The lagged coherency is defined as the modulus term of the complex coherency of Eq. 2.13 ($|\gamma_{jk}(\omega, d)|$). It is a measure of the similarity between the seismic motions at two different stations and indicates the degree to which the data recorded at the two stations are related by means of a linear transfer function. It assumes value equal to one if one signal can be obtained through a linear transformation of the other signal, while it assumes value equal to zero if the signals are totally uncorre-

lated $(0 \leq |\gamma_{jk}(\omega, d)| \leq 1)$.

It is expected that at low frequencies and short separation distances, the motions will be similar and, therefore the lagged coherency will tend to unity as frequency and station separation distance tend to zero. On the other hand, at large frequencies and long station separation distances, the motions will become uncorrelated, and the lagged coherency will tend to zero. The value of the lagged coherency in-between these extreme cases will decay with frequency and station separation distance.

It is important to highlight that, as noted by Abrahamson et al. (1991), the correlation of additional wave components, related to scattered energy and noise, could be appreciable at high frequencies and distances, leading to non-zero values of lagged coherency at large d or .

In addition to the lagged coherency, the complex coherency of Eq.(2.13) can be expressed in term of unlagged coherency or plane wave coherency.

Unlagged coherency

The unlagged coherency is defined as the real part of the complex coherency function:

$$\gamma^U(d, \omega) = Re\left\{\gamma(d, \omega)\right\} \tag{2.15}$$

It measures the coherency assuming no time lag between locations under the hypothesis of vertical wave propagation. The coherent part of the wave passage effect can lead to negative values of the unlagged coherency, indicating that the ground motion at the two stations are out of phase. An unlagged coherency of -1 indicates that the ground motion is 180° out of phase due to wave passage effect.

Plane wave coherency

Abrahamson et al. (1991) noted that the lagged coherency describes only the deviations of the ground motions from plane wave propagation at each frequency, but does not consider the deviations of the motions from a single plane wave at all frequencies. In other words, if the analyzed segment contains wave components in addition to the plane wave, as happens at the higher frequencies where scattered energy or noise contribute significantly to the records, the correlation of these additional wave components is reflected in the lagged coherency as if they were part of the plane wave.

To express the departure of the data from that of plane wave propagation at all frequencies (e.g. to measure the coherency relative only to a single plane wave velocity for each earthquake), Abrahamson et al. (1991) introduced the concept of the plane-wave coherency.

The Plane-Wave Coherency can be estimated from the time histories by taking the real part of the smoothed cross-spectrum after aligning the ground motions based on the best plane-wave velocity:

$$\gamma^{PW}(d, \omega) = Re \left\{ \frac{S_{jk}(\omega, d)}{\sqrt{S_{jj}(\omega) \cdot S_{kk}(\omega)}} \right\}_{plane-wave-direction} \tag{2.16}$$

A crucial passage in the determination of $\gamma^{PW}(d, \omega)$ is the evaluation of the direction of plane-wave propagation: it can be found from the earthquake ground motion signals by determining an angle ϕ for which the correlation coefficient between the two horizontal components (after being rotated by angle ϕ) is equal to zero.

It is important to notice that the assumptions behind the unlagged and plane wave coherency definitions cannot apply for near-fault ground motions. However, in problems of soil-structure-interaction, where a single plane wave speed and single direction at all frequencies is assumed, only the plane wave coherency should be considered.

Phase spectrum

Concerning the phase spectrum, it incorporates two effects:

- **wave passage effect**: i.e. time delay due to plane wave propagation with velocity c:

$$\theta_{jk}^{WP} = -\frac{\omega \cdot d}{c} = -\omega\tau_0 \tag{2.17}$$

- **random phase variability** at each station, owing to variations of the geologic structure underneath the array and, also, to deviations of the propagation pattern of the waves from that of plane wave propagation.

The time lags caused by the wave passage effect appear as deterministic (d/c) in Eq. 2.17. However, the phase spectrum also incorporates random, station dependent time delay fluctuations around these deterministic delays that affect the coherency and should be given proper consideration.

Autocorrelation (autocovariance) function is symmetric with respect to $\tau = 0$ and is peaked at $\tau = 0$ (see Figure 2.2a), whereas the cross covariance function is not symmetric around $\tau = 0$ and is peaked, generally, at the time lag $\tau_0 \neq 0$ (see Figure 2.2b). Thus, if the duration of the lag window (see Appendix A) is selected such that the peak of the cross covariance function at τ_0 is excluded from the evaluation, the bias of the estimate will be significantly affected leading to an erroneous evaluation of the coherency. An approach to remedy this problem is through the alignment of the time histories (see Section 2.1.3).

(a)   (b)
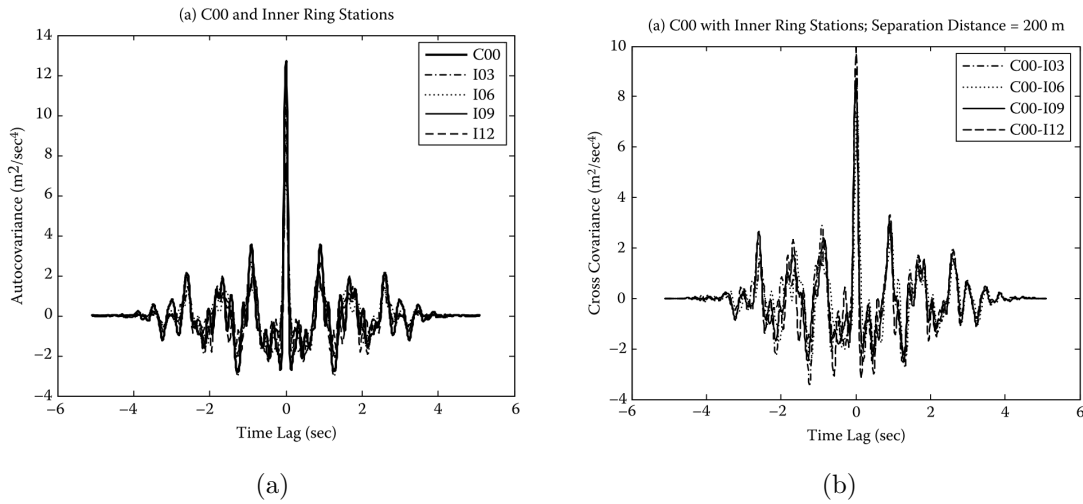
Figure 2.2: Example of autocovariance (autocorrelation) and crosscovariance (cross correlation) functions for the SMART 1 array, Taiwan. Adapted from Zerva (2009)

Time histories alignment

The arrival time perturbation affects the lagged coherency producing a bias estimation as described previously. For this reason in the evaluation of the spatial coherency, the wave passage effect is removed by aligning the time histories with respect to a reference station before evaluating their cross spectra. The alignment is achieved by shifting the time axis of a time history with respect to a reference station by an amount corresponding to the time lag associated to the peak of the cross covariance function between two time series.

Boissières and Vanmarcke (1995) modelled the fluctuation of the time delay considering that the time lag between to stations as the sum of the time lag between

the two stations, j and k, due to the average propagation of the waves $\left(\Delta t_{jk}^{wp} = \dfrac{d_{jk}}{c} \right)$ and the random fluctuations (Δt_{jk}^{r}):

$$\Delta t_{jk} = \Delta t_{jk}^{wp} + \Delta t_{jk}^{r} \tag{2.18}$$

In practice, the time lag is estimated by looking at the absolute maximum of the cross correlation function inside the interval of (length 1 s) centred at Δt_{jk}^{wp} (which is roughly evaluated as the ratio between the station distance and a typical apparent propagation velocity). In case the maximum is at one of the end-points of the interval, the estimate is chosen as corresponding to the closest relative maximum outside the interval.

This procedure allows to reduce the computational time and, for stations which are far apart, reduces the chance of selecting a spurious peak corresponding to an unrealistic lag value (since the shape of the accelerogram is distorted as the wave travels a relatively long distance, several different shifts in time of one accelerogram with respect to the other one can produce comparable peaks in the cross-correlation function).

2.2   Procedure

In this section the procedure adopted in this study for the estimation of coherency is presented. It can be subdivided in the following steps:

1. the time histories recorded at each station are aligned with respect to the reference one, which is identified as the one nearest to the centre of the array, as explained in Sec. 2.1.3.

2. nearly-stationary segments of the time series, containing the strongest phase of shaking dominated by shear (S) waves , are selected following the procedure explained in Appendix B;

3. a Tukey (tapered cosine) window with tapering length equal to 5% of the length of stationary part of the signal is then applied to the time history;

4. from the windowed and tapered time signals, the power and cross spectra are calculated given by the following equations (see Zerva 2009):

$$S_{jj}(\omega) = \frac{2\pi}{T}|A_j(\omega)|^2 \tag{2.19}$$

$$S_{jk}(\omega) = \frac{2\pi}{T}|A_j(\omega)||A_k(\omega)|\exp[i(\theta_k(\omega) - \theta_j(\omega)] \tag{2.20}$$

where: T is the considered time window for the signal, $A_j(\omega)$ is the Fourier transform of the signal $a_j(t)$, and $|A_j(\omega)|$ is its modulus, while $\theta_k(\omega) - \theta_j(\omega)$ is the phase spectrum. The absolute value of $S_{jk}(\omega)$ represents the cross amplitude spectrum:

$$|S_{jk}(\omega)| = \frac{2\pi}{T}|A_j(\omega)||A_k(\omega)| \tag{2.21}$$

The cross amplitude spectrum is controlled by the Fourier amplitudes of the motions at the two stations, and the phase spectrum indicates whether the frequency component of the time history at one station precedes or follows the other time series at that frequency;

5. a 11 point ($M = 5$) Hamming spectral window is applied to smooth the power and cross spectra (see Appendix A for more detail). The bandwidth of smoothed frequency (BW) can be calculated as:

$$BW = 2M \cdot \frac{f_s}{N_f} \tag{2.22}$$

where f_s is the sampling frequency ($f_s = 1/\Delta t$), N_f is the number of frequency points, and frequency step, $\Delta f = f_s/N_f$.

Abrahamson et al. (1991), in evaluating an optimal window for the estimation of the coherency, suggested an 11-point (M=5, being N=2M+1 the number of points of the smoothing window) Hamming (spectral) window, if the coherency estimate is derived from time windows less than approximately 2000 samples and is to be used in structural engineering applications, with damping coefficient 5% of critical.

The criterion adopted in this study is consistent with the Abrahamson's recommendations, as it implies the use of a 11-point (M=5) Hamming window. In our case of studies, when dealing with real recordings where the sampling rate (Δt) is equal to 0.005 s and $N_f = 2048$ points are imposed, a smoothing bandwidth of 1 Hz provides an 11 point Hamming window. When dealing with numerical simulations, instead, a bandwidth of 0.5 Hz is considered since the time histories are, in general, characterized by a sampling rate of 0.01s while keeping $N_f = 2048$.

6. the complex valued coherency is estimated using Eq. 2.11 and, then, the lagged coherency is calculated from its absolute value.

The procedure above is repeated for each station pair of interest and, for each station pair, is typically applied to the three components of ground motion, namely, two horizontal components (East-West: EW; North-South: NS) and vertical (UD). Since emphasis is placed in this work to the near-field region of moderate to severe earthquakes, where source directivity/directionality effects may be predominant and lead to polarization of ground motion in the strike normal and parallel components, the two horizontal components projected along the direction parallel and normal to the fault strike (FP = Fault Parallel and FN = Fault Normal, respectively), are taken into consideration. For this reason, in the following results will be, in fact, discussed in terms of FP, FN and UD coherency estimates.

2.2.1 Validation

The procedure, just described, has been validated through comparison of the results published in Zerva (2009) with reference to the SMART-1 array recordings, obtained during the M6.7 21 Jan 1981 earthquake at epicentral distance of around 30 km. . In particular, Zerva (2009) illustrated the derivation of the stochastic estimators

needed for the evaluation of SVEGM by showing the results obtained from the data recorded at the SMART-1 array during M6.7 21 Jan 1981 earthquake. Thus, starting from the same input data the procedure, described in Section 2.2, is applied and the results compared to those of Zerva (2009) in order to check its correctness.

Figure 2.3,a shows the lagged coherency between two stations at a separation distance of 200 m estimated by Zerva (2009) for different values of Hamming window lengths (M = 1, 3, 5, 7 and 9), while in Figure 2.3,b the comparison between the lagged coherency function obtained by Zerva (2009) (black line) and the one obtained by the application of our procedure (magenta line) for M = 5 (11-points Hamming window) is illustrated.
The two curves exhibit a excellent agreement meaning that our procedure is valid.
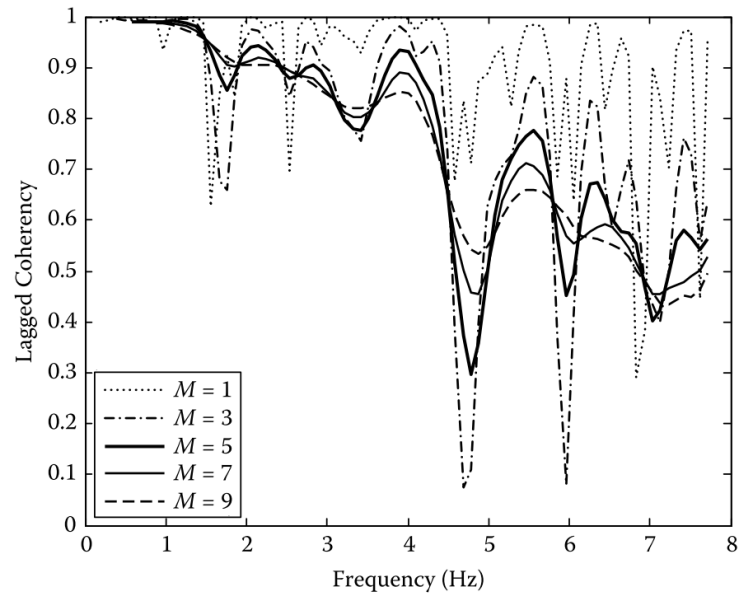
(a)
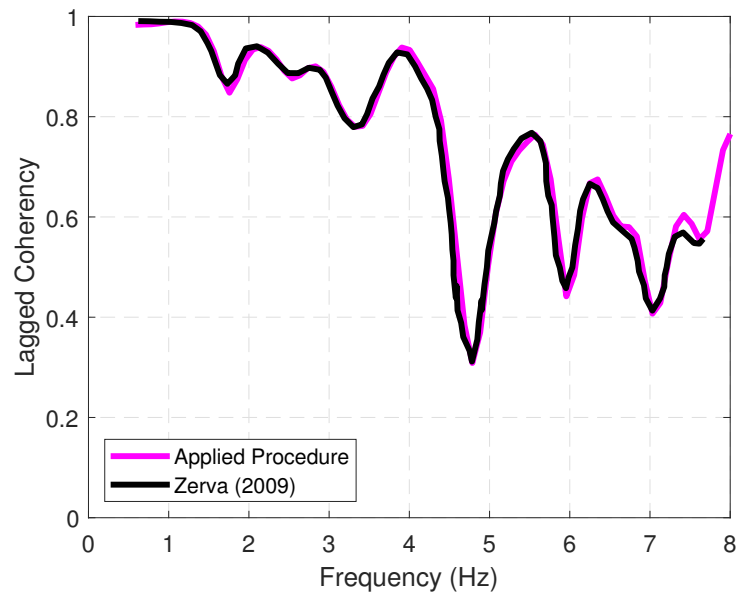
(b)

Figure 2.3: Comparison between lagged coherency estimated by Zerva (2009) and by the application of the procedure followed in this study.

2.3 Existing engineering models for spatial coherency

This section presents some of the spatial coherency models that have been widely used in the literature for engineering applications; it may not be noted, however, that the list of models presented is not exhaustive.

There are two main classes of spatial coherency models:

1. **Semi-empirical models**: they refer to functional forms obtained by theoretical considerations and calibrated for specific cases and contexts using available earthquake data. Usually, their expressions are given by theoretical considerations and their parameters are calibrated by using recorded data.

2. **Empirical models** referring to functional forms obtained directly by means of statistical analysis and regression of recorded data.

2.3.1 Semi-empirical models

One of the most widely used coherency models is the one introduced by Luco and Wong (1986). It is based on the analysis of shear waves propagating through random media. The expression for the lagged coherency between two pairs of acceleration processes at two different stations with a separation distance d is given by:

$$|\gamma_{jk}(\omega, d)| = \exp\left[-(\alpha \cdot \omega \cdot d)^2\right] \qquad (2.23)$$

where $\alpha = \dfrac{\eta}{V_s}$, being η a constant, which depends on the relative variation of the elastic properties in the medium, and V_s the average shear wave velocity of the medium along the wave path. α is the coherency drop parameter controlling the exponential decay of the coherency with distance and frequency. The authors suggests a typical value of α in the range from $2 \cdot 10^{-4}$ s/m to $3 \cdot 10^{-4}$ s/m.

A theoretical model for the coherency function describing the spatial variability of earthquake ground motions was developed by Der Kiureghian (1996).

The model, based on the random processes theory, is defined by the product of three terms: the incoherence effect, due to scattering of waves in the ground medium and their differential superpositioning when arriving from an extended source; the wave-passage effect, arising from the difference in the arrival times of waves at separate stations; and the site-response effect, arising from the difference in the local

soil conditions at two stations.

Starting from of the Luco and Wong (1986) model, Zerva and Harada (1997) developed a site-specific coherency model that approximates the site topography by a horizontally extended layer with random characteristics overlaying an half-space bedrock.

Their model includes the effects of wave passage with constant velocity on the ground surface, the loss of coherence due to scattering of the waves as they travel from the source to the site, and the local site effects. In particular, they showed that the site contribution is concentrated in the vicinity of the predominant frequency of the layer and yields a drop in the value of the coherence (see Figure 2.4).

Figure 2.4 shows the functional forms of the Luco and Wong (1986) and Zerva and Harada (1997) models as a function of frequency at different separation distances.

An other important contribution was given by Konakli et al. (2014) who used the Luco and Wong (1986) model by fitting the model parameters (α) based on the accelerograms recorded by the UPSAR array during the 2004 Parkfield earthquake.

The study showed that the rate of decay of coherency with frequency tends to decrease with increasing separation distance, and the rate of decay of coherency with distance tends to decrease with increasing frequency (see Figure 2.5). This result proved that the assumption of a constant rate of decay of the lagged coherency with frequency and distance, which is at the base of the Luco and Wong (1986) model is incorrect.

Moreover, Konakli et al. (2014) observed that the rates of decay for the vertical component are slightly larger than those for the two horizontal components, which tend to be close to each other.
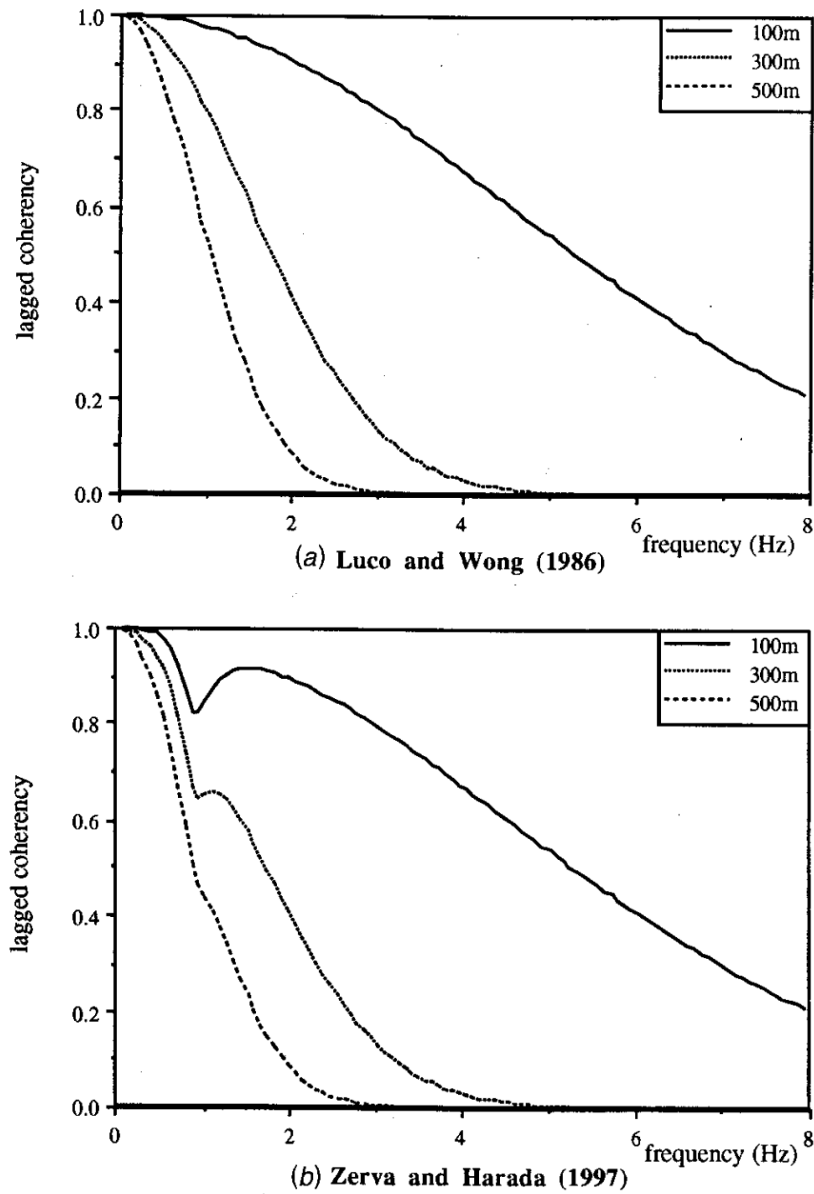
Figure 2.4: Variation of Luco and Wong (1986) and Zerva and Harada (1997) spatial coherency models with frequency at separation distances of 100, 300, and 500 m. From Zerva and Zervas (2002)
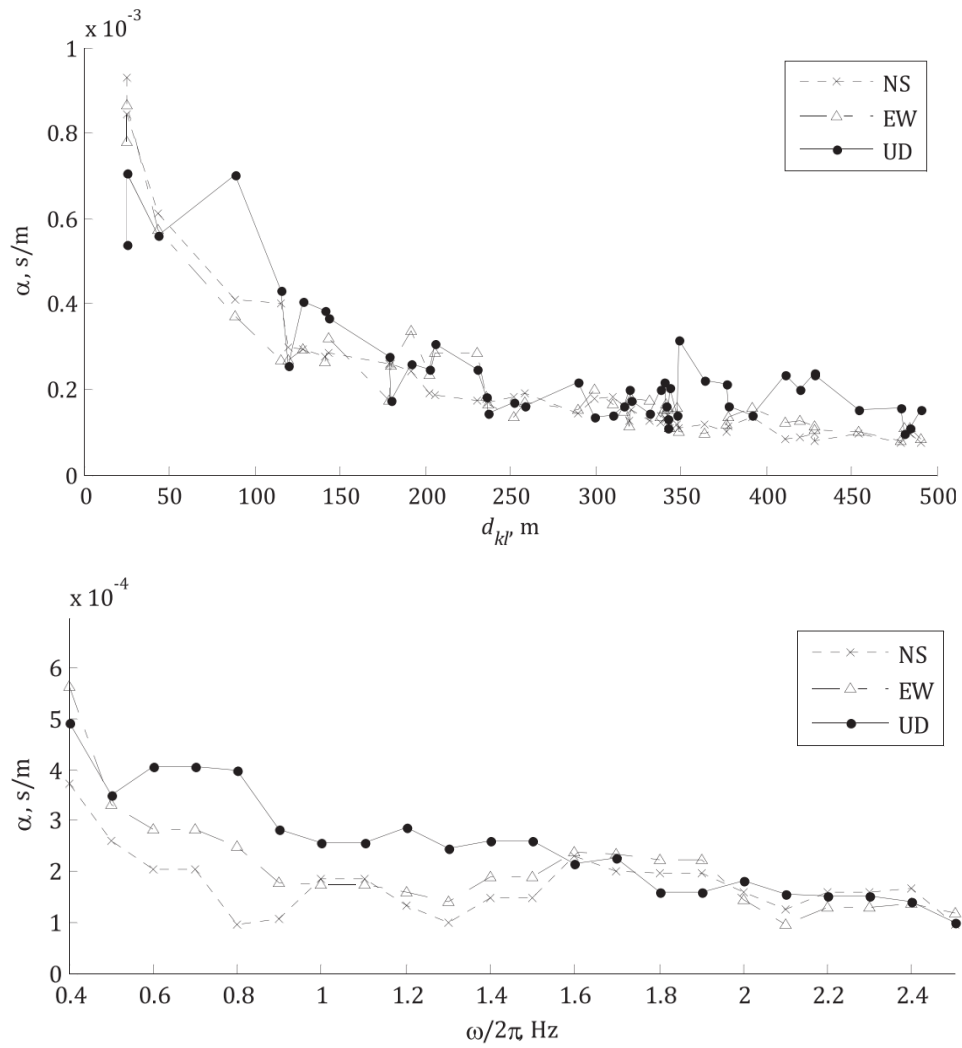
Figure 2.5: Variation of α as a function of station separation distance (above) and of frequency (below). From Konakli et al. (2014)

2.3.2 Empirical models

Empirical models take as input seismic recordings from dense seismic arrays and need specific post-processing procedures to define the parameters characterizing the model itself. Therefore, they are intrinsically dependent on the calibration dataset, including both the dense arrays and events considered. Table 2.2 summarizes the main properties of the most popular models available in the literature, including some recent works. Table 2.1 lists the dense arrays whose recordings were used in the definition of the spatial coherency models shown in Table 2.2.

Because of the variability in seismic data recorded at different sites and during different events, the differences in the numerical processing of the data used by various investigators, and the different functional forms used in the regression fitting of a function through data, there is a multitude of spatial variability expressions in the literature which are difficult to be compared. The development of empirical models began with the construction of the SMART-1 dense array (1980), located in Taiwan at Lotung. SMART-1 was the first large digital array of strong-motion seismographs specially designed for engineering and seismological studies of near-field properties of earthquakes.

Since the array is located in a high seismicity region, an extensive database was already available at the time of the first empirical models. Among them, the first two empirical coherency models are those of Harichandran and Vanmarcke (1986) and Abrahamson et al. (1991) .

The first developed an isotropic model for the horizontal component of the lagged coherency based on data from four earthquake events recorded by SMART-1.

The isotropy implies that the rotation of the random field on the ground surface will not affect the joint probability density functions. As a consequence of this assumption, the lagged coherency is a function of separation distance only and not direction.

Their model of lagged coherency (see Figure 2.6b), applicable for separation distances greater than 100 m, is given by:

$$|\gamma(d,\omega) = A \exp\left[-\frac{2d}{\alpha\theta(\omega)}(1 - A + \alpha A)\right] + (1 - A)\exp\left[-\frac{2d}{\theta(\omega)}(1 - A + \alpha A)\right]$$

$$(2.24)$$

where $\theta(\omega) = k \left[1 + \left(\dfrac{\omega}{\omega_0} \right)^b \right]^{-\frac{1}{2}}$, $A = 0.736$, $\alpha = 0.147$, $k = 5120$, $\omega_0 / 2\pi = 1.09$ and $b = 2.78$.

The model of Abrahamson et al. (1991) for horizontal lagged coherency was defined by using the data from the Large Scale Seismic Test (LSST) array (located within the SMART-1 array, it allows investigations of spatial variability for horizontal separations as small as 6 m). It is applicable only to small separation distances, i.e., $d \leq 100m$, since it was observed that extrapolation to distances greater than 100 m will underestimate the coherency. The expression of the lagged coherency is given by:

$$\tanh^{-1} \left[|\gamma(d, \omega)| \right] = a(d) \cdot \exp[(-0.115 - 0.00084d)\omega] + \frac{\omega^{-0.878}}{3} + 0.35 \qquad (2.25)$$

where $a(d) = 2.54 - 0.012d$.

This model was subsequently revisited by Ancheta et al. (2011) (see Figure 2.6a) by analysing the performance of the model with respect to the data recorded at the BVDA arrays (Borrego Valley Differential Array) in California during near and far field events of magnitude 2.5–4.9. The authors found that the model of Abrahamson et al. (1991) is good for the separation distance higher than 30 m for all frequencies, but underestimates coherency for distances less than 30 m and frequencies less than 10 Hz. From a parametric study, the authors proposed to change the coefficient $a(d)$ of Abrahamson et al. (1991) model (Eq. 2.25) as follows: $a(d) = 3.79 - 0.499 \ln(d)$.

Finally, Abrahamson (2006) analyzed the data recorded at ten different arrays (see Table 2.2) and proposed the following empirical model for plane wave coherency:

$$|\gamma^{PW}(d, f)| = \left[1 + \left(\frac{f \cdot \tanh(a_3 d)}{f_c \cdot a_1} \right)^{n_1} \right]^{(-0.5)} \cdot \left[1 + \left(\frac{f \cdot \tanh(a_3 d)}{f_c \cdot a_1} \right)^{n_2} \right]^{(-0.5)} \qquad (2.26)$$

with empirical coefficients a_1, a_2, a_3, f_c, n_1, n_2 derived separately for horizontal and vertical components by non-linear regression of seismic data.

The model of Abrahamson (2006) is applicable for all type of soil since it was derived from data acquired by variety of arrays which include both soft soil and hard rock (see Table 2.2).

Note that the Abrahamson (2006) model does not give reliable results because it does not account for the differences between rock and soft sites. Therefore, in the subsequent study Abrahamson (2007) developed two separates models: one for hard rock and one for soil sites using the data obtained at the arrays specified in Table 2.2.

The plane-wave coherency model of Abrahamson for hard rock sites and for soil sites take almost the same functional form of Eq. 2.26 with different value of the parameters:

$$|\gamma^{PW}(d,f)| = \left[1 + \left(\frac{f \cdot \tanh(a_3 d)}{f_c \cdot a_1}\right)^{n_1}\right]^{(-0.5)} \cdot \left[1 + \left(\frac{f \cdot \tanh(a_3 d)}{a_1}\right)^{n_2}\right]^{(-0.5)} \quad (2.27)$$

Figure 2.7 shows the functional form of Abrahamson (2007) models for horizontal components.

(a) Ancheta et al. (2011)   (b) Harichandran and Vanmarcke (1986)
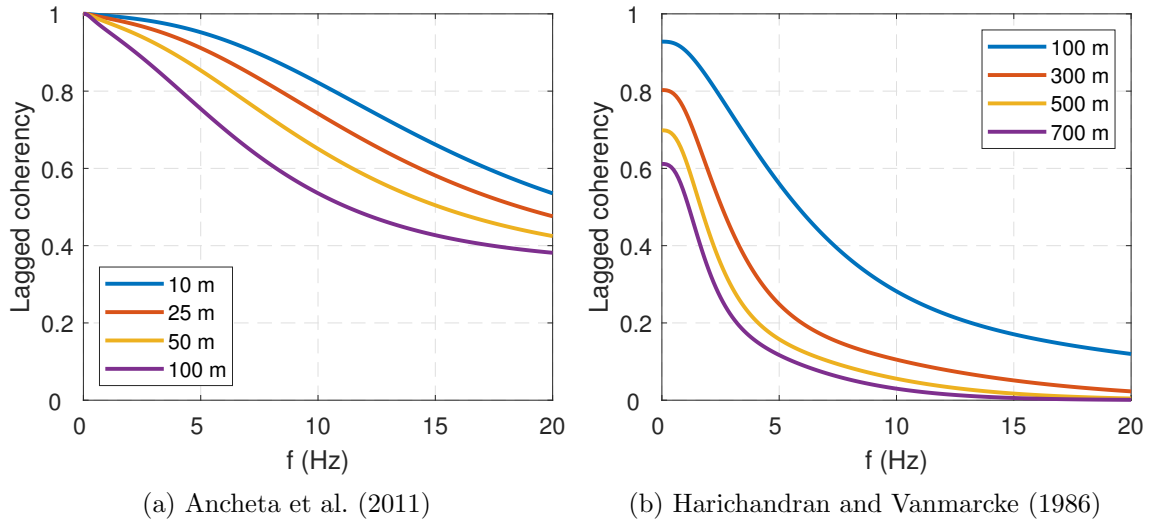
Figure 2.6: Variation of Ancheta et al. (2011) (left) and Harichandran and Vanmarcke (1986) (right) lagged coherency models, for horizontal components, with frequency at four separation distances.

(a) rock   (b) soil
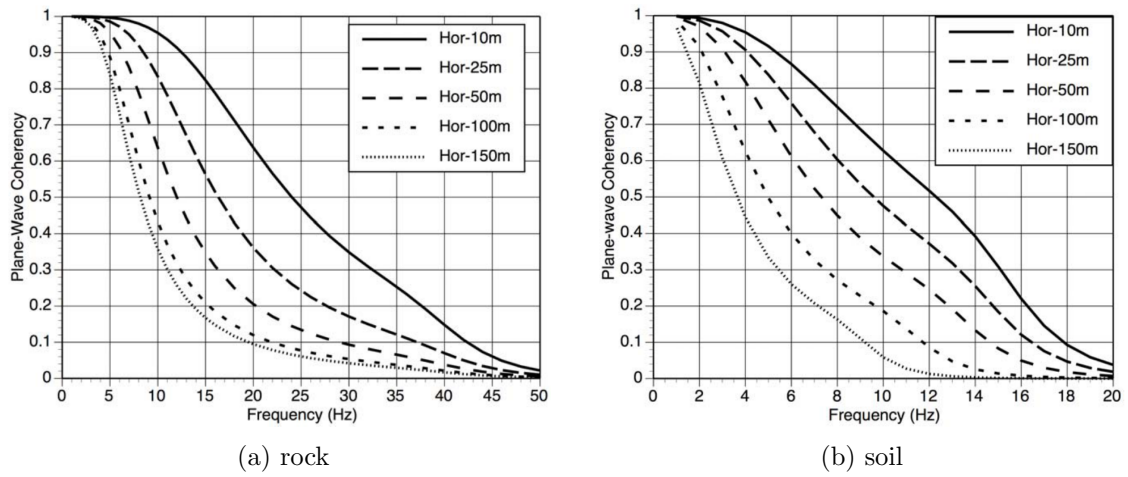
Figure 2.7: Abrahamson (2007) plane wave coherency models for hard rock sites (left) and soil sites (right) for horizontal components.

Code	Array	Location	Site type	Topography	N° stations	Inter-station distance range [m]
1	EPRI LSST	Taiwan	Soil ($V_{s,30} = 210$)	flat	15	3 - 85
2	UPSAR	CA	Soft Rock ($V_{s,30} = 400$)	flat	13	24-952
3	Chiba	Japan	Soil ($V_{s,30} = 290$)	flat	15	5 - 319
5	Imperial Valley differential	CA	Soil ($V_{s,30} = 180$)	flat	5	18 -213
6	Hollister Differential	CA	Soil ($V_{s,30} = 215$)	flat	4	61-256
7	Stanford	CA	Soil	flat	4	32-185
8	Coalinga	CA	Soft rock	flat	7	32-185
9	UCSC ZIYA	CA	Soft rock	mountains	6	25-300
10	Pinyon Flat	CA	Hard Rock ($V_{s,30} = 1030$)	flat	58	7-340
11	SMART-1	Taiwan	Soil ($V_{s,30} = 210$)	flat	39	100-4000
12	Borrego Valley	CA	Soil ($400< V_{s,30} <600$)	flat	6	10-160
13	SMART-2	Taiwan	Soil ($V_{s,30} = 210$)	flat	8	200-750
14	Argostoli	Greece	Soil + Rock	flat	21	10-180

Table 2.1: List of the dense arrays whose recordings were used in the definition of the spatial coherency models reported in Table 2.2.

References	Array Code	Site type	Inter-station distance [m]	Magnitude	Sorce-to-site Distance [km]	Applicability
Harichandran and Vanmarcke 1986	11	Soil ($V_{s,30} = 210$)	100-1000	4.9-6.9	8-116	d>100 m
Abrahamson et al 1991	1	Soil ($V_{s,30} = 210$)	3 - 85	3.7-7.8	5-80	30 m <d<100 m
Abrahamson et al 2006	1,2,3,5,6,7, 8,10,11,13	all soil types	3-750	3-7.8	5-113	All type of soil
Abrahamson et al 2007	10	Hard rock ($V_{s,30} = 1030$)	7-340	2-3.6	14-39	Hard rock, d<150 m
Abrahamson et al 2007	1,3,5,6	Soft soil ($180<V_{s,30}<290$)	3-319	3-7.8	5-113	Soft soil ($180<V_{s,30}<290$), d<150 m
Ancheta et al 2011	12	Soil ($400<V_{s,30}<600$)	10-160	2.5 - 4.9	3 - 79.4	d<100 m

Table 2.2: List of some of the empirical models present in literature. The column "Array Code" associates the spatial coherency empirical models with the dense arrays, whose recordings were used in the definition of the models themselves, which are reported in Table 2.1.

Chapter 3

Spatial coherency of seismic ground motion from recordings

This section presents the statistical analyzes of the spatial coherency of seismic ground motions obtained from data recorded at four different dense arrays: the ICEARRAY (Iceland), the UPSAR array (California), the L'Aquila array (Central Italy) and the Mirandola array (Northern Italy).

First, a brief description of the arrays and earthquakes under study are reported, then the procedure adopted to estimate the SVEGM is summarized and finally the results are shown and commented.

3.1 Case studies

The recording dataset used in this study has been provided by four dense arrays: the ICEARRAY, the UPSAR array, the L'Aquila array and the Mirandola array. These arrays collects data from locations with different geological, geomorphological and seismological properties making a comparison between the results very interesting.

If on one side ICEARRAY and UPSAR array consists on 14 and 13 stations, respectively, allowing to effectively take advantage of the statistical properties of coherency as a descriptor of a stochastic process; on the other side the Italian arrays are composed by only four arrays each leading to strong bias and variance in the results providing difficulties in the interpretation of the results itself. However, they are analyzed in the study herein since they give a contribution to the study of SVEGM based on data taken from the Italian territory.

As a common feature to all case studies, the recordings at each station consist of three components (north-south NS, east-west EW, and vertical UP), sampled at time intervals $\Delta t = 0.005 \ s$.

In the following pages a brief description of the arrays and the earthquakes analyzed are reported. Some of the relevant informations are summarized in Table 3.1.

Array	N° stations	Inter-station distance range [m]	Soil Type ($V_{s,30}$ m/s)	Earthquake date	R_{epi} [km]	M_w
ICEARRAY (Iceland)	14	50 - 1873	Rock	May 2008 (Ölfus)	7.2	6.3
UPSAR (CA)	13	21 - 731	Rock (580)	Sep 28, 2004 (Parkfield)	12.0	6.0
				Dec 22, 2003 (San Simeon)	56.0	6.5
L'Aquila	4	295 - 1157	Rock (570)	Apr 6, 2009 (Aquila)	5	6.3
				Apr 9, 2009 (Aquila)	14.5	5.4
				Aug 24, 2016 (Amatrice)	36.8	6.0
				Oct 30, 2016 (Norcia)	54.0	6.5
Mirandola	4	2 - 943	Soil (210)	May 29, 2012	4	6

Table 3.1: Summary of information on the dense station networks used for the evaluation of the SVEGM

3.1.1 ICEARRAY

The ICEARRAY is the first small-aperture strong-motion array in Iceland. It is located in the town of Hveragerði, in the Ölfus District of South Iceland. The high seismicity and the presence of numerous lifeline systems such as bridges, cross-country pipelines, electric transmission systems make the ICEARRAY one of the most interesting dense arrays to be studied.

It consists on 14 stations located on a rock site (see Figure 3.2) and distributed within an area of about 1.23 km^2. The array has an aperture of 1.9 km and a minimum inter-station distance of 50 m.

The analysis has been focused on the recordings of the 29 May 2008 Ölfus earthquake ($M_w = 6.3$): a shallow crustal earthquake caused by the rupture of a nearly vertical north-south trending (strike-angle equal to 0°), right-lateral strike-slip fault. Note that the recordings data were kindly provided by Prof. Rajesh Rupakhety (University of Iceland).

Due to the relatively strong magnitude earthquake and the small source-to-site distance (7.2 km), the Ölfus earthquake represents a perfect scenario for the study of the spatial coherency in near-fault situation.

(a)   (b)
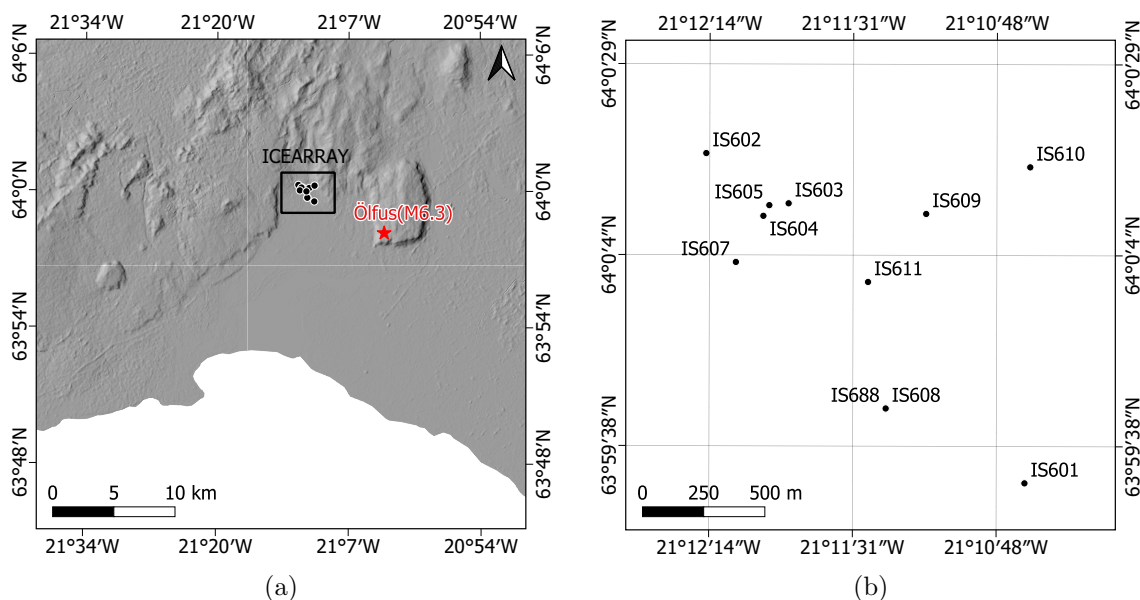
Figure 3.1: Location of ICEARRAY: a) Geographical overview and b) ICEARRAY geometry
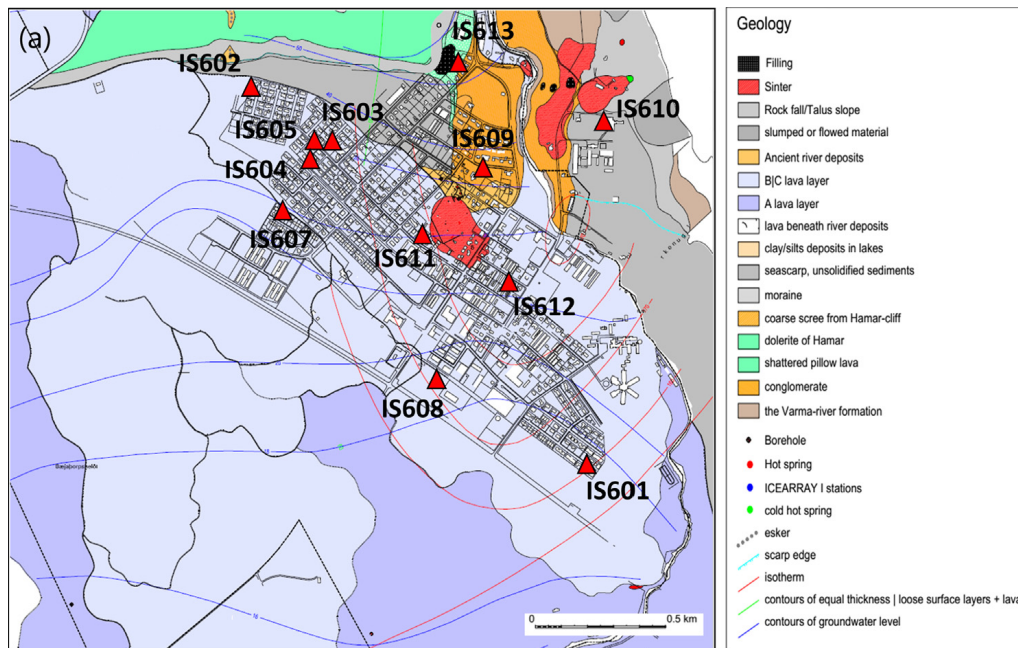
Figure 3.2: Geological map of Hveragerði showing that most of the town is located on lava. The ICEARRAY I station locations are marked as red triangles. Adopted from Rahpeyma et al. (2016).

The complete dataset, consisting of the ground acceleration time histories recorded by the 14 available stations in the three horizontal components (two horizontal components and one vertical component), is shown in Figures 3.3, 3.4, 3.5, respectively. At variance with standard processing schemes based on band-pass filtering, the horizontal components have been rotated along the strike-parallel (positive towards north) and strike-normal (positive towards east) directions. The acceleration shown is the raw recorded data.
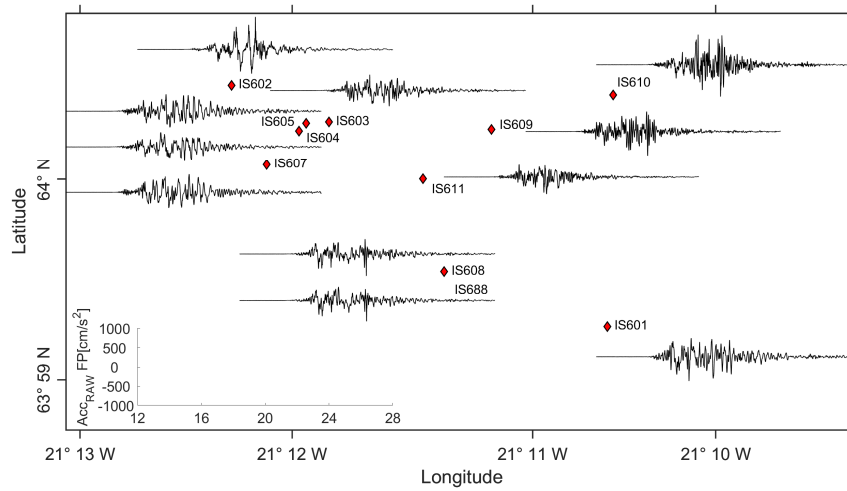
Figure 3.3: North–south (strike-parallel) component of recorded acceleration across ICEARRAY during the earthquake of 29 May 2008.
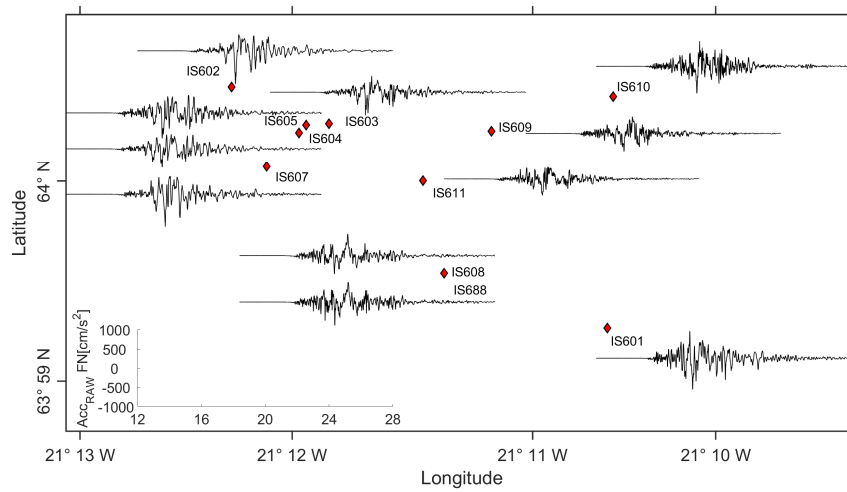
Figure 3.4: East–west (strike-normal) component of recorded acceleration across ICEARRAY during the earthquake of 29 May 2008.

34
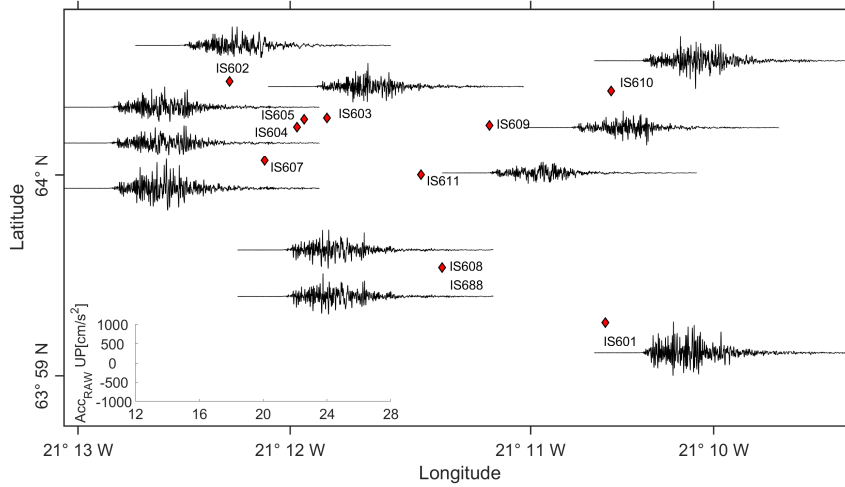
Figure 3.5: Vertical component of recorded acceleration across ICEARRAY during the earthquake of 29 May 2008

eBasco procedure - Computation of permanent displacement

The raw recording of the earthquake mainshock coming from the 13 stations composing the ICEARRAY were elaborated thought the semi-automatic processing scheme, eBASCO, which was proposed by D'Amico et al. (2019) and allows to recover the tectonic filing (permanent displacement) from near-source records. The method, based on a piecewise linear detrend of the strong-motion (SM) recordings, is applied to reconstruct the ground displacement field of the 29 May 2008 Ölfus earthquake ($M_w = 6.3$).

Without entering too much in detail, the baseline shift of an acceleration record is subdivided into three contributions defined by the following time windows (see Figure 3.6,d): (1) pre-event window between the time of the first sample T0 and the time T1 from which the ground starts moving toward the PD; (2) transient window, between time points T1 and T2; and (3) postevent window from T2 to the end of the signal.

First, we subtract from the acceleration trace the amplitude of the first sample so that the velocity equals zero in T0 through least-squares fitting. A further least-squares fitting is used to remove the linear trend in the postevent window (from T2 to the end of the signal) of the velocity waveforms.

In the transient phase, a baseline offset that is representative of the complex shift in baseline during the strong shaking is removed in the acceleration transient

windows and then the latter is integrated to obtain the velocity. The pre-event, transient, and postevent windows are then combined into the corrected velocity waveform. Finally, the corrected displacement and acceleration traces are computed by integration and derivation of the corrected velocity time series, respectively (Figure 3.6,d). Since the time steps T1 and T2 are variable and the final result is very sensitive to their value, they must be choice accurately: according to D'Amico et al. (2019), the best solution is the one characterized by the maximum value of the flatness indicator f in the region between T3 and the end of the signal:

$$f = \frac{r}{|b| \cdot \sigma} \tag{3.1}$$

where r is the linear correlation coefficient, b is the slope of the linear fit, and σ is the variance of the residual displacement. The Figure 3.6 offers a schematic view of the conceptual model, the raw time series, and the results the corrected one through the eBasco procedure.
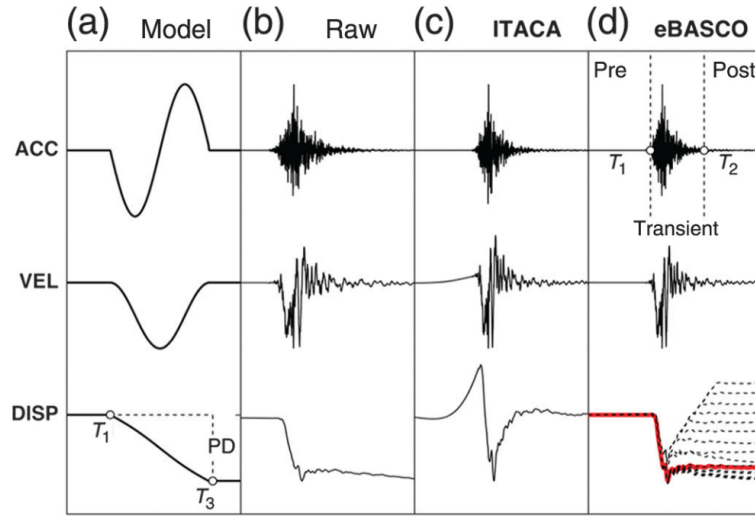
Figure 3.6: eBasco procedure. (a) Analytical model of the fling step. (b) Raw acceleration, velocity and displacement time histories (c) ITACA procedure (it will not be treated in the present implementation) (d) the piecewise linear detrend. Pre-event, transient, and postevent windows are highlighted; red line, extended BASeline Correction (eBASCO) ground displacement corresponding to the optimal choice of T1 and T2 time correction points (maximum f-value); dashed black lines, solution set corresponding to different combinations of T1 and T2 correction points. From D'Amico et al. (2019)

The computed velocity and displacement time histories are shown for each station

and component in Figures 3.7, 3.8, 3.9, 3.10, 3.11, 3.12.
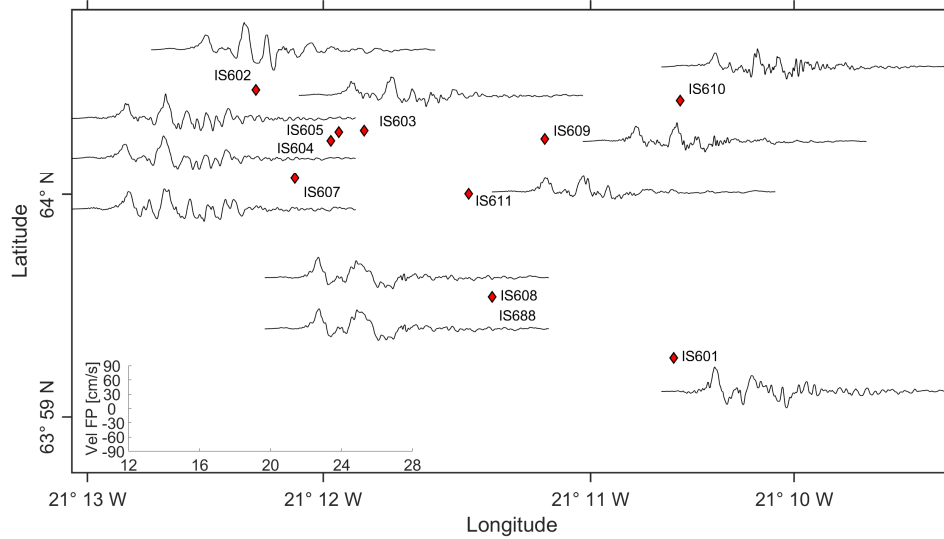
Figure 3.7: North–south (strike-parallel) component of recorded and corrected velocity across ICEARRAY during the earthquake of 29 May 2008.
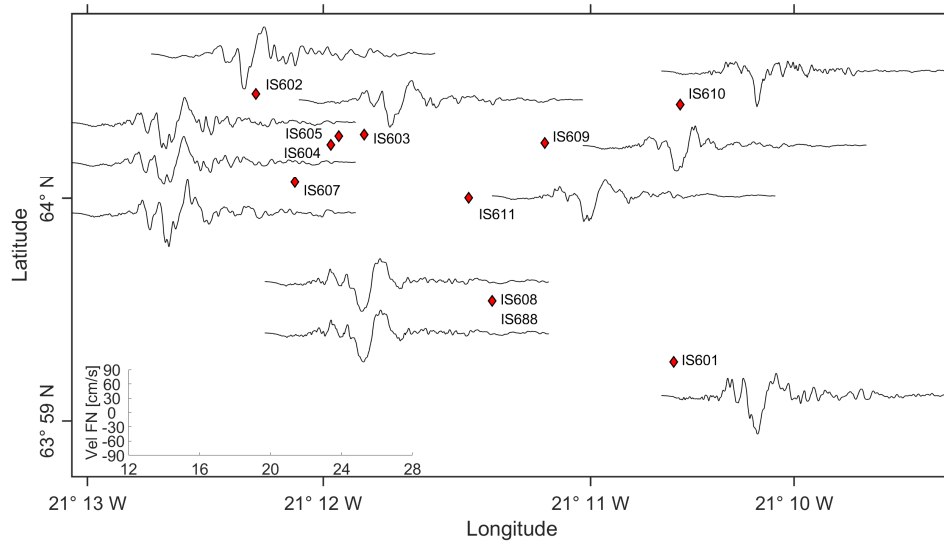
Figure 3.8: East–west (strike-normal) component of recorded and corrected velocity across ICEARRAY during the earthquake of 29 May 2008.
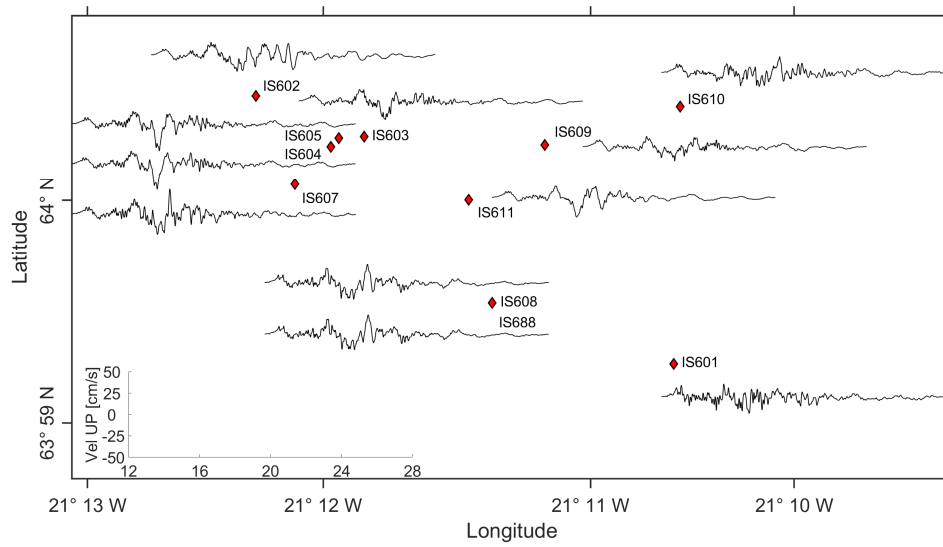
Figure 3.9: Vertical component of recorded and corrected velocity across ICEAR-RAY during the earthquake of 29 May 2008.
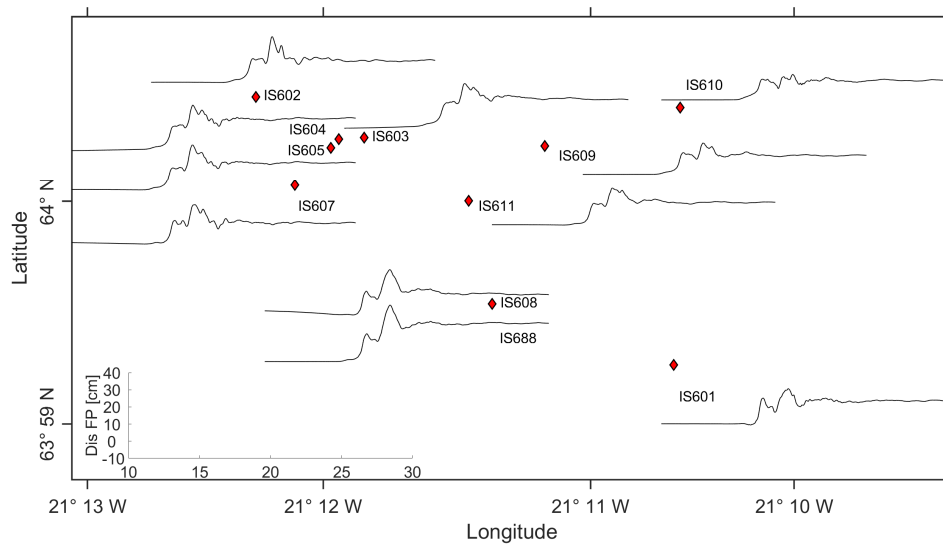
Figure 3.10: North–south (strike-parallel) component of recorded and corrected displacement across ICEARRAY during the earthquake of 29 May 2008.
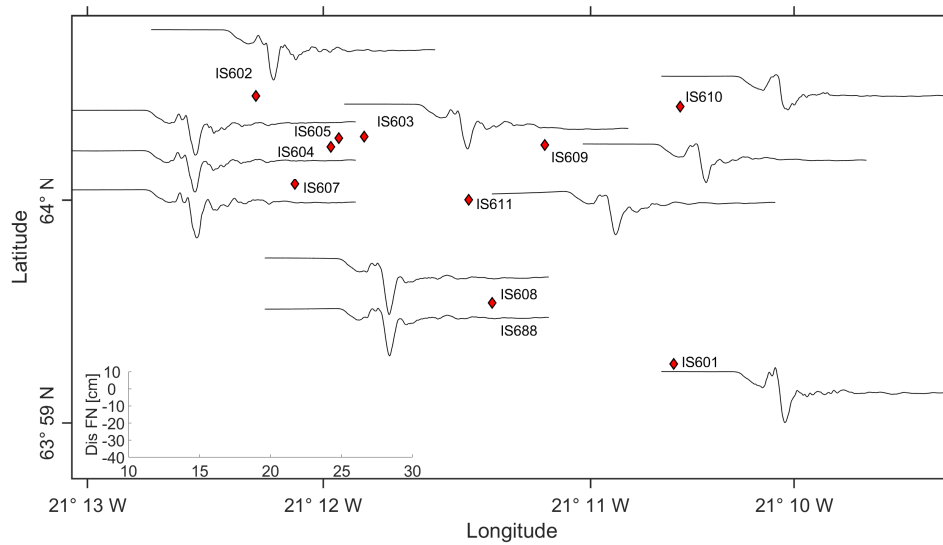
Figure 3.11: East–west (strike-normal) component of recorded and corrected displacement across ICEARRAY during the earthquake of 29 May 2008.
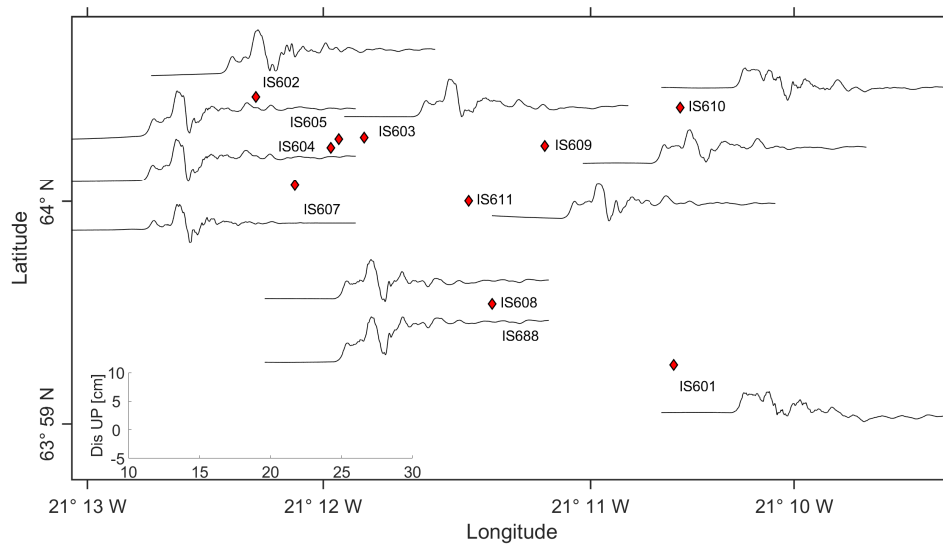
Figure 3.12: Vertical component of recorded and corrected displacement across ICEARRAY during the earthquake of 29 May 2008.

Peak values of motion and attenuation curves

Before showing the results of spatial coherency analysis on ICEARRAY recordings, the distribution of peak ground motion values and their attenuation with distance is studied.

Tables 3.2,3.3 and 3.4 show, with respect to each station, the focal distance (R_{HYP}), the Joyner-Boore distance (R_{JB}) and the peak ground acceleration (PGA), velocity (PGV) and displacement (PGD), respectively, in each component of motion as well as the parameters HGM, FN/FP, UD/HGM which defines, respectively, the geometric mean between of the horizontal components, the ratio fault-normal over fault-parallel and the ratio between the vertical component and the mean between the horizontal one.

It is interesting to note that PGA, PGV and PGD are higher, almost for all the stations, in the FN component with respect to the FP one (ratio FN/FP). This is in agreement with the common observation that the fault-normal component is excited with more power than the fault-parallel: as observed by Somerville et al. (1997), in near-fault region the fault-normal direction ground motions are systematically larger than the ones in strike-parallel direction dose to faults at spectral periods longer than 0.6 second due to rupture directivity effects. Note that in the present case study the effects of rupture directivity appears also since spectral period equal to 0 second (PGA).

As observed by Somerville et al. (1997), site which are aligned to the direction of rapture, of slip and of wave propagation experience the maximum intensity of the directivity effect. The conditions for the forward directivity effect are easily met in strike-slip faulting: the maximum in the SH radiation pattern (which act in FN direction) is oriented in the direction along the strike, which is also the slip direction (see Figure 3.13).

In dip-slip faulting mechanisms (normal and reverse), the directivity conditions are also met especially in sites directly up-dip from the hypocenter whereas stations located along the strike do not experience directivity effects because the horizontal rupture direction coincides with a minimum in the total S radiation pattern.

Figure 3.14 shows how actually changes the FN velocity time history between a site forward to the rupture propagation (Lucerne) and one backward (Joshua Tree).
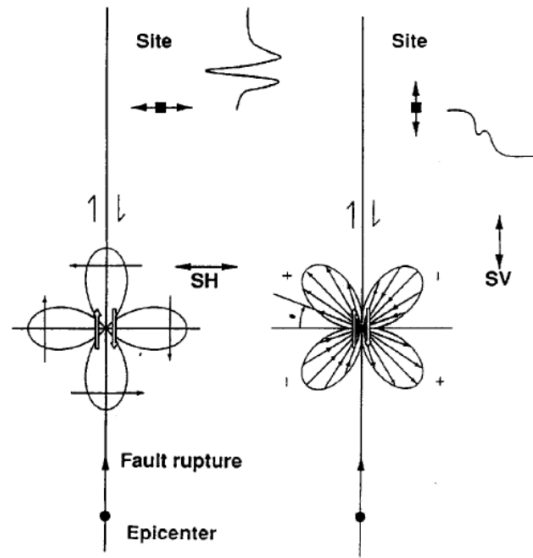
Figure 3.13: SH and SV radiation patterns for a vertical strike-slip fault. From Somerville et al. (1997)
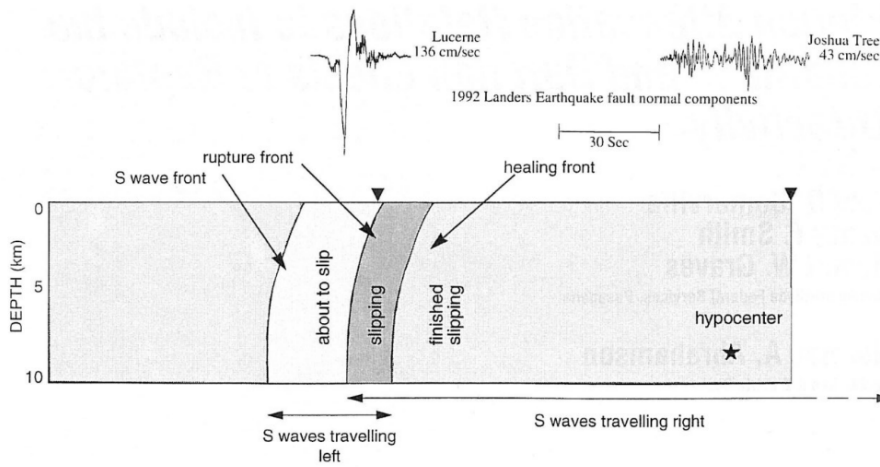
Figure 3.14: Rupture propagation and directivity effects. From Somerville et al. (1997)

Station ID	R_{HYP} [km]	R_{JB} [km]	PGA $[cm/s^2]$					
			FP	FN	UD	HGM	$\frac{FN}{FP}$	$\frac{UD}{HGM}$
IS601	8.31	0.9	628.8	813.9	808.2	715.4	1.3	1.1
IS610	8.78	1.0	825.3	700.4	729.7	760.3	0.8	1.0
IS609	8.98	1.4	627.2	465.5	458.7	540.4	0.7	0.8
IS608	8.80	1.5	541.0	612.5	594.5	575.7	1.1	1.0
IS688	8.80	1.5	569.4	566.6	525.4	568.0	1.0	0.9
IS611	9.04	1.6	445.4	431.2	289.2	438.2	1.0	0.7
IS603	9.39	1.9	413.6	600.4	612.4	498.3	1.5	1.2
IS604	9.44	2.0	377.5	492.9	458.2	431.4	1.3	1.1
IS605	9.44	2.0	439.5	656.6	531.3	537.2	1.5	1.0
IS607	9.45	2.1	473.1	848.7	775.5	633.6	1.8	1.2
IS602	9.71	2.3	844.0	858.9	487.8	851.4	1.0	0.6

Table 3.2: Peak ground acceleration (PGA), recorded at the ICEARRAY during the 2008 Ölfus earthquake. PGA values along the FN, FP, UD components together with the ratios FN/FP and UD/HGM are listed.

Station ID	R_{HYP} [km]	R_{JB} [km]	PGV $[cm/s]$					
			FP	FN	UD	HGM	$\frac{FN}{FP}$	$\frac{UD}{HGM}$
IS601	8.31	0.9	51.6	81.2	18.7	64.7	1.6	0.3
IS610	8.78	1.0	38.5	75.2	19.1	53.8	2.0	0.4
IS609	8.98	1.4	39.6	53.8	15.9	46.2	1.4	0.3
IS608	8.80	1.5	42.4	61.1	23.5	50.9	1.4	0.5
IS688	8.80	1.5	42.4	63.0	22.5	51.7	1.5	0.4
IS611	9.04	1.6	34.3	54.2	22.6	43.1	1.6	0.5
IS603	9.39	1.9	39.8	57.8	21.1	47.9	1.5	0.4
IS604	9.44	2.0	47.7	54.9	29.9	51.2	1.2	0.6
IS605	9.44	2.0	52.2	54.8	30.6	53.5	1.1	0.6
IS607	9.45	2.1	42.5	71.4	30.6	55.1	1.7	0.6
IS602	9.71	2.3	57.5	73.5	18.2	65.0	1.3	0.3

Table 3.3: Same as in Table 3.2 but for Peak Ground Velocity (PGV).

Station ID	R_{HYP} [km]	R_{JB} [km]	PGD [cm]					
			FP	FN	UD	HGM	$\frac{FN}{FP}$	$\frac{UD}{HGM}$
IS601	8.31	0.9	20.8	29.7	3.7	24.8	1.4	0.2
IS610	8.78	1.0	14.8	29.1	7.2	20.7	2.0	0.3
IS609	8.98	1.4	18.2	25.8	6.6	21.7	1.4	0.3
IS608	8.80	1.5	33.0	25.0	7.1	28.7	0.8	0.2
IS688	8.80	1.5	23.6	26.1	8.6	24.8	1.1	0.3
IS611	9.04	1.6	21.4	28.5	4.6	24.7	1.3	0.2
IS603	9.39	1.9	26.2	27.2	7.9	26.7	1.0	0.3
IS604	9.44	2.0	27.0	33.2	6.9	30.0	1.2	0.2
IS605	9.44	2.0	26.9	22.8	5.8	24.8	0.8	0.2
IS607	9.45	2.1	21.7	19.8	3.5	20.7	0.9	0.2
IS602	9.71	2.3	26.7	23.1	5.2	24.9	0.9	0.2

Table 3.4: Same as in Table 3.2 for the Peak Ground Displacement (PGD).

Furthermore PGA and PGV, obtained for the two horizontal components, as a function of the focal distance (Figures 3.15,a and 3.16,b) and Joyner-Boore distance (Figures 3.15,b and 3.16,b) have been compared with the Bindi et al. (2014) (class of site A) and Akkar et al. (2014) ($Vs, 30 = 800m/s$) ground motion prediction equations (GMPE). Note that Bindi et al. (2014) provides models for both PGA and PGV while Akkar et al. (2014) defines, only, the attenuation function model for PGA.

Ground Motion Prediction Equations (GMPEs) are, in general, predictive relationships usually expressing ground motion parameters as functions of magnitude (M), source-to-site distance (R), site classification and in some cases, other variables (e.g. fault mechanism). They are developed by regression analyzes of recorded strong motion databases starting from a functional form which aim at reflecting the mechanics of the ground motion process as closely as possible. In particular, GMPEs like Bindi et al. (2014) and Akkar et al. (2014) describe the trend of PGA and/or PGV as a function of a specific metric of source-to-site distance (epicentral R_{epi}, hypocentral R_{HYP} and distance to the surface projection of the rupture, R_{JB} are most commonly used).

It is interesting to note that the observed peak ground motion values fall system-

atically above the median curve of the GMPEs - in many cases also above the 84th percentile curves - meaning that the actual near-fault ground motions exceed significantly the values predicted by the commonly used empirical models.
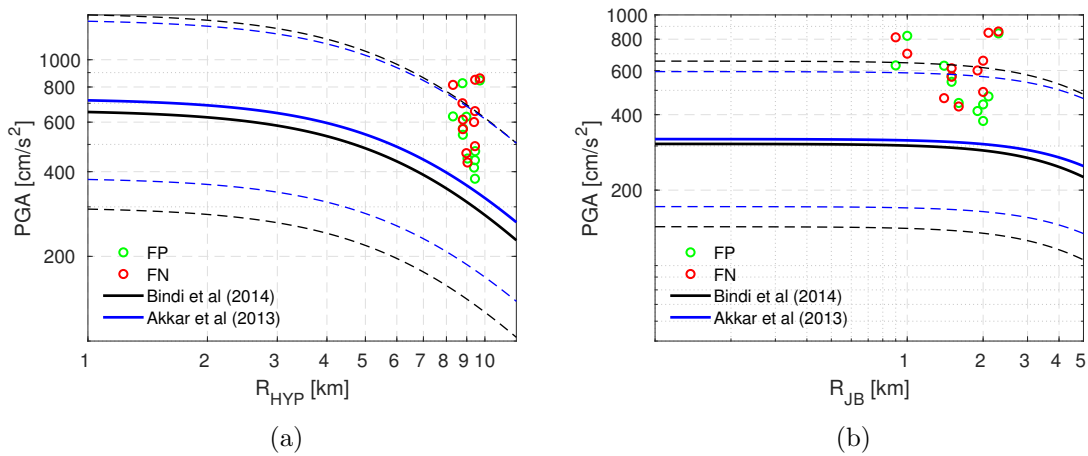
Figure 3.15: Comparison between the recorded values of PGA obtained during the Öflus earthquake and the attenuation curves developed by Bindi et al. (2014) and Akkar et al. (2014). The dotted lines represent the 16 and 84 percentile of the probabilistic distribution that characterize Bindi et al.(2014) relationship.
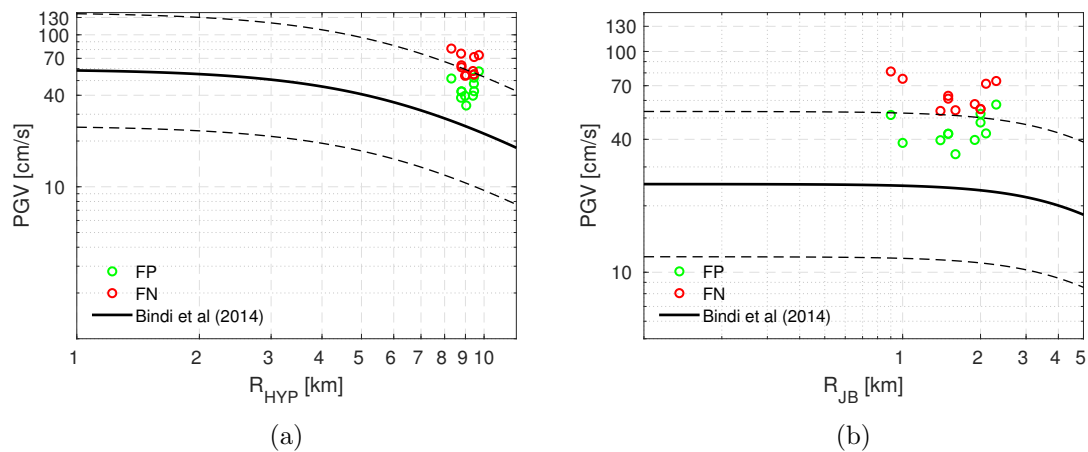
Figure 3.16: Comparison between the recorded values of PGV obtained during the Öflus earthquake and the attenuation curves developed by Bindi et al. (2014). The dotted lines represent the 16 and 84 percentile of the probabilistic distribution that characterize Bindi et al.(2014) relationship.

3.1.2 UPSAR

The US Geological Survey Parkfield Seismograph Array (UPSAR), located at the southern end of the section of the San Andreas fault on a rock site, is composed by 13 stations. The array has an aperture of 0.74 km and a minimum inter-station distance of 21 m .

A detailed description of the array and the topography of the site are given by Fletcher et al. (1992).

In this study two earthquake events has been analyzed: the 2003 San Simeon earthquake ($M_w = 6.5$) and the 2004 Parkfield ($M_w = 6.0$). They were originated by two ruptures of the San Andreas fault (strike-slip fault trending with a strike angle of 320° and 140°, respectively, with respect to the north) which took place, respectively, at about 45 and 12.5 km from the UPSAR array.

Figure 3.17a shows the position of the UPSAR with respect to the epicenters of the two events considered, while Figure 3.17b depicts relative locations of the stations of the UPSAR network, where station P5 is selected as the reference station.
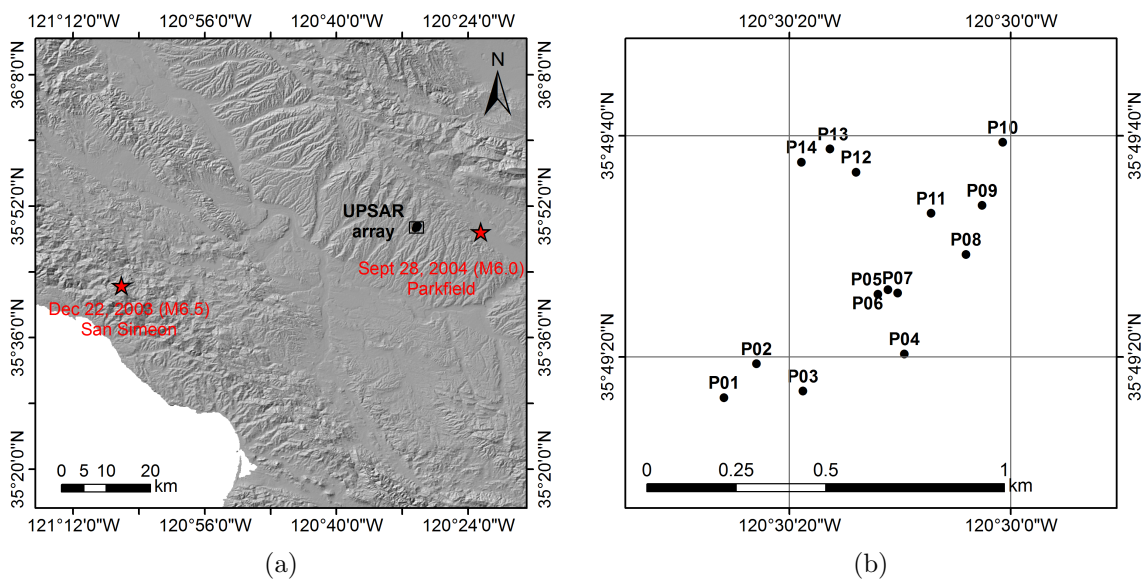
Figure 3.17: Location of UPSAR array: a) Geographical overview and b) UPSAR array geometry

The original array consists of 14 stations, but the instruments at P4 and P14 failed to record, thus only 12 stations are actually available. The recordings at each station consist of three components of acceleration time histories, sampled at time intervals

45

$\Delta t = 0.005$ s. Figures 3.19 (strike-angle 140°) and 3.20 (strike-angle 320°) show the acceleration time histories relative to Parkfield and San Simeon, respectively, for the fault-parallel (FP), fault-normal (FN), and vertical (UP) components.

Since the array covers a very small area (0.45 km^2), these data offer some interesting insights into spatial variations of seismic ground motions

Figure 3.18 shows a map illustrating the relative position between the San Simeon (M 6.5) and the Parkfield (M 6.0) earthquakes, with the respective faults' projections on ground surface, and UPSAR array. Note that in the map are reported also other events (aftershock) which are not considered in the present study.
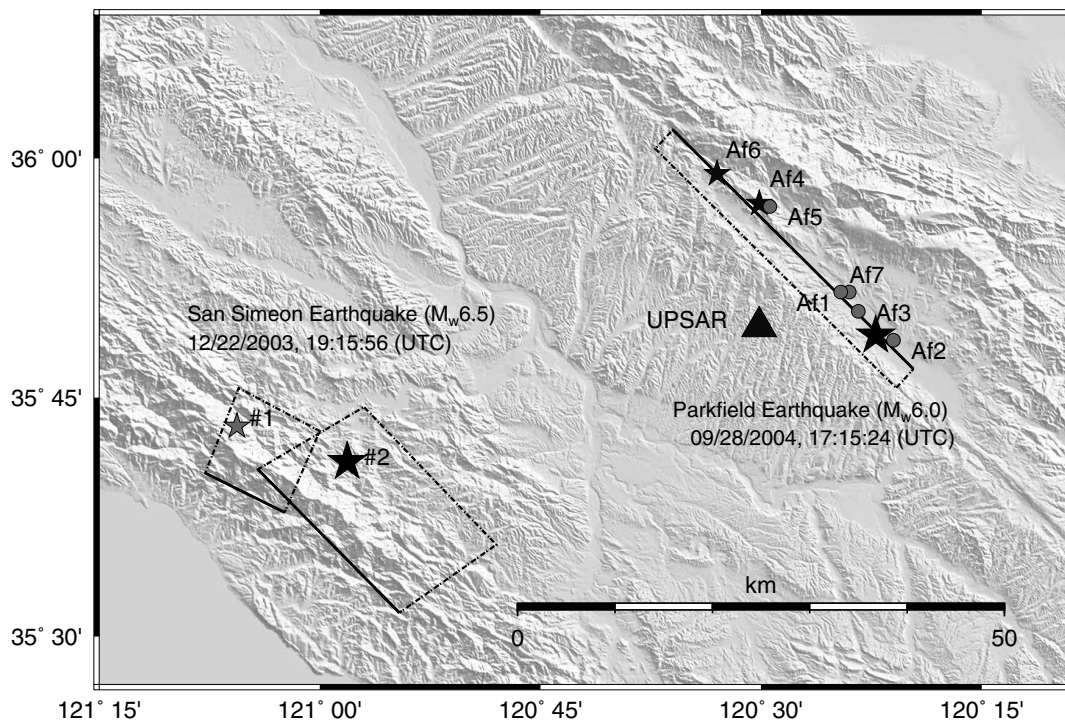
Figure 3.18: Map showing epicenters of the 2003 San Simeon (M 6.5) and the 2004 Parkfield (M 6.0) earthquakes (two large dark stars). The rectangular areas surrounded by solid and broken lines indicate projections of the fault rupture planes on ground surface. The solid lines indicate the top edge of the fault planes. Original times and other parameters of these events are listed in Table 1 and 3. The large filled triangle indicates the location of the UPSAR. From Wang et al. (2006).
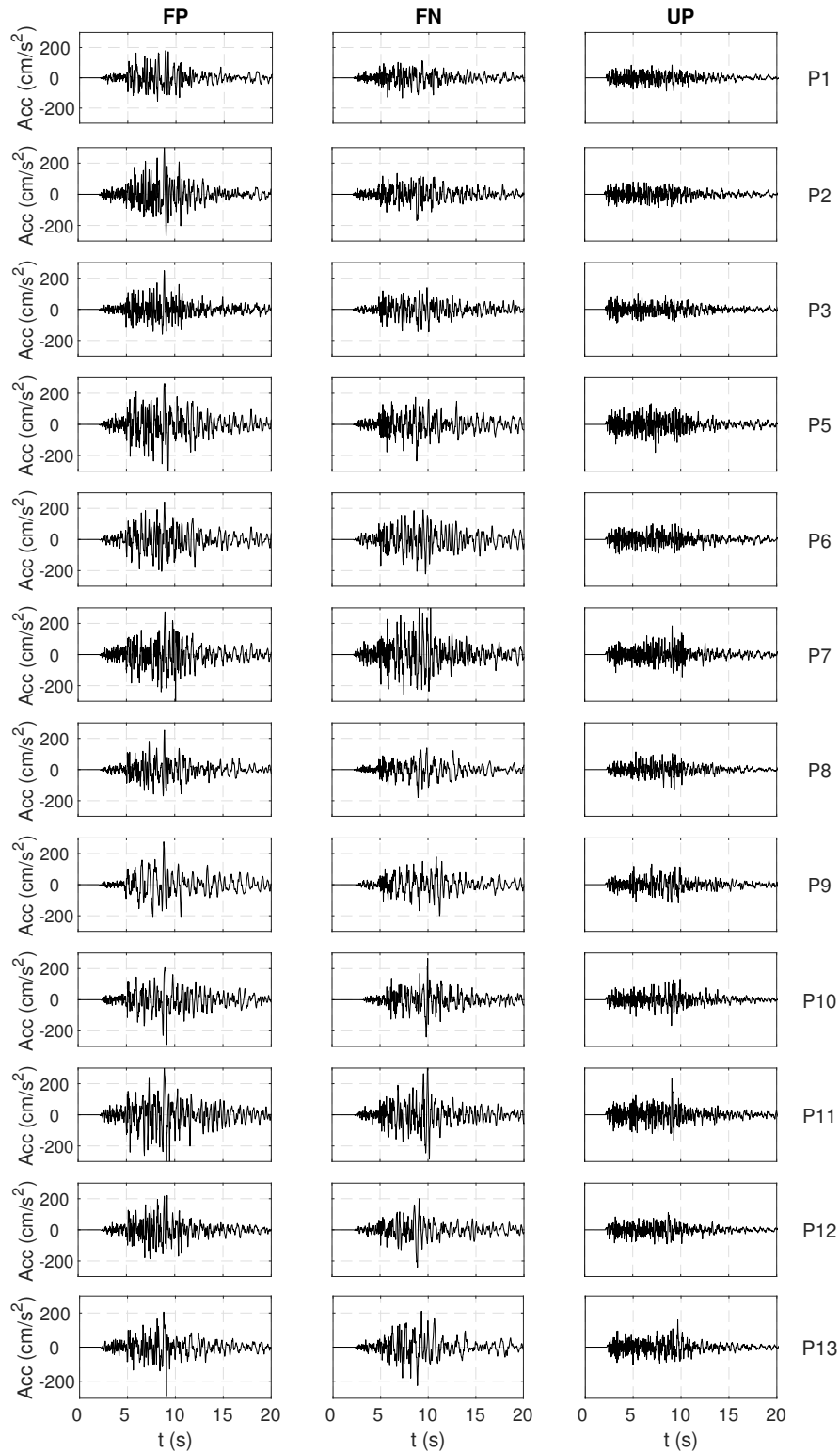
Figure 3.19: Parkfield earthquake acceleration time histories.
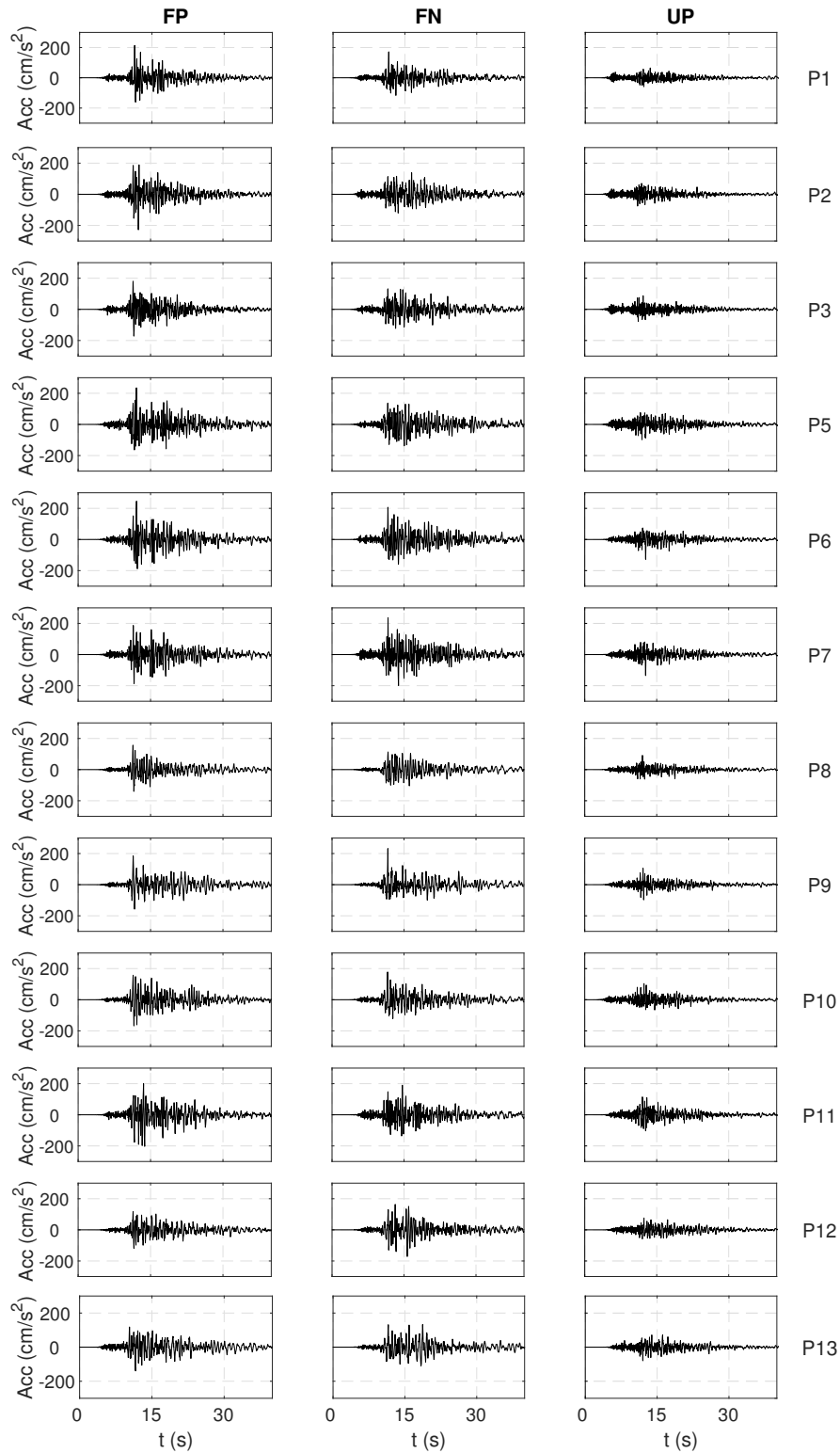
Figure 3.20: San Simeon earthquake acceleration time histories.

Peak values of motion and attenuation curves

Before showing the results of the SVEGM analysis carried out on UPSAR array recordings, the distribution of peak ground motion values and their attenuation with distance is studied.

Considering Parkfield event, Tables 3.5,3.6 and 3.7 show, with respect to each station, the focal distance (R_{HYP}) and the peak ground acceleration (PGA), velocity (PGV) and displacement (PGD), respectively, in each component of motion as well as the parameters HGM, FN/FP, UD/HGM. Tables 3.8,3.9 and 3.10 show the same quantities computed for Parkfield but for San Simeon earthquake. Note that the PGD values are computed without considering the permanent component of displacement time histories (fling steps effect).

In the case studies herein, the behaviour observed for the ICEARRAY case for which the fault-normal component of ground motions was, at all stations, characterized by higher values than the fault-parallel one is not found. The reason could be linked to the fact that: the UPSAR array is not perfectly aligned with the strike slip faults directivity and, moreover, the directivity effect losses its effectiveness increasing the source-to-site distance. Indeed, as shown in Figure 3.18 UPSAR array is not aligned with the faults who generated Parkfield and San Simeon earthquakes.

Station ID	R_{HYP} [km]	PGA [cm/s^2]					
		FP	FN	UD	HGM	$\frac{FN}{FP}$	$\frac{UD}{HGM}$
P1	14.42	200.9	144.3	88.4	170.3	0.7	0.5
P2	14.36	302.0	212.8	86.0	253.5	0.7	0.3
P3	14.27	246.6	151.9	104.9	193.5	0.6	0.5
P5	14.14	287.5	307.2	180.7	297.2	1.1	0.6
P6	14.13	251.1	220.4	110.1	235.3	0.9	0.5
P7	14.11	333.0	395.6	187.0	363.0	1.2	0.5
P8	13.99	300.1	183.6	131.9	234.7	0.6	0.6
P9	13.97	305.1	176.1	133.3	231.8	0.6	0.6
P10	13.95	368.7	148.0	170.8	233.6	0.4	0.7
P11	14.06	328.9	434.0	233.0	377.9	1.3	0.6
P12	14.21	297.3	251.2	111.7	273.3	0.8	0.4
P13	14.27	263.0	185.3	161.0	220.7	0.7	0.7

Table 3.5: Peak ground acceleration (PGA), recorded at the UPSAR array during the 2004 Parkfield earthquake. PGA values along the FN, FP, UD components together with the ratios FN/FP and UD/HGM are listed.

Station ID	R_{HYP} [km]	PGV [cm/s]					
		FP	FN	UD	HGM	$\frac{FN}{FP}$	$\frac{UD}{HGM}$
P1	14.42	15.9	8.6	5.6	11.7	0.5	0.5
P2	14.36	21.9	9.0	3.7	14.0	0.4	0.3
P3	14.27	15.5	11.0	4.6	13.1	0.7	0.3
P5	14.14	23.7	16.8	6.2	20.0	0.7	0.3
P6	14.13	19.0	14.6	5.1	16.7	0.8	0.3
P7	14.11	21.5	17.5	5.9	19.4	0.8	0.3
P8	13.99	17.3	9.5	5.3	12.8	0.5	0.4
P9	13.97	21.3	13.0	8.9	16.6	0.6	0.5
P10	13.95	27.4	11.1	6.7	17.4	0.4	0.4
P11	14.06	21.4	19.2	9.0	20.3	0.9	0.4
P12	14.21	25.5	15.1	8.1	19.6	0.6	0.4
P13	14.27	24.9	11.5	8.0	16.9	0.5	0.5

Table 3.6: Same as in Table 3.5 but for Peak Ground Velocity (PGV).

Station ID	R_{HYP} [km]	PGD [cm]					
		FP	FN	UD	HGM	$\frac{FN}{FP}$	$\frac{UD}{HGM}$
P1	14.42	12.3	20.5	6.2	15.9	1.7	0.4
P2	14.36	12.6	21.0	5.0	16.3	1.7	0.3
P3	14.27	13.0	20.0	5.6	16.1	1.5	0.3
P5	14.14	15.0	20.2	5.1	17.4	1.3	0.3
P6	14.13	15.2	17.1	7.0	16.1	1.1	0.4
P7	14.11	14.6	18.0	7.0	16.2	1.2	0.4
P8	13.99	15.7	19.6	7.0	17.5	1.2	0.4
P9	13.97	18.9	22.1	6.8	20.5	1.2	0.3
P10	13.95	17.2	14.9	7.1	16.0	0.9	0.4
P11	14.06	17.2	22.8	7.7	19.8	1.3	0.4
P12	14.21	18.0	21.5	7.1	19.7	1.2	0.4
P13	14.27	20.3	20.0	4.9	20.1	1.0	0.2

Table 3.7: Same as in Table 3.5 but for Peak Ground Displacement (PGD).

Station ID	R_{HYP} [km]	PGA [cm/s^2]					
		FP	FN	UD	HGM	$\frac{FN}{FP}$	$\frac{UD}{HGM}$
P1	45.80	187.5	150.0	64.8	167.7	0.8	0.4
P2	45.90	174.5	155.6	75.8	164.8	0.9	0.5
P3	45.97	145.1	153.6	87.6	149.3	1.1	0.6
P5	46.22	186.2	212.8	98.4	199.0	1.1	0.5
P6	46.25	217.1	194.8	127.7	205.7	0.9	0.6
P7	46.27	189.4	214.4	135.4	201.5	1.1	0.7
P8	46.44	152.6	136.9	91.3	144.5	0.9	0.6
P9	46.52	256.6	132.8	105.2	184.6	0.5	0.6
P10	46.63	180.5	175.6	104.1	178.0	1.0	0.6
P11	46.41	190.7	176.1	114.9	183.3	0.9	0.6
P12	46.30	140.4	176.3	76.4	157.3	1.3	0.5
P13	46.26	156.2	121.8	80.2	138.0	0.8	0.6

Table 3.8: Peak ground acceleration (PGA), recorded at the UPSAR array during the 2003 San Simeon earthquake. PGA values along the FN, FP, UD components together with the ratios FN/FP and UD/HGM are listed.

Station ID	R_{HYP} [km]	PGV [cm/s]					
		FP	FN	UD	HGM	$\frac{FN}{FP}$	$\frac{UD}{HGM}$
P1	45.80	17.5	10.2	4.7	13.4	0.6	0.3
P2	45.90	16.7	13.2	4.6	14.9	0.8	0.3
P3	45.97	16.0	11.4	5.3	13.5	0.7	0.4
P5	46.22	15.7	14.8	6.7	15.2	0.9	0.4
P6	46.25	13.3	15.2	7.4	14.2	1.1	0.5
P7	46.27	14.3	12.6	7.3	13.4	0.9	0.5
P8	46.44	16.5	13.7	5.2	15.0	0.8	0.3
P9	46.52	21.0	10.8	4.9	15.1	0.5	0.3
P10	46.63	19.7	11.7	4.7	15.2	0.6	0.3
P11	46.41	14.3	15.8	8.3	15.0	1.1	0.5
P12	46.30	13.6	12.4	6.3	13.0	0.9	0.5
P13	46.26	15.1	10.6	6.1	12.7	0.7	0.5

Table 3.9: Same as in Table 3.8 but for Peak Ground Velocity (PGV).

Station ID	R_{HYP} [km]	PGD [cm]					
		FP	FN	UD	HGM	$\frac{FN}{FP}$	$\frac{UD}{HGM}$
P1	45.80	5.4	4.1	2.0	4.7	0.8	0.4
P2	45.90	5.4	4.1	2.0	4.7	0.8	0.4
P3	45.97	5.5	3.8	2.0	4.6	0.7	0.4
P5	46.22	5.3	4.1	2.2	4.6	0.8	0.5
P6	46.25	5.3	4.0	2.3	4.6	0.8	0.5
P7	46.27	5.2	4.0	2.3	4.5	0.8	0.5
P8	46.44	5.3	3.9	2.4	4.6	0.7	0.5
P9	46.52	5.0	3.5	2.2	4.2	0.7	0.5
P10	46.63	4.9	3.4	2.2	4.1	0.7	0.5
P11	46.41	5.3	3.5	2.1	4.3	0.6	0.5
P12	46.30	5.1	3.8	2.3	4.4	0.8	0.5
P13	46.26	4.8	3.7	2.1	4.2	0.8	0.5

Table 3.10: Same as in Table 3.8 but for Peak Ground Displacement (PGD).

Considering both UPSAR case studies , the PGA and PGV, obtained for the two horizontal components, as a function of the focal distance (Figures 3.21,a and 3.22,a for Parkfield and 3.21,b and 3.22,b for San Simeon) have been compared with the Bindi et al. (2014) (class of site B) and Akkar et al. (2014) ($Vs, 30 = 580m/s$) ground motion prediction equations (GMPE).

It is interesting to note that on one side all peak ground motion values obtained from the Parkfield recordings fall between the 50th and 84th percentile curves whereas on the other side the observed peak ground motion values from San Simeon fall even above the 84th percentile curves meaning that the San Simeon earthquake was characterized by an attenuation with distance which was lower than the one expected by the empirical models.

(a) Parkfield   (b) San Simeon
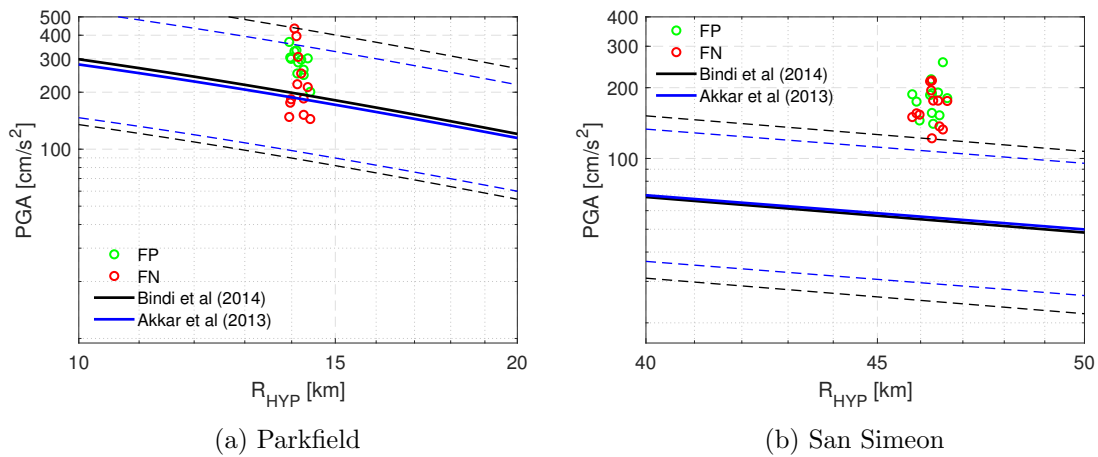
Figure 3.21: Comparison between the recorded values of PGA obtained during the Parkfield (a) and San Simeon (b) earthquakes and the attenuation curves developed by Bindi et al. (2014) and Akkar et al. (2014). The dotted lines represent the 16 and 84 percentile of the probabilistic distribution that characterize Bindi et al. (2014) relationship.

(a) Parkfield
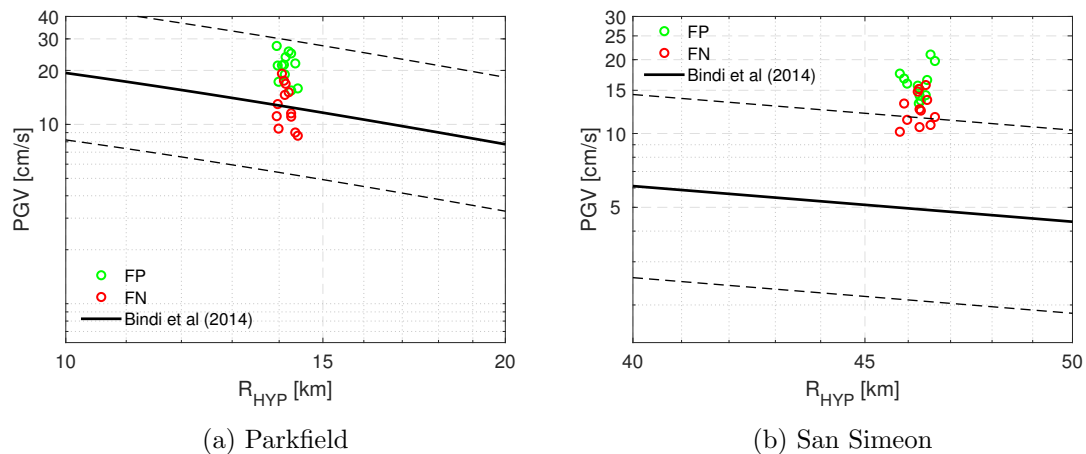
(b) San Simeon

Figure 3.22: Comparison between the recorded values of PGV obtained during the Parkfield (a) and San Simeon (b) earthquakes and the attenuation curves developed by Bindi et al. (2014). The dotted lines represent the 16 and 84 percentile of the probabilistic distribution that characterize Bindi et al.(2014) relationship.

3.1.3 Italian dense arrays: L'Aquila and Mirandola

Within the Italian territory there is a general lack of proper dense arrays (a group of stations characterized by an inter-station distance of maximum 1 km and half). L'Aquila and Mirandola arrays offers two examples small dense arrays in Italy. They are located both in Italy, L'Aquila in central while Mirandola in northern, and they are both constitutes by four stations. Unfortunately, AQM station failed to record all the event considered in this study, thus, as a matter of fact only 3 stations are actually available at the Aquila array.

As shown in Table 3.1 four events of magnitude ranging between 5.4 and 6.5 and source-to-site distance between 5 and 56 km occurred in the L'Aquila area are accounted while one event of magnitude 6 and source-to-site distance of 4 km is analyzed using the data provided by the Mirandola array. Table 3.11 summarize the main properties of the earthquakes considered in this study for the L'Aquila and Mirandola dense arrays.

The low number of stations leads to a lack of statistical redundancy which causes limited robustness of in the results: when a huge number of data is available, through statistical operations (stacking) is possible to reduce the noise in the results; this become unfeasible when few stations are present leading to unstable results. Never-

54

theless, they are very useful to our aim since they allows to study the SVEGM also over the Italian territory.

Figures 3.23a and 3.24a show the position of L'Aquila and Mirandola arrays, respectively, with respect to the epicenters of the events considered, while Figures 3.23b and 3.24b illustrate relative locations of the stations within the respective network.

(a)   (b)
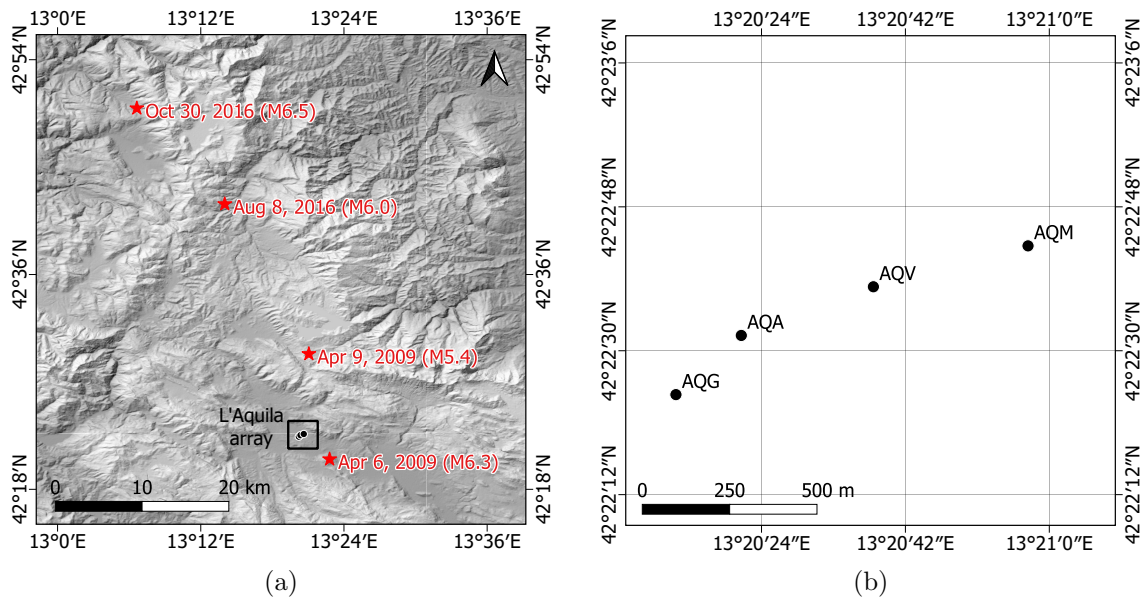
Figure 3.23: Location of L'Aquila array: a) Geographical overview and b) L'Aquila array geometry

| (a) | (b) |
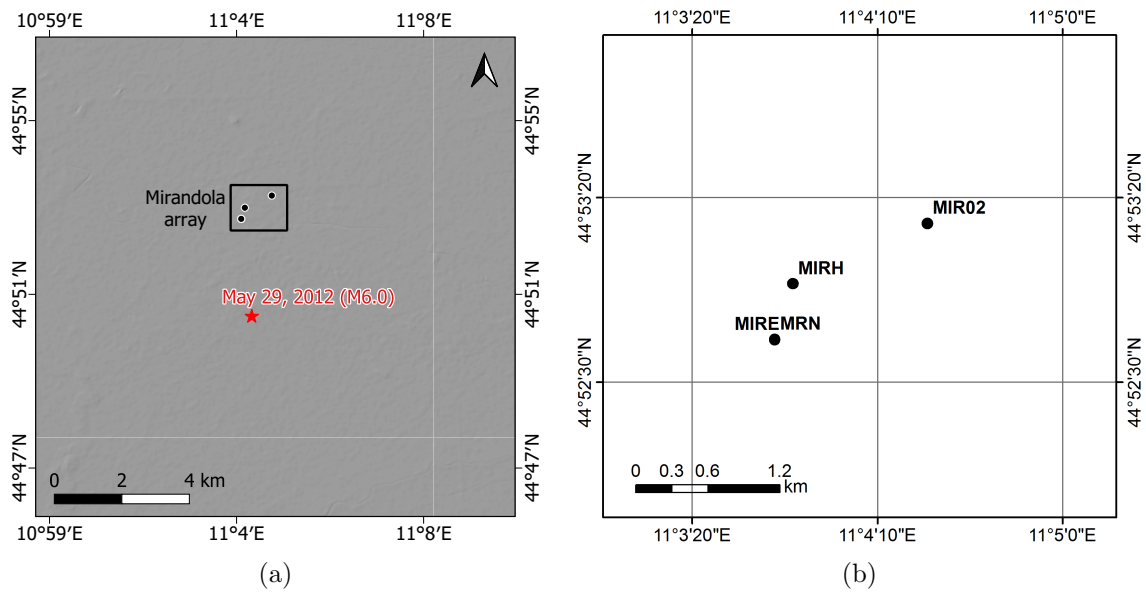
Figure 3.24: Location of Mirandola array: a) Geographical overview and b) Mirandola array geometry

Event Date	EventName	M_w	Lat (°)	Lon (°)	Depth (km)	Fault mech.	Strike (°)	R_{epi} (km)
Apr 6, 2009	L'Aquila mainshock	6.3	13.38	42.35	9.5	N	150	5
Apr 9, 2009	L'Aquila aftershock	5.4	13.35	42.49	11	N	150	14.5
Aug 24, 2016	Amatrice	6.0	13.23	42.69	8.1	N	156	36.8
Oct 30, 2016	Norcia	6.5	13.11	42.83	9.2	N	151	54
May 29, 2012	Emilia	6.0	11.08	44.85	10.4	R	95	4

Table 3.11: Italian case studies. Source parameters. N = Normal fault, R = Reverse fault.

Apr 6, 2009

Apr 9, 2009
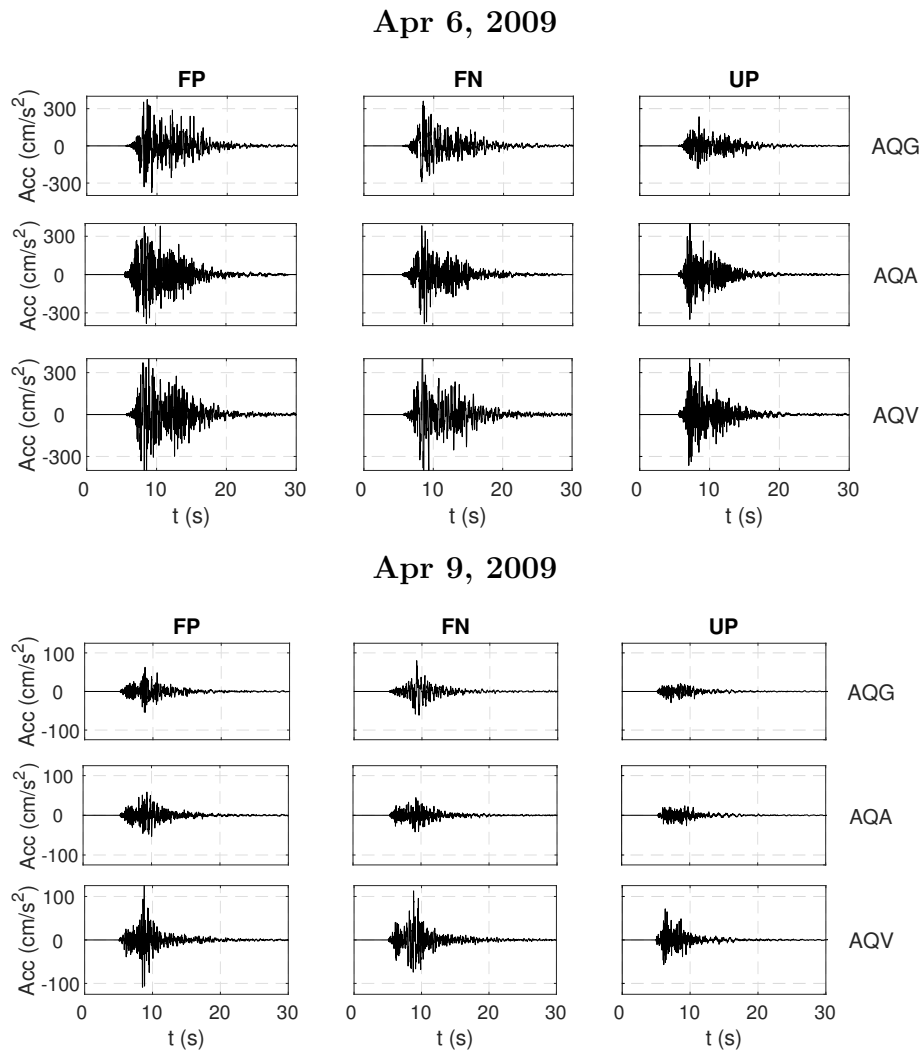
Figure 3.25: L'Aquila earthquakes acceleration time histories.

Aug 24, 2016

Oct 30, 2016
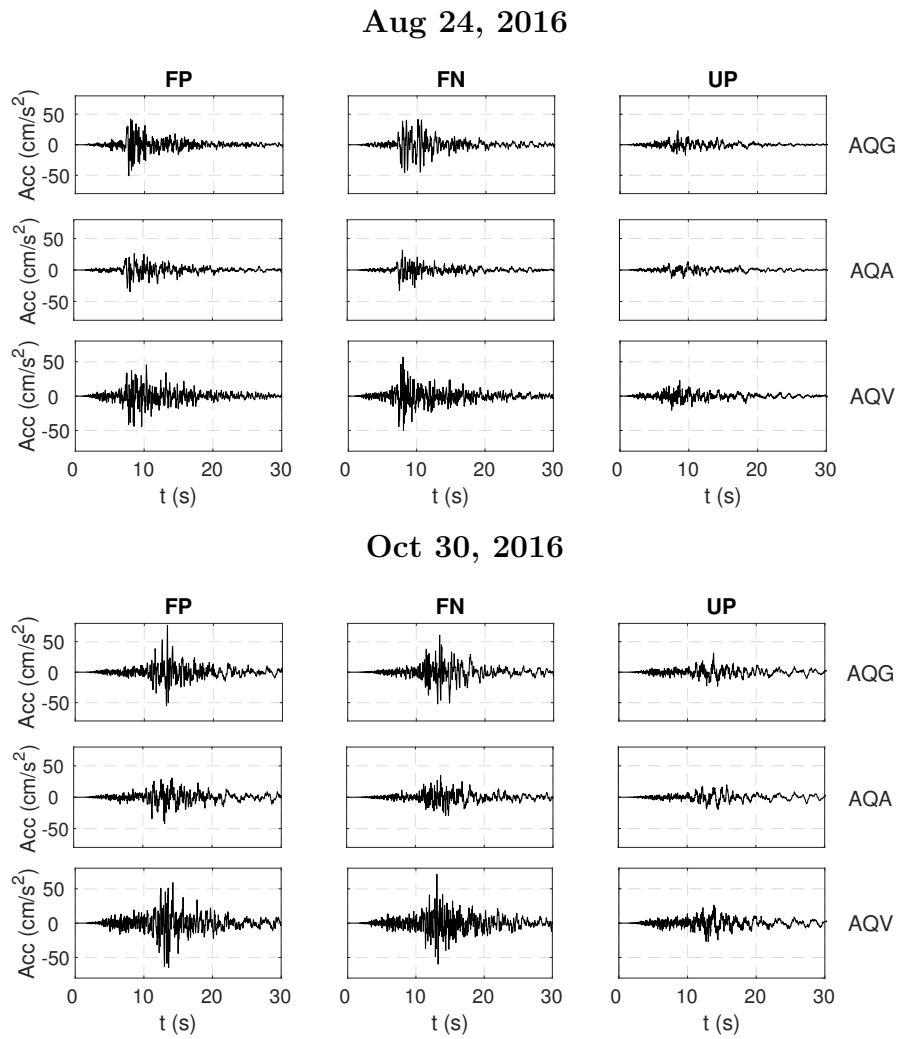
Figure 3.26: Amatrice and Norcia earthquakes acceleration time histories.

May 29, 2012
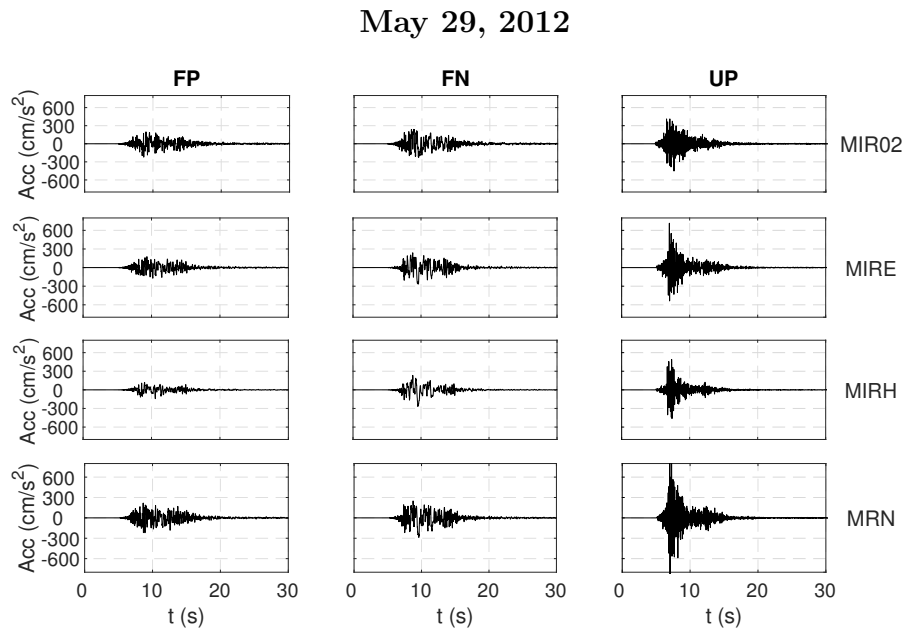
Figure 3.27: Emilia earthquake acceleration time histories.

Peak values of motion and attenuation curves

Before showing the results of the SVEGM analysis carried out on L'Aquila and Mirandola arrays recordings, the distribution of peak ground motion values and their attenuation with distance is studied.

Regarding L'Aquila case studies, Tables 3.12, 3.13 and 3.14 show, with respect to each station, the focal distance (R_{HYP}) and the peak ground acceleration (PGA), velocity (PGV) and displacement (PGD), respectively, in each component of motion as well as the parameters HGM, FN/FP, UD/HGM. Tables 3.15, 3.16 and 3.17 show the same quantities computed for L'Aquila array but for Mirandola array.

It could be noted that the forward directivity effects appear clearly for all events strictly in near-fault region (L'Aquila main and aftershock and Emilia) whereas, as expected, for earthquakes characterized by a focal distance higher than 35 km (Aug 24, 2016 and Oct 30, 2016 events) it loss its relevance.

Event	Station ID	R_{HYP} [km]	PGA [cm/s^2]					
			FP	FN	UD	HGM	$\frac{FN}{FP}$	$\frac{UD}{HGM}$
	AQG	9.68	388.7	373.3	234.6	380.9	1.0	0.6
Apr 6, 2009	AQA	9.70	384.5	389.4	435.4	387.0	1.0	1.1
	AQV	9.65	472.5	755.1	486.7	597.4	1.6	0.8
	AQG	16.94	60.4	78.9	29.2	69.0	1.3	0.4
Apr 9, 2009	AQA	16.76	57.6	42.6	26.4	49.5	0.7	0.5
	AQV	16.60	129.0	118.2	71.6	123.5	0.9	0.6
	AQG	37.94	48.4	45.2	23.2	46.8	0.9	0.5
Aug 24, 2016	AQA	37.77	32.9	32.7	13.6	32.8	1.0	0.4
	AQV	37.68	46.2	55.4	22.7	50.6	1.2	0.4
	AQG	55.00	76.2	60.7	31.4	68.0	0.8	0.5
Oct 30, 2016	AQA	54.86	42.3	34.4	19.9	38.1	0.8	0.5
	AQV	54.81	64.3	71.2	27.0	67.7	1.1	0.4

Table 3.12: Peak ground acceleration (PGA), recorded at the L'Aquila array during the L'Aquila (2009), Amatrice (2016) and Norcia (2016) earthquakes. PGA values along the FN, FP, UD components together with the ratios FN/FP and UD/HGM are listed.

Event	Station ID	R_{HYP} [km]	PGV [cm/s]					
			FP	FN	UD	HGM	$\frac{FN}{FP}$	$\frac{UD}{HGM}$
	AQG	9.68	27.7	33.6	10.4	30.5	1.2	0.3
Apr 6, 2009	AQA	9.70	20.8	32.2	9.4	25.9	1.5	0.4
	AQV	9.65	30.7	39.0	12.4	34.6	1.3	0.4
	AQG	16.94	2.3	6.0	1.5	3.7	2.6	0.4
Apr 9, 2009	AQA	16.76	3.1	4.2	1.6	3.6	1.4	0.4
	AQV	16.60	5.9	7.0	1.8	6.4	1.2	0.3
	AQG	37.94	5.0	5.2	2.6	5.1	1.0	0.5
Aug 24, 2016	AQA	37.77	4.1	3.1	2.6	3.6	0.8	0.7
	AQV	37.68	4.4	3.1	2.7	3.7	0.7	0.7
	AQG	55.00	4.6	6.1	3.6	5.3	1.3	0.7
Oct 30, 2016	AQA	54.86	4.4	3.8	3.7	4.1	0.9	0.9
	AQV	54.81	5.3	4.4	3.9	4.9	0.8	0.8

Table 3.13: Same as in Table 3.12 but for Peak Ground Velocity (PGV).

Event	Station ID	R_{HYP} [km]	PGD [cm]					
			FP	FN	UD	HGM	$\frac{FN}{FP}$	$\frac{UD}{HGM}$
	AQG	9.68	4.2	5.9	1.9	5.0	1.4	0.4
Apr 6, 2009	AQA	9.70	3.2	5.9	1.7	4.3	1.9	0.4
	AQV	9.65	5.3	5.7	2.5	5.5	1.1	0.4
	AQG	16.94	0.4	0.8	0.4	0.5	2.0	0.7
Apr 9, 2009	AQA	16.76	0.4	0.7	0.4	0.5	1.6	0.7
	AQV	16.60	0.5	0.8	0.5	0.6	1.7	0.7
	AQG	37.94	1.0	1.0	0.8	1.0	1.0	0.8
Aug 24, 2016	AQA	37.77	1.1	1.1	0.8	1.1	1.0	0.8
	AQV	37.68	1.0	0.8	0.8	0.9	0.8	0.9
	AQG	55.00	1.7	2.6	1.7	2.1	1.5	0.8
Oct 30, 2016	AQA	54.86	1.7	2.3	1.7	2.0	1.3	0.9
	AQV	54.81	1.9	2.3	1.7	2.1	1.2	0.8

Table 3.14: Same as in Table 3.12 but for Peak Ground Displacement (PGD).

Station ID	R_{HYP} [km]	PGA $[cm/s^2]$					
		FP	FN	UD	HGM	$\frac{FN}{FP}$	$\frac{UD}{HGM}$
MIR02	9.6	221.4	238.8	452.3	230.0	1.1	2.0
MIRE	9.1	177.8	265.8	715.3	217.4	1.5	3.3
MIRH	9.3	142.5	269.0	490.4	195.8	1.9	2.5
MRN	9.1	219.2	289.2	840.7	251.7	1.3	3.3

Table 3.15: Peak ground acceleration (PGA), recorded at the Mirandola array during the 2012 Emilia earthquake. PGA values along the FN, FP, UD components together with the ratios FN/FP and UD/HGM are listed.

Station ID	R_{HYP} [km]	PGV $[cm/s]$					
		FP	FN	UD	HGM	$\frac{FN}{FP}$	$\frac{UD}{HGM}$
MIR02	9.6	33.2	55.2	12.0	42.8	1.7	0.3
MIRE	9.1	25.7	59.0	24.6	38.9	2.3	0.6
MIRH	9.3	22.1	55.6	19.1	35.0	2.5	0.5
MRN	9.1	27.0	58.0	26.4	39.6	2.1	0.7

Table 3.16: Same as in Table 3.15 but for Peak Ground Velocity (PGV).

Station ID	R_{HYP} [km]	PGD $[cm]$					
		FP	FN	UD	HGM	$\frac{FN}{FP}$	$\frac{UD}{HGM}$
MIR02	9.6	10.7	16.4	5.1	13.2	1.5	0.4
MIRE	9.1	7.4	15.0	6.4	10.5	2.0	0.6
MIRH	9.3	7.2	16.4	5.3	10.9	2.3	0.5
MRN	9.1	9.3	16.3	4.9	12.4	1.7	0.4

Table 3.17: Same as in Table 3.15 but for Peak Ground Displacement (PGD).

The following Figures (3.28, 3.29 and 3.30) show PGA and PGV, for the two horizontal components of ground motion, as a function of the focal distance have been compared with the Bindi et al. (2014) (class of site B) and Akkar et al. (2014) ($Vs, 30 = 570m/s$) ground motion prediction equations (GMPE).
Note that Bindi et al. (2014) provides models for both PGA and PGV while Akkar

et al. (2014) defines, only, the attenuation function model for PGA; moreover, L'Aquila earthquakes are generated by normal faults while Mirandola case study by a reverse fault mechanism.

It is interesting to note that for all case studies the GMPEs predict properly the observed values.

Apr 6, 2009
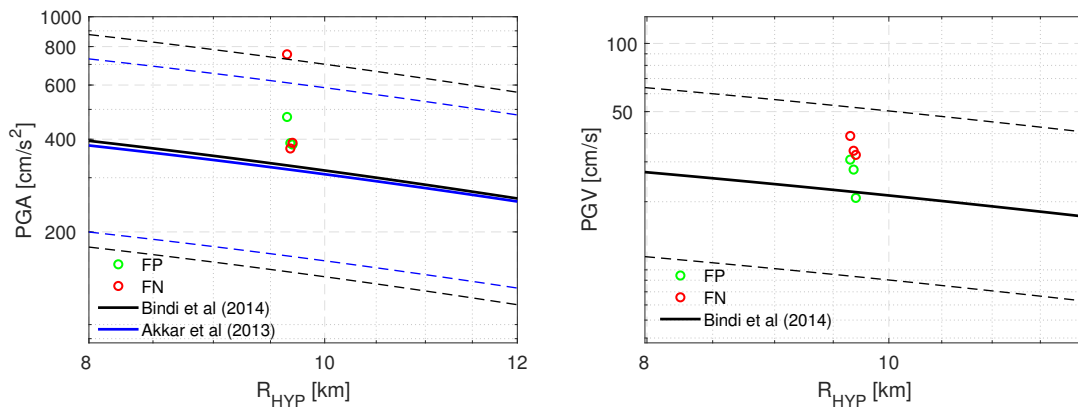
Apr 9, 2009
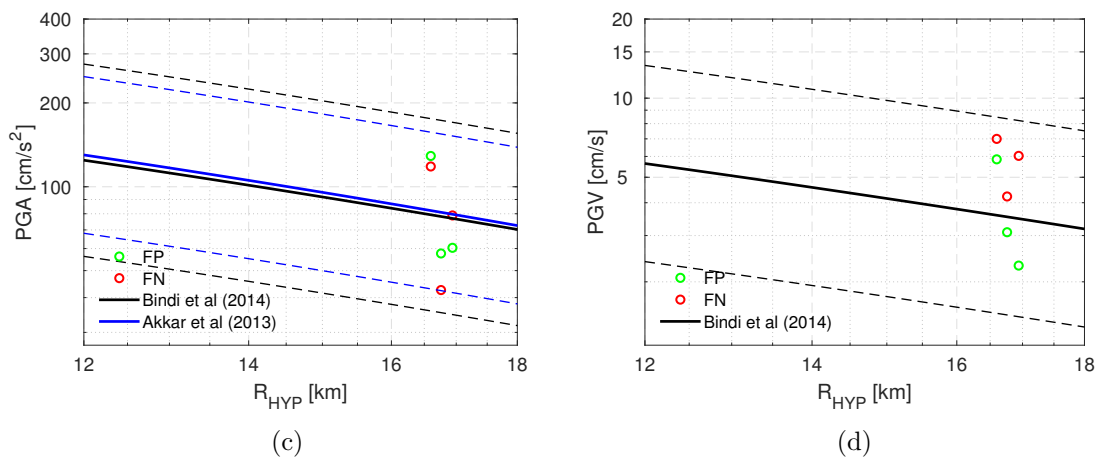
Figure 3.28: Comparison between the recorded values of PGA and PGV obtained during the L'Aquila earthquakes and the attenuation curves developed by Bindi et al. (2014) (black lines) and Akkar et al. (2014) (blue lines). The dotted lines represent the 16 and 84 percentile of the probabilistic distribution that characterize Bindi et al. (2014) and Akkar et al. (2014) relationships.

Aug 24, 2016
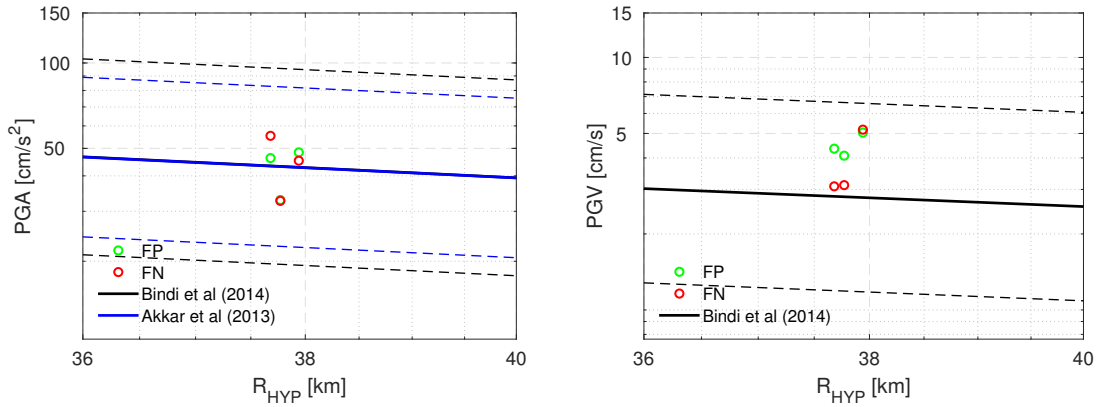
Oct 30, 2016
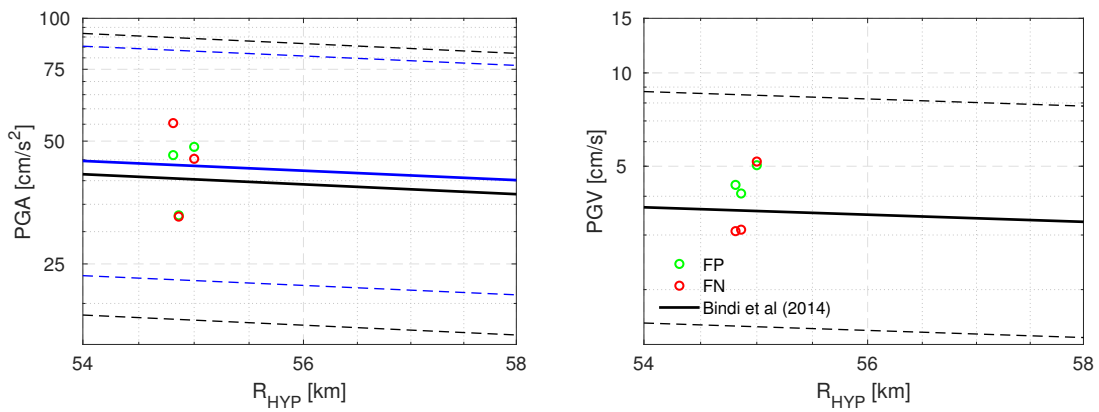
Figure 3.29: As for Figure 3.28 but for Amatrice and Norcia earthquakes
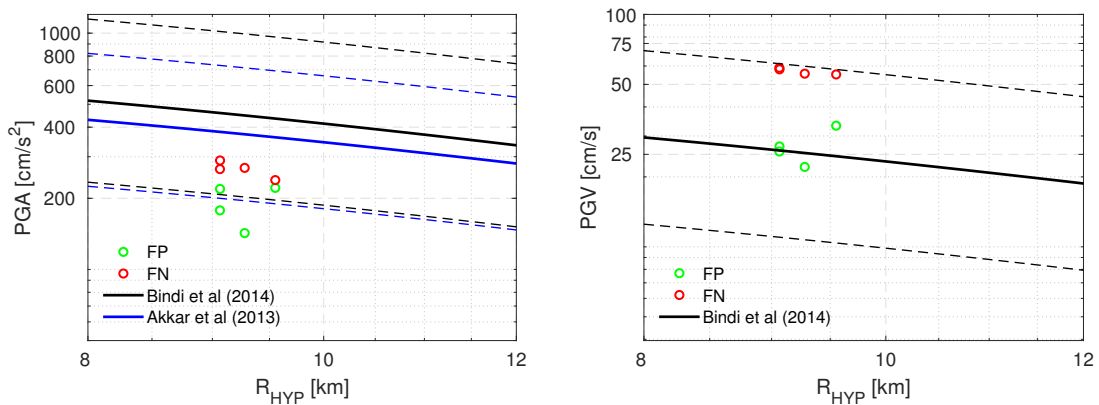
Figure 3.30: As for Figure 3.28 but for Mirandola case study

64

3.2 Analysis and Results

In this section the lagged coherency estimates, computed following the procedure explained in Section 2.2, will be presented. Each case of study will be treated separately. In the following reference is made only to the lagged coherency so that the term lagged will be omitted. Inter-station distances are grouped in distance bin of 100-m, with each bin represented by the average distance of the station pairs belonging to it.

Stations pairs are selected considering all the possible pairs among all the stations composing the dense array.

3.2.1 ICEARRAY: the Ölfus earthquake

For the present case study the analysis will be focused on the estimates of lagged coherency for eight 100 m distance bins in the interval 0-1000 m (the bins 100-200 m and 700-800 m have been excluded from the present implementation since they were constitutes by only one station pair each leading to an excessive bias in the results).

As an illustrative example, Figures 3.31 and 3.32 show the individual coherency curves associated with each pair of stations (thin grey line) along with the mean curve (black thick line) for the two horizontal ground motion components, FP and FN, respectively, is computed from the recording of the Öflus ($M_w = 6.3$) earthquake. The title of each subplot shows the component of motion considered, the distance bin and the average distance among all the pairs belonging to the specific distance bin.

The averaging process is possible under the assumption for which the random field for each component of ground motion is stationary, meaning that the value of coherency at a certain frequency depends only on the inter-station distances and not on the absolute locations of the stations.

This assumption is reasonable for a relatively small spatial region.

It is clear from Figures 3.31 and 3.32 that the mean curves are strongly affected by the number of station pairs that constitute the distance bin: mean curves from a low number of samples fluctuate a lot with many ups and downs while when the distance bins are more populated the curves are more stable leading to more reliable

results (the noise is strongly reduced).

The results obtained from the recordings of the Öflus ($M_w = 6.3$) earthquake are, finally, shown in Figure 3.33: mean FP (black line), FN (red line) and UD (blue line) coherency curves are computed, as described previously, and reported in the same subplot.

No clear differences are visible among different components while it is clear the decay of coherency with distance mostly between inter-station distances less and higher than 100 m. Indeed, looking at the first two subplot from the top-left of Figure 3.33 there is a huge jump in the trend of $|\gamma(f)|$ while for higher distance bins coherency seems to settle on rather constant values. This behaviour can be explained by considering the geometry (Figure 3.1b) and geology (Figure 3.2) of the array: station pairs characterized by inter-station distances less than 100 m are very close one to the other on homogeneous site conditions (the average distance is 43 m) whereas distance bins higher than 200 m grope stations which are located on different site conditions in addition to the essential decay due to scattering and wave passage effect.

It is important, also, to note how huge is the variance which characterize the stochastic process related to SVEGM. Indeed, from Figures 3.31 and 3.32 it appears clearly that individual coherency curves (grey lines) reach $|\gamma|$ values strongly above and below the mean at a fixed frequency and distance bin. Therefore, in order to have correct and meaningful interpretation of the SVEGM from earthquakes recordings, the importance of having as much as possible stations within a dense array become even more clear.
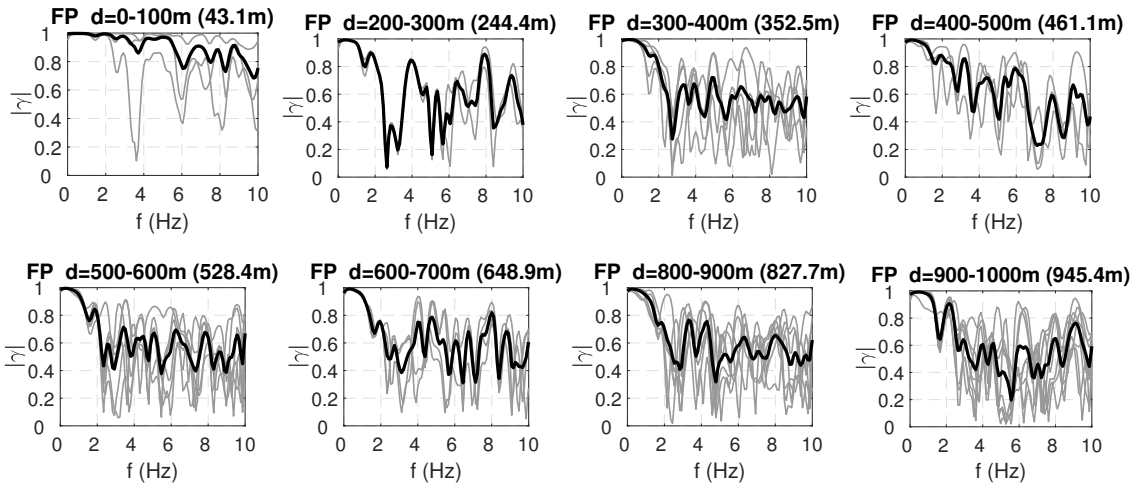
Figure 3.31: Öflus ($M_w = 6.3$) - ICEARRAY, FP component. Eight 100m distance bins in the interval 0-1000 m are shown. Grey thin lines denote the individual coherency curves for each pair of stations while the black thick line represents the mean curve.
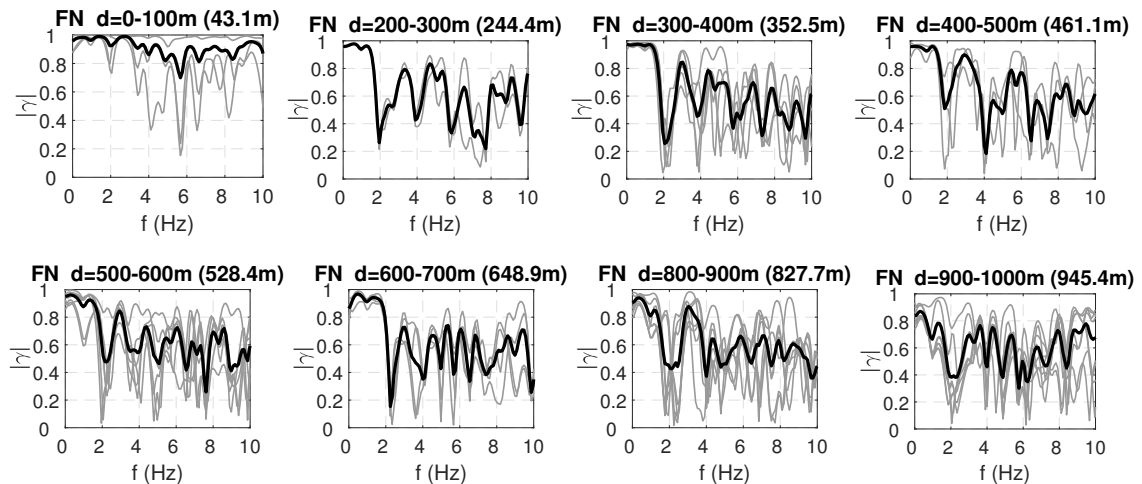
Figure 3.32: Öflus ($M_w = 6.3$) - ICEARRAY, FN component. Eight 100m distance bins in the interval 0-1000 m are shown. Grey thin lines denote the individual coherency curves for each pair of stations while the black thick line represents the mean curve.
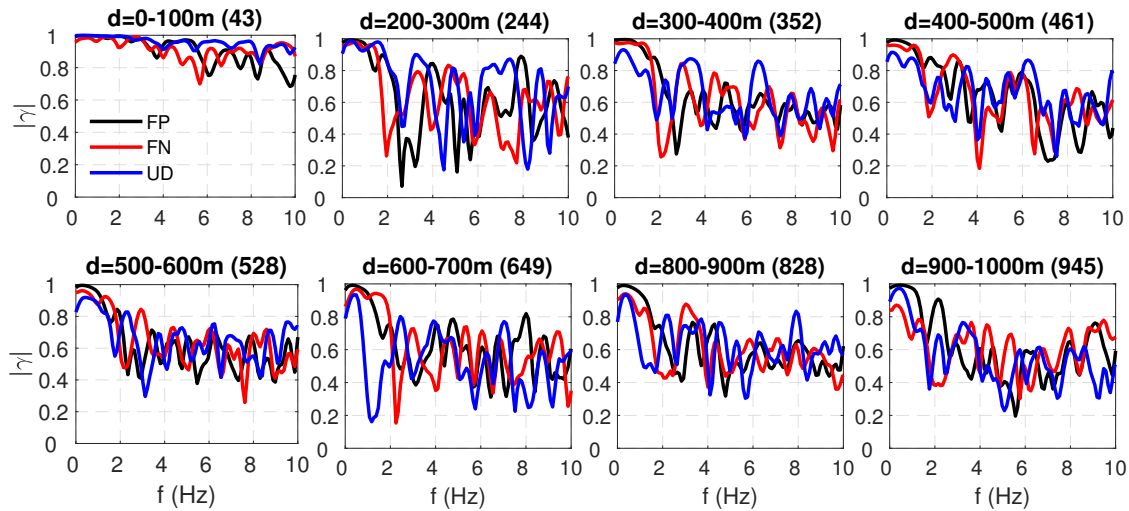
Figure 3.33: Öflus ($M_w = 6.3$) - ICEARRAY: lagged coherency as a function of frequency, in the range 0-10 Hz, for eight 100m distance bins in the interval 0-1000 m, for the three components of ground motion, FP (black line), FN (red line) and UD (blue line). Each curve represents the mean coherency curve computed from the recordings.

3.2.2   UPSAR array: Parkfield and San Simeon earthquakes

Similarly to what seen in Section 3.2.1, here, the mean coherency curves have been computed from the recordings of Parkfield and San Simeon earthquakes. Distance bins of 100m in the interval 0-700m have been adopted and the results are shown in Figures 3.34 and 3.35.
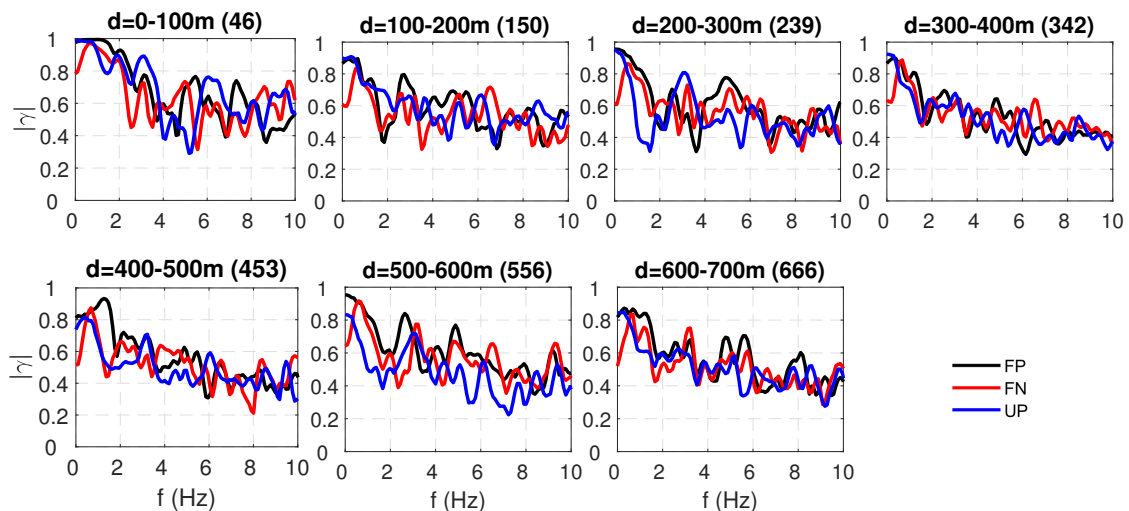
Figure 3.34: Parkfield ($M_w = 6.0$) - UPSAR. Same purpose of Figure 3.33
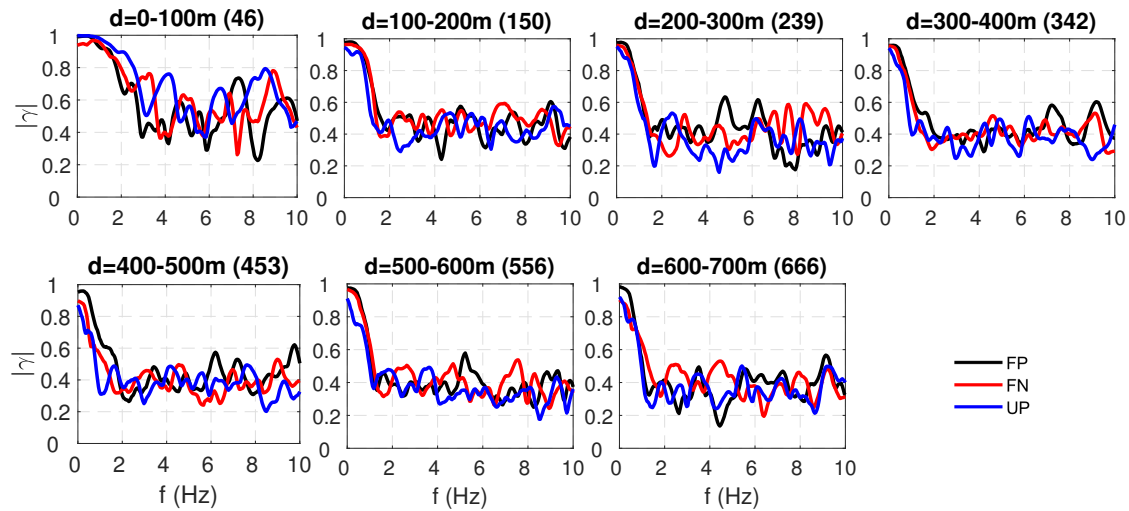
Figure 3.35: San Simeon ($M_w = 6.5$) - UPSAR. Same purpose of Figure 3.33

The decay of lagged coherency with frequency and distance is evident for both cases while no apparent significant difference is visible between components of motion.

Comparing the two events, a part from very low frequencies, the Parkfield coherency is, in general, higher than the San Simeon one. The reason could be associated to the coupling between source-to-site distance effect, which lead to a decreasing of coherency with increasing distance between source and site, and extended fault effect, for which a larger fault provides a more irregular propagation path of waves. In this case of study, the latter effect tends to prevail.

Moreover, it is interesting to notice that $|\gamma(f)|$ at almost all distance bins decay like a linear function for the Parkfield case while for San Simeon there is a huge drop between 0 and 2 Hz escort by an approximately constant trend with frequency.

These observations strengthen the idea that spatial coherency of ground motion is very affected not only by the specific site conditions but also by the specific source and propagation path.

3.2.3 L'Aquila array: L'Aquila, Amatrice and Norcia earthquakes

In this section, the results coming from the L'Aquila array are analyzed.
Since, as seen in Section 3.1.3, L'Aquila case studies could actually take advantage of the recording at only three stations, coherency estimates are characterized by a

huge variance and bias. Indeed, here it is not possible to effectively reduce the bias which characterize the single coherency estimate by computing the mean among each coherency function belonging to the same distance bin as done for the ICEARRAY and UPSAR case studies.

Figure 3.36 shows the mean coherency computed for each station pair among the three ground motion components.

Due to the lack of statistical samples, in order to evaluate the general trend of $|\gamma|$ with frequency and distance, mean is computed among the single coherency estimates (obtained from each station pair) for each ground motion component (FP, FN and UP). The drawback consists on the loss of any information on the behaviour of each component.

The decay of coherency with frequency appears clearly for all case studies (except for 9 Apr 2009 L'Aquila earthquake) whereas less visible appears the dependence on inter-station distance. Note that as observed in the other case studies, the rate of decay of coherency with distance tend to decrease a with increasing inter-station distance.

Furthermore, it is interesting to observe that, despite their higher source-to-site distance (see Table 3.11), coherency estimates from Amatrice and Norcia events are characterized by lower values than ones from L'Aquila earthquake. This observation should be considered with caution due to the lack of receivers within the array.

6 Apr 2009 L'Aquila Earthquake

9 Apr 2009 L'Aquila Earthquake

24 Aug 2016 Amatrice Earthquake

30 Oct 2016 Norcia Earthquake
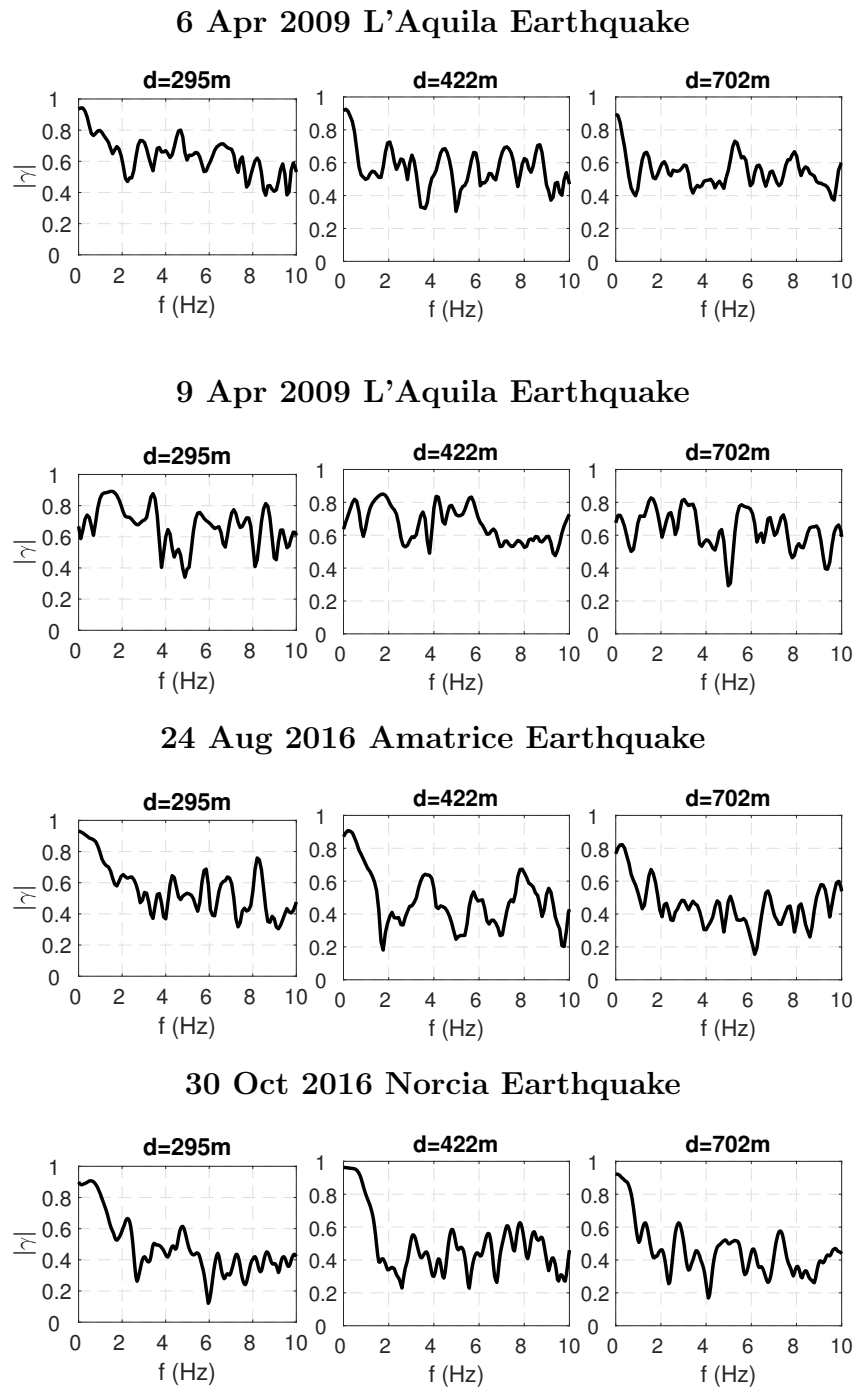
Figure 3.36: L'Aquila. Mean coherency among the ground motion components of each individual coherency estimate

71

3.2.4 Mirandola array: the 29 May 2012 earthquake

The same procedure applied in Section 3.2.3 is carried out here for the Mirandola array. Figure 3.37 shows the mean coherency computed for each station pair among the three ground motion components (fault-parallel FP, fault-normal FN and vertical UP).

The decay of lagged coherency frequency and distance is clear and moreover, as expected, the lagged coherency between two station 2 m spaced is practically equal to unit at all frequencies.
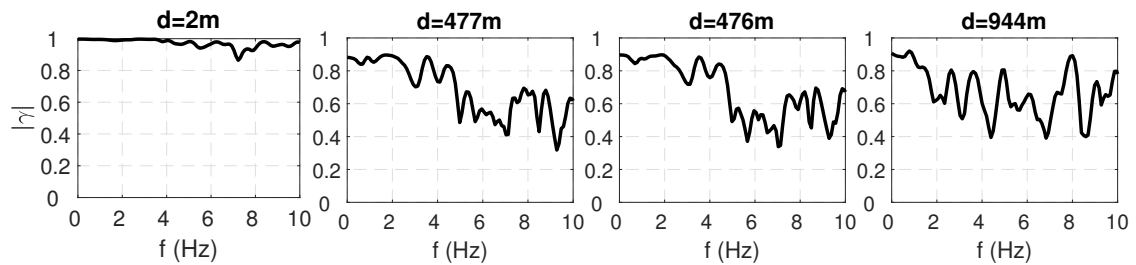
Figure 3.37: Mirandola. Mean coherency among the ground motion components of each individual coherency estimate

3.3 Comparison between observations and existing coherency models

In this section, coherency estimates from the recordings described in Sec. 3.1 are compared with the empirical models of Harichandran and Vanmarcke (1986) and by Ancheta et al. (2011) and the semi-empirical model of Luco and Wong (1986). Figure 3.38 compares the aforementioned models with the corresponding estimates of the lagged coherency based on the ICEARRAY and UPSAR data as a function of frequency for each inter-station distance bin.

The curves corresponding to the empirical data (black line) is obtained by computing the arithmetic mean of the lagged coherency estimates associated to FP and FN components (see Sec. 3.2). This procedure is allowed under the assumption of isotropy of the coherency function.

These models are computed considering the average distance of each distance bin, reported in the title of each subplot (number in brackets).

The model by Ancheta et al. (2011) is compared with the estimates for distances less than 100m while the model of Harichandran and Vanmarcke (1986) is compared with the estimates for distances greater than 100m. The comparison with Luco and Wong (1986) is carried out by imposing the coefficient $\alpha = 2.5 \cdot 10^{-4}$ which is the value suggested by the authors themselves.

Considering inter-station distances up to 100 m both Luco and Wong (1986) and Ancheta et al. (2011) are in good agreement with the ICEARRAY estimates while they tend to underestimate the decay of coherency with distance for the UPSAR case studies.

Regarding inter-station distances between 200 and 300 m, Luco and Wong (1986) model agrees almost perfectly with estimates up to 3 Hz for all the case studies while for higher frequencies Harichandran and Vanmarcke (1986) has a better (but non so good) agreement with data. Finally, for distance bin higher than 400 m the models, in general, do not capture the observed trend of lagged coherency underestimating it. The only exception appears at the San Simeon case were Luco and Wong (1986) reproduce almost perfectly the empirical curve up to 2 Hz. In general, for distance bin higher than 100 m, both models tends to overestimate the decay of coherency with frequency for $f > 3 - 4$ Hz.

In assessing the divergence of the ICEARRAY and UPSAR estimates from the em-

pirical and semi-empirical models, it is important to recall that both ICEARRAY and UPSAR array are located on rock, whereas the empirical models considered herein are based on recordings coming from both soil and rock sites.

Moreover, it should be noticed that Harichandran and Vanmarcke (1986) model provide values smaller than unity at zero frequency, which is not realistic. The estimated coherency for zero frequency depends on the level of smoothing, but, on physical grounds, the modulus of the coherency function must approach unity at zero frequency because waves of infinite wavelength are perfectly coherent. Thus, comparisons at low frequency with Harichandran and Vanmarcke (1986) become meaningful.
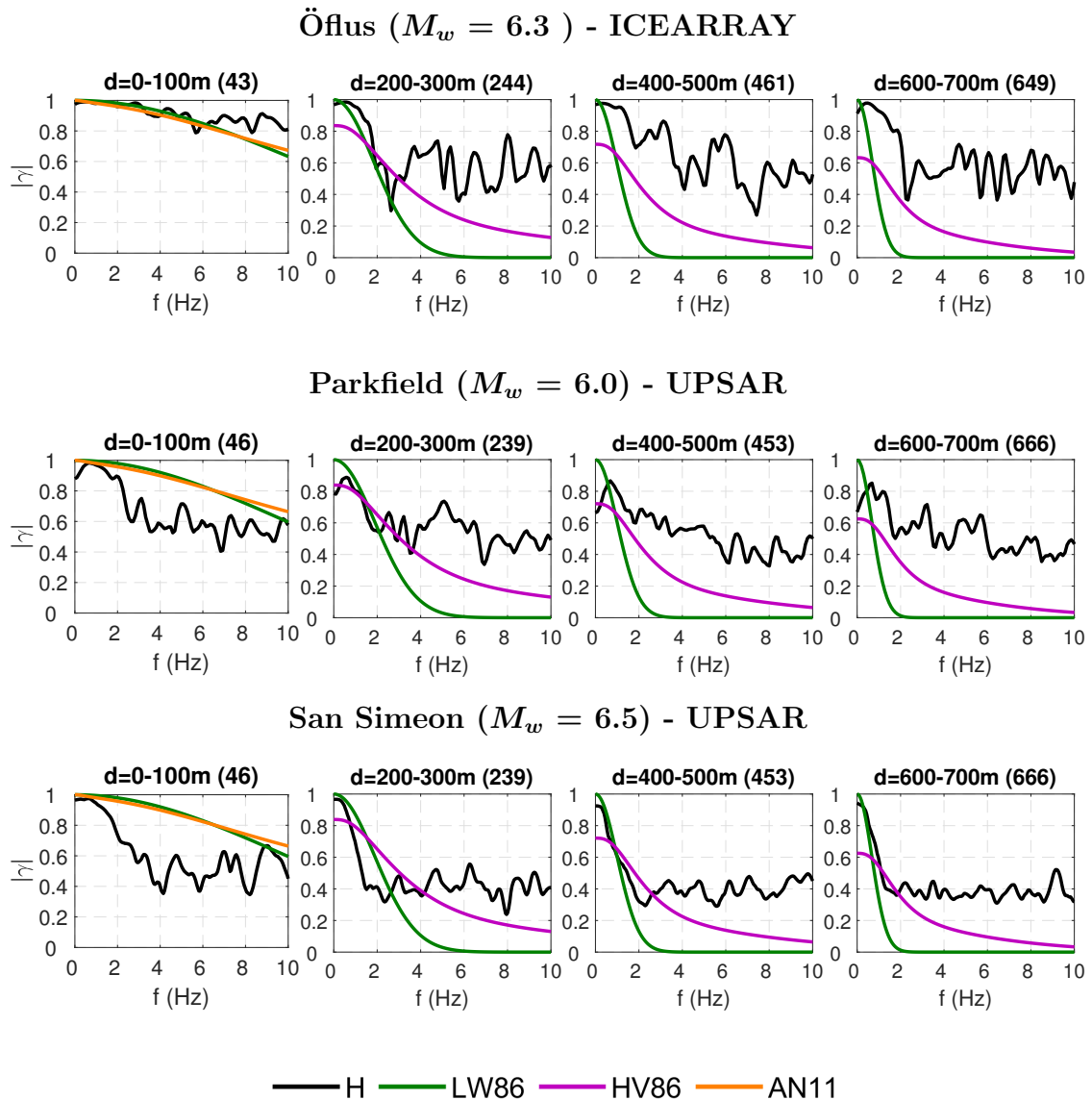
Figure 3.38: Mean lagged coherency from the arithmetic mean of two horizontal (H) components (black line) compared with LW86 ([Luco and Wong (1986)]), AN11 ([Ancheta et al. (2011)]) and HV86 ([Harichandran and Vanmarcke (1986)]) models.

3.3.1 Regression of results based on LW86 model

Given the variety of case studies considered in this work and the multiplicity of variables on which the lagged coherency depends, it is helpful to find a concise measure of spatial coherency, apt for identifying common trends and performing some statistics. To this end, the value of the parameter α of LW86 model (see Eq. 2.23) is computed by non-linear least-squares regression of the coherency es-

timates for each distance bin and ground motion component. Because the lagged coherency is not homoscedastic (meaning that variance increases as a function of frequency, as coherency decreases for increasing frequencies), the least-squares minimization is applied on the variance-stabilizing transformation $tanh^{-1}|\gamma(f)|$. The transformed coherency is normally distributed and has a constant variance inversely proportional to the duration of the strong motion window and the bandwidth of the smoothing spectral window. Moreover, the $tanh^{-1}|\gamma(f)|$ transformation produces approximately normally distributed data.

In practice, the estimates of $tanh^{-1}|\gamma(f)|$ are obtained by averaging over all pairs of accelerograms in the bin (homogeneity assumption) and the parameter α is fitted in the range of frequency between (0.4,4) as suggested by Konakli et al. (2014). An example of the output of the non-linear least-squares regression is illustrated in Figure 3.39 with reference to the ICEARRAY case. The case of fault-parallel component has been chosen as representative. The best-fitting model is represented by the red lines.
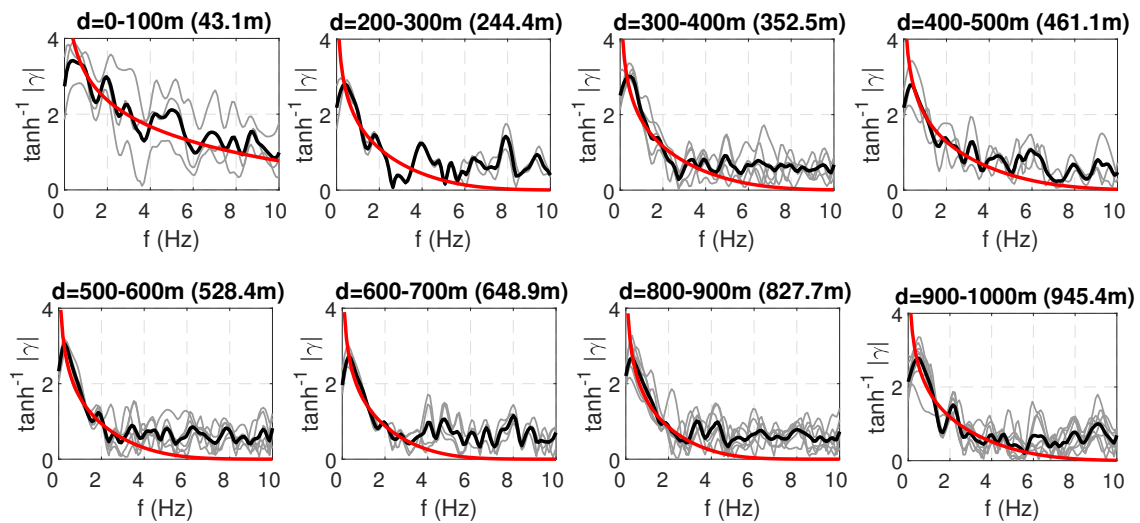
Figure 3.39: Example of non-linear least-squares regression of lagged coherency with LW86 model: the Ölfus (Mw=6.3), ICEARRAY, case study is considered. Results for fault-parallel (FP) component are shown. Grey thin lines denote the individual coherency curves used for regression while the thick black line represents the mean curve. The fitted LW86 model is depicted with red line.

The best fitting α value of LW96 are shown in Figures 3.40 and 3.41. Results are computed separately for each ground motion component and than plotted, as a function of distance, putting in the same subplot the horizontal components (Figure

3.40) while the vertical in another (Figure 3.40).

Results indicate a strong non-linear dependence of α on distance: α turns out to decrease with increasing inter-station distance at a rate which tends to be higher at smaller distances (mostly for the UPSAR case of study). Therefore, the decay parameter α cannot be constant, as suggested by Luco and Wong (1986), but should depend on distance to fit the estimated curves. Konakli et al. (2014) who analyzed the recordings of Parkfield at UPSAR, observed a similar trend of α with distance confirming both this hypothesis and the goodness of the procedure applied in the present implementation for the estimation of the lagged coherency.

When observing the trend of α is important to recall that higher values of α are associated with lower coherency and vice-versa. Moreover, α is a concise parameter which allows to interpret effectively the coherency estimates, but it inevitably lost some information underestimating the real curve in some point while overestimating in some other. However, it will be used largely in the present presentation due to its capability of highlight the sensitivity of lagged coherency to physical parameters.

In light of the above, some further observation on the results could be make:

- the ICEARRAY curves are associated to lower values of α with respect to the UPSAR case meaning that coherency estimated is, in general, greater. Moreover, the non-linear dependence of α with distance is less accentuated: the decreasing of α with increasing inter-station distance is still present but with less intensity. This behaviour is reasonable since ICEARRAY is located on a rock site so coerent waves are expected.

- Comparing the two events recorded by UPSAR, San Simeon is characterized by less coherency (greater α) for all inter-station distances higher than 100 m both for horizontal than vertical components. The physical reason is not so clear, since the opposite would be expected due to the site-to-source distance which is much more higher for San Simeon, but it can be associated to the fact that the higher magnitude and thus the higher effective fault tend to produce waves which radiates with more irregular path.

- It is also noted that horizontal and vertical coherency estimates show comparable values, most likely due to the significance of vertical ground motions in near-fault conditions.

In Section 3.3.1 other significant comments will be made.

(a) ICEARRAY

(b) UPSAR
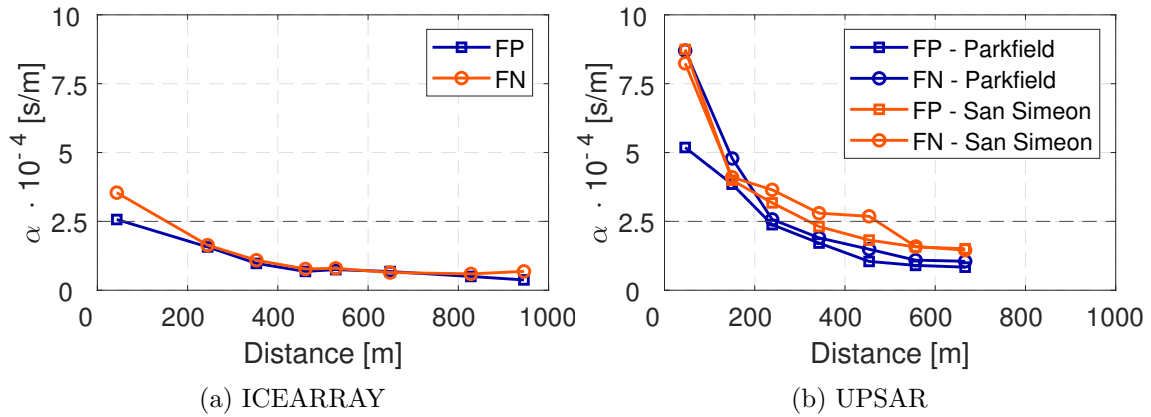
Figure 3.40: Best fitting α value of LW86 model for horizontal components as a function of separation distance for Ölfus earthquake (a) and for Parkfield and San Simeon earthquakes (b).

(a) ICEARRAY

(b) UPSAR
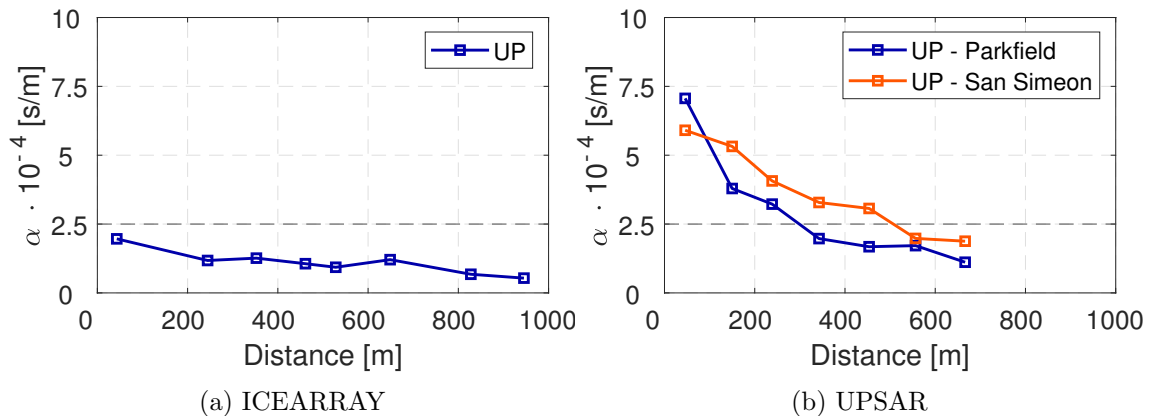
Figure 3.41: Best fitting α value of LW86 model for vertical component as a function of separation distance for Ölfus earthquake (a) and for Parkfield and San Simeon earthquakes (b).

The nature of the variation of seismic phases in the earthquake data is rather complex. Thus it is difficult to relate the spatial coherency directly to physical parameters. However, in the present study we investigate the sensitivity of the coherency estimates with respect to some parameters such as the ground motion component, magnitude, source-to-site distance.

The investigation of these issues becomes further complex when dealing with real recordings and dense arrays for which the limited number of data lead to bias in

the results. The dependence on these factors will be investigated further in the next chapter, based on numerical simulations.

In this section some general assessment on the dependence of lagged coherency on ground motion component from earthquake recordings has been carried out. To this aim, the ratios α_{FN}/α_{FP} and α_H/α_{UP} with α_{FP} (or α_{FN} or α_{UP}) representing the fitted α value on the FP (or FN or UP) component and α_H representing the average between the fitted α computed for the horizontal components, have been computed for each distance bin and for each case study.

(a) ICEARRAY   (b) UPSAR

Figure 3.42: α_{FN}/α_{FP} ratios

(a) ICEARRAY   (b) UPSAR
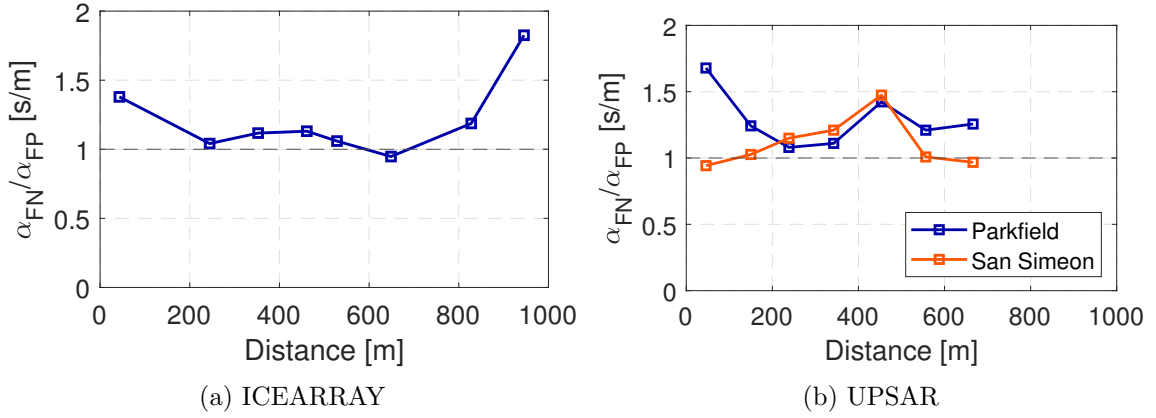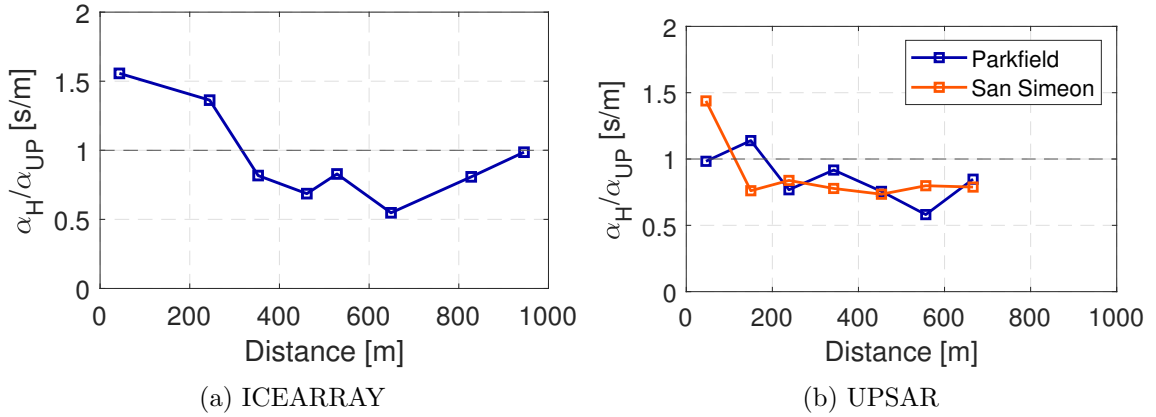
Figure 3.43: α_H/α_{UP} ratios

For all three cases, the ratio α_{FN}/α_{FP} ranges between one and 1.8 meaning that the FN component exhibits lower coherency for all distance bins. This behaviour may be explained based on the fact that, FN components are largely affected by rupture propagation effects, especially in near-fault conditions and for strike-slip events.

Considering ratio α_H/α_{UP} a variable trend is shown due to the limited number of stations. In this conditions it is difficult to extract from the result a reliable physical interpretation.

Chapter 4

Spatial coherency of seismic ground motion from physics-based numerical simulations

Engineering models of SVEGM are usually calibrated on the basis of strong motion measurements from dense seismic arrays during past earthquakes and neglect the aspects related to the proximity to the seismic source. In spite of the increasing availability of high-quality strong motion records, observations at dense arrays are still very scarce especially in near-source conditions even on a worldwide scale. As an alternative powerful method, numerical simulations of earthquake ground, based on physical models of the seismic source, the propagation path from the source to the site and local geologic irregularities, can be used to simulate spatially variable ground motions when recorded data are lacking.

This approach has been extensively used in this study, where 3D physics-based numerical simulations of earthquake ground motion play a key role. Note that the numerical approach has the advantage of allowing one to investigate the dependence of SVEGM on physical factors, such as magnitude, near-source effects, local site conditions, for a variety of "virtual", albeit realistic, conditions.

In this chapter, spatial coherency estimates obtained from a rather wide set of 3D physics-based numerical simulations of near-source seismic ground motion in different areas of Italy and the dependence on parameters, such as the magnitude, distance, rupture directivity, azimuth, and site conditions will be discussed. The numerical results are obtained using the high-performance computer code SPEED (`http://mox.polimi.it/it/progetti/speed`), based on the Discontinuous Galerkin Spec-

tral Element method [Mazzieri et al. (2013)].

The primary aim is, precisely, to investigate the issues regarding the SVEGM based on numerically-based approaches.

4.1 Numerical modelling of seismic ground motion - SPEED

Physics-based numerical modelling of the seismic response of arbitrarily complex earth media has gained major relevance in recent years, owing to the ever-increasing progress in computational resources and to the growing interest towards the development of deterministic scenarios within seismic hazard and risk assessment studies. In particular, 3D physics-based numerical simulations allow to obtain synthetic ground motion time histories starting from a rigorous seismic-wave propagation model (i.e., including source, path, and site effects) and the numerical integration of the elastodynamics equations.

4.1.1 SPEED: SPectral Elements in Elastodynamics with Discontinuous Galerkin

In the present implementation attention will be focused on the SPectral Elements in Elastodynamics with Discontinuous Galerkin (SPEED) numerical code (SPEED: `http://mox.polimi.it/it/progetti/speed`).

SPEED is an high performance open-source code which has been developed by the joint research activity between the Department of Structural Engineering and of Mathematics of Politecnico di Milano and allows one to perform simulation of seismic wave propagation in heterogeneous three-dimensional Earth's media.

At first, SPEED is a spectral element(SE) method (Faccioli et al., 1997): the finite dimensional space is discretized in finite elements which are interpolated by high-order functions (the Lagrangian polynomials) sampled at the Legendre-Gauss-Lobatto (LGL) quadrature points. This discretization technique makes the SE method capable of providing an arbitrarily accurate numerical solution by simply enhancing the polynomial approximation degree.

Flexible numerical strategies in elastodynamics codes are necessary because of the following reasons:

- the intrinsic multiscale nature of seismic wave propagation problems, involving a relative broad range of wavelengths;

- the complexity of the geometric constraints which characterize engineering problems;

- the necessity of keeping the computational effort low.

For this reasons, a non-conforming discretization approach, such as the discontinuous Galerkin (DG) technique (see [Mazzieri et al. (2013)]), has been coupled with the SE method to further improve its capabilities. Indeed, DGSE methods can handle non-uniform polynomial degree distribution (N-adaptivity), as well as a locally varying mesh size (h-adaptivity) in such a way the spatial discretization and/or the local polynomial degree can be tailored to the region of interest (e.g. civil engineering structures in contact with large-scale soil domains). Moreover, DGSE technique DGSE methods enjoy a high level of intrinsic parallelism, allowing the application of parallel computations massively (low coputational effort)

In Figure 4.1 an example of discontinuos Galerkin tecnicque of discretization is shown. The whole domain is composed of different non-overlapping polygonal subdomains, made by hexahedral elements with a non- uniform polynomial degree distribution (N-adaptivity, e.g., $N_1 = 2$ in Ω_1 and $N_2 = 3$ in Ω_2), as well as a locally varying mesh size (h-adaptivity between subdomains Ω_1, Ω_2, Ω_3, Ω_4). Moreover, the surface between two neighbouring subdomains Ω_k and Ω_i, may not be a complete side of Ω_k and Ω_i (e.g., Λ and Λ').
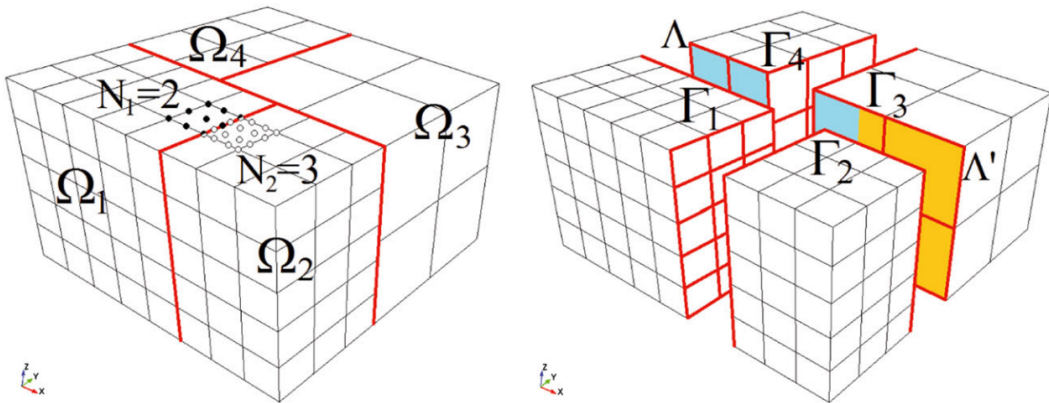
Figure 4.1: 3D example of non-conforming domain decomposition. From Mazzieri et al. (2013)

The SPEED code allows to treat linear and non-linear visco-elastic soil materials. The non-linear viscoelastic soil model is implemented as a generalization to 3D load condition of the classical degradation curves ($G - \gamma$ and $D - \gamma$) (e.g. Kramer 1996) where G and D values are updated step by step, so that the initial values of the dynamic soil properties are recovered at the end of the excitation (Mazzieri et al. (2013))]. Moreover, in order to model the visco-elasticity, frequency proportional quality factor Q is used in such a way that all frequency components are equally attenuated with distance(Kosloff and Kosloff (1986) approach)

Paraxial boundary conditions are used to reduce spurious reflections from outgoing waves inside the computational domain, while time integration can be performed either by the second-order accurate explicit leap-frog scheme or the fourth-order accurate explicit Runge–Kutta scheme (Paolucci et al., 2015).

Definition of the seismic source

In the field of engineering applications, kinematic source models, where heterogeneous distribution of co-seismic slip and a slip source function are applied together along the fault, are implemented in SPEED.

In particular, the finite-fault source is represented by a suitable distribution of double-couple point sources, whose mathematical representation is given by the seismic moment tensor density which is a function of: fault area, shear modulus, rupture velocity, rise time, slip distribution and fault spatial orientation. In order to take into account of the fault finiteness and heterogeneity, the fault is subdivided in subfaults each one associated with prescribed values of the parameters listed before.
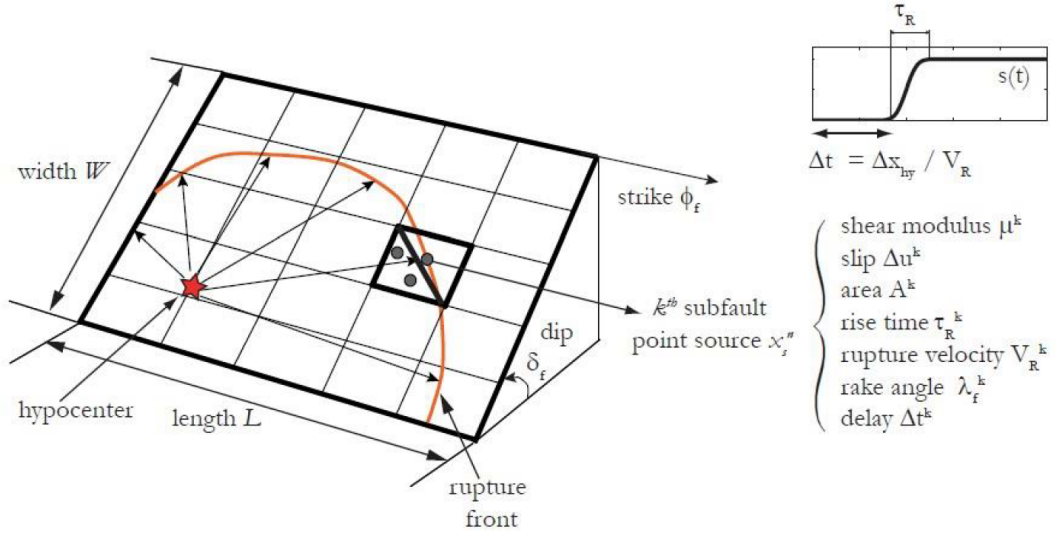
Figure 4.2: Sketch of kinematic numerical modelling of an extended seismic source.

The code allows to define an arbitrarily complex seismic source, by assigning realistic distributions of co-seismic slip along an extended fault plane through ad hoc pre-processing tools. These tools allow to reproduce in a semi-automatic way realistic fault rupture models. Furthermore, it is also possible to define stochastically correlated random source parameters, in terms of slip pattern, rise time, rupture velocity and rupture velocity distribution along the fault plane, which may be crucial in deterministic simulations to reach high frequency components of ground motion (Smerzini and Villani, 2012).

In the present implementation, the fault geometry parameters are defined following the scheme shown in Figure 4.3.
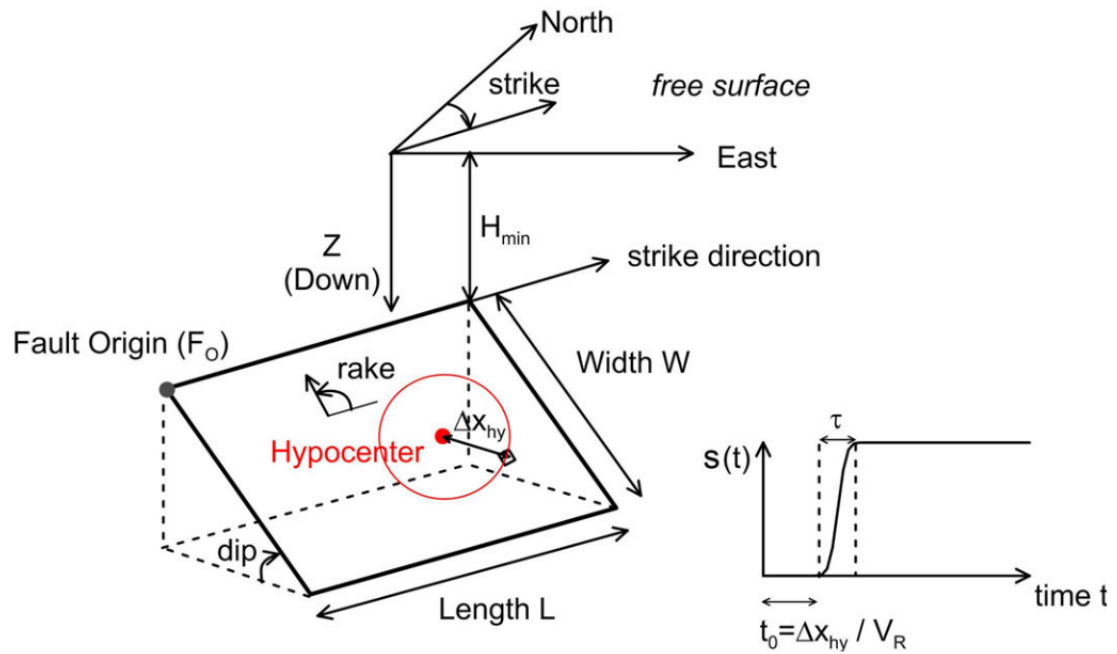
Figure 4.3: Sketch of fault geometry parameters required for the definition of the kinematic fault model implemented in SPEED.

4.2 Spatial coherency of seismic ground motion from numerical models

In the field of study related to the spatial variability of seismic ground motion, deterministic numerical models play a very important role relying on the following main advantages:

- possibility to locate an arbitrary number of receivers at the desired locations, with the desired inter-station distances and at desired soil conditions (soft/stiff soil vs rock);

- generation of arbitrary, albeit realistic, earthquake scenarios with prescribed magnitude at a given source-to-site distance, giving the possibility to study near-source motions which are poorly represented by earthquake recordings;

- possibility to investigate the physical mechanisms underlying the SVEGM in a more systematic way than the analysis of empirical recordings can do owing to the intrinsic lack of data.

On the other hand, the main drawback of 3D physics-based numerical simulations is the frequency threshold of computed results: even in the presence of an ideal case when a perfect seismic source model excite the whole frequency spectrum, the accuracy of numerical models in the high-frequency range is limited by the increased computational burden as the mesh gets finer and by the lack of detailed knowledge to construct a geological model with sufficient details also at short wavelengths, especially for complex configurations. As a result, accuracy is achieved for frequencies hardly larger than about 2 Hz, and the related limit in the minimum spacing between mesh nodes.

In the recent years, the aim of numerical simulations has became the extension of the frequency band of synthetics ground motion. Broadband (BB) waveforms are generally produced by a hybrid (HYB) approach combining low-frequency results from deterministic Physic-Based Simulations (PBS) with high frequency signals from stochastic approaches.
To this aim, Paolucci et al. (2018) proposed a novel approach making use of Artificial Neural Networks (ANNs), trained on a set of strong-motion records, to predict the response spectral ordinates at short periods. The main idea behind this procedure is to use trained ANN to estimate the short-period response spectral ordinates

(that is, for periods $T \leq T^*$, in which T^* is the minimum period of validity of the physics-based numerical model) using as input the long-period ones obtained by the PBS and, then, the PBS time histories are enriched at short periods by scaling iteratively their Fourier spectrum, with no phase change, until their response spectrum matches the ANN target spectrum (See Figure 4.4). Make reference to Paolucci et al. (2018) for a detailed explanation of the methodology,

In future, the development of BB numerical simulation, surely, will give an important contribution also to the study of the SVEGM and its effect on engineering applications.
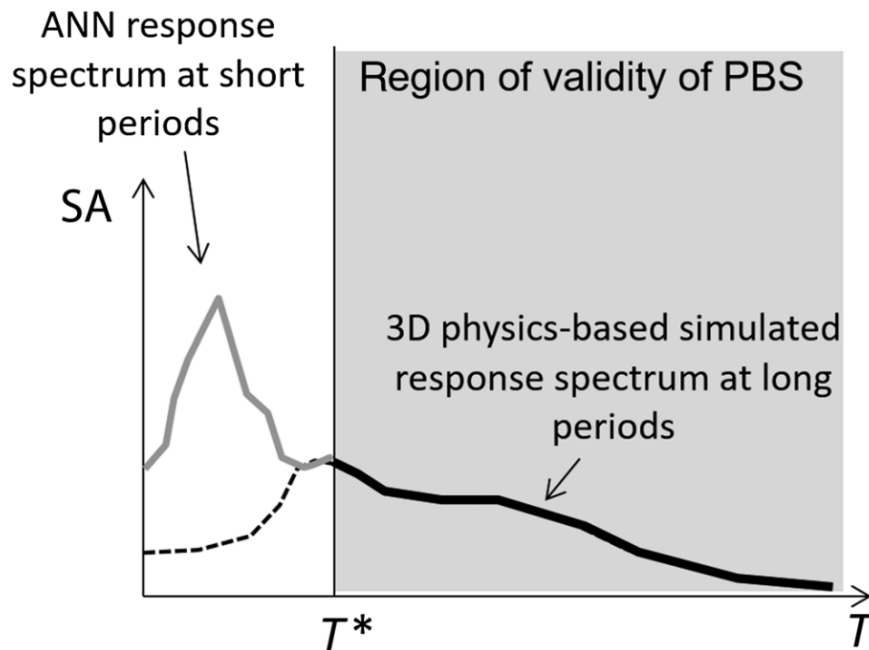
Figure 4.4: Sketch illustrating the idea behind the proposed Artificial Neural Network (ANN)-based approach to generate broad- band (BB) ground motions. From Paolucci et al. (2018)

In this section the different case studies will be presented and the results showed: at first an overview on the geological, seismological and geomorphological layout of each case study will be showed, then the result in term of lagged spatial coherency $|\gamma|$ will be provided following the procedure described in section 2.2, finally an overall comparison among case studies and the analysis of the dependence of the lagged coherency on physical parameters will be reported.

Commonly to all case studies, inter-station distances are grouped in ten 100-m bins, with each bin represented by the average distance of the station pairs belonging to

it and stations pairs are selected with reference to the array's central station which remain fixed. Since, the maximum frequency of the coherency estimates is equal to the maximum frequency of the numerical models, ranging between 1.5 and 2 Hz, a common frequency axis between 0 and 2 Hz will be adopted.

Although the numerical simulations are limited to a rather limited frequency range, specifically up to about 1.5-2 Hz, they can provide meaningful insights into the dependence of SVEGM on physical parameters, such as earthquake magnitude, source-to-site propagation path and site conditions.

The analysis shown herein is focused on the evaluation spatial coherency coming from three different areas in Italy:

- **Marsica** (Central Italy): the historical M_w 6.7 Jan 13 1915 earthquake, with normal mechanism, and three arrays (two inside the soft basin, A1 and A2, belonging to a soil class C/D characterized by $V_{s,30} = 180$ m/s and one on outcropping bedrock with $V_{s,30} = 1000$ m/s) are taken into account;

- **Emilia** (Northern Italy): the M_w 6.0 May 29 2012 earthquake, with reverse focal mechanism, and 4 different arrays (A1-A4) on the surface of the Quaternary sediments of the Po Plain (soil class C with $V_{s,30} = 300$ m/s), are considered;

- **Norcia** (Central Italy): the M_w 6.5 Oct 30 2016 earthquake and 12 hypothetical scenarios of M_w 6.5, 6.0, 5.5, 4.0 are considered. 18 different arrays (A6 in soil class B with $V_{s,30} = 490$ m/s while the others are located on the outcropping bedrock belonging to soil class A) in near-fault region are defined;

Table 4.1 summarizes the main properties of the different scenarios analyzed in the present implementation.

Location	Arrays	EC8 site class	Earthquake Scenario	Fault Type	M_w	References
Marsica (Central Italy)	A1-A3	A1-A2: C/D A3: A	Jan 13 1915	Normal	6.7	Paolucci et al. (2016)
Emilia (Northern Italy)	A1-A4	A1-A4: C	May 29, 2012	Reverse	6.0	Paolucci et al. (2015)
Norcia (Central Italy)	A1-A18	A6: B others: A	Oct 30, 2016 Hypothetical	Normal	6.5 4.0 5.5 6.0 6.5	Özcebe et al. (2019)

Table 4.1: List of 3D numerical simulations used for the estimation of SVEGM

It is worth recalling that all cases studies considered in this work have been validated against earthquake recordings in previous works. As an example, in Figure 4.5 the three-component velocity waveforms obtained by the three-dimensional physics-based numerical simulations of the Emilia case study are compared with the actual recording at 10 representative SM stations. The latter were chosen to provide a relatively uniform sample in terms of their geographic distribution. The agreement between synthetics and records is good in both time and frequency domain, especially on the horizontal NS and vertical component for almost all considered stations. In particular, the agreement of the NS velocity pulse, with PGV around 50 cm/s at the closest stations to the epicenter (i.e. MRN and MIR01) is remarkable. For a complete discussion, the reader is referred to Paolucci et al. (2015).
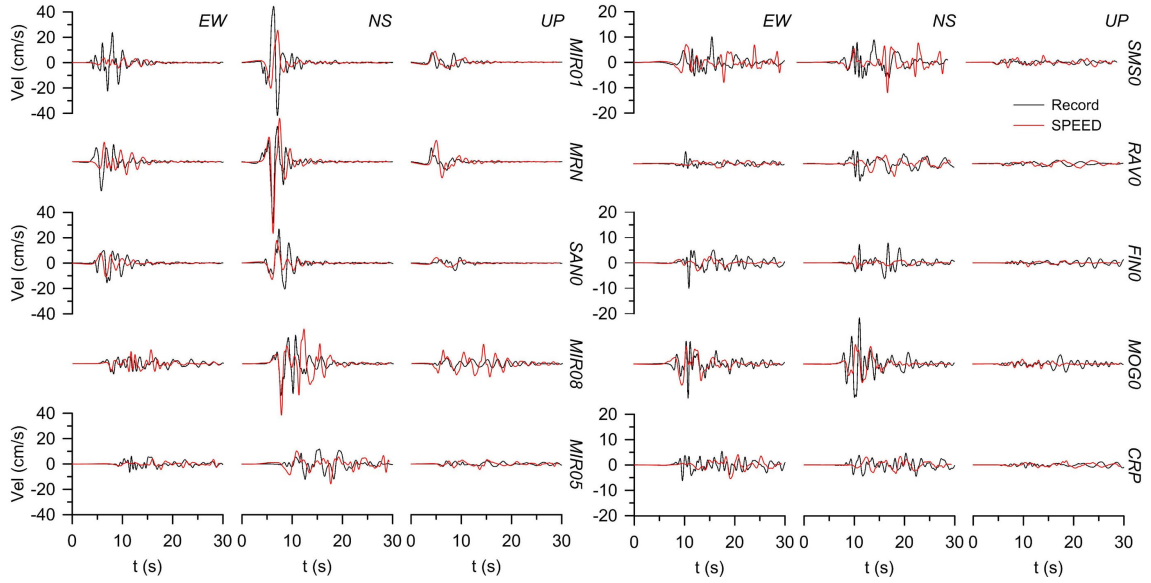
Figure 4.5: Comparison between recorded (black line) and simulated (red line) three-component velocity waveforms for a representative subset of 10 SM stations. Data are band-pass filtered between 0.1 and 1.5Hz. From Paolucci et al. (2015).

Estimates of lagged spatial coherency $|\gamma|$ are provided in this section on the basis of the procedure described in Section 2.2, for the different cases studies under consideration. In the following reference is made only to the lagged coherency so that the term lagged will be omitted.

Furthermore, as commented previously, coherency estimates are given in the frequency band of validity of numerical modelling. Future studies will address the challenge of spatial coherency from broadband physics-based ground motions.

4.2.1 Marsica case

On January 13, 1915, a catastrophic earthquake devastated Marsica, Southern Abruzzi, Central Italy, causing around 33 thousand of fatalities and substantial damage to the majority of buildings. Despite at that time the availability of seismic recording was very poor leading to a complex and difficult determination of the exact earthquake magnitude, many sources in literature estimated the magnitude in the range between 6.6 and 7.0.

The seismic event, originated by the Fucino fault system consisting of an array of NW-SE striking normal faults, dipping mainly SW, hit an area characterized by large thickness sedimentary basin, thus enhancing the hazard typical of near-source conditions.

The Fucino basin is the most important intra-mountain depression of the Central Apennines; it is surrounded by an outcropping bedrock made up of high carbonate ridges of Meso-Cenozoic age and it consists on Quaternary lacustrine and subsequent alluvial sedimentations.

The 3D numerical model, proposed and validated by Paolucci et al. (2016), includes the geological and geotechnical model of the Fucino area and a kinematic source model of the fault.
Concerning the geological and geotechnical model (Figure 4.7), it is built by assembling the topographic layer, obtained by a 250 m Digital Elevation Model, with the underlying layers describing the bedrock morphology and the lacustrine sediment layer, assumed to behave as a non-linear visco-elastic medium characterized by a single profile of density (ρ) and shear wave velocity (V_s). The shear wave velocity profile adopted to model the Fucino basin, which was found to be in good agreement with experimental measurement of resonance frequency by Standard Spectral Ratio (SSR) and Horizontal-Vertical Spectra Ratio (HVSR) methods, is defined by the following expression Paolucci et al. (2016):

$$V_s(z) = 100 + 10 \cdot z^{0.60} \tag{4.1}$$

Outside the basin, a crustal model is adopted: it is characterized by five horizontal and parallel layers resting on a half-space at a depth of 20 km (see Table 4.2).

Regarding the kinematic source model, the parameters describing the fault are summarized in Table 4.3 and the assumed slip distribution based on Bernard and Herrero (1994) are shown in Figure 4.8.

In order to study the SVEGM, 3 dense arrays were defined: A1 and A2 are located over the Fucino basin, hangingwall side, while A3 is positioned over the outcropping bedrock on the footwall side (see Figure 4.6). The arrays location was not defined by chance, conversely, their position was accurately studied to analyze the dependence of the spatial coherency on the fault directivity, the source-to-site distance and the geological conditions.
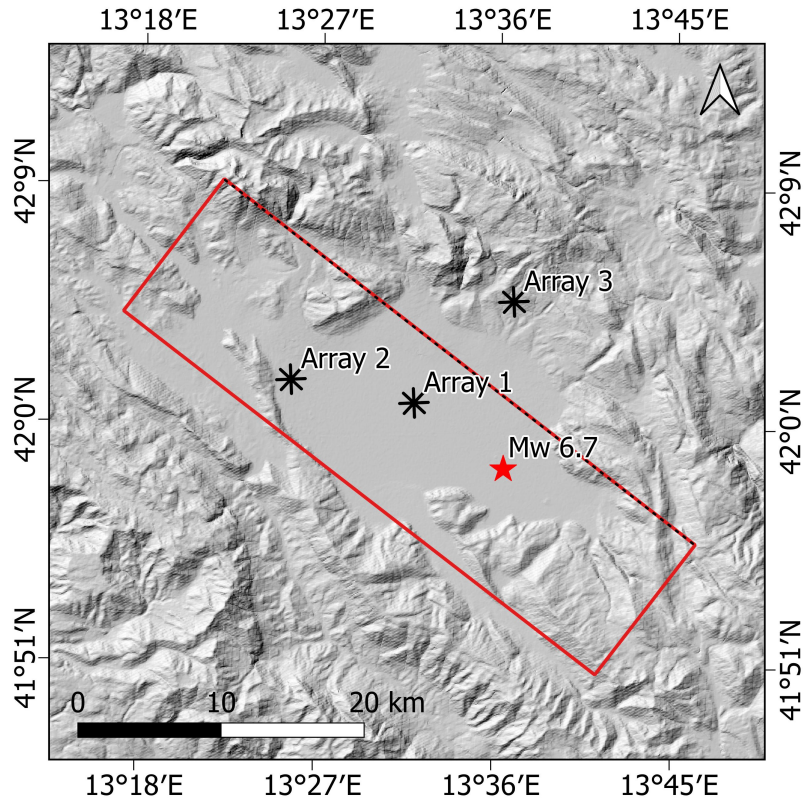
Figure 4.6: Map representing the three dense arrays, the fault projection ad the epicenter. The back ground represent the DEM of the area
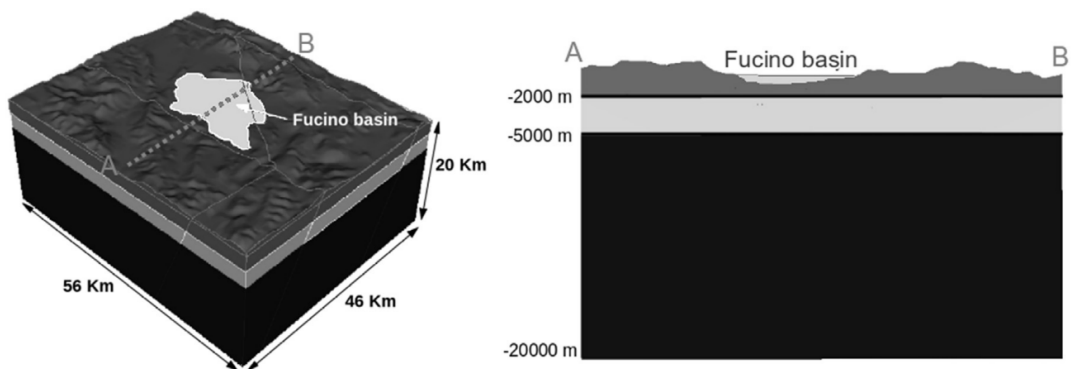
Figure 4.7: 3D numerical domain, with a representative cross-section transverse to the Apennine chain.From Paolucci et al. (2016).
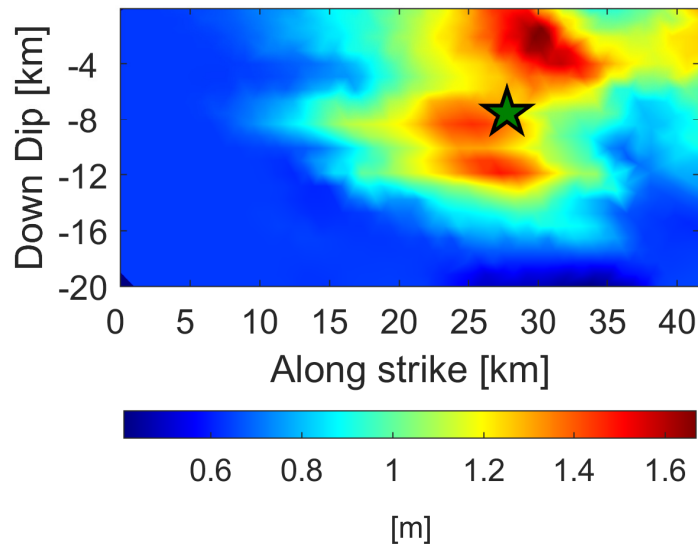
Figure 4.8: Slip distribution. Note that the vertical axis denotes the downdip direction and its origin lies at 337 m depth.

H [m]	V_S [m/s]	ρ [kg/m³]	Q
500	1000	2300	100
1000	1700	2500	150
2000	2600	2840	250
5000	3100	2940	300
20000	3500	3180	350

Table 4.2: Horizontally stratified crustal model assumed for the 3D numerical simulations. From Paolucci et al. (2016).

Fault Parameters	Present study
Fault Origin F_0 (Lat,Lon)	(42.15 N, 13.37 E)
Top Depth of Fault H_{min} (km)	0.337
Length along Strike L (km)	41.6
Width along Dip W (km)	20
epicenter (Lat,Lon)	(41.97 N,13.60 E)
Focal Depth (km)	6.4
Strike (°)	127.8
Dip (°)	53.3
Rake (°)	260
Seismic Moment M_0 (Nm)	$1.25 \cdot 10^9$
Rise time τ (s)	0.7
Rupture Velocity V_R (m/s)	0.85 V_S

Table 4.3: Fault parameters (the nomenclature refers to Figure 4.3). From Paolucci et al. (2016).

Results

To present an overview of the results obtained for each array, mean FP (black line), FN (red line) and UD (blue line) coherency curves, computed by averaging the coherency functions evaluated for each couple of station belonging to a prescribed distance bin and ground motion component, are given in Figures 4.9.
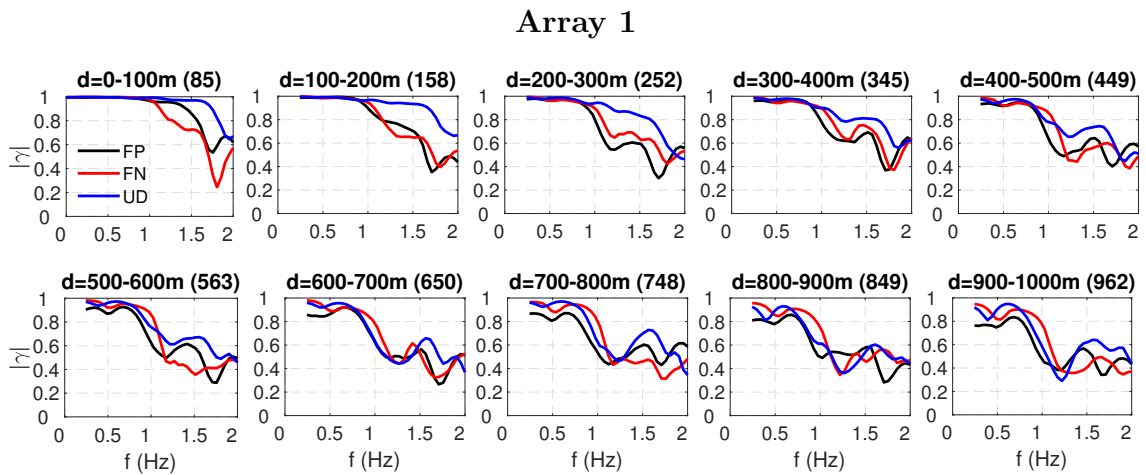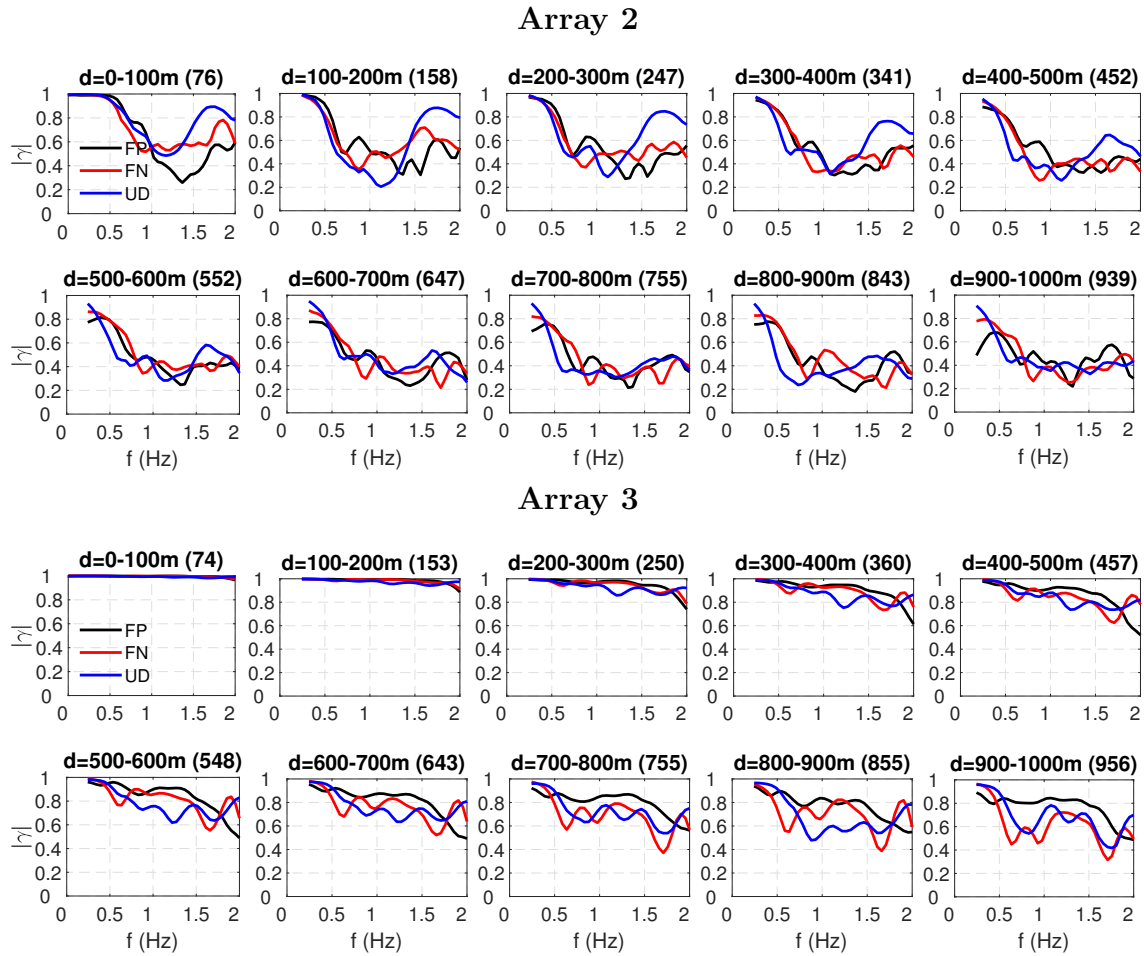
Array 1

Figure 4.9

Comparing the results coming from the three arrays, the first observation that can be made is the strong effect due to the soil condition: the curves belonging to the Arrays 1 and 2 present much lower values of $|\gamma(f)|$ at every distance bin, than the one belonging to the Array 3. Array 1 and 2 are located on the Fucino basin, which is characterized by a very low shear-wave velocity and variable sediment depth leading to a huge enhancement of the loss of coherency which, in general, is expected in sites located on soil instead of rock.

It is, also, interesting to note that coherencies evaluated at Array 2, reach very low value since the first distance bin (0-100m). This could be explained by the fact that Array 2 is located at the boundary of the Fucino basin where the soft soil layer become thinner leading to the generation large amount of surface waves that,

summing up with the effect of soft soil, provides a strong decrease in the spatial coherency.

4.2.2 Emilia case

Between 2012 May and June, a sequence of earthquakes struck a densely populated area in the Po Plain, about 20km north of Modena and west of Ferrara, in the Emilia-Romagna region, Northern Italy, causing fatalities and substantial damage especially to industrial facilities and historical monuments. The seismic sequence culminated, on May 29, with a strong earthquake of M_w 6.0.

The seismic event, which was produced by the rupture of reverse fault (22 km length and 12 km width) trending nearly EW (Strike = 95°) and dipping south (Dip = 60°), took place at a complex geological area: the Po Plain is a deep and large sedimentary basin with sharp variability of sediment thickness from a few tens of metres to about 7.5 km.

In Figure 4.11 a representative NS cross-section of the 3D velocity model passing through Mirandola shows how the Quaternary and Pliocene sediment thickness vary, producing prominent trains of surfaces waves which strongly affects the near-field spatial coherency.

The numerical model, proposed and validated by Paolucci et al. (2015), is characterized by:

- a kinematic representation of the seismic fault rupture, defined following the approach developed by Bernard and Herrero (1994), whose parameters are summarized in Table 4.5. Figure 4.12 shows the slip distribution of the source model which was adjusted by Paolucci et al. (2015) allowing a satisfactory agreement of the numerical simulations with the near-source records introduced in the previous section.

- a 3D velocity model of the Po Plain: it allows to consider the spatial variation of the most relevant geological discontinuities beneath the surface sediments which have significant effects on the seismic wave propagation: they produce prominent trains of surfaces waves which strongly affects the near-field spatial coherency. Figure 4.4 shows a representative NS cross-section of the 3D velocity model.

The validation process, developed by Paolucci et al. (2015), consisted on the comparison between the synthetic waves produced by SPEED with real recordings observed at the INGV stations present in the area. Despite the complex geological layout, the agreement between synthetics and records resulted to be good in both time and

frequency domain, especially on the horizontal NS and vertical component for al-
most all considered stations.

In order to study the SVEGM, 4 dense arrays were defined: A1 and A2 are located
at about 12 km south and north respectively from the fault over a thick Quaternary
sediment layer while A3 and A4 are actually over the fault where the Quaternary
and Pliocene layers become thinner (see Figure 4.10 and 4.11). The arrays location
defined to analyze the dependence of the spatial coherency on the fault directivity,
the source-to-site distance and the geological conditions.
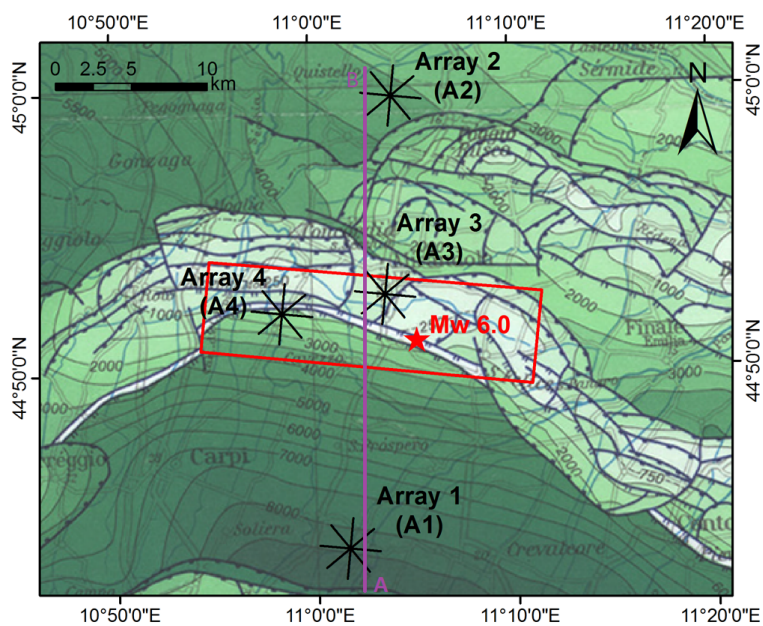
Figure 4.10: Structural map of the Emilia Area, reproduced from Bigi (1992), where
the different shades of green denote the depth of the base of Pliocene; the epicenter
(stars) and fault of the May 29 (M_w 6.0) are also indicated.
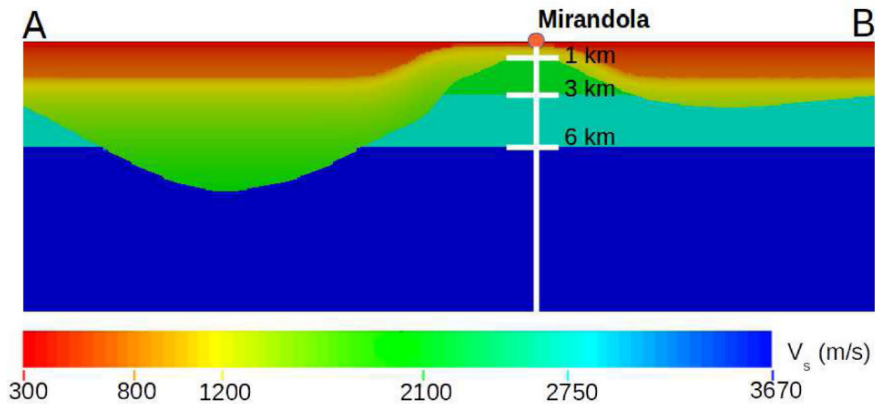
Figure 4.11: Representative NS cross-section of the numerical model passing through Mirandola, showing the VS model adopted in the 3D numerical simulations for both Quaternary-Pliocene deposits and bedrock. From Paolucci et al. (2015).
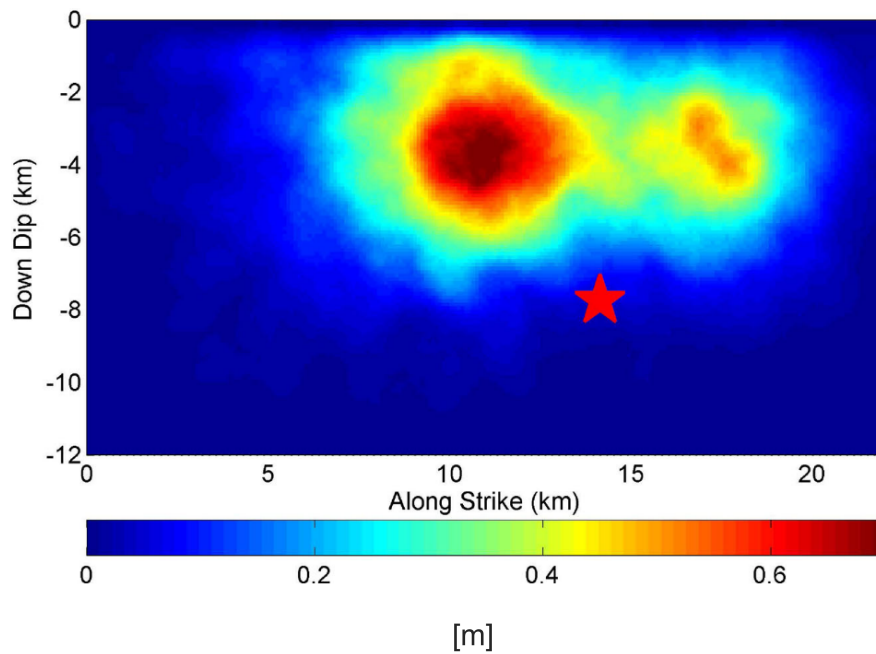
Figure 4.12: Slip distribution. Note that the vertical axis denotes the downdip direction and its origin lies at 3.7 km depth

H [m]	V_S [m/s]	ρ [kg/m³]	Q
150	250	1800	25
500	800	2100	80
1000	1200	2100	150
3000	2100	2200	200
6000	2750	2400	250
>6000	3670	2800	350

Table 4.4: Horizontally stratified crustal model assumed for the 3D numerical simulations. From Paolucci et al. (2016).

Fault Parameters	Present study
Fault Origin F_0 (Lat,Lon)	(44.900 N, 10.914 E)
Top Depth of Fault H_{min} (km)	3.7
Length along Strike L (km)	22
Width along Dip W v	12
epicenter (Lat,Lon)	(44.851 N,11.086 E)
Focal Depth (km)	10.4
Strike (°)	95
Dip (°)	60
Rake (°)	90
Seismic Moment M_0 (Nm)	$9.35 \cdot 10^{27}$
Rise time τ (s)	0.7
Rupture Velocity V_R (m/s)	0.85 V_S

Table 4.5: Fault parameters (the nomenclature refers to Figure 4.3). From Paolucci et al. (2016).

Results

To present an overview of the results obtained for each array mean coherency curves estimated for each ground motion component are given in Figure 4.13.
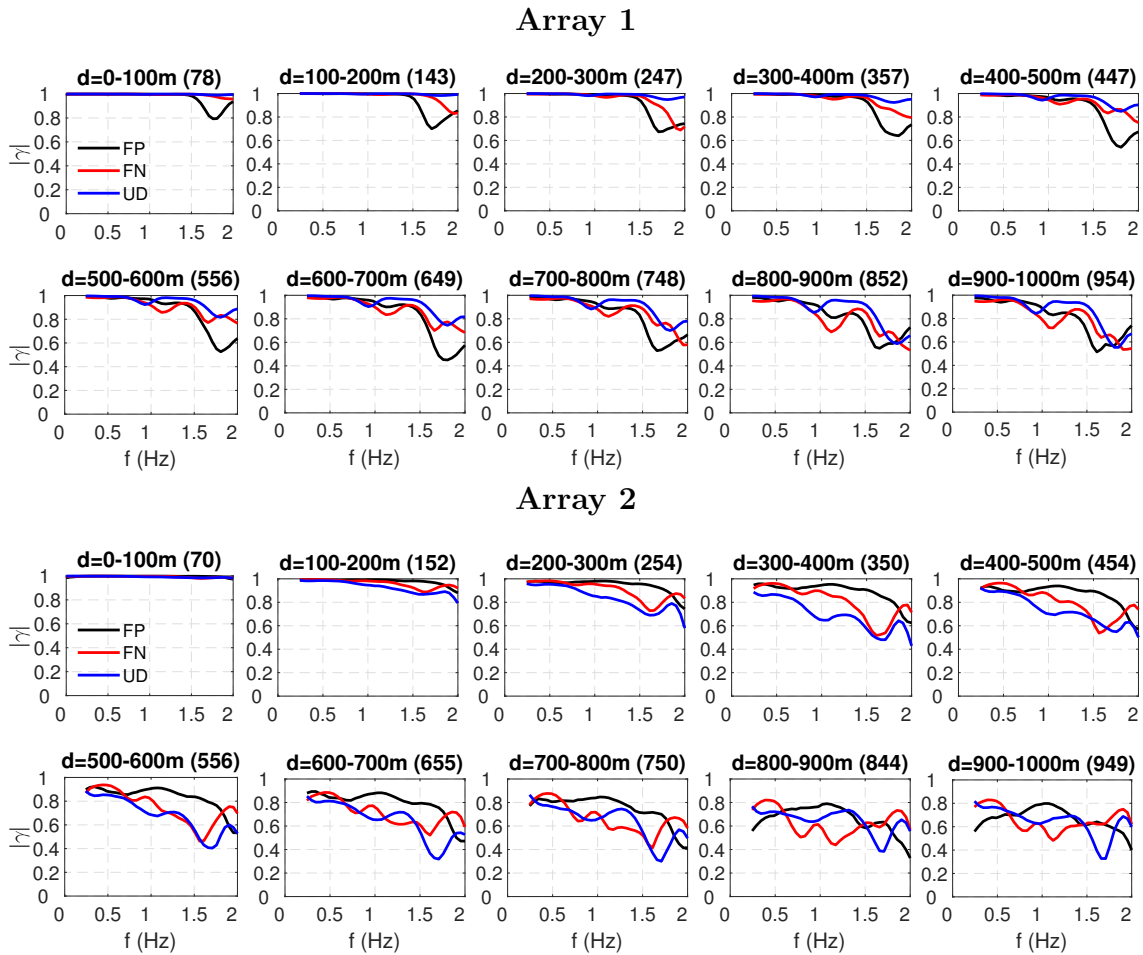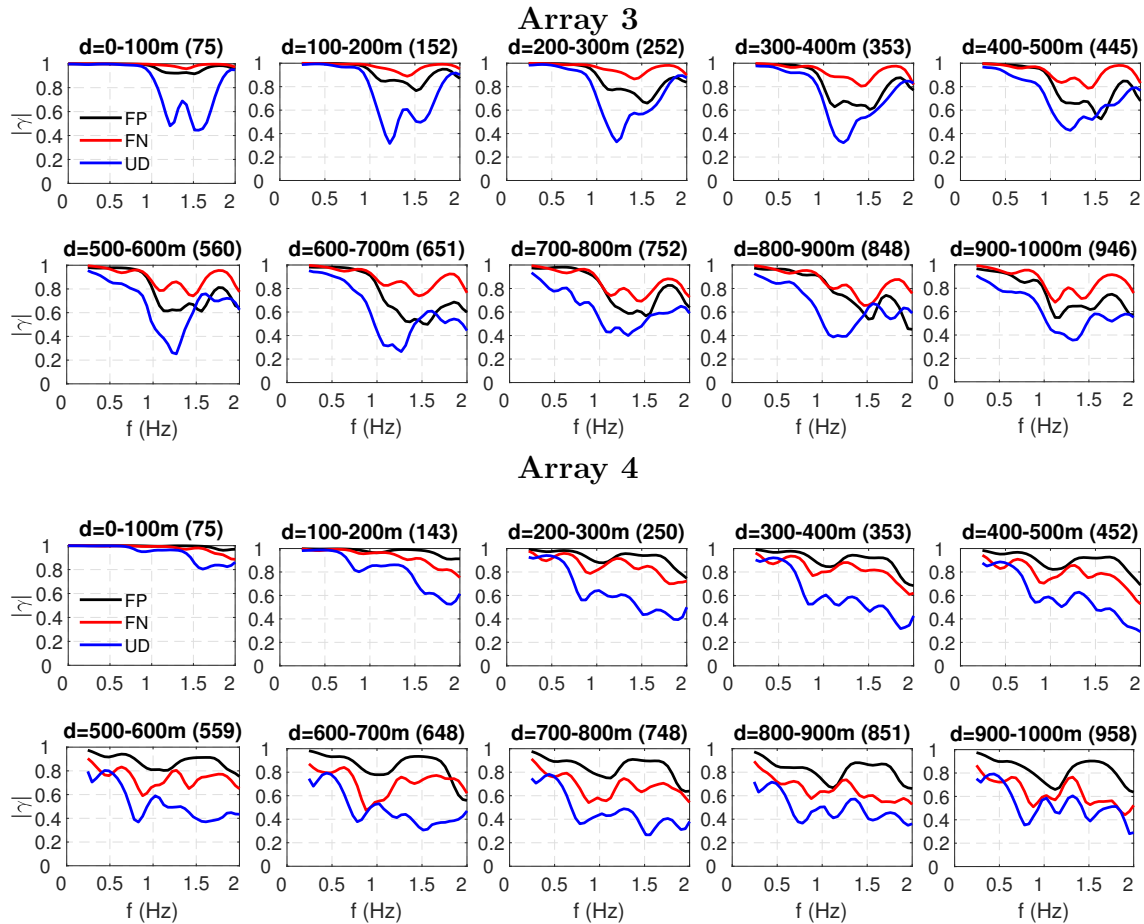
Figure 4.13: Array from 1 to 4. Mean coherency curves estimated for each component of ground motion FP (black line), FN (red line) and UD (blue line). The number within brackets represents the average distance between the pairs falling within each distance bin

Looking at Figure 4.13 some peculiarity appear clearly:

- Array 1 and 2, which are located at about 12 km from the source over a thick sedimentary layer, present a trend of the lagged coherency with distance and frequency which is rather similar to each ground motion component, while Array 3 and 4, which are instead located directly above the fault over a thin sedimentary layer, show strong differences between the components in particular regarding the vertical component.

  This is due to the strong impact of the seismic source and, hence, extended fault effects on spatial coherency, for site which are located on the surface projection of the fault: the incident rays coming from the source do not constitute

a field of vertical parallel rays which hit the site almost simultaneously as usually happens in far-fault region, on the opposite due to the extension of the source waves which are propagating from different regions of the fault would travel through different path leading to a consistent reduction of coherency.

- Array 1 and, especially, Array 3 show an higher coherency, at almost all frequencies and distances, of the fault normal component with respect to the fault parallel one. The physical reason should be associated to the fact that the up-dip movement of the hangingwall in direction normal to the fault produces stronger and more coherent waves which radiates up-dip in normal direction rather than in parallel one owing to directivity effects. As a matter of fact, directivity effects are known to produce the simultaneous arrival of different packages of waves (thus leading higher coherency of ground motions) and these effects are more pronounced along the FN direction.

  The opposite happens for the other two arrays: since Array 4 is located laterally to the line normal to the fault and passing through the hypocenter, it is less affected by this phenomenon while experiencing more the effect of the change in layer thickness in NS direction which produces loss of coherency (due to scattering); Array 2, instead, belonging to the footwall is not interested by this phenomenon due to the downdip direction of the wave front that produces the coherent front of waves in the direction opposite to the array.

In the Section 4.4 these and others observations will be treated in detail.

It is worth recalling the definition of directivity effect and its properties since it is an important and peculiar mechanism which distinguishes near-fault regions.
The rupture directivity effect consists on the following physical mechanism: the radiation pattern of the shear waves on the fault causes a large pulse of motion, coming at the beginning of the record and carrying most of the seismic energy, to be oriented in the direction perpendicular to the fault (see Figure 4.14,a). This effect is maximum when site, rupture propagation and hypocenter are on the same line.

In the field of SVEGM, the directivity effect provides, generally, an higher coherency in FN direction rather than in FP one: as shown in Figure 4.14,a a site located forward to direction of waves propagations experiences synchronous arrival of waves radiated by the fault in normal direction leading to a more coherent motion. In dip-slip earthquakes, the rupture directivity pulse is expected in the direction normal to

the fault dip, which in the horizontal plane reflects on the strike-normal direction.
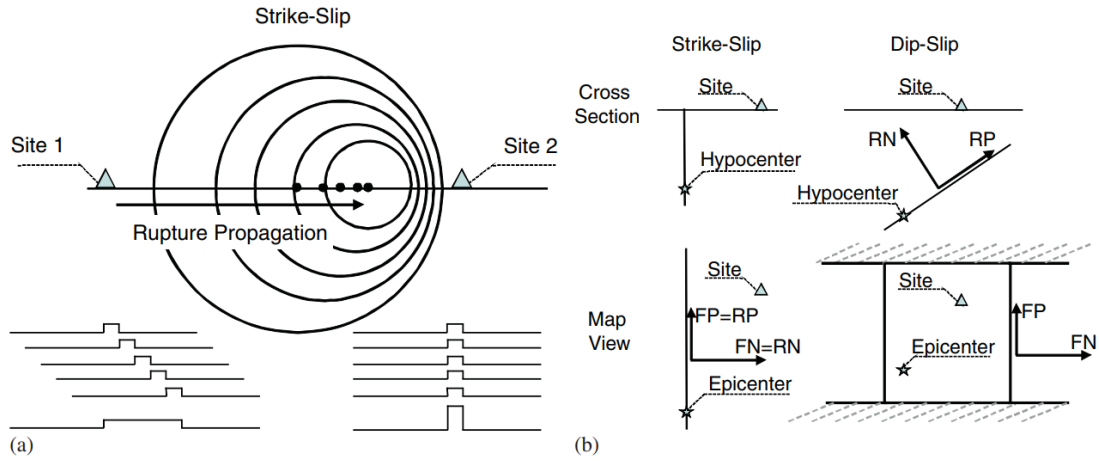
Figure 4.14: a) Schematic representation of the fault directivity effect for the case of strike-slip mechanism. b) directivity effects orientation for strike-slip and dip-slip cases. Adopted from Chioccarelli and Iervolino (2010).

4.2.3   Norcia case

Numerical model setup

Belonging to the group of the intra-mountain basins present within the Central
Apennines, Norcia basin is filled up by Pleistocene to Holocene age deposits and the
bedrock units consist of limestone and pelagic marls of Jurassic to Miocene age.
The 3D depth-velocity models of the Norcia basin was generated, under the assump-
tion of homogeneous material throughout the basin, starting from the results of a
microzonation study of the area and to a set of geophysical information.
Figure 4.15 shows the shear velocity profiles of Norcia basin included in the numer-
ical model.
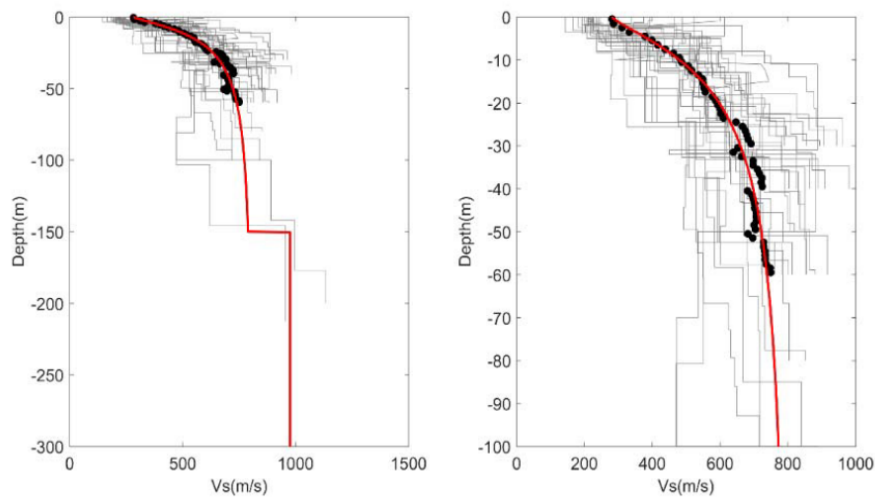
Figure 4.15: Left panel: Shear wave velocity profiles until 300 meters depth. Right
Panel: Close-up view of shear wave profiles until 100 meters depth. Results of in-situ
shear wave velocity tests (gray lines), representative mean values of in-situ results
until 60 meters (black dots), idealization of the shear wave velocity-depth profile
(red lines). From Özcebe et al. (2019).

In addition to 3D depth velocity of the basin defined previously, the other key ingre-
dient in constructing the 3D numerical model is the definition of the crustal velocity
model, which was developed based on the 1D crustal model on Evangelista et al.
(2017).
Table 4.6 summarizes the parameters adopted for the crustal model which was im-
plemented in the SPEED code.

H [m]	V_S [m/s]	ρ [kg/m³]	Q
1000	1700	2500	400
2000	2600	2840	400
5000	3100	2940	400
21000	3500	3150	400

Table 4.6: Crustal model defined according to Evangelista et al. (2017). H: thickness, ρ: density, V_S: shear wave velocity, Q: quality factor for S-waves
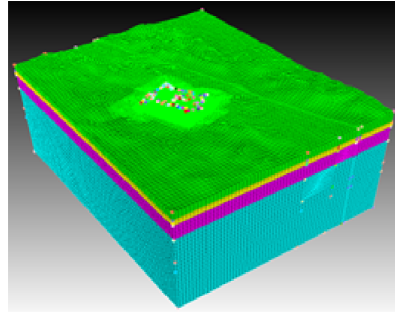
Figure 4.16: Crustal model. Model dimensions= 40 km (E-W) x 50 km (N-S) x 21 km (depth).

In the present implementation, different scenarios have been simulated using SPEED (see Table 4.8): all of them are characterized by the same geomorphological model but they differ from the point of view of the kinematic source model. Indeed, Scenario 1 and 2 are charactered by a distribution of slip that focus its peaks at the upper part of the fault (see Figure 4.17,a) while the others are associated to a distribution of slip which presents its peaks at the lower part of the fault (see Figure 4.17,b). As it could be seen in the next pages, considering different distributions of slip while keeping constant all the others fault parameters has many relevant effects in term of spatial coherency of ground motion.

Table 4.7 summarize the fault parameters common to all scenarios while Table 4.8 shows the specific parameters that characterize each case study.

(a) Scenarios 1 and 2

(b) Scenarios 3-13
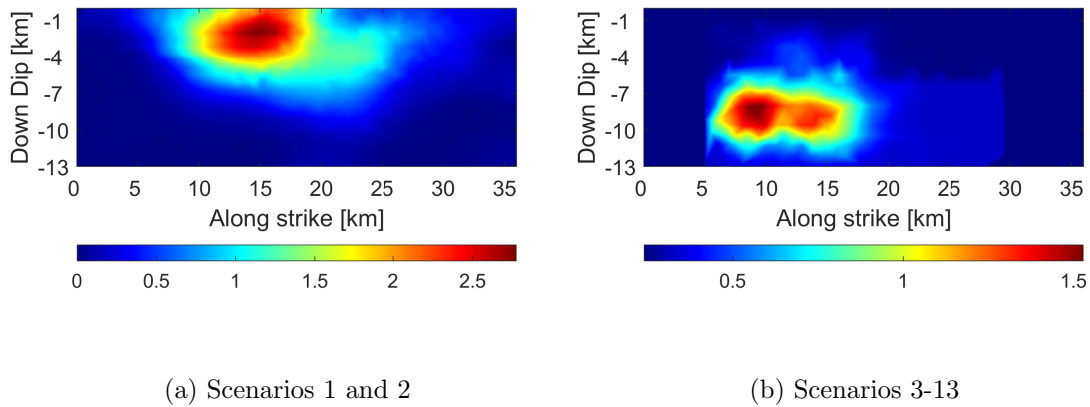
Figure 4.17: Slip distribution. Scale of slip in metres. Note that the vertical axis denotes the down-dip direction and its origin lies at 1.8 km depth.

Fault Parameters	Present study
Fault Origin F_0 (Lat,Lon)	(44.900 N, 10.914 E)
Top Depth of Fault H_{min} (km)	1.8
Length along Strike L (km)	36
Width along Dip W (km)	13
Strike (°)	160
Dip (°)	40
Rake (°)	-90
Rise time τ (s)	0.7
Rupture Velocity V_R (m/s)	1700

Table 4.7: Fault parameters (the nomenclature refers to Figure 4.3). From Özcebe et al. (2019).

| ID | Case study | M_w | Slip | hypocenter | | | Effective fault | |
				Lat	Lon	Depth (km)	Width (km)	Length (km)
1	30/10/2016	6.5	a	42.85	13.12	-6.33	9	24
2	30/10/2016 OB*	6.5	a	42.85	13.12	-6.33	9	24
3	Hypothetical	6.5	b	42.85	13.12	-6.33	11	21
4	Hypothetical	6.0	b	42.77	13.15	-6.71	9	12
5	Hypothetical	5.5	b	42.89	13.07	-7.81	6	5
6	Hypothetical	4.0	b	42.85	13.12	-6.33	point-like	point-like
A	Hypothetical	6.5	b	42.89	13.15	-2.47	11	21
B	Hypothetical	6.5	b	42.81	13.19	-2.48	11	21
C	Hypothetical	6.5	b	42.81	13.19	-2.48	11	21
D	Hypothetical	6.5	b	42.87	13.07	-8.26	11	21
E	Hypothetical	6.5	b	42.79	13.11	-8.26	11	21
F	Hypothetical	6.5	b	42.71	13.15	-8.26	11	21

Table 4.8: List of scenarios simulated through SPEED. Scenario 2 consist on numerical simulation of the real 30/10/2016 Norcia earthquake with the peculiarity that the Norcia basin is modelled as an outcropping bedrock. The column slip refers to the distribution of slip assumed in the simulation: a means Figure 4.17,a while b means Figure 4.17,b.

The Norcia case of study could rely on a wide and complete availability both of dense arrays (18) and simulated scenarios (13), this allowing one to study and analyze an extensive set of properties which characterize the spatial variability of ground motion. For this reason, in the following pages, the scenarios will be arranged in three main groups which will be analyzed separately:

1. **Group 1**: Scenarios 1 and 2 will be used to study the effect of soil condition on the SVEGM since they are practically the same smulation a part from the modelling of the Norcia basin. Indeed, in scenario 1 the Norcia basin is modelled as a non linear soil material characterized by a shear-wave velocity profile of Figure 4.15 while in scenario 2 Norcia basin is simply art of the outcropping bedrock (crustal model).

2. **Group 2**: Scenarios 3, 4, 5, 6 will be analyzed to study the effect of magnitude: they are made up by the same distribution of slip and almost the same

position of the hypocenter, what change is the magnitude of the earthquake and consequently the effective fault.

3. **Group 3**: Scenarios A to F will be employed to analyze the effect of the position of the hypocenter with respect to the fault. Indeed, in this scenarios the only property that changes is the hypocenter position, while the slip distribution is unchanged.

Group 1 - Effect of soil condition

To study the effect of soil condition coherency estimates from the Scenarios 1 and 2 are analyzed focusing on the comparison between the results at Array 6. Indeed, Array 6, in the SPEED model of Scenario 1, is located over the Norcia basin modelled with the actual geological properties while in Scenario 2 the model provides outcropping bedrock condition over the entire domain (i.e. the basin is artificially filled in with the outcropping bedrock material).

Figure 4.19 shows the Norcia area and the eighteen arrays defined in the present study; the epicenter of Scenarios 1 and 2 and the Array 6 (site under analysis) are highlighted. Furthermore, Figure 4.18 illustrates the distribution of slip and the position of the hypocenter of the two simulations.
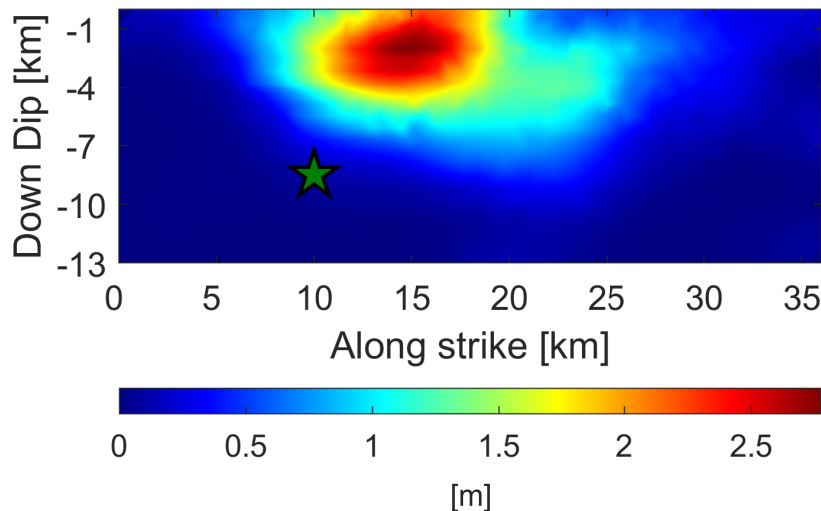
Figure 4.18: Group 1. Slip distribution and position of hypocenter.

Figure 4.19: Map of Norcia area showing the position of the arrays, the fault projection and the epicenter of the Group 1 earthquake scenarios.

Figure 4.20 shows, as an illustrative example, the coherency estimates as a function of frequency obtained from the analysis of the different magnitude scenarios at three distance bins (0-300m, 300-600m, 600-900m). As, expected, the curves related to soil condition are always below the rock ones. Note that the difference between the curves decreases increasing the inter-station distance. Deeper analysis will be given in Section ??.

Figure 4.20: Array 6. Mean coherency curves as a function of frequency, in the range 0 - 2 Hz, for three distance bins in the interval 0-900m, for the three component of motion. Estimates from the two scenarios are shown in same subplot.

Group 2 - Effect of magnitude

In order to study the effect of magnitude on SVEGM four scenarios of different magnitude (4.0, 5.5, 6.0, 6.5) have been simulated. They are characterized by the same crustal model, distribution of slip allowing to effectively capture the only dependence on magnitude without any contaminations generated by other variables. The analysis will be focused on three specific arrays (6, 9, 14) where the result coming from the four earthquakes will be compared. Furthermore, in section 4.4 some global analysis on all the arrays will be presented.

Figure 4.21 illustrates the Norcia area, the dense arrays and the position of the epicenters of the four scenarios considered. As for the previous group, Figure 4.22 shows the distribution of slip which characterizes the scenarios and the position of the hypocenters.
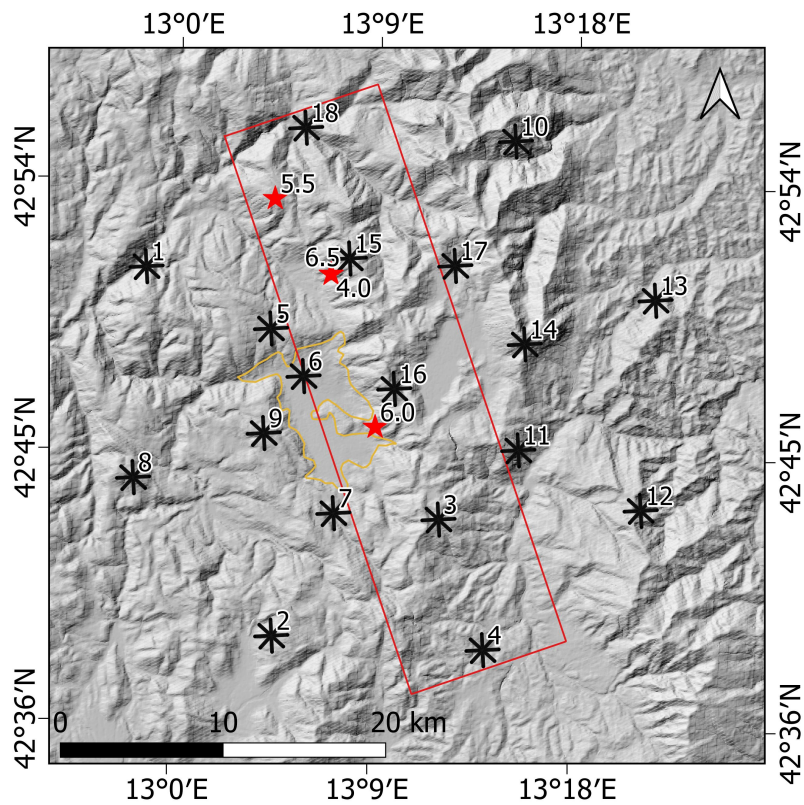
Figure 4.21: Map of Norcia area showing the position of the arrays, the fault projection and the epicenters of the Group 2 earthquake scenarios

113
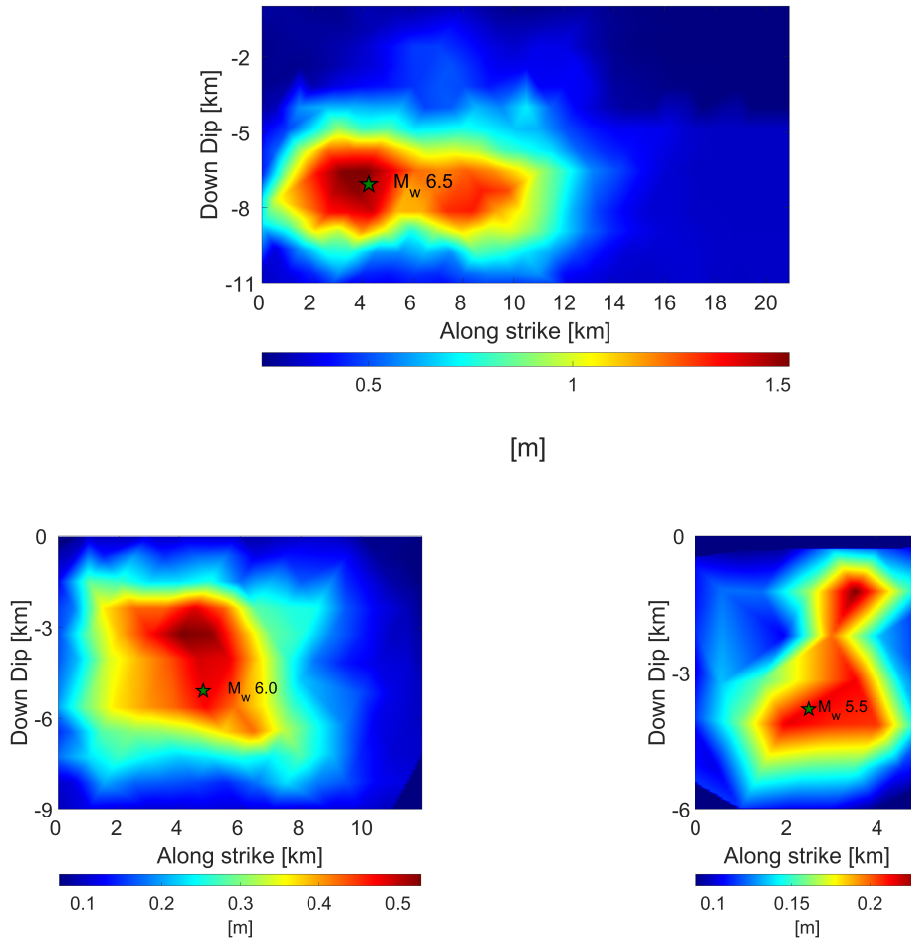
Figure 4.22: Group 2. Slip distribution and position of hypocenters.

Figure 4.23 shows, as an illustrative example, the coherency estimates as a function of frequency obtained from the analysis of the different magnitude scenarios at three distance bins (0-300m, 300-600m, 600-900m). It appears rather clearly that curves related to the event of magnitude 4 are almost always below the others whereas a definite difference is not apparent among the higher magnitude earthquake. Deeper analysis will be given in Section 4.4.2.
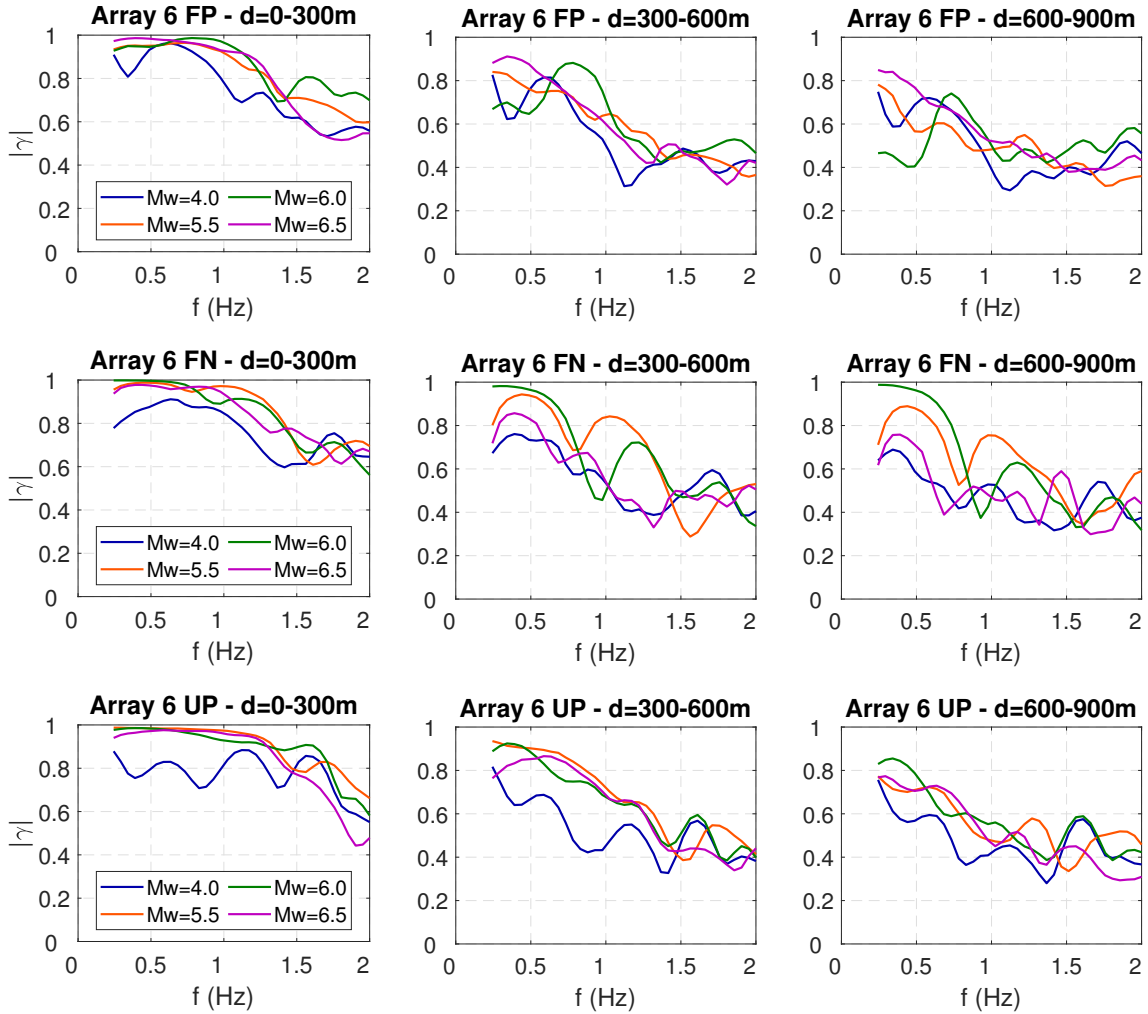
Figure 4.23: Array 6. Mean coherency curves as a function of frequency, in the range 0 - 2 Hz, for three distance bins in the interval 0-900m, for the three component of motion. Estimates from the four scenarios are shown in same subplot.

Group 3 - Effect of hypocenter position

The last group has been created to analyze the effect and the dependence of SVEGM on the hypocenter position. By keeping constant the crustal model, the slip distribution and the magnitude, a regular pattern of six hypocenter position have been defined. The comparison between the results from each scenario will take place at three arrays (9, 14 and 16) since they are located in strategic position: next to (or directly above) the fault and at the longitudinal mid span of the fault. Moreover array 9 have the same distance from the fault but array 9 is on the hangingwall while 14 on footwall. This distribution of hypocenters and arrays allows to accurately

study the effect of hypocenter depth (arrays A, B and C are superficial hypocenters while D, E and F are deep) on both hangingwall and footwall.

Figure 4.26 shows, as an illustrative example, the $|\gamma(f)|$ obtained from the analysis of the different scenarios at three distance bins (0-300 m, 300-600 m, 600-900 m). It appears that the dependence on the hypocenter position is quite high: if we imagine to envelope the maximum and minimum absolute values among all curves at each frequency, it could be seen that the ratio between the maximum envelope and the minimum one is on average around 20%.

In Section 4.4.6, further and deeper analysis will be carried out.
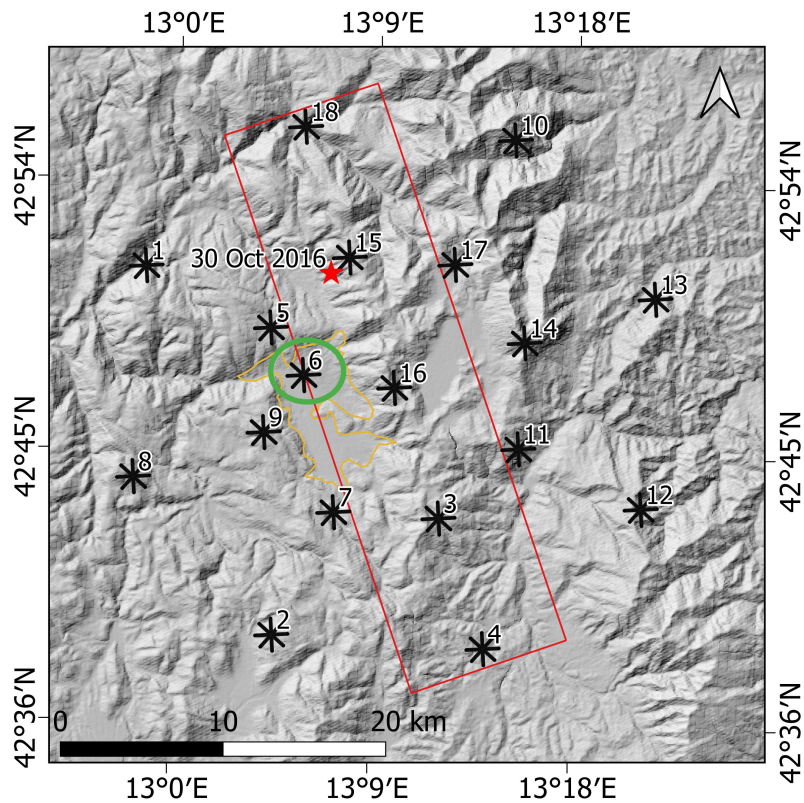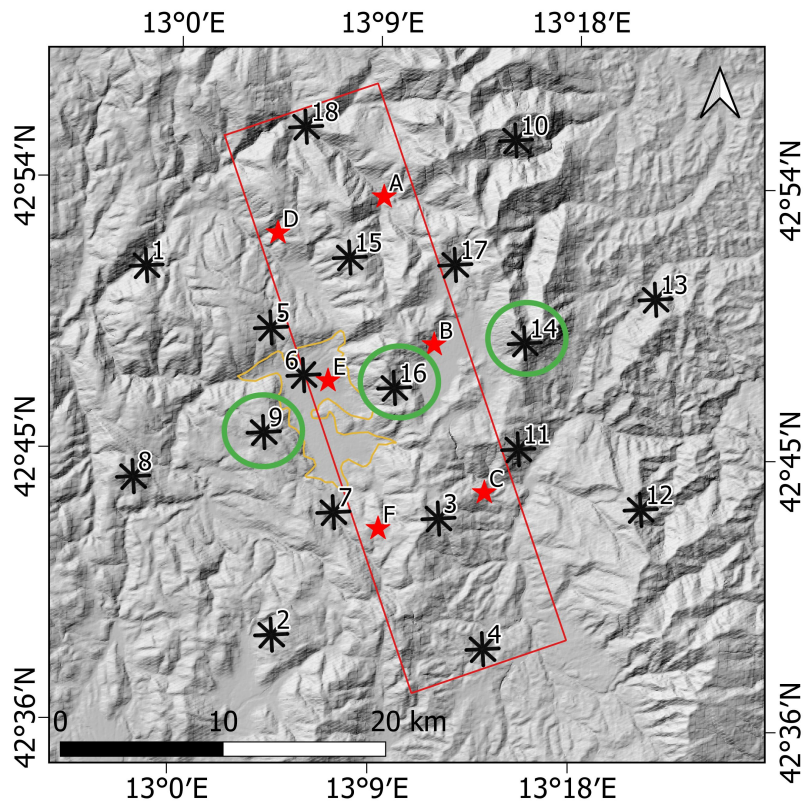

Figure 4.24: Map of Norcia area showing the position of the arrays, the fault projection and the epicenters of the Group 3 earthquake scenarios.
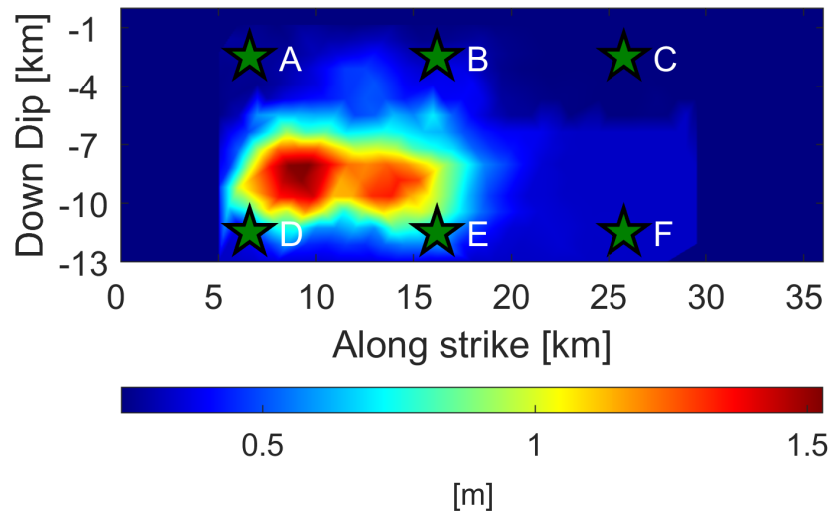
Figure 4.25: Group 3. Slip distribution and position of hypocenters for M_w 6.5 scenarios.
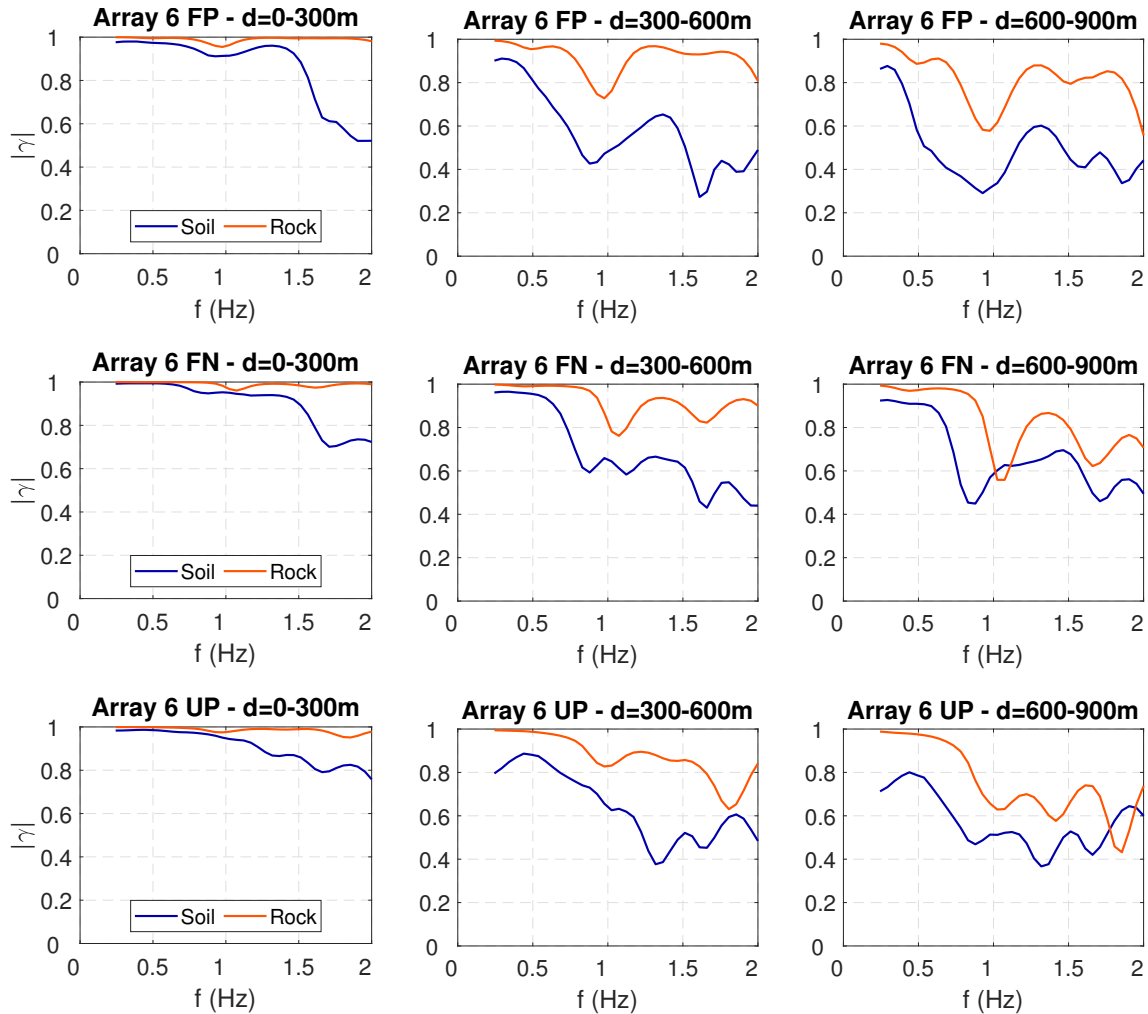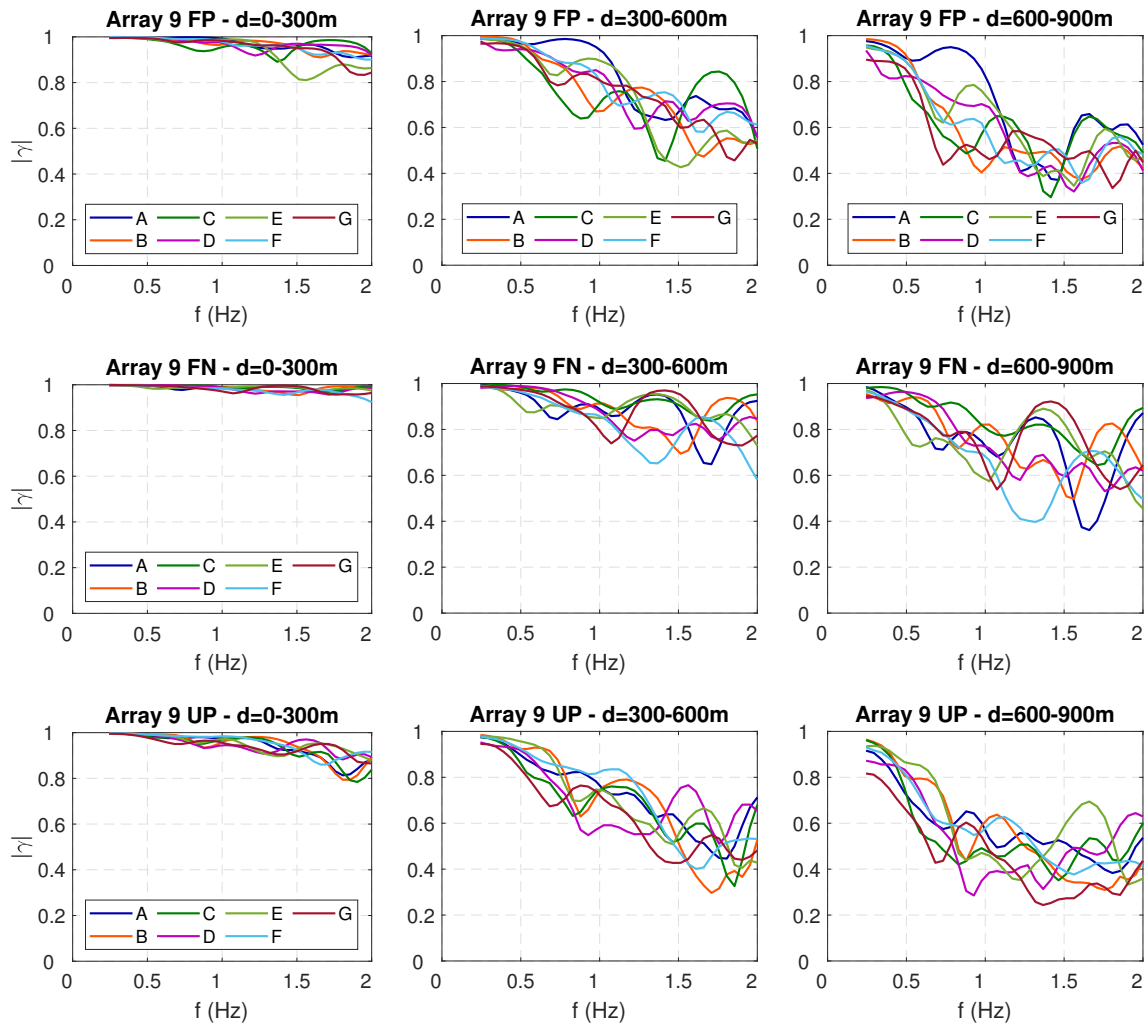
Figure 4.26: Array 9. Mean coherency curves as a function of frequency, in the range
0 - 2 Hz, for three distance bins in the interval 0-900m, for the three component of
motion. Estimates from each scenario are shown in same subplot.

4.3 Comparison between observations and existing coherency models

In connection to what has been done in the Chapter 3, the results coming from the 3D physic-based numerical simulations described in previous sections are compared in the section herein with the empirical models of Harichandran and Vanmarcke (1986) and by Ancheta et al. (2011) and the semi-empirical model of Luco and Wong (1986).

Figures 4.27, 4.28, 4.29 compare the models cited previously with the corresponding estimates of the lagged coherency based on the Marsica, Emilia and Norcia numerical simulations, respectively, as a function of frequency for five inter-station distance bin (0-100m, 200-300m, 400-500m, 600-700m, 800-900m). Regarding Marsica and Emila case studies the result coming from all the available arrays are shown while for Norcia the analysis is focused on arrays 6, 9, 14, 16. The latter choice is due to the fact that those arrays are the most significant ones since they are close to the fault and provide a wide set of the main parameters affecting the SVEGM: Array 6 is both on soil condition and hangingwall, Array 9 is next to Array 6 but on rock, Array 14 is on footwall and finally Array 16 is perfectly above the source at its centroid.
Furthermore, the coherency estimates from Scenario 3 (see Table 4.8) are reported.

The curves corresponding to the empirical data (black line) is obtained by computing the arithmetic mean of the lagged coherency estimates associated to FP and FN components. This procedure is allowed under the assumption of isotropy of the coherency function.

These models are computed considering the average distance of each distance bin, reported in the title of each subplot (number in brackets).

The model by Ancheta et al. (2011) is compared with the estimates for distances less than 100m while the model of Harichandran and Vanmarcke (1986) is compared with the estimates for distances greater than 100m. The comparison with Luco and Wong (1986) is carried out by imposing the coefficient $\alpha = 2.5 \cdot 10^{-4}$ which is the value suggested by the authors themselves.

Looking at Figure 4.27, considering inter-station distances up to 100 m both Luco and Wong (1986) and Ancheta et al. (2011) are in good agreement with the Array 3 estimates while they describes correctly Array 1 and 2 estimates only at low frequencies (up to 0.5 Hz) exhibiting, at larger frequencies, strong divergence with the empirical curves. As observed in Section 4.2.1, due to the combination of very low shear-wave velocity and variable sediment thickness which characterize the site where Array 1 and 2 are located on, the coherency decay is strongly enhanced.

Regarding higher inter-station distances, for Array 3, both Luco and Wong (1986) and Harichandran and Vanmarcke (1986) models tend to overestimate the decay of coherency with frequency.

As a general observation, the models are in good agreement with the observed trend of lagged coherency for Array 1 at the distance bins 200-300 m and 400-500 m while the same happens for Array 2 but for the last two distance bins (600-700 m and 800-900 m). Furthermore, Luco and Wong (1986) tends to have a better behaviour at low frequencies while Harichandran and Vanmarcke (1986) at higher ones.

Considering now the Emilia case study (Figure 4.28), at inter-station distances up to 100 m both Luco and Wong (1986) and Ancheta et al. (2011) are in perfect agreement with coherency estimates for all the dense arrays.

Models' curves begin to diverge from distances higher than 200 m an the degree of divergence increase with increasing inter-station distances. This observation is valid for all the arrays which shows, in general, the same macroscopic trend.

Finally, looking at Norcia case study (Figure 4.29), as happened for the Emilia case, at the first distance bin (0-100 m) both models are able to capture almost perfectly the trend of estimated curves with frequency. A small exception regards Array 6 whose curve shows an higher decay with frequency than the models starting from about 1.5 Hz (remember that Array 6 is the only one which is located on soil condition).
Note that for Array 14 it has been not possible to find station pairs belonging to the first distance bin.

Regarding Array 6, it is interesting to note that: for distance bins higher than 200 m, the estimated curves are in general agreement with Luco and Wong (1986) at low frequencies (below 1 Hz) whereas for higher frequencies Harichandran and Vanmarcke (1986) fits rather perfectly the lagged coherency curves.

Similar behaviour is shown at Array 16 but with a general minor agreement.
Arrays 9 and 14 appear to have almost the same results in term of mean coherencies:
an expected insight since the are located on same soil condition and at the same
distance from the fault (remember that the curves shown in this section are mean
horizontal coherencies, thus effects related to the polarization of the ground motion
like source directivity effect could not be seen). From the comparison with existing
coherency models, both Luco and Wong (1986) and Harichandran and Vanmarcke
(1986) tend to overestimate the decay of coherency with frequency.
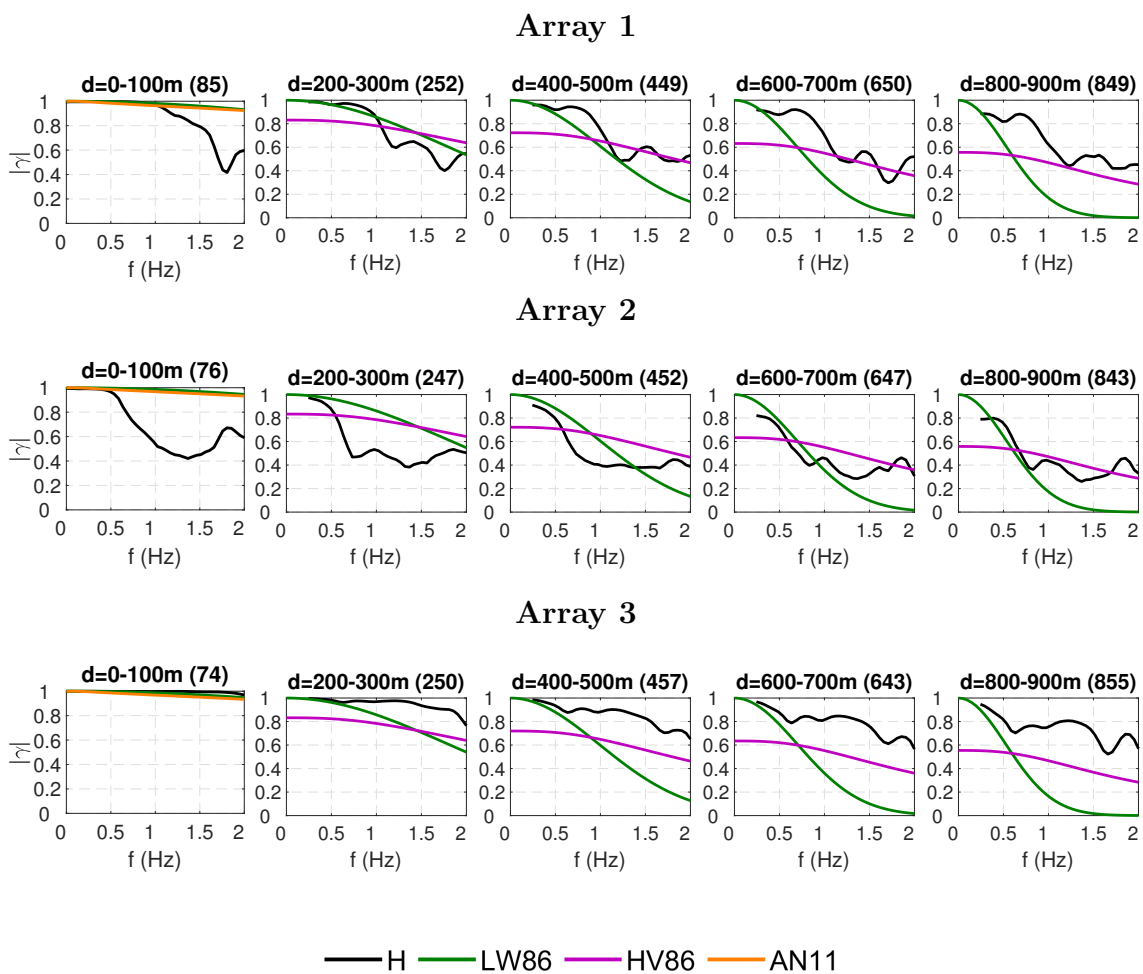
Figure 4.27: Marsica. Comparison with existing models. Mean lagged coherency
from the arithmetic mean of two horizontal (H) components (black line) com-
pared with LW86 (Luco and Wong, 1986), AN11 (Ancheta et al., 2011) and HV86
(Harichandran and Vanmarcke, 1986) models.

Array 1

Array 2
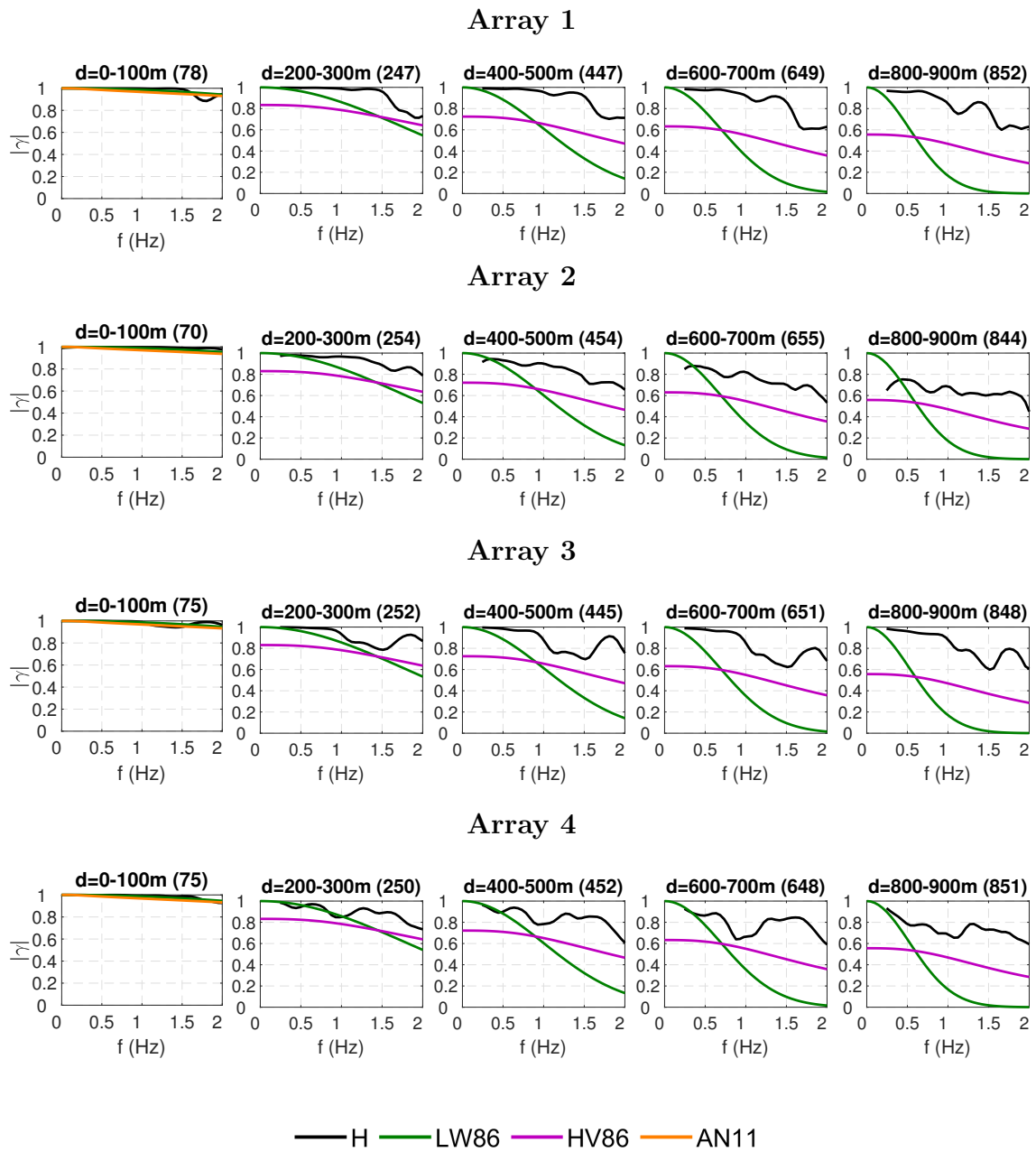
Array 3

Array 4

Figure 4.28: As Figure 4.27 but for Emilia case study.

Array 6

Array 9
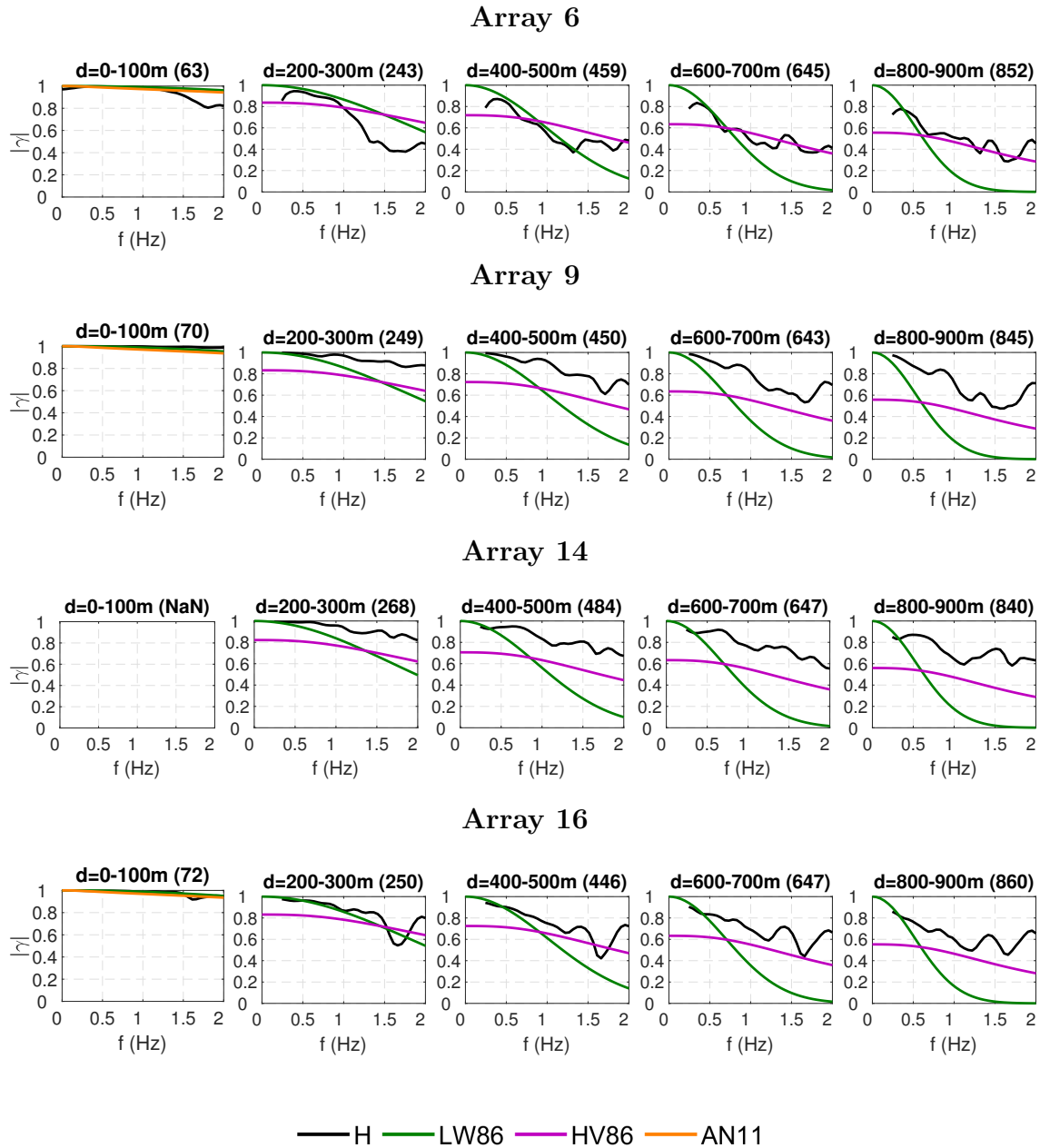
Array 14

Array 16

Figure 4.29: As Figure 4.27 but for Norcia case study. Note that for Array 14 it has been not possible to find station pairs belonging to the first distance bin.

4.3.1 Regression of results based on LW86 model

In line with what has been done in Section 3.3.1 to analyze coherency estimates from earthquake recordings, in the section herein, the value of the parameter α of LW86 model (see Eq.2.23) is computed from the synthetic ground motions obtained

from the 3D numerical simulations. Note that the parameter α is fitted in the range of frequency between 0.25 Hz (half of bandwidth) and 2 Hz (maximum frequency reachable by the numerical models in this study).

The parameter α allows a concise measure of spatial coherency, apt for identifying common trends and performing some significant statistics. In particular, in the present section the dependence of α with distance as been studied aiming also to compare the different case studies (Marsica, Emilia and Norcia). It should be clarified that for Norcia case, in conformity to what done in the previous section, Array 6, 9, 14, 16 are analyzed under the Scenario 3 (see Table 4.8).
Note that the plotted values of fitted α are multiplied by a 10^4 factor and represented in $\log_{10}$ scale to better appreciate their variability.

The best fitting α values of the LW86 model are illustrated in Figure 4.30.
Results indicate a strong non-linear dependence of α on distance: α turns out to decrease with increasing inter-station distance at a rate which tends to be higher at smaller distances. This trend is enhanced at dense Arrays which are located on soil condition (Marsica - Array 1 and 2, Emilia - Array 3 and 4, Norcia - Array 6) whereas for rock soil condition the rate of decay of α with distance is strongly attenuated leading to rather constant value of α with distance.
Furthermore, fitted α shows a large variability taking values in the following ranges for the different case studies: $\sim 8.7 \cdot 10^{-5} \div 1.1 \cdot 10^{-3}$, for Marsica; $\sim 4.7 \cdot 10^{-5} \div 5.7 \cdot 10^{-4}$, for Emilia; $\sim 7.3 \cdot 10^{-5} \div 4.2 \cdot 10^{-4}$, for Norcia. As a general observation, α values show a reasonable range of variability, from about $4.7 \cdot 10^{-5} \div 1.1 \cdot 10^{-3}$. Konakli et al. (2014) estimated best fitting α values in the range $\sim 6 \cdot 10^{-5} \div 1 \cdot 10^{-3}$ for the UPSAR array, in agreement with most of the values obtained in this work.

The large variability observed in the results testifies how a complex stochastic process like SVEGM is dependent on a huge number of physical parameters which make difficult the postulation of general models valid for all case studies. The use of numerical simulations could provide a decisive help to the characterization of the different physical parameters. For this reason, in the following section, the dependence of fitted α on a series of physical parameters, such as ground conditions (soft soil vs rock), ground motion component (FN vs FP vs UD), magnitude, source-to-site distance, source directivity, hypocenter depth and and slip distribution will be discussed.
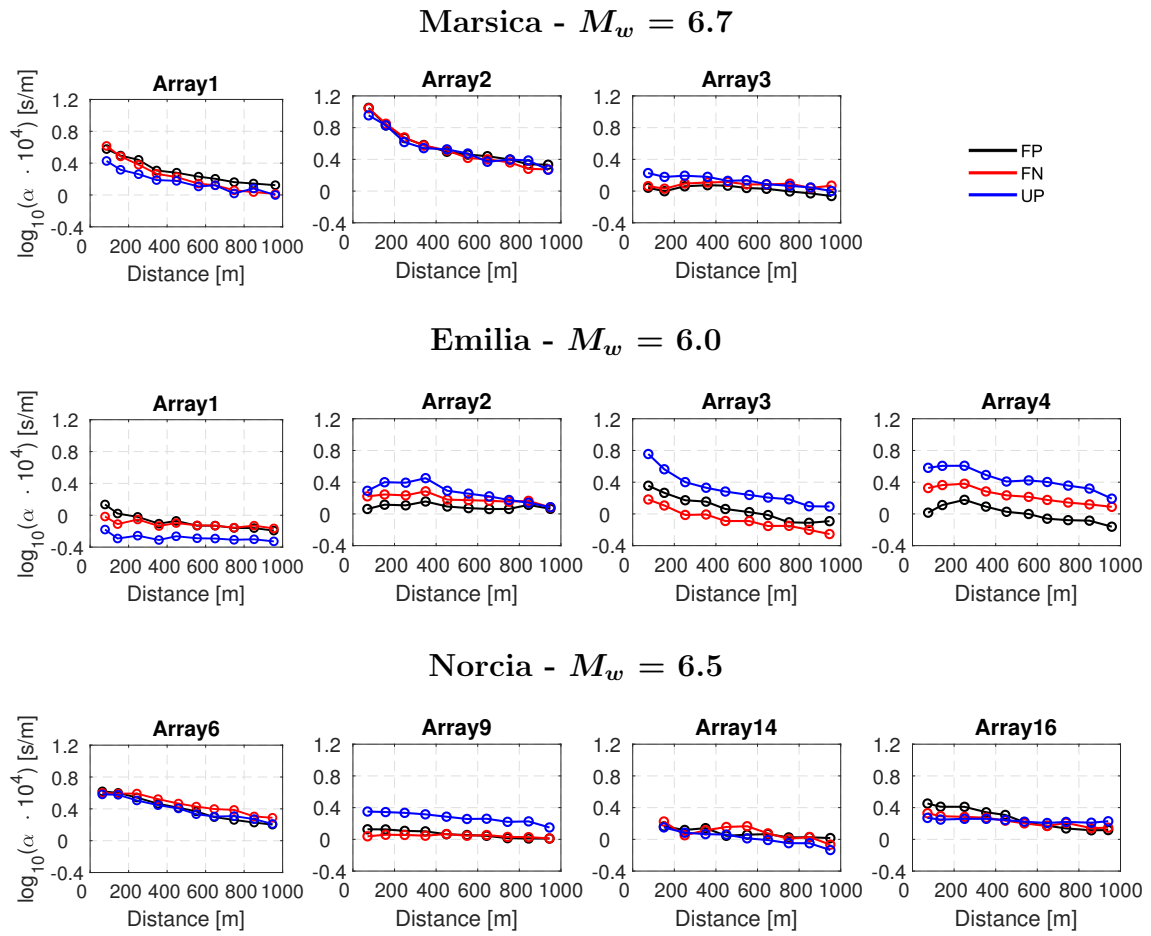
Figure 4.30: Best fitting α value of LW86 model as a function of separation distance. Fault-parallel (FP) component in black, fault-normal (FN) in red and vertical (UP) in blue.

4.4 Dependence on physical parameters of earthquake process

The nature of the variation of seismic phases in the earthquake data is rather complex. Thus it is difficult to relate the spatial coherency directly to physical parameters. However, a robust statistical analysis of the physic-based numerical simulations could reveal some physical insights into the possible causes underlying the loss of coherency.

The main objective of this section is to identify those simulation parameters which have a large influence on simulated coherency functions in near-fault region, and therefore need to be well constrained for the simulation of the strong ground motion field. In the present study we investigate the dependence of the coherency estimates with respect to: the specific ground motion component, magnitude, relative position between source and array, soil condition, source directivity, hypocentral depth and slip distribution. The results of the analyzes are reported in the following sections.

4.4.1 Ground motion directionality

To study the dependence of coherency on ground motion components, the ratios α_{FN}/α_{FP} and α_H/α_{UP} with α_{FP} (or α_{FN} or α_{UP}) representing the fitted α value on the FP (or FN or UP) component and α_H representing the average between the fitted α computed for the horizontal components, have been computed for each distance bin and for each case study.

Figure 4.31 illustrates the ratios α_{FN}/α_{FP} (left) and α_H/α_{UP} (right) for Marsica (Mw=6.7), Emilia (Mw=6.0).

For Norcia case study, the above mentioned ratios have been computed for three distance bins of width 300 m from 0 to 900 m and for the entire set of arrays. Figures 4.32 and 4.33 show a maps of Norcia area where each dot, whose colour identifies the value of the corresponding ratio (α_{FN}/α_{FP} and α_H/α_{UP}, respectively), represents an array. The position of the arrays is identified by the coordinates of their central station. Scenarios 3 and 6 are reported in order to analyze the behaviour of both an extended fault ($M_w = 6.5$) and a point-like source ($M_w = 4.0$). Furthermore, the projection of the effective fault on the ground plane is also shown.

Note that, in general, a value of the ratio α_a/α_b less (or larger) than 1 means that the coherency for component "a" is larger (smaller) than that for component "b".

It could be noted that:

- **Orientation of horizontal components:** For Emilia, α_{FN}/α_{FP} tends to be smaller than 1, i.e., coherency of FN component is larger than that of FP component, for receivers which are aligned with the hypocenter in fault normal direction and located on hanginwall (A1 and A3). The opposite is found for the other two arrays due to the fact that the FN component corresponds to the direction where complex site effects, associated with the propagation of prominent trains of surface waves, control earthquake ground motion and, hence, may induced a significant loss of coherency.

  For Marsica the polarization along the direction perpendicular to fault strike owing to the synchronous arrival of waves radiated by the fault provides $\alpha_{FN}/\alpha_{FP} < 1$ for arrays A1 and A2 which are directly above the fault on hangingwall. The opposite occurs for array A3 (located on footwall) where ratios larger than 1 are obtained.

  Norcia maps show the common trend of $\alpha_{FN}/\alpha_{FP} < 1$ for most of arrays and distance bins except for some isolated case. This behaviour is greater for Scenario 3 ($M_w = 6.5$) where the polarization of waves is stronger due to the fact that the rupture involves a significantly larger portion of the fault.

- **horizontal versus vertical components**: For Marsica case study, Array 3, which is on rock shows α_H/α_{UP} less than one whereas the opposite is true for the two arrays on soil (A1 and A2). The reason could be associated to the presence of a very low velocity basin which cause a stronger loss of coherency for horizontal components due to the generation of consistent trains of surface waves leading to loss in coherency.

  Emilia case confirms the trend of $\alpha_H/\alpha_{UP} < 1$ except for Array 1 which on the contrary shows a coherency in vertical component which is 150% higher than the horizontal one.

  Norcia maps show that, for Scenario 3, α_H/α_{UP} turns out to be commonly lower than one on the hangingwall side of the fault whereas it becomes higher

than one on the footwall. This may be interpreted in light of the fact that in up-dip direction (footwall) the trains of waves which are generated by the relative slip between hanginwall and footwall produces more coherent motion in vertical direction rather than the mean of FN and FP ground motion. For the lower magnitude earthquake, the ratio is in general lower than one meaning that coherency of horizontal components is larger than that of vertical component.
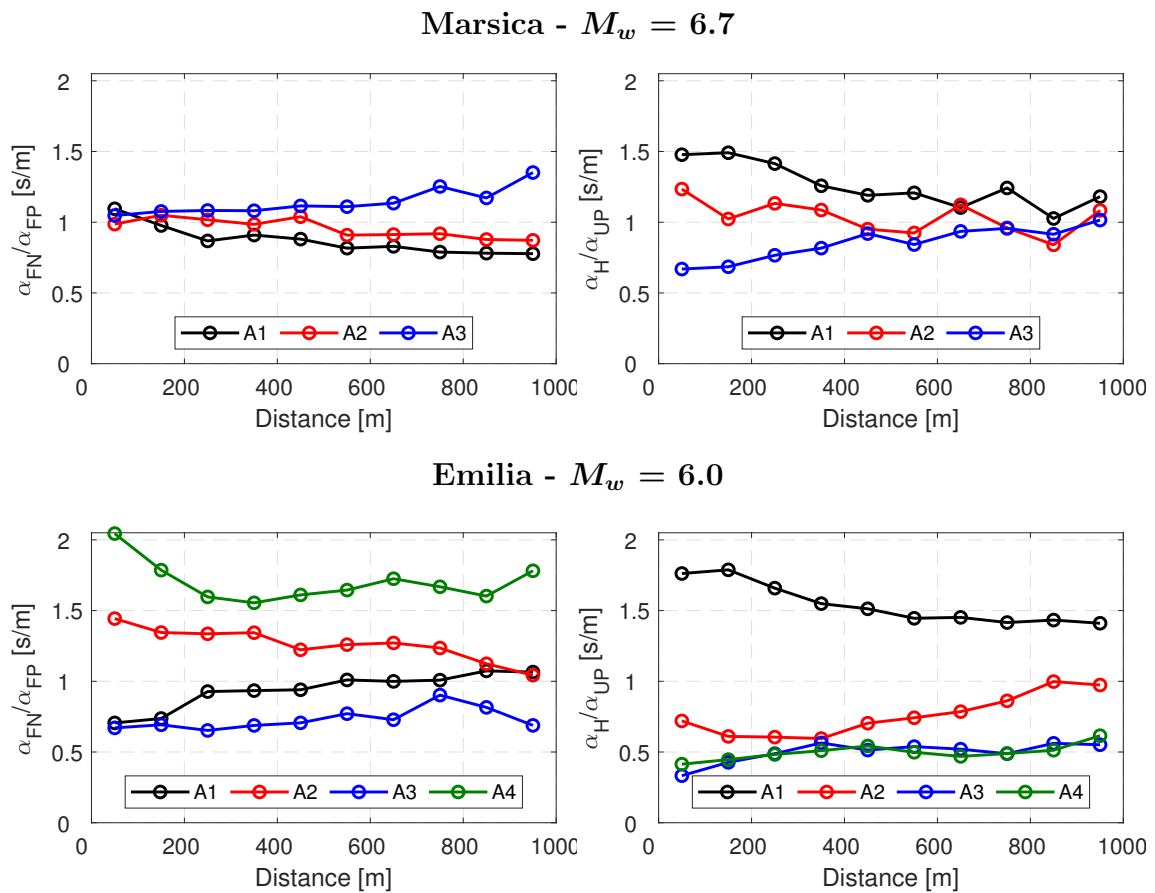
Figure 4.31: α_{FN}/α_{FP} (left) and α_H/α_{UP} (right) for Marsica (Mw=6.7), Emilia (Mw=6.0) case studies.
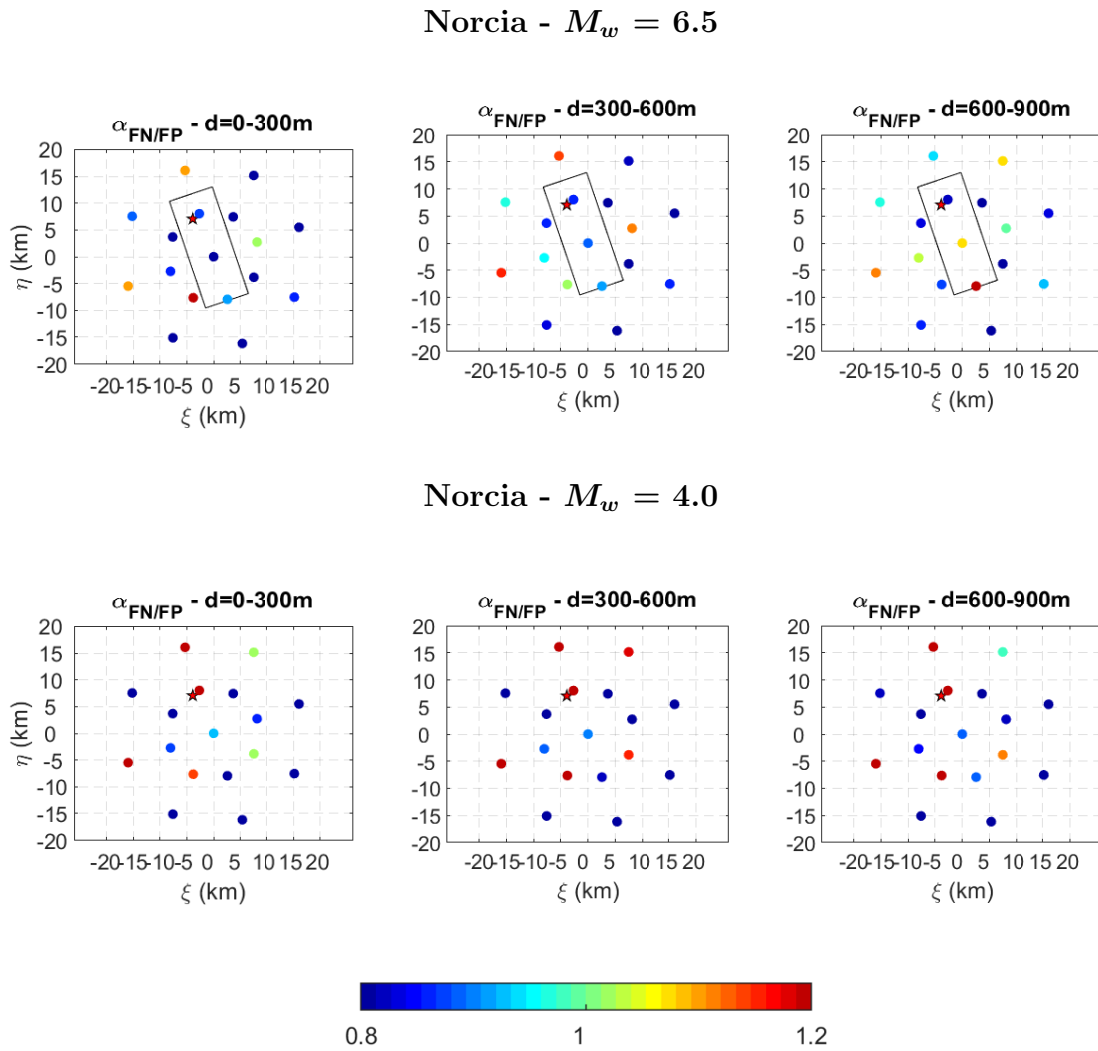
Figure 4.32: Maps of α_{FN}/α_{FP} ratios for Norcia case studies. Each dot represents the value of the ratio at the corresponding array and distance bin (0-300 m, 300-600 m or 600-900 m). First row refers to Scenario 6.5, second row to Scenario 4.0

Norcia - $M_w = 6.5$

Norcia - $M_w = 4.0$
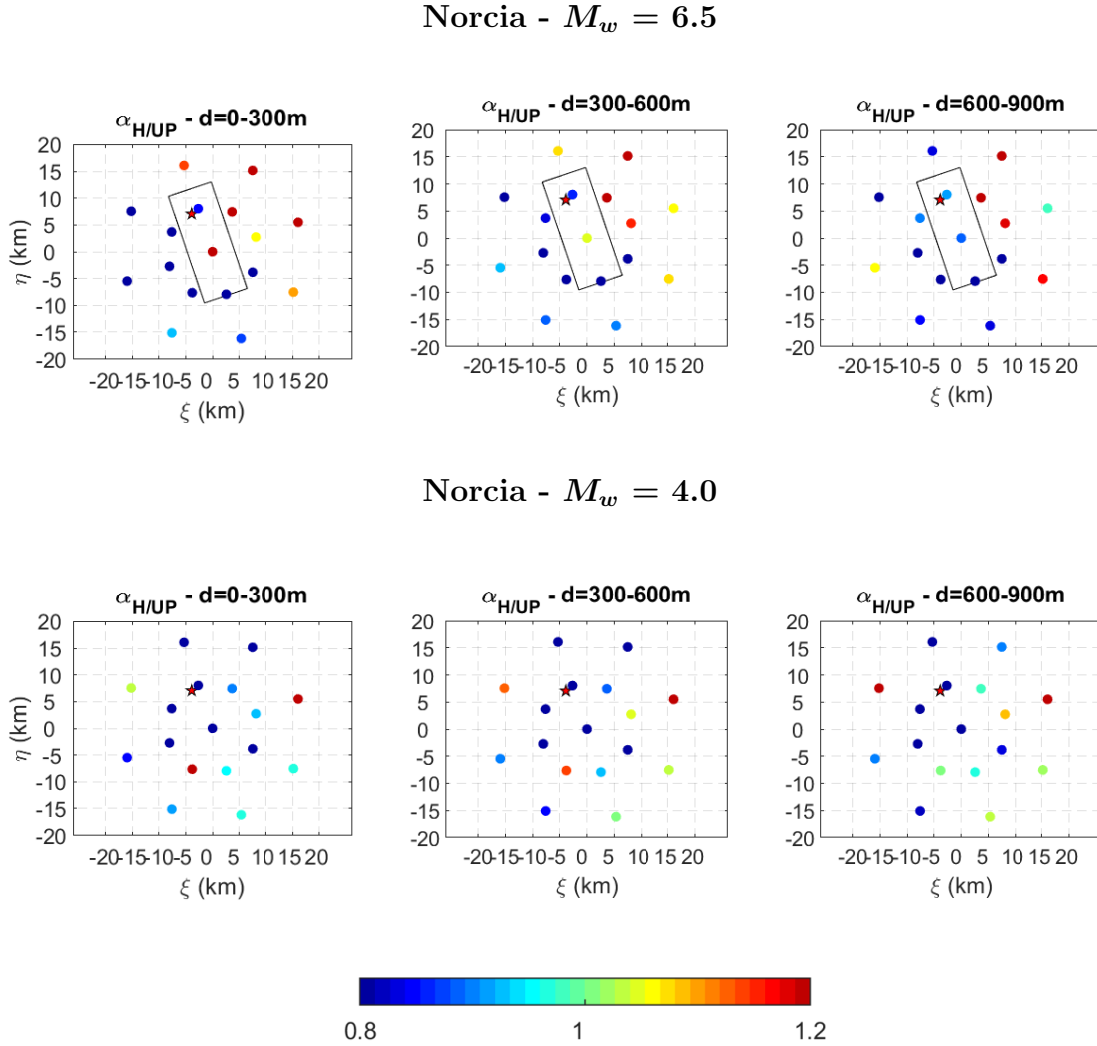
Figure 4.33: Maps of α_H/α_{UP} ratios for Norcia case studies. Each dot represents the value of the ratio at the corresponding array and distance bin (0-300 m, 300-600 m or 600-900 m). First row refers to Scenario 3, second row to Scenario 6.

4.4.2 Event magnitude

Abrahamson et al. (1991) showed some evidence of magnitude dependence of coherency. At frequencies below 5 Hz small magnitude events tend to have lower coherency than large magnitude events, while at frequencies of 6–10 Hz, the reverse is true. Somerville et al. (1988) suggested that coherency for aftershocks is greater at all frequencies than that for mainshock in the near-field. This was also confirmed, more recently, by the results of AfifChaouch et al. (2016) using simulations by means of the Empirical/Hybrid Green Function (H/EGF) techniques.

From a theoretical point of view, a reduction of coherency for large magnitudes in near-field should be expected with respect to small magnitude events owing to the increase of the variability of wave paths involving different portions of the fault rupture. Figure 4.34 illustrates the magnitude dependence of the best fitting α values as a function of distance for Norcia 3, 4, 5 and 6 scenarios (see Table (4.8)), respectively. Results for the three ground motion components, FN, FP and UD, at arrays 6, 9, 14 are reported.

As a general observation, the magnitude 4.0 earthquake presents a lower coherency (i.e. larger α) than the other scenarios. This is agreement to what observed by Abrahamson et al. (1991). Regarding the other scenarios no clear dependence is shown: if we imagine to sort the scenarios from the one characterized by the highest α to the one with the lowest α, it appears clearly that depending on the array and the ground motion component the order changes.
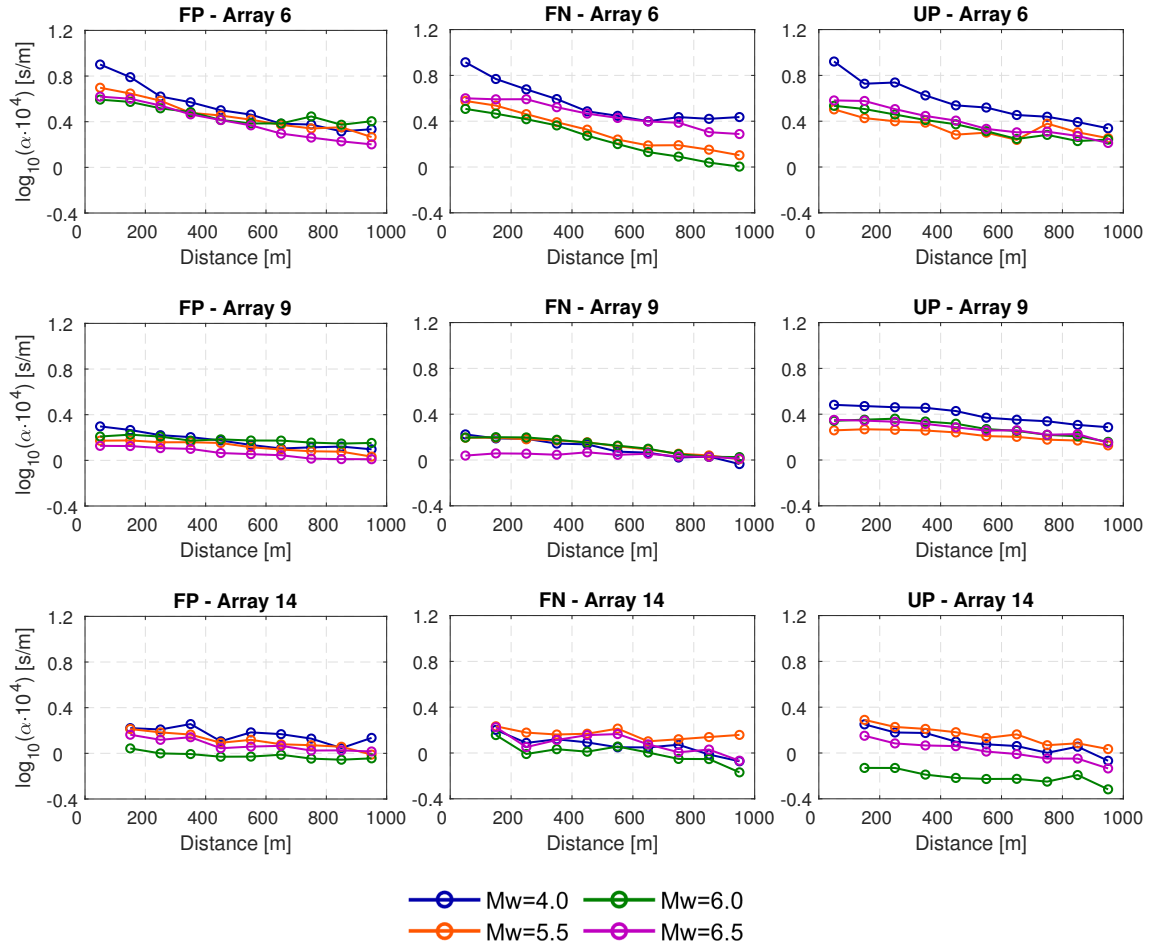
Figure 4.34: Magnitude dependence of best fitting α values of LW86 model for Norcia case study.

4.4.3   Relative position between source and site

Figures 4.35, 4.36, 4.37 and 4.38 show maps of Norcia area in which each dot represents one array (see Figure 4.21) whose colour report the value of the best fitting α of LW86 model computed for the different magnitude earthquakes at three distance bins (0-300 m, 300-600 m, 600-900 m). It is also reported the projection of the effective fault on the ground surface.

It could be noted that, as a common trend, that arrays situated on the hangingwall (west) are characterized by higher values of α with respect to ones on footwall meaning that waves which propagate through the hangingwall are less coherent than the ones through footwall. This aspect is more pronounced the vertical component of

motion.

The reason may be associated to that fact that, in normal faulting mechanism, the up-dip movement of footwall generates more coherent waves which travel in up-dip direction toward sites (directivity effect). On the contrary on the hanging wall coherent trains of waves travels away from the sites due to the down-dip direction providing less coherent ground motion. Note that in low-moderate magnitude earthquakes (M_w equal to 4.0 and 5.5) this effect become negligible since the rupture involves a small portion of the fault (the effective fault have small dimensions).
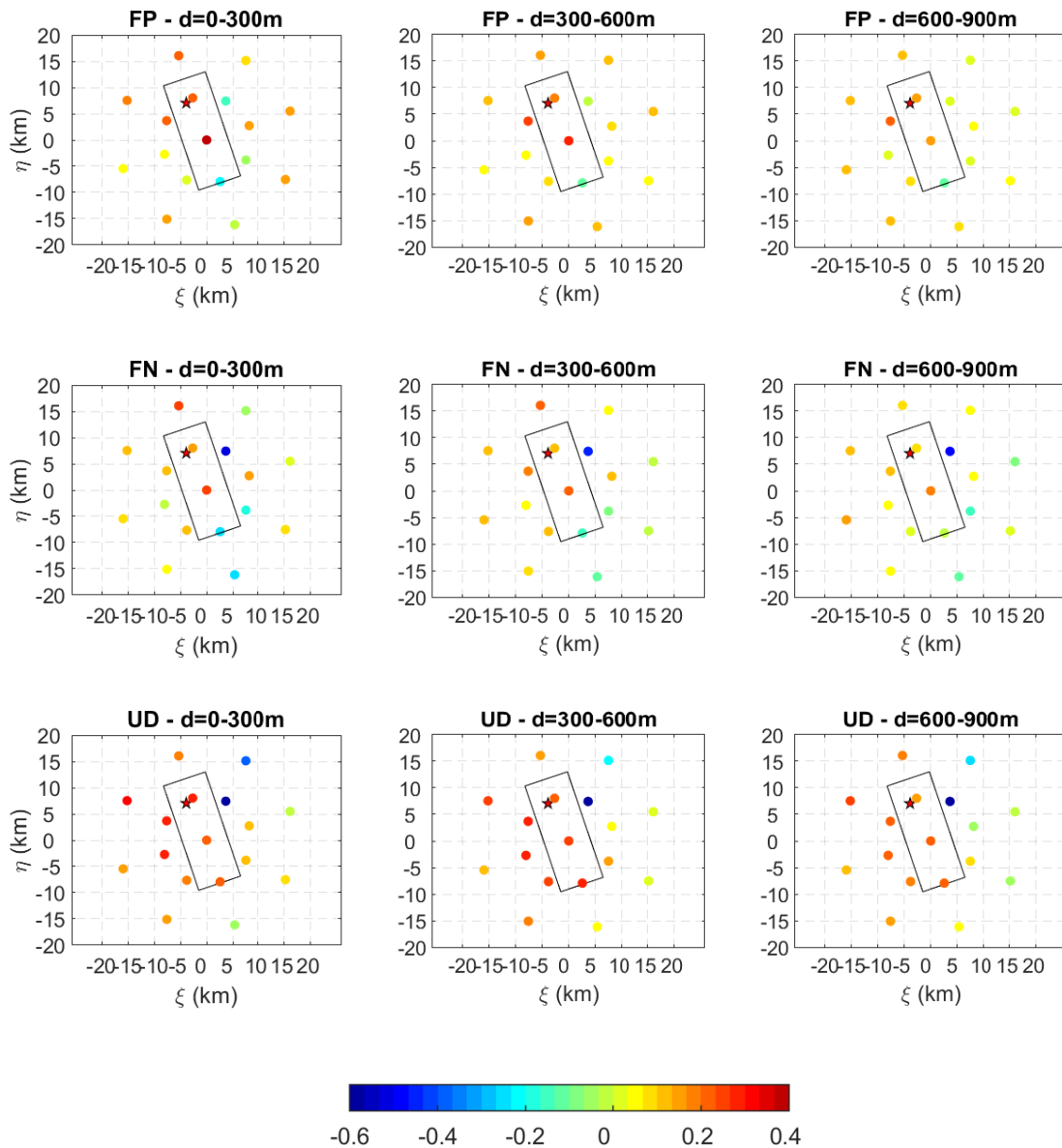
Figure 4.35: Map of fitted α for Norcia - Scenario 3 ($M_w = 6.5$). Scale of colours is in $log_{10}(\alpha \cdot 10^4)$.
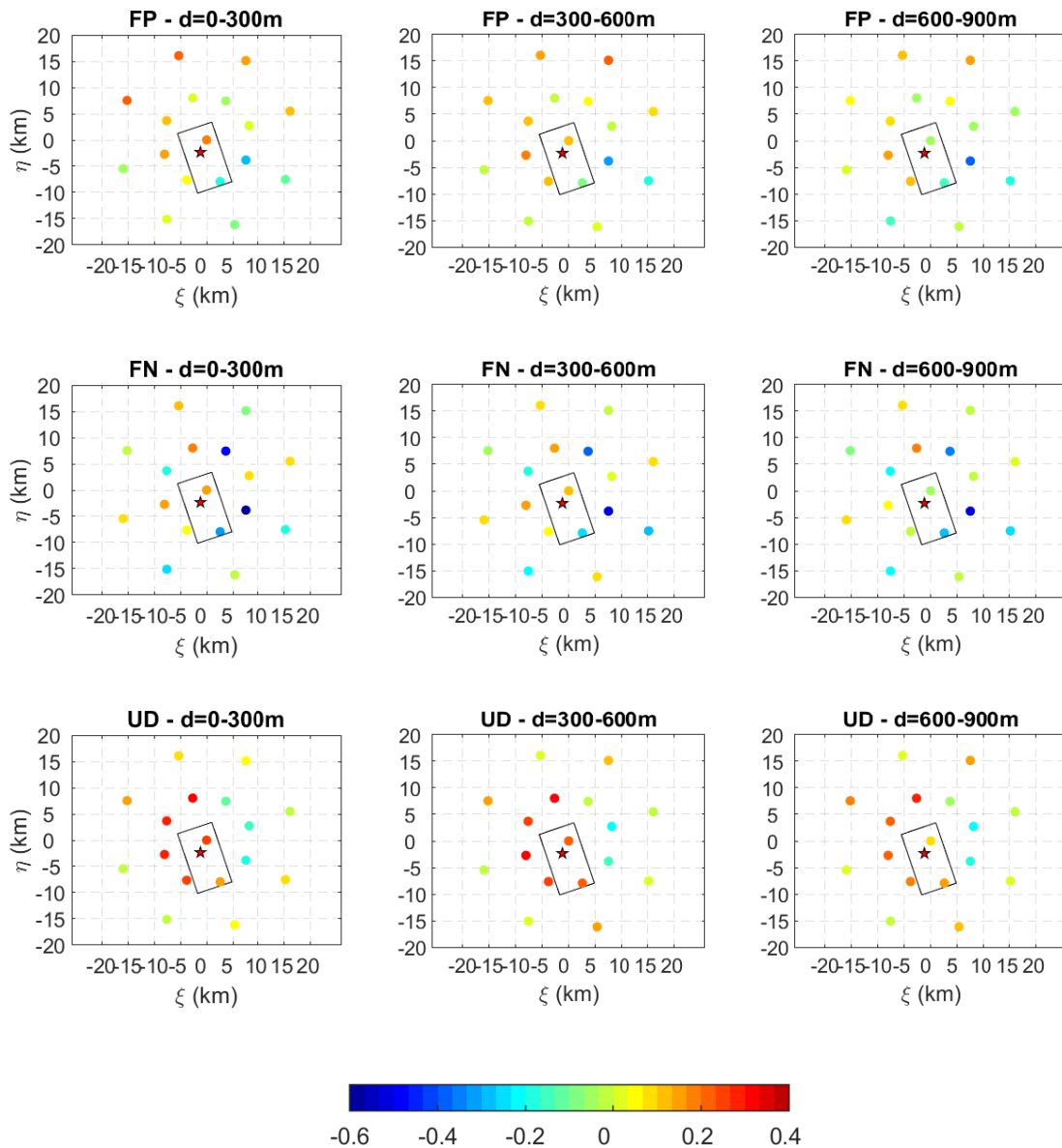
Figure 4.36: Map of fitted α for Norcia - Scenario 4 ($M_w = 6.0$). Scale of colours is in $log_{10}(\alpha \cdot 10^4)$.
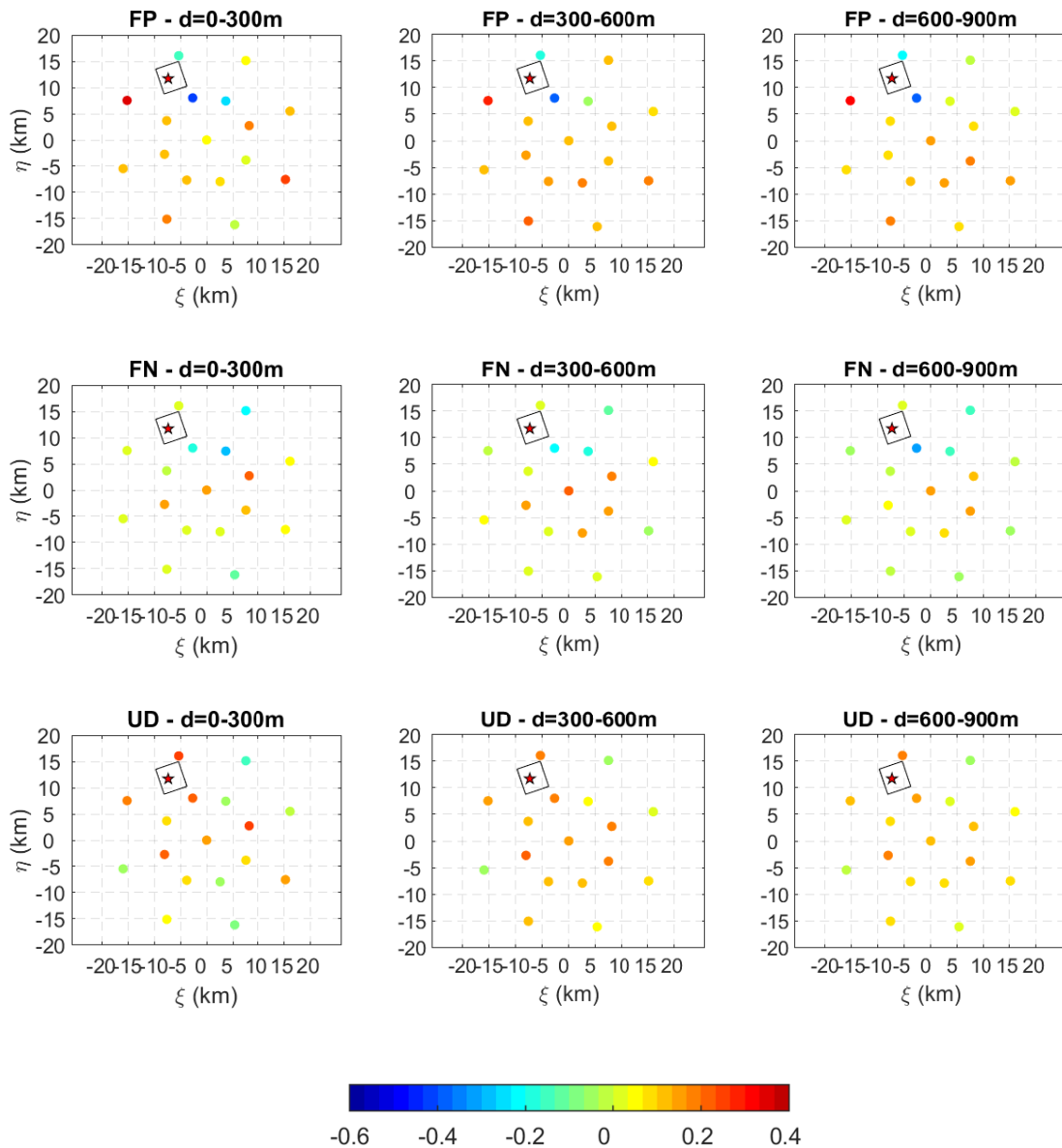
Figure 4.37: Map of fitted α for Norcia - Scenario 5 ($M_w = 5.5$). Scale of colours is in $log_{10}(\alpha \cdot 10^4)$.
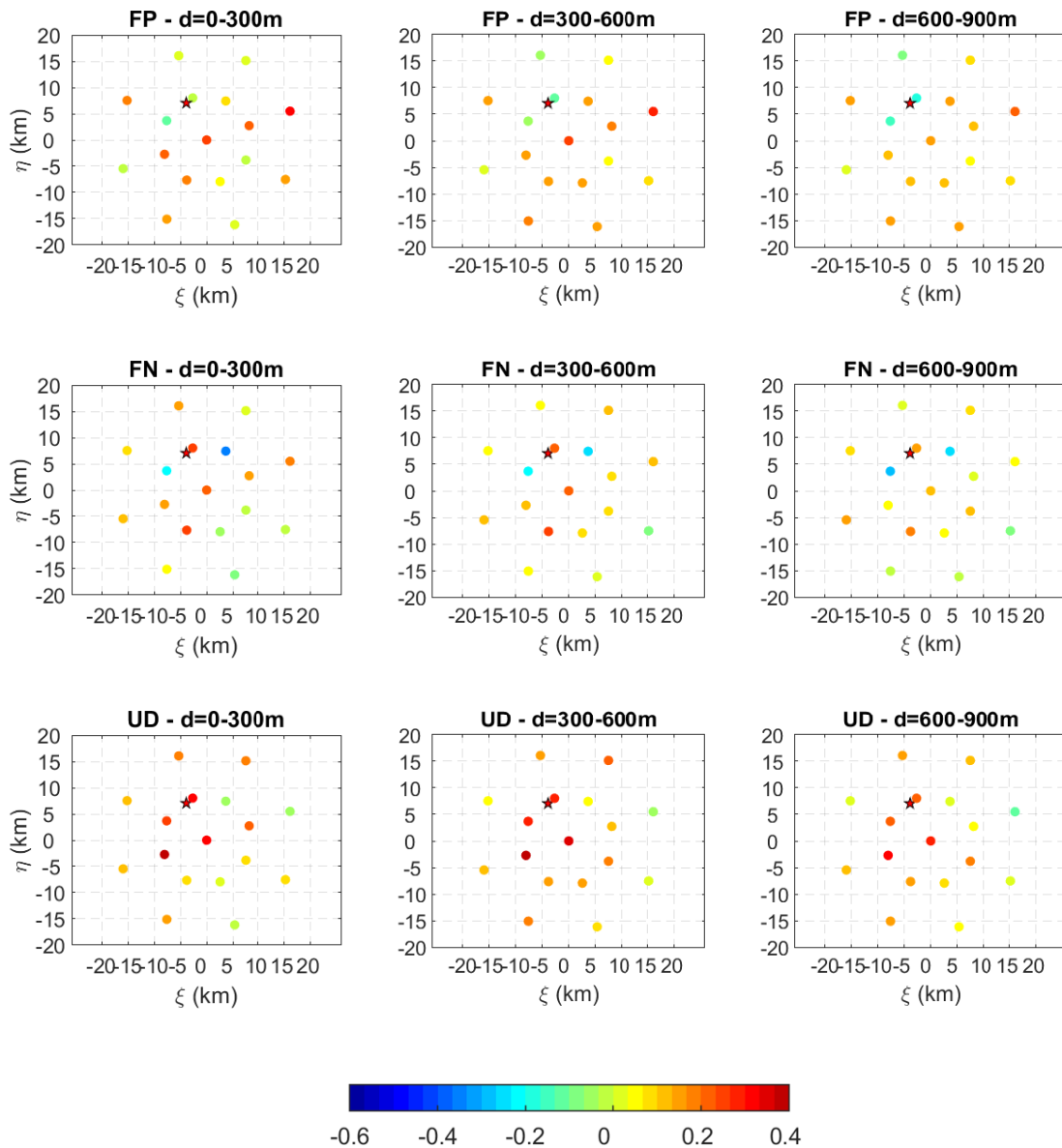
Figure 4.38: Map of fitted α for Norcia - Scenario 4 ($M_w = 4.0$). Scale of colours is in $log_{10}(\alpha \cdot 10^4)$.

4.4.4   Source-to-site distance

Abrahamson et al. (1991), using data recorded on soil site at the LSST array in Lotung, Taiwan, observed that coherency in the near-field was lower than that in the far-field at low frequencies, which was interpreted as a source effect. Whereas the reverse was true for higher frequencies, which was interpreted as a path effect.

Similar results were found by Somerville et al. (1988). This section investigates the importance of this effect for different Joyner-Boore distances.

The Emilia and Norcia case studies offers the possibility to investigate the effect of source-to-site distance on spatial coherency. The first row of Figure 4.39 presents the best fitting α values (FP vs FN vs UD) as a function of separation distance for the four Emilia arrays, grouped into two sets: $A3 \div A4$ (blu lines), located on the hangingwall of the fault at Joyner-Boore (R_{JB}) distances equal to 0, and $A1 \div A2$ (red lines), located farther from the fault at $R_{JB} = 12$ km .
The second row instead, illustrate the Norcia case study (Scenario 3) where the arrays are grouped into two set : $R_{JB} = 0$ km and $R_{JB} > 0$ km. To the first group belong arrays 3, 4, 15, 16, 18 (see Figure 4.21) while to the second the others. Array 6 is excluded from the analysis in order to isolate the only dependence on source-to-site distance from the one on soil condition: Array 6 is on soil whereas all the others are on rock.

It turns out that the proximity to the extended seismic source produces less coherent motion, as intuitively expected, owing to the differential motion induced by wave packets radiated from different portion of the fault. This effect is more significant at small separation distances. As a matter of fact, in the near-field, a cause of loss of coherency is the extended source effect: wave packets radiating from different portion of the fault cause differential motion owing to the differences in relative geometry of the source and the sites, implying different azimuths, incidence angles and ray paths. Getting farther from the source, ground motion is less affected by the details of the finite-fault rupture and waves propagating from the fault tend to arrive almost synchronously at nearby stations. Furthermore, when larger Joyner-Boore distances are involved, the dependence of α with inter-station distance become less pronounced (α remains almost constant at). Note that for Emilia array the coherency at A3 and A4 for the vertical component is very low due to the propagation of surface waves, generated by the buried morphological irregularity of the Mirandola site α values leading to the huge difference which appears in Figure 4.39 component UP.
Norcia curves give in general more reliable results, since no local site effects are present. Thus, from Norcia it can be seen the actual effect of the source-to-site distance in near-fault region: the effect seem to be not relevant but it is important to recall that we are dealing with receivers which are all in near-fault region (for a

$M_w 6.5$ event, the near-field region extends up to at least one fault length, i.e. 40 km approx.) and thus the extended fault effect always applies. Therefore, the effect observed by Abrahamson et al. (1991) and Somerville et al. (1988) applies not only comparing arrays in near-field and in ones in far-field but it is also relevant among arrays in near-field.
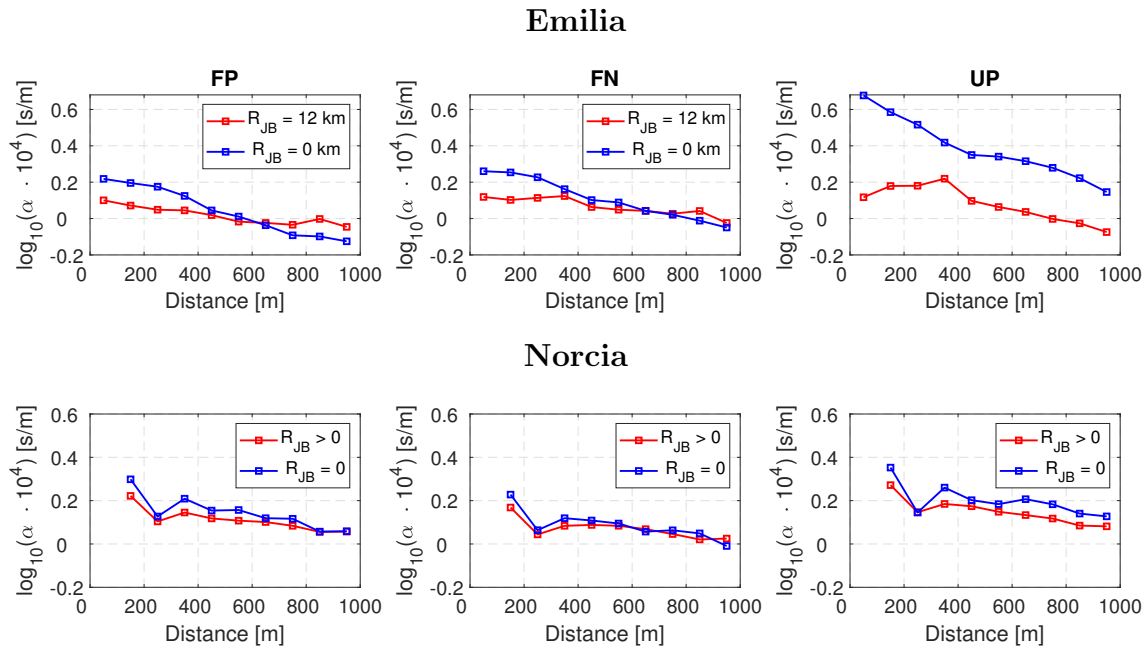
Figure 4.39: Source-to-site distance dependence of best fitting α values of Luco and Wong (1986) model for the Emilia (first row) and Norcia (second row) case studies.

4.4.5 Soil condition

To investigate the dependence on site condition (soil vs rock), the Marsica and Norcia case studies are taken into account because for these two numerical models a dense array on outcropping bedrock is available. Figure 4.40 illustrates the effect of site condition on spatial coherency in terms of variability of best fitting α as a function of separation distances, for the three ground motion components (FP vs FN vs UD). For Marsica case of study the best fitting α obtained from the arrays A1 and A2 as a function of distance have been averaged to obtain a common estimation of the coherency at soil site, whereas the rock curve is computed only using the A3 data. Note that Marsica Arrays A1 and A2 are located within the very soft alluvium basin with superficial $V_S = 180 \ m/s$ (soil class C/D), while Array A3 is characterized by $V_{S,30} \sim 1000 \ m/s$.

For Norcia, instead, the best fitting α has been obtained from scenarios belonging to group 1 (see Section 4.2.3) at Array 6: the two scenarios (1 and 2, see Table 4.8), of magnitude 6.5, are provided by the same numerical model except for modelling of the Norcia basin, over which Array 6 is located; indeed, in Scenario 1 the Norcia basin is modelled with its actual $V_{S,30}$ profile, while in Scenario 2 it is modelled like an outcropping bedrock. The availability of these two simulation allows to directly isolate the dependence of SVEGM on soil condition.

It turns out that, for all ground motion components, spatial coherency on soft soils can be significantly lower than that on rock, owing to the influence of local subsurface irregularities which modify the amplitude and frequency content of incident waves. Such an effect seems to be more pronounced at small separation distances, whereas it decreases at larger separation distances, according to the fact that the decay of α with inter-station distance is less relevant for hard rock site. The physical reason connected to loss of coherency in sedimentary basin is associated to the basin effect: the strong lateral geological discontinuities (basin-edge) generate surface waves and trapping of wave within the basin inducing a marked inhomogeneity in terms of ray paths, amplification and frequency content, hence implying a significant loss of coherency. This in agreement with literature studies (Abrahamson et al., 1991; Dabaghi and Der Kiureghian, 2014).
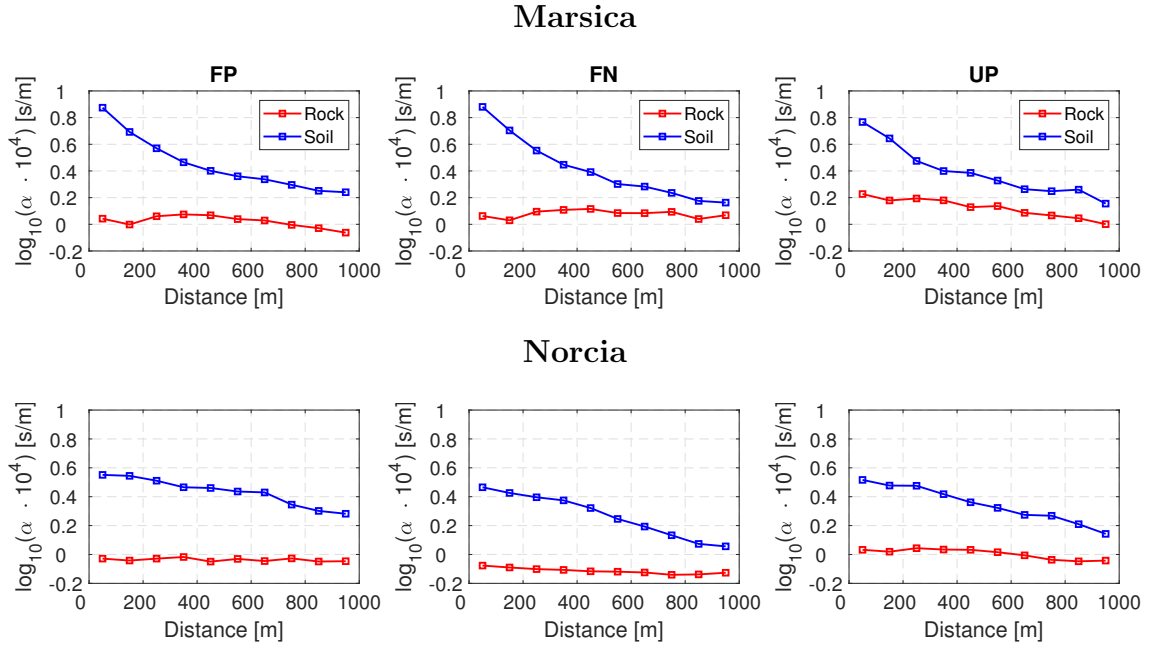
Figure 4.40: Site condition dependence of best fitting α values of Luco and Wong (1986) model for the Marsica (first row) and Norcia (second row) case studies: blue lines refer to soil sites, while red lines refer to rock sites.

4.4.6 hypocenter position

In this section the dependence of spatial coherency of the hypocentral position is studied.

To this aim Norcia case studies belonging to Group 3 (see Section 4.2.3) are considered and grouped in two main categories: superficial and deep hypocenters. With reference to Table 4.8, scenarios A, B and C belongs to the first category, since they took place at about 2.5 km below the ground surface, while scenarios D, E and F are deep hypocenters: they are located at 8.26 km depth.

Note that all the six scenarios are characterized by the same magnitude ($M_w = 6.5$), same slip distribution and crustal model, the only difference is the position of the hypocenter (see Figures 4.24 and 4.25).

Figure 4.41 shows the best fitting α values of Luco and Wong (1986) model as a function of distance, for three representative arrays (Array 9, 14 and 16) and for each component of motion (FP, FN, UD).

Looking at curves of Array 14, located on footwall in up-dip direction, the orange (superficial hypocenters) and green (deep hypocenters) curves differ up to 10% one with respect to the other. It appears that, generally, a superficial hypocenter provides lower coherency estimates than the deep one. This sentence is verified clearly for stations on footwall due to the substantial reduction of the source-to-site distance with strong enhancement of the extended fault effect, whereas clear exceptions are represented by the fault-normal component of Array 9 and vertical component of Array 16. The reason should be associated to the fact that for Array 9 other effects acts: at Array 9 the directivity effect may be very strong (fault-normal component is more coherent than fault parallel one) and it is enhanced for superficial sources.
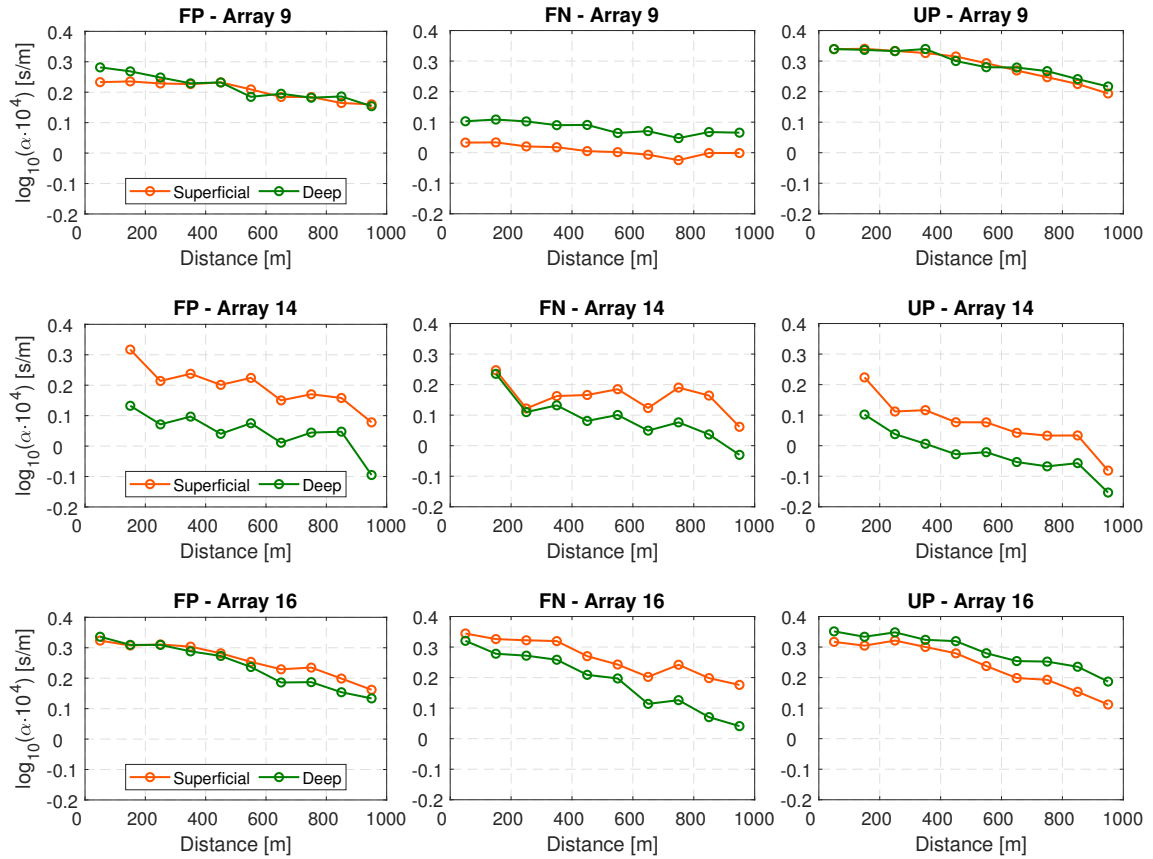
Figure 4.41: hypocenter depth dependence of best fitting α values of Luco and Wong (1986) model for Norcia case studies: orange lines refer to superficial hypocenters, while green lines refer to deep hypocenters.

4.4.7 Slip distribution

To investigate the dependence of spatial coherency on slip distribution results, in term of best fitting α of Luco and Wong (1986) model, coming from Scenario 1 and Scenario 3 (see Table 4.8) are compared. Indeed, Scenario 1 and 3 numerical models are characterized by the same crustal model, hypocenter position and magnitude but differ from the from the point of view of the slip distribution: Scenario 1 is associated to the distribution of slip shown in Figure 4.18 whereas Scenario 3 to the slip distribution of Figure 4.22.

Note that the first distribution of slip shows its peak values in the superficial region of the fault away from the hypocenter, while for the second hypocenter and peaks of slip are located at larger depths.

Figure 4.42 illustrates the best fitting α values of Luco and Wong (1986) model as a function of distance, obtained from the two scenarios under analysis, for three representative arrays (Array 6, 9 and 16) and for each component of motion (FP, FN, UD). Scenario 1 is associated to slip 1 curves (red lines) while Scenario 3 to slip 2 curves (blue lines).
As a common trend, slip 2 generates less coherent ground motion than slip 1 (except for Array 9 FN component and in part Array 6 FP). The difference between the two cases reaches 20% which is a value not negligible at all meaning that slip distribution is a parameter that clearly affect the SVEGM.
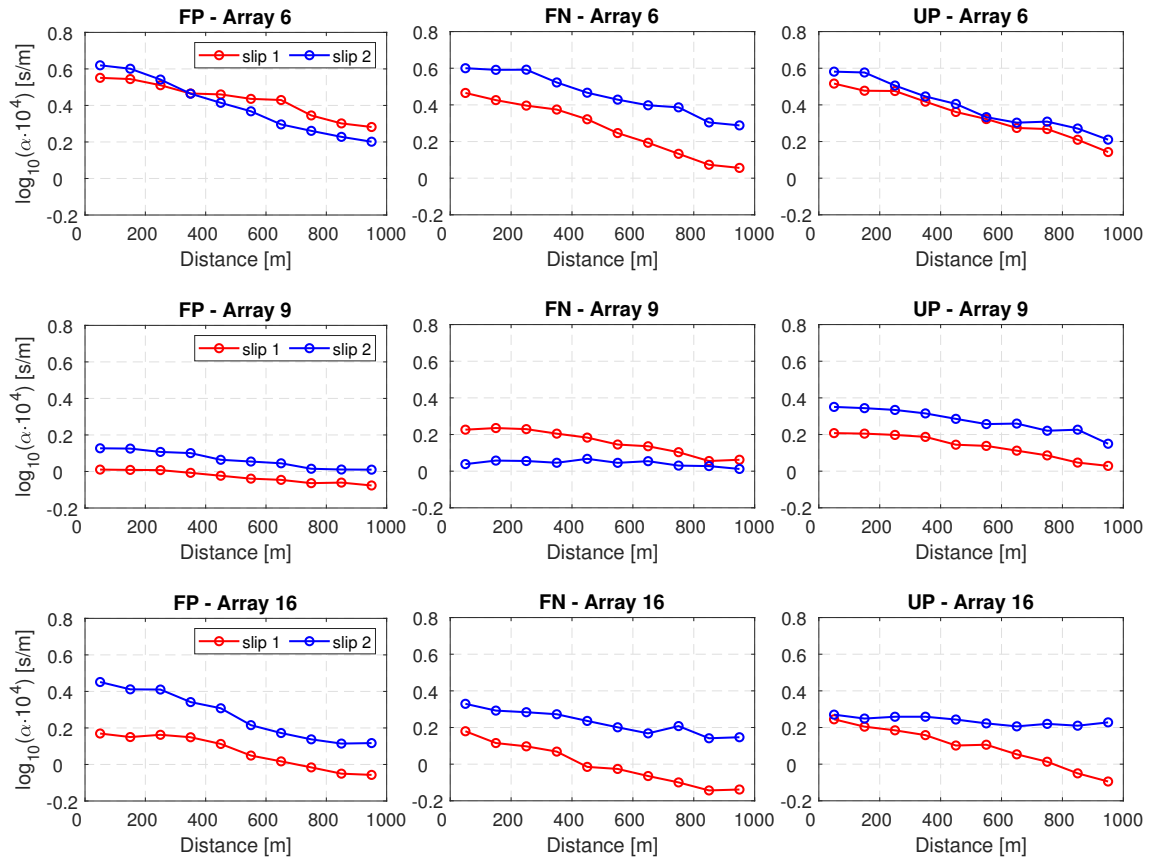
Figure 4.42: Slip distribution dependence of best fitting α values of Luco and Wong (1986) model for Norcia case studies: red lines refer to distribution of slip n°1 (Scenario 1), while blue lines refer to slip n°2 (Scenario 3).

Chapter 5

Effect of SVEGM on the seismic response of a bridge structure

The current state-of-the-art approaches for the seismic analysis of spatially extended structures, such as bridged and viaducts, are typically based on the use of artificial accelerograms. In spite of their ease of use, these artificial accelerograms are generated through stochastic methodologies such that they satisfy a prescribed spatial coherency model, calibrated on a limited amount of data coming from different seismo-tectonic contexts and neglecting near-source conditions. Indeed, as shown in the previous chapters, the coherency is strongly affected by many factors associated with both site conditions and earthquake source leading to results which cannot be accurately predicted by literature coherency models and are not necessarily representative of near-source conditions.

Therefore, the aim of this Chapter is to study the impact of the spatial variability of seismic input on a bridge structure by considering direct application at the different foundation points of earthquake ground motion obtained from 3D physic-based numerical simulations. 3D physic-based numerical simulations have the great advantage of reproducing accurately the seismic motion and its spatial variability by directly modelling the actual properties of both source and site conditions and their relative position at any site of interest. These features could not be reached by applying earthquake ground motion recordings obtained from a dense array network during a strong earthquake since they are strongly region- and earthquake-specific. Furthermore, 3D physic-based simulations allow to predict the motion at a specific point of the surface, e.g. at the supports of a bridge, whereas earthquake ground motion recordings needs to be spatially interpolated to adapt the phase and

amplitude of records to the actual position of the foundation points.

For this purpose, a regular, idealized RC bridge, belonging to the class of the integral abutment bridges, excited by earthquake ground motions obtained from physic-based numerical simulations, an induced seismic event in the Groningen gas field area has been considered.
Dynamic time histories analyzes (DTHA) has been carried out through fiber-based structural modelling in SeismoStruct [2020], under different assumptions regarding the features of input motion (synchronous vs. spatially variable).
Finally, the impact of different hypothesis on both ground motion numerical model and structural model have been analyzed.

5.1 3D physic-based numerical simulations of induced seismicity in the Groningen gas field

In this study, the near-source acceleration provided by the 3D physic-based numerical simulations of Groningen gas field area will be considered, to determine the multiple-support seismic excitation. Groningen gas field area (see Figure 5.1), located in the Netherlands, is characterized by a moderate earthquake activity attributed to nontectonic origin and directly related to the reservoir depletion of the gas field itself. In the area there is a network of seismic instruments, installed by the seismological service of the Royal Dutch Meteorological Institute (KNMI), which provides recordings of the seismological activity starting from 1997.

Paolucci et al. (2020) developed a physics-based numerical approach to characterize earthquake ground motion due to induced seismicity in the Groningen gas field. To this end, a large-scale (20 km × 20 km) heterogeneous 3D seismic wave propagation model was constructed, based on available geological, geophysical, geotechnical, and seismological data. Numerical simulations were performed using the code SPEED.

The site of interest is characterized by a flat topography and soft-soil condition ($V_{S,30}$= 150 m/s). The shear-wave velocity profile (V_S) characterizing the crustal model is shown in Figure 5.2. The geological setting of the site can be seen as a set of seven horizontal layers, each one characterized by a specific value of shear-wave velocity.

Paolucci et al. (2020) developed four different numerical models each one defined
through different hypothesis on subsoil model, quality factor and shear-wave velocity
with the aim of studying the sensitivity of the results to the modelling assumptions.
Two subsoil models were defined: a 3D model able to reproduce the laterally hetero-
geneous subsoil structures and a 1D model consisting of flat horizontal layers built
by simplifying the actual geologic interfaces. Moreover, considering the 1D model,
both hysteretic ($Q = V_S/10$) or frequency-proportional Q-factor were implemented
in SPEED, the latter being defined as:

$$Q(f) = Q_0 \cdot \frac{f}{f_0} \tag{5.1}$$

where $Q_0 = V_S/10$ and $f_0 = 5$ Hz.

Finally, a 1D model able to include stochastic fluctuations of wave velocity was also
built.

Table 5.1 provides an overview of the numerical simulations exploited in the present
study.

Label	Subsoil model	Q factor	Stochastic velocity
1D-Qf	1D	Frequency-proportional: Qf	No
3D-Qf	1D	Frequency-proportional: Qf	No
1D-Qf-S	3D	Frequency-proportional: Qf	Yes

Table 5.1: Overview of the numerical simulations performed by Paolucci et al. (2020)
to simulate the Zeerjip event and exploited in the study herein.
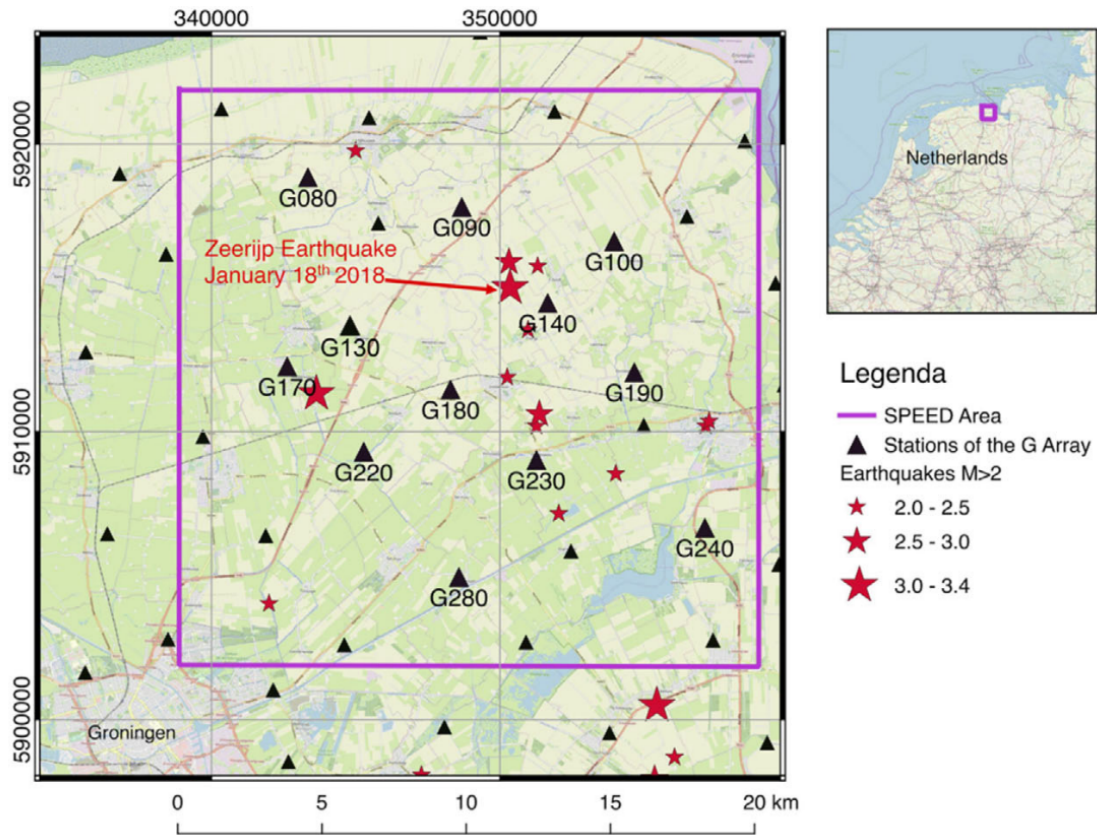
Figure 5.1: Map of the Groningen gas field covered by the 3D numerical model (see superimposed box). The stars indicate the epicenters of the induced earthquakes with local magnitude larger than 2, including the Zeerijp earthquake (08.01.2018). The stations of the G network of KNMI are also shown by triangles. From Paolucci et al. (2020)
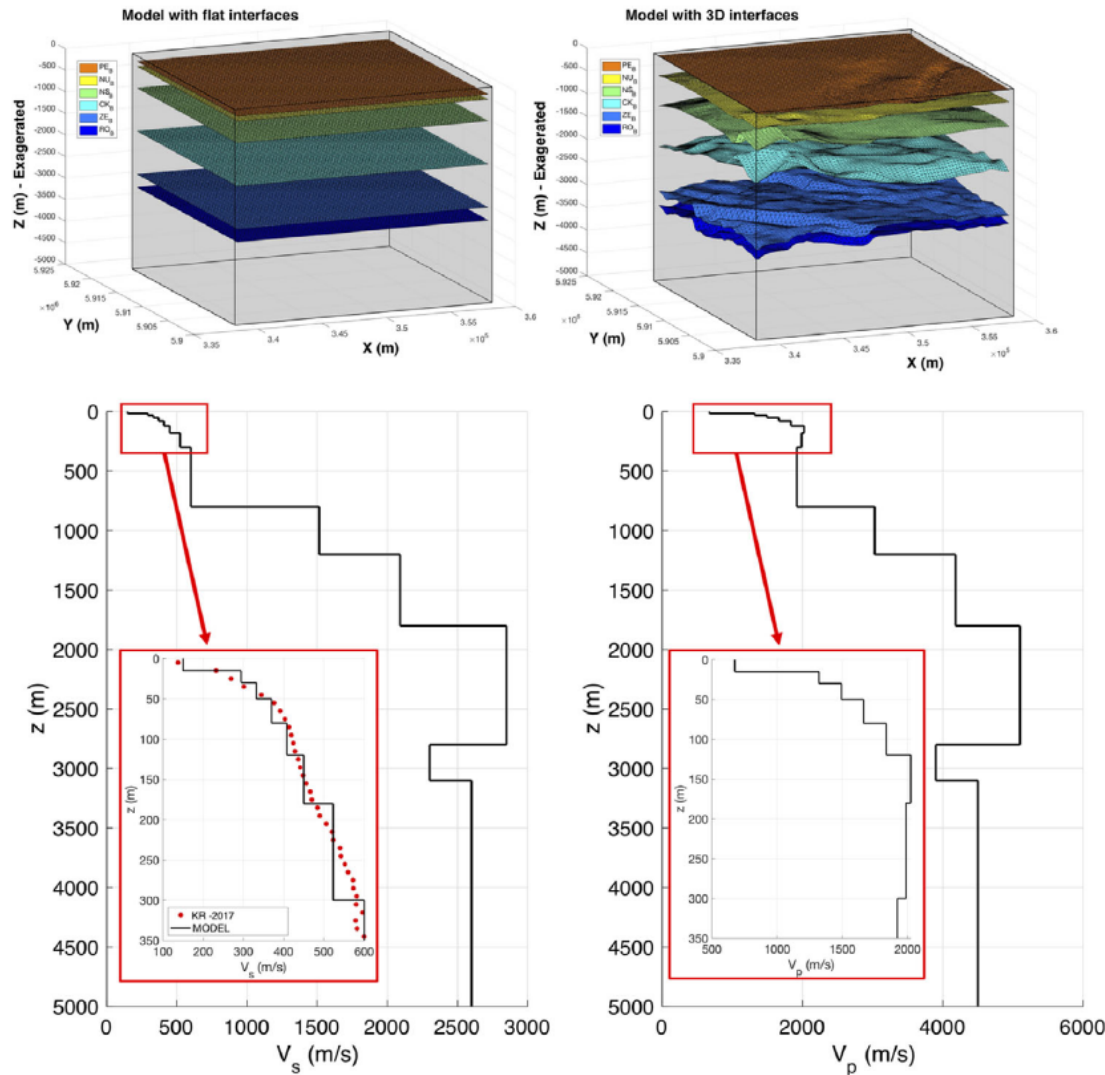
Figure 5.2: Implementation of the SPEED subsoil model. Top: geological interfaces (left: 1D; right: 3D), x and y are in UTM-32N coordinates. Bottom: S- and P-wave velocities within each soil subdomain. From Paolucci et al. (2020)

The M_L 3.4 Zeerijp earthquake of January 8, 2018 was selected for calibration and validation of SPEED simulations. The event, shown in Figure 5.1, took place at Lon = 53.36°N, Lat = 6.75°E and 3 km depth.

A satisfactory agreement was found between numerical simulations and records for most G-stations at $R_{epi} < 10$ km especially in terms of intermediate-to-low frequency components (i.e., PGV and PGD). Figure 5.4 shows the maps of peak ground acceleration [log_{10}(PGA)] and velocity [log_{10}(PGV)] for all components of motion obtained through 1D-Qf model, with the corresponding peak values recorded at G stations. As an illustrative example, Figure 5.3 shows the comparison between records and

simulations (model 1D-Qf) time histories for station G180 at about 4 km from the epicenter.

It is important to note that due to the strong discretization of the numerical model (at ground surface element size reach the minimum dimensions of 40 m × 40 m × 15 m), it turned out that the numerical mesh is able to accurately propagate frequencies up to about 10 Hz. This feature makes the numerical simulation Zeerijp earthquake of particular interest for earthquake engineering applications. Note that usually physic-based models, like the ones studied in Chapter 4, are limited to frequency bands up to 2 Hz.

For these peculiarities, the numerical simulations of January 8, 2018 Zeerijp earthquake have been used, in the study herein, to generate synthetic ground motions to be applied to the bridge model.

The main limitation is the low magnitude of the considered event and, thus, of input ground motion. Nonetheless, the main aim herein is to check the feasibility of the proposed approach of coupling physics-based synthetics with bridge response.
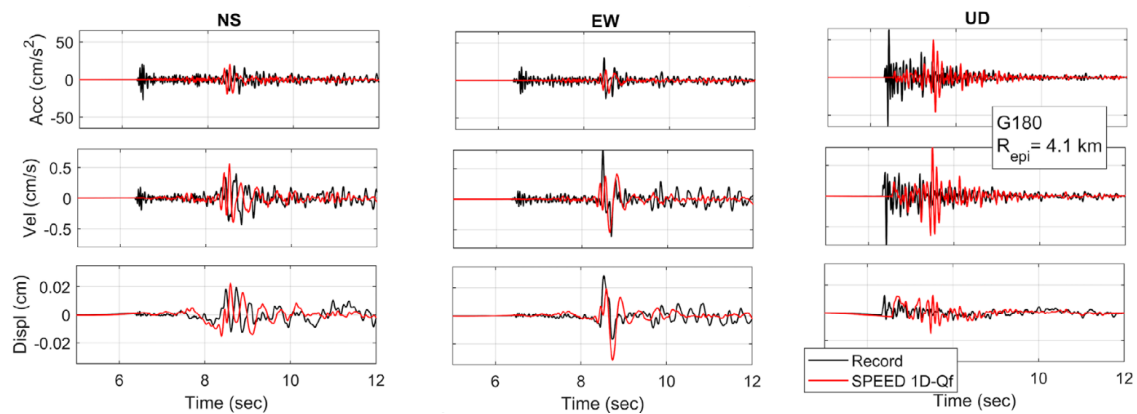
Figure 5.3: Comparison between simulated (1D-Qf, red) and recorded (black) time histories for station G140
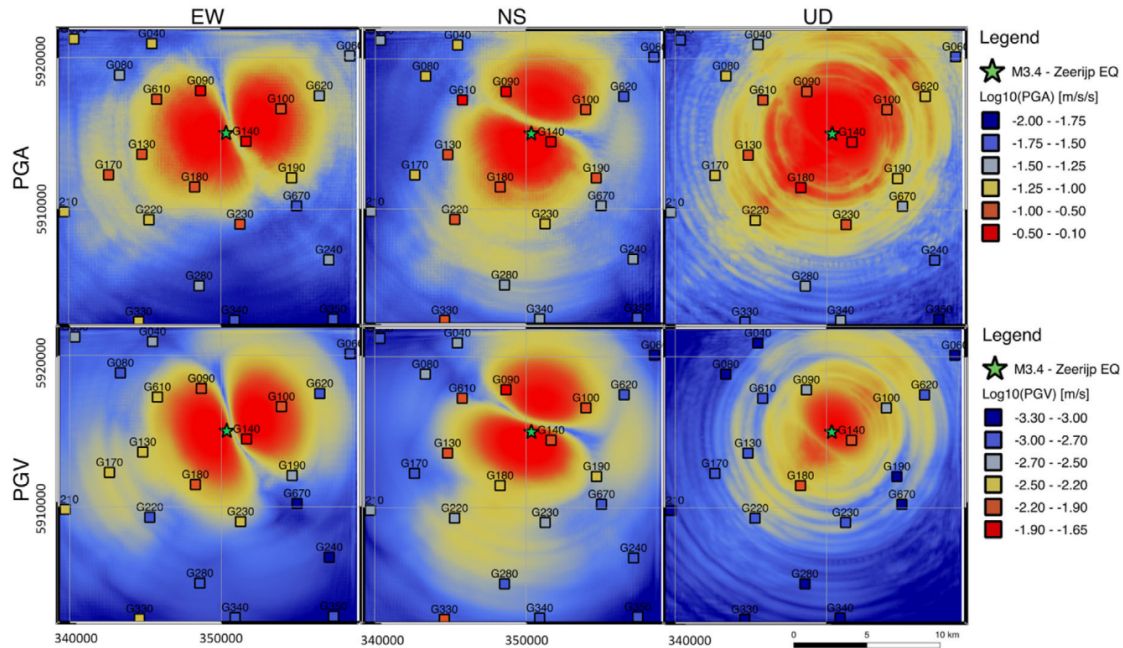
Figure 5.4: Ground motion maps in terms of PGA (log_{10}, top) and PGV (log_{10}, bottom) for the EW (left), NS (center) and UD (right) components. Recorded peak values are shown by the coloured dots (with the same colour map of simulations). From Paolucci et al. (2020)

An array of 10 receivers, located near to station G240, is selected, within the entire set of available stations in the SPEED model (about 300 thousand), and assumed to be, hypothetically, the supports of the bridge piers. Indeed, each pier base is ideally positioned exactly over one of those stations leading to a perfect estimation of the ground motion under each pier without needing any interpolation procedure. Figure 5.5 shows the position of the ten piers of the bridge model and the corresponding receivers of the SPEED model. Note that the selected stations, and consequently the bridge, are aligned perfectly to North therefore no 2D rotations of the horizontal ground motion components is needed.
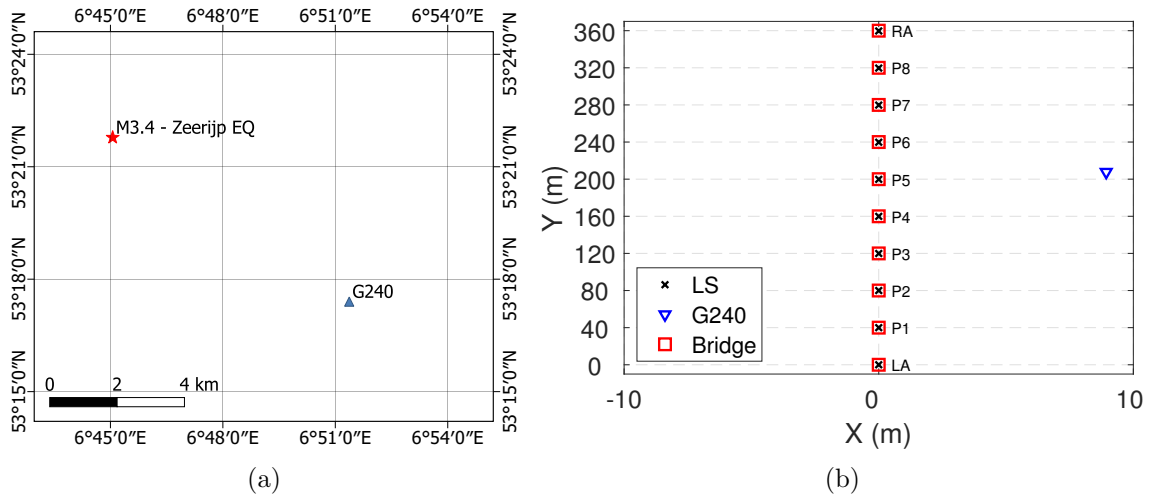
Figure 5.5: a) Map of Groningen area representing the epicenter of M_L 3.4 Zeerijp earthquake and the position of the station G240. b) Layout of the bridge model and the corresponding receivers of the SPEED model.

5.1.1 Coherency Estimates

Before presenting the numerical model of the bridge, in this section an overview of the main features of spatial coherency of the Zeerijp earthquake numerical simulations at the selected array is provided.

Since the subsoil of the Groningen area is geologically simple with relatively uniform local site condition and the Zeerijp earthquake has very low magnitude (extended fault effect negligible) no strong decay of coherency with distance and frequency is expected. Estimates of the lagged spatial coherency are obtained from the synthetic time series of ground acceleration, after proper synchronization of time series, through the procedure explained in Section 2.2. Figure 5.6 shows the lagged coherency estimates from the synthetic signal recorded the base of each pier for 100 m wide distance bins in the range 0–400 m (which is approximately the length of the bridge analyzed) and for the two horizontal components of ground motion (NS, EW).

The coherency curves are reported for each of the three simulations considered in this study: 1D-Qf (1D subsoil model with frequency independent Q-factor), 1D-Qf-S (1D subsoil model with frequency proportional Q-factor and stochastic velocity field) and 3D-Qf (3D subsoil model with frequency proportional Q-factor).

Note that for each distance bin, the plotted coherency curve is the mean of the coherency curves over all possible pairs of stations belonging to the same bin.

The 1D-Qf-S provides the lowest values of coherency, as expected, due to the stochastic velocity field which generates heterogeneity of wave velocity in the uppermost layers leading to a certain degree of incoherence. In order of decreasing coherency, after 1D-Qf-S, there is the 3D-Qf simulation where loss of coherency is caused by the 3D geological irregularities, consisting mainly of small tunnel valleys, characterized by lower values of shear waves velocity (see Figure 5.7). Finally, the simple 1D-Qf provides very coherent propagation of seismic waves.

Note that the 3D interfaces produces a limited effect in term of loss of coherence with respect to the 1D case since the dynamic impedance contrast at the interface of the tunnel valleys is small, with a relatively low geometric aspect ratio (see Figure 5.7).
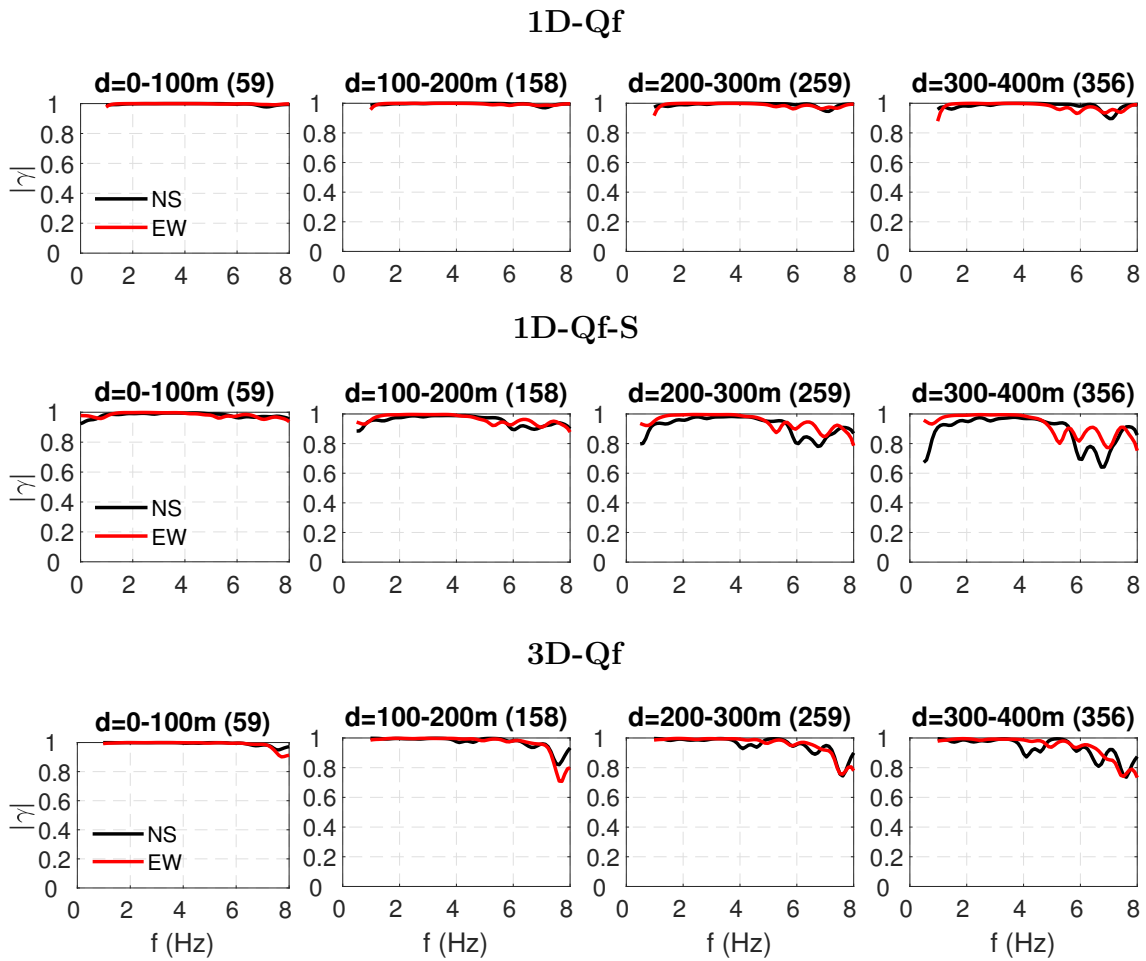
Figure 5.6: Mean lagged coherency estimates from the selected array (NS, EW) during the Zeerijp earthquake for 100 m wide distance bins form 0 to 400 m.
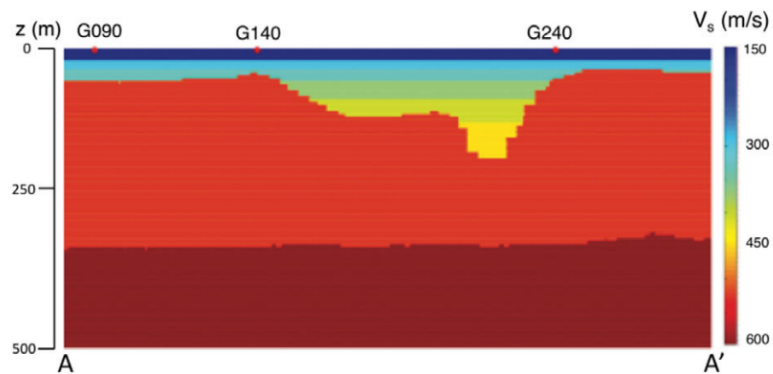
Figure 5.7: V_S profile of the 3D-Qf model

5.2   Structural Modelling

In this work, an idealized bridge structure, inspired by the HBMC Bridge, in California, USA, is considered. The bridge structure considered in this study is a 360-m long, 10-m wide, and 12-m high nine span composite RC bridge with four precast and prestressed concrete I-girders and cast-in-place concrete slabs (see Fig. 5.8). The nine bays have equal lengths of 40 m. The structural model has been implemented in SeismoStruct [2020] and modified after by Özcebe et al. (2018).

To focus on the effect of the SVEGM alone, an idealized jointless (i.e., integral abutment) bridge system was considered with the following simplified modelling assumptions:

1. the superstructure system is connected to the vertical supports as cast-in-situ without any connection elements or hinges;

2. foundation-subsoil and abutment-backfill soil interaction phenomena are not modelled, by providing fixed restraints at base nodes.

Hypothesis 1 is motivated by the fact that the HBMC is an integral abutment bridge without any type of classical bearings, instead the connections at superstructure level are maintained with shear keys and rebar nails with two expansion joints, whose non-linear effects have not been modelled herein. Referring to the second hypothesis, although it is recognized that Soil Structure Interaction (SSI) effects may play a relevant role in very soft site conditions (like in Groningen), was settled to focus the analysis on the effect of the SVEGM alone. However, the impact of this hypothesis in term of structural responses will be analyzed in Section 5.5.

Superstructure nodes	Lumped mass (tons)
s1 *and* s10	313.27
from s2 *to* s9	351.7

Superstructure system elastic rigidities		
Axial rigidity	EA	9.66e7 *kN*
Flexural rigidity-weak	EI_{22}	4.70e7 *kNm²*
Flexural rigidity-strong	EI_{33}	4.70e8 *kNm²*
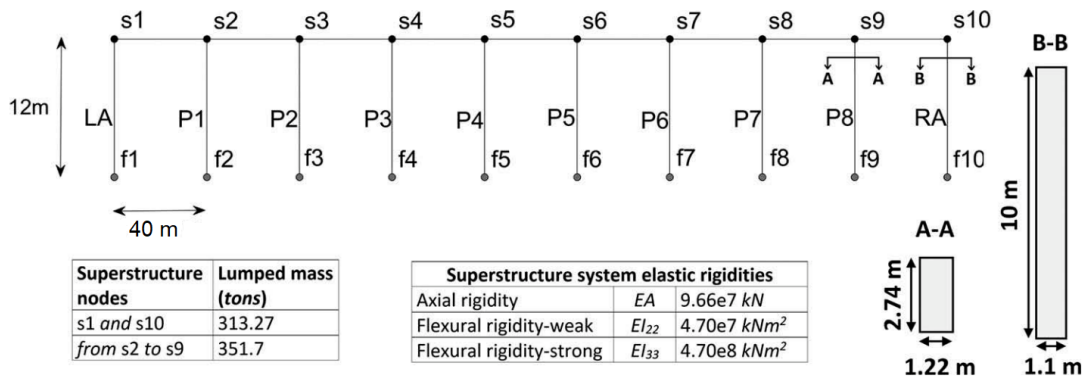
Figure 5.8: The HBMC bridge model (LA: left abutment; RA: right abutment; P: pier). A vertical exaggeration factor is applied for graphical purposes.

The structural model takes into account the non-linear properties of the bridge by modelling both plastic behaviour of concrete and reinforcing steel though fiber-based modelling.

To model the initiation and spread of nonlinearity with sufficient accuracy, piers and abutments are modelled through force-based elements Spacone et al. (1996) with 10 Lobatto integration sections. To cope with the distribution of plasticity within each cross section, rectangular RC sections are discretized with 300 and 900 fibers for piers and abutments, respectively; each concrete fiber's nonlinear uniaxial behaviour is modelled with Mander confined concrete model Mander et al. (1988) with properties: $f_c = 28$ MPa (unconfined compressive strength); $f_t = 2.2$ MPa (tensile strength); $E_c = 24,870$ MPa (modulus of elasticity of the uncracked concrete); $\epsilon_c = 0.002$ (strain at peak strength). In the abutments the confined zone is taken as 2 m.

The nonlinear behaviour of reinforcing steel, whose detail are shown in Table 5.2, is modelled by using the constitutive relation of Menegotto–Pinto Menegotto and Pinto (1973). Properties of steel layers are: $E_s = 2 \cdot 10^5$ MPa (modulus of elasticity of the reinforcement steel); $f_{ys} = 415$ MPa (yield strength); r = 0.008 (isotropic strain hardening parameter); and $\epsilon_{su} = 0.10$ (fracture strain of the steel).

Since in fiber-based modelling of nonlinearity, a significant portion of the damping sources (such as material inelasticity, repetitive crushing/cracking) is inherently considered, Rayleigh damping corresponding to 2% damping ratio is provided (Özcebe et al., 2018).

Element type		Longitudinal Reinf.	Transversal Reinf.		Conf. factor
			Along depth	Along width	
Pier		$36\phi32$	$5\phi14/100$	$3\phi14/100$	1.23
Abudment	Conf.	$106\phi32$	$4\phi14/100$	$4\phi14/100$	1.28
	Unconf.			-	1

Table 5.2: Reinforcement distributions and corresponding confinement factors for pier and abutment sections.

5.2.1 Overview of Numerical analyzes

To study the impact of recorded asynchronous input, dynamic time history analysis (DTHA) have been carried out on the bridge model, under the hypothesis of bidi-

rectional horizontal input (X + Y). To evaluate the beneficial or detrimental effect of asynchronous excitation, for each model, two classes of analyzes are conducted: (a) synchronous motion analyzes (referred to as SYN hereafter), and (b) spatially variable motion analyzes (SV).

For SYN analyzes, a single ground motion was selected as the closest one to the mean spectral acceleration response, in the range of periods around the fundamental longitudinal and transverse vibration periods of the bridge. In such conditions, the idealized uniform scenario is expected to induce approximately the same average modal forces as induced by the SV case. It turned out that the motion at the base of Pier P5, corresponds to average SYN scenario for all the numerical simulations analyzed in the present study, see Figure 5.9.

The results of all the numerical analyzes obtained for the numerical ground motion simulation 1D-Qf-S will be illustrated in Section 5.3, while in Section 5.4 the impact of the different assumptions on the SPEED model (1D-Qf and 3D-Qf) will be discussed.

1D-Qf

1D-Qf-S

3D-Qf
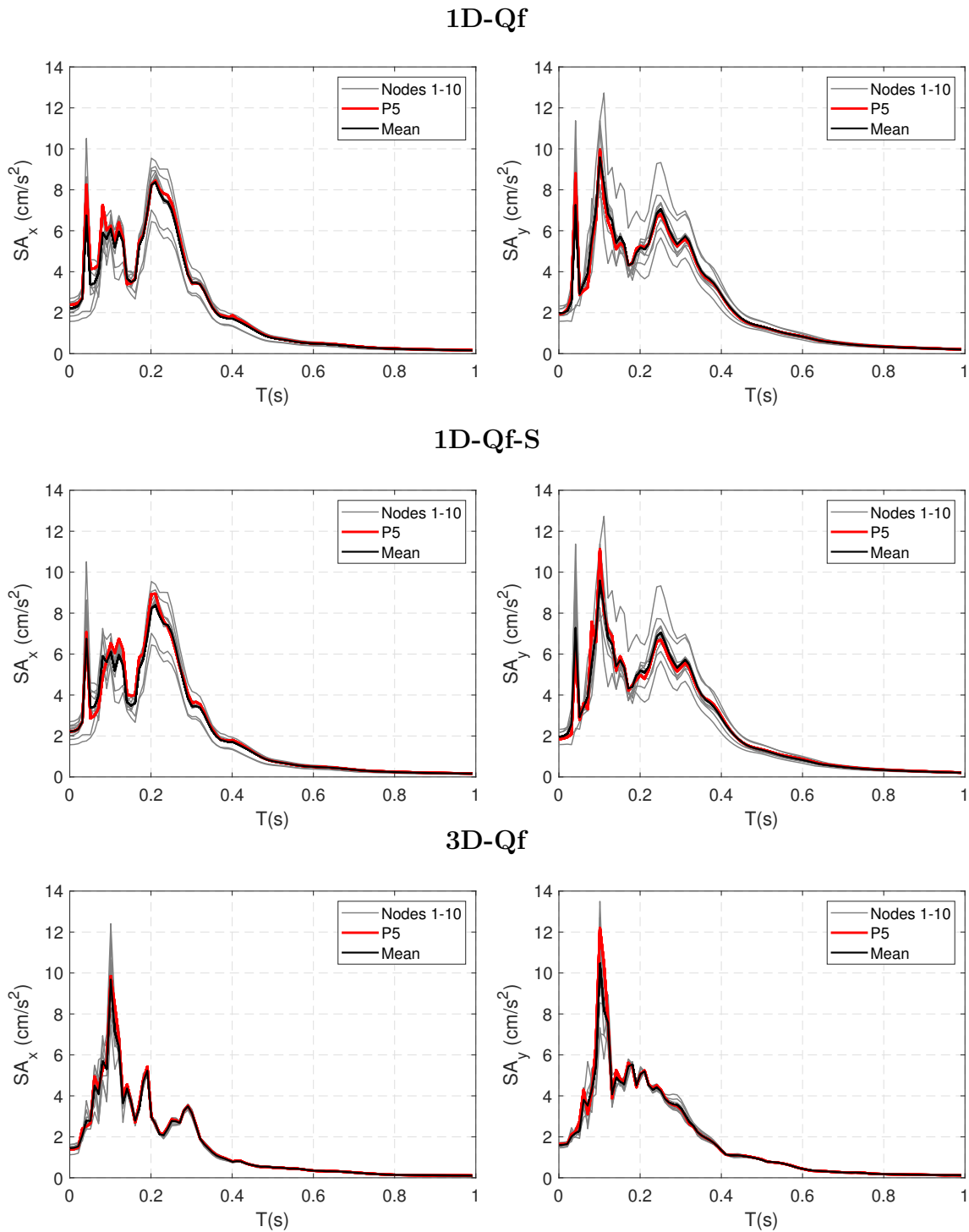
Figure 5.9: Two percent damped elastic acceleration response spectra of the 10 ground motions used as spatially variable input for bridge analyzes, along the longitudinal X (left) and transverse Y (right) direction of the bridge. The ground motion corresponding to SYN scenario is highlighted in red (P5).

5.3   Effects on the Bridge Response

5.3.1   Eigenvalue analysis

Before addressing the impact of spatially varying input motion on the bridge response, the modal response properties of the structure (see Table 5.3) are evaluated through the eigenvalue analysis.

As can be noted by looking at the effective modal mass percentages, the response in longitudinal (X) direction is dominated by a single vibration mode, with a fundamental frequency of $f_{1X} = 2.35$ Hz (mass participation factor = 100%). On the other hand, the transverse (Y) response is multimodal: besides the first mode at $f_{1Y} = 2.82$ Hz, with percent mass participation = 73.4%, further contributions are found from higher modes, mainly $f_{2Y} = 3.56$ Hz and $f_{5Y} = 18.66$ Hz, with mass participation factors of 7.0% and 17.5%, respectively. In Figure 5.10, the vibration mode shapes and corresponding mass participation factors are provided for the main translational modes.

Mode	T (s)	f (Hz)	m_X (%)	m_Y (%)
1X	0.43	2.35	100	0.0
1Y	0.35	2.82	0.0	73.4
2Y	0.28	3.56	0.0	7.0
3Y	0.22	4.56	0.0	1.8
4Y	0.05	18.66	0.0	17.5

Table 5.3: Modal response properties. Modal periods (T), frequencies (f), and corresponding modal mass percentages in global coordinates (mi with i = X, Y), from eigenvalue analysis.

f_{1X}= 2.35 Hz
m_{1X}= 100.0%

f_{1Y}= 2.82 Hz
m_{1Y}= 73,4 %

f_{2Y}= 3.56 Hz
m_{2Y}=7.0%

f_{3Y}= 4.36 Hz
m_{3Y}=1.8%
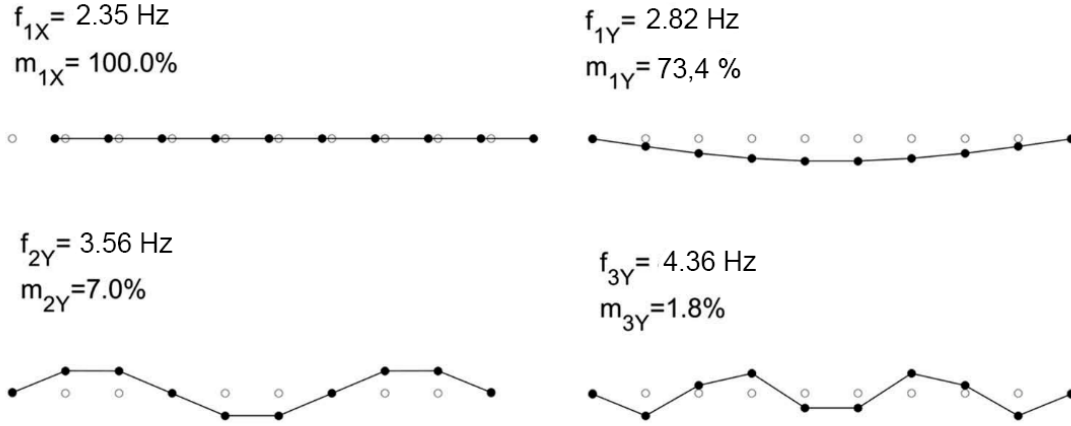
Figure 5.10: Vibration mode shapes (top view) corresponding to selected translational modes along the longitudinal (X) and transverse (Y) directions. Modal mass factors are also shown.

5.3.2 Amplification Function

Amplification function of pier response along the horizontal directions (longitudinal X or transverse Y) is computed in the frequency domain as the ratio of the Fourier transform of any response time history (acceleration/velocity/displacement) at a given point on the superstructure over the one of the corresponding base nodes. Figure 5.11 shows the longitudinal and transverse amplification functions for Piers P1, P5 and P8 computed as the ratio between the corresponding pier top node and base node. These amplification curves also compared with the amplification response curve of a Single-Degree-Of-Freedom (SDOF) system with longitudinal and transverse natural periods equal to 0.43 and 0.35 s, respectively and damping ratio ξ = 2%. The amplification factor (N) of a damped SDOFs is given by the following expression:

$$N = \frac{1}{\sqrt{1 - 2(1 - 2\xi^2)\beta^2 + \beta^4}} \tag{5.2}$$

where β is defined as the ratio between the analyzed frequency and the natural frequency of vibration of the SDOFs ($f_0 = \frac{1}{T_0}$): $\beta = \frac{f}{f_0}$.

In practice, the amplification function measures, in the frequency domain, how much the response (acceleration/velocity/displacement) at the top of the pier is magnified with respect to the one at the corresponding base due to the structural response

itself.

For all piers, the SYN and SV longitudinal response is rather similar to the one of a SDOF with $f_0 = f_{1X} = 2.35 Hz$, as the X response is fully governed by the first vibration mode. However, SV leads to perturbations at higher vibration frequencies (around 4.8 Hz), especially for P1 and P8, with minor effects on the dominant vibration mode. Note that the SYN response is 20% and 45% higher than SV response at fundamental mode for edge-piers (P1 and P8) and central pier (P5), respectively. Furthermore, regardless of the presence of spatial variability, the amplification response at the deck level is almost the same from pier to pier because of the large axial stiffness of the deck which restrains the piers to move together in longitudinal direction.

Considering the transverse (Y) amplification response, which is multimodal (f_{1Y} = 2.82 Hz, f_{2Y} = 3.56 Hz, and f_{3Y} = 4.56 Hz, see Table 5.3), as easily identifiable from the SYN response, it can be noted that:

- SYN motion excites constructively each natural vibration frequency whereas SV motions induce, a part from first mode which is constructively amplified, higher frequencies of vibration, strong destructive interference at frequencies higher than about 3 Hz (the amplification functions present troughs in correspondence of the modal frequencies).

- Under SYN input, the amplification functions show a different behaviour for the mid-span (P5) and end-span piers (P1 and P8). The fist mode is strongly amplified for pier P5 whereas the opposite occurs for piers P1 and P8 where the magnification at is almost 3 times less than for P5.
  The reason is linked to the dynamic response close-by the abutment: abutments which are characterized by high stiffness tends to constrain the movement of near piers while far from the bridge edges this effect tends to disappear. Furthermore, the SYN motions in piers close-by the abutments tends to excite more higher vibration modes.

- SV ground motion provides different structural responses at the different piers. For P1, it constructively amplifies first mode more than SYN case whereas for piers P5 and P8 the response is reduced and remains unaltered, respectively, with respect to SYN ground motion.

P1

P5

P8
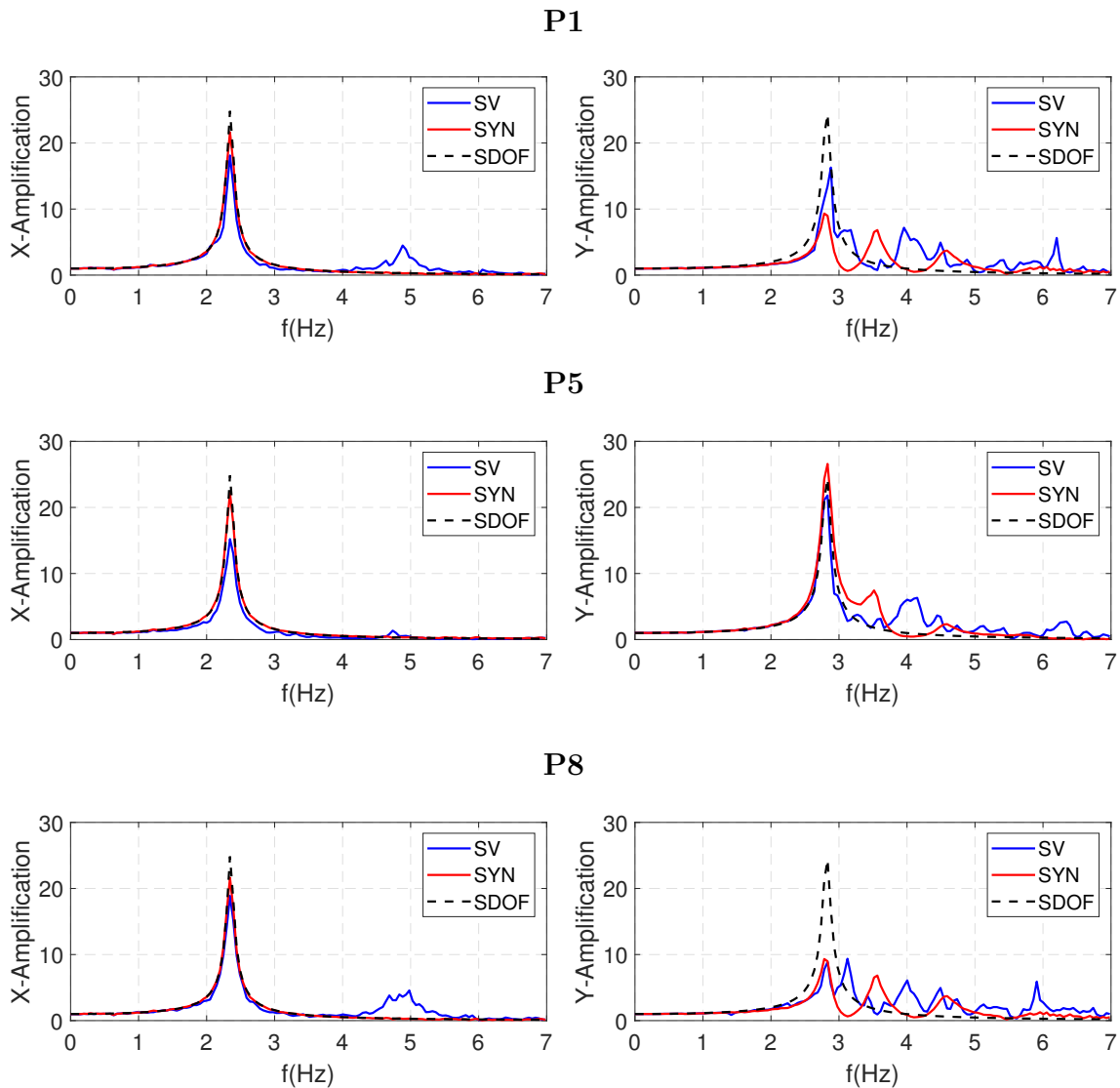
Figure 5.11: Deck amplification functions along longitudinal X (left) and transverse Y (right) direction for Piers P1, P5 and P8 under SYN-synchronous (red line) and SV-spatially variable (blue line) input. The theoretical SDOF amplification curve is also reported (black line).

5.3.3 Structural Response

The effect of spatial variability of ground motion on the peak structural response is evaluated in terms of relative deck displacement (with respect to the base) and shear force for selected elements, namely Piers P1, P5, and P8. Results are presented in a compact format using synthesis plots, where the x-axis values correspond to the results of SV analyzes and the y-axis values are from the SYN analyzes. Using this

graphical representation, alignment of values along the bisecting 1:1 line means that
SV ground motion response does not affect the response. Moreover, the 1:1.50 and
1.5:1 dashed lines correspond to 50% reduction and 50% increment, respectively, in
the peak response due to SV ground motion.

It is important to note that, due two the very low magnitude earthquake gener-
ating PGA at the site in the order of $2 \div 2.5 \ cm/s^2$, the response of the bridge
remains totally linear-elastic. Therefore, the pier relative displacement and base
shear are linearly correlated (as confirmed by Figures 5.12 and 5.13).
Figures 5.12 and 5.13 illustrate the variations of peak relative displacement values
(D_x and D_y) and maxima of the shear forces (D_x and D_y).

Referring to the longitudinal response, it comes out that SYN motion tends to
increase the displacement demand for a factor between 20% and 35% with respect
to the SV scenario. As shown in Figure 5.11 the synchronous ground motion ampli-
fies the fundamental mode, for every pier, more than the spatially variable one.

The effect of SVEGM in transverse direction appears differently at each pier: at
P5 and P8 the effect of SV motion is beneficial (around 20% for P5 and 8% for
P8) reducing the displacement demand whereas the opposite happens at P1 where
the increase of displacement due to asynchronous motion reaches the 20%. This
behaviour is in agreement to what amplification functions show (see Figure 5.11): it
appears clearly that SV motion amplifies strongly the response at the fundamental
mode for pier P1 while for piers P5 and P8 the response is reduced or equal to the
SYN one, respectively.
Similar conclusions apply to the maxima of the shear force (see Figure 5.13)
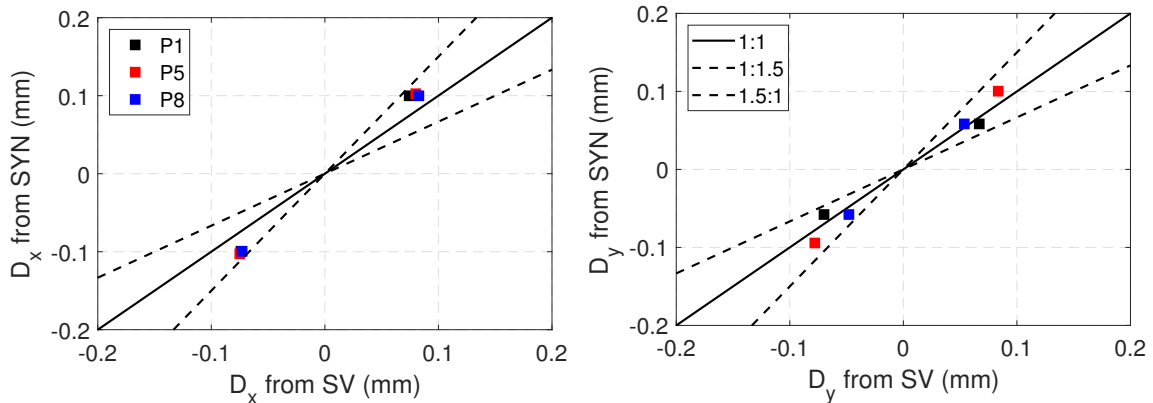
Figure 5.12: Deck displacement maxima along the longitudinal X (D_x, left) and transverse Y (D_y, right) direction, from SV analysis on the x-axis and SYN analysis on the y-axis, for Piers P1, P5, and P8.
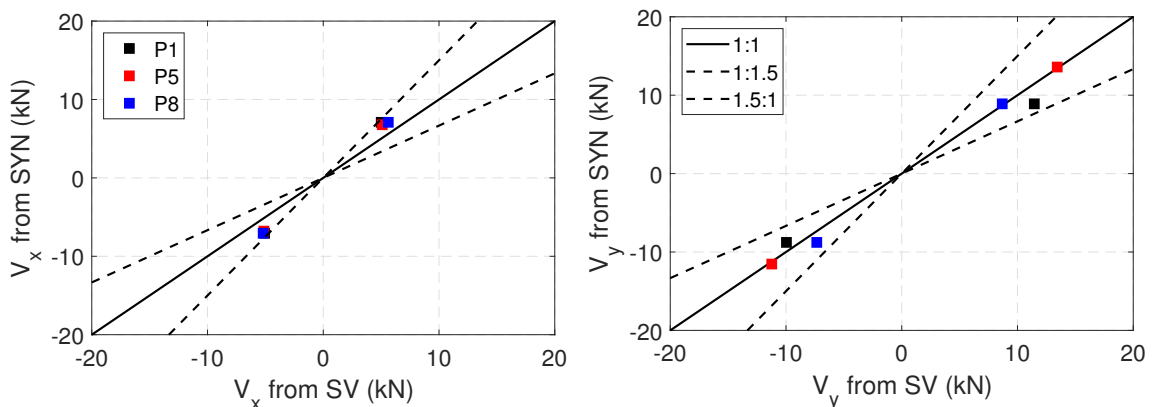
Figure 5.13: Same as in Figure 5.12 but for pier shear forces along the longitudinal X (V_x, left) and transverse Y (V_y, right) direction.

Total base shear time histories have been selected as a parameter indicating the global structural response. Time histories of total base shear (both X and Y components) are provided in Figure 5.14. In general, the asynchronous motion appears to have beneficial effect by reducing the total shear demand. This effect is more relevant in the longitudinal direction rather than the transversal one.

However, when dealing with spatially variable seismic actions, local element demand parameters (see following discussion), play a more important role than global parameters like total base shear since the motion acting on the supports by definition varies leading to different local responses rather than a unique global one.
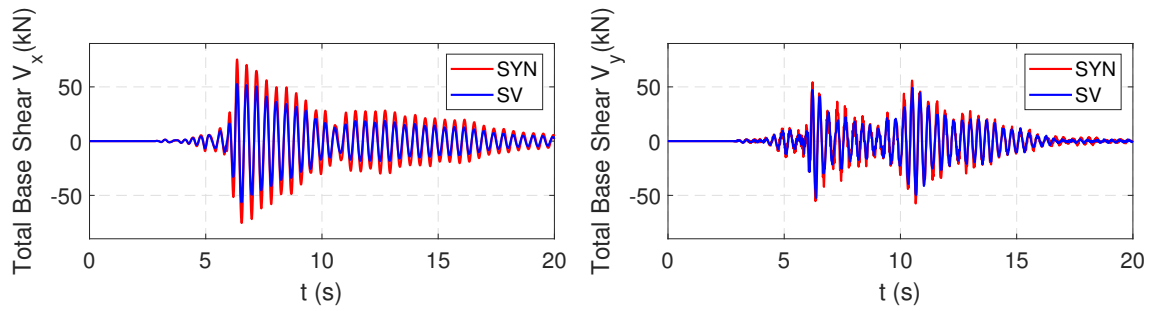
Figure 5.14: Time histories of longitudinal (left) and transverse (right) base shear from SYN and SV analyzes.

5.4 Effect of different hypotheses on SPEED model

A set of sensitivity analyzes is carried out to investigate the effect of different assumptions on the numerical model, which provide the synthetic ground motions, on the structural response, namely, with reference to labels in Table 5.1, 3D-Qf: 3D geological interfaces, to assess the influence of the tunnel valleys (see Figure 5.7); 1D-Qf: to evaluate the effect of the stochastic fluctuations of the seismic wave velocity field at shallow depths.

To this aim the absolute maximum relative top displacement D^{max} is considered as engineering demand parameter. Figure 5.15 shows the ratios of D^{max} from each SYN analysis (1D-Qf-S, 1D-Qf, 3D-Qf) over the respective one from the SV computations. It can be noted that:

- Due to restrain imposed by the axial stiffness of the deck, the response in longitudinal direction is homogeneous in the sense that the synchronous response is amplified with respect to the SV one of the almost the same quantity for each pier.

- The simulation 1D-Qf-S gives the highest values in term of $D_x^{max}(SYN)/D_x^{max}(SV)$ (on average 1.35), followed by 1D-Qf one (on average 1.15) and as last 3D-Qf (on average 1.07). The reason becomes clear by looking at Figure 5.9: all spectral accelerations associated to 3D-Qf model appears very close to the mean for periods around the fundamental one meaning that for that range of frequencies the ground motions are almost perfectly correlated (it is visible also in term of coherency at Figure 5.6), whereas the other two simulations exhibit less coherence.

- Considering the transversal component, the situation is completely different: all the simulations express similar behaviour which is characterized by a general amplification of the structural response for SV motion for piers before the mid-length of the bridge (P1, P2, P3) whereas it produces beneficial effects for piers P5, P6, P8. In transversal direction the piers are poorly linked one to the other, therefore the spatially variable motion locally increase and decrease displacement demands owing to coupling of amplification/reduction of vibration amplitude at the fundamental mode and constructive/destructive interference with higher modes, respectively. Note that for the pier P3 SV motion causes an increase of 50% of demand.

- The absolute values of $D^{max}(SV)$ show, for both directions, ground motion

from 1D-Qf provides the highest demand while 3D-Qf the lowest. The difference between the simulations is not negligible, up to 200 %, meaning that the structural response is sensitive to the accuracy of the physic-based numerical model used to generate synthetic ground motions.

Furthermore, according to what observed in the previous point the SV motion tends to amplify strongly the response at the first three piers in traversal direction at higher vibration shapes due to the constructive interaction with vibration modes.
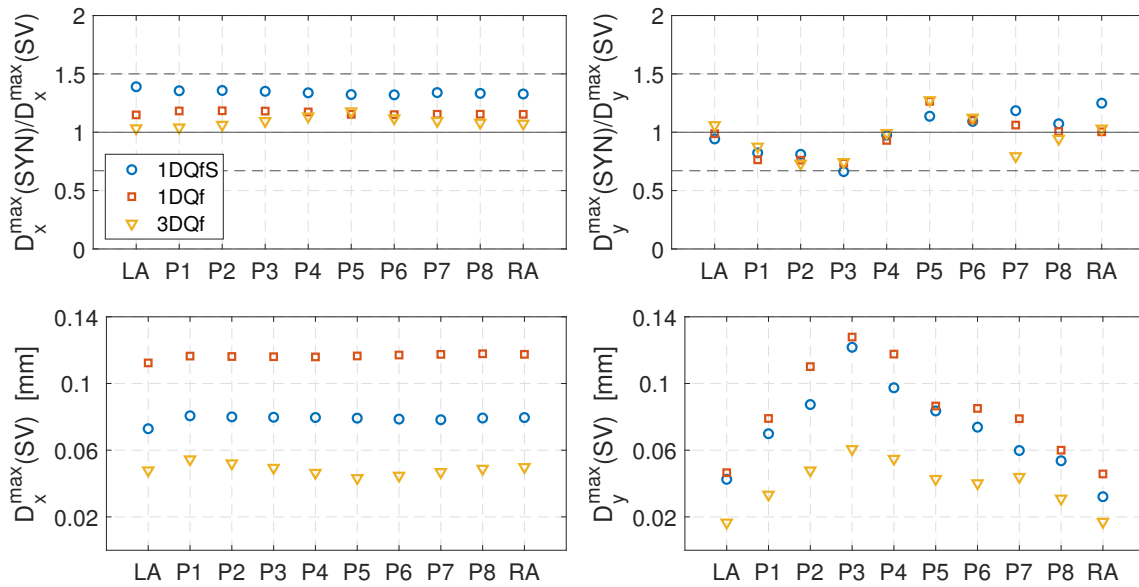
Figure 5.15: Ratio of maximum top pier displacement D^{max} (left: X direction ; right: Y direction) obtained from SYN analysis through the application of the ground motion provided by the three different simulations (1D-Qf-S, 1D-Qf and 3D-Qf) over those from the corresponding SV analyzes. The absolute values of D_{max} from SV analyzes are shown in the bottom panel.

5.5 Effect of Soil Structure Interaction

In this section the effect of considering the Soil Structure Interaction (SSI) mechanisms in the analysis of bridge structures under spatially variable ground motion excitation will be assessed by comparing the results coming from the analysis of two different structural models:

1. the bridge model shown in Section 5.2 subjected to ground motion provided by 1D-Qf-S numerical simulation (fixed-base model);

2. a bridge model accounting for the SSI effects but keeping the same structural model and ground motion (SSI model).

The seismic response of a structure founded on a deformable ground, like the one in Groningen area, may differ from the one founded on firm soil due to dynamic interaction between soil and structure.

5.5.1 Theoretical background

The SSI is characterized by two main effects:

- **Kinematic interaction**: The inability of the foundation to conform to the deformations of the free-field motion would cause the motion at the base of the structure to deviate from the free-field motion. It mainly manifest itself through the filtering of the high frequency components of the ground motion at the base of the structure with respect to the free-field and the increment of the rocking motion of the structure.

  Since in our case of study the we are analysing a shallow foundation the effects due to the kinematic interaction could be neglected remaining on the safe side.

- **Inertial interaction**: The dynamic response of the structure itself would induce deformation of the supporting soil. It mainly manifests itself through the increment of the natural period of vibration of the structure and the dissipation of part of the vibration energy by wave radiation into the foundation medium and internal friction generated at the soil-foundation interface.

A standard approach for handling soil-structure-interaction problems is the so-called substructure approach, which allows splitting kinematic and inertial interaction in different sub-steps and considering their combined effects using the principle of superposition (Kramer, 1996). Note that being based on the principle of superposition,

it strictly applies only to linear problems.

The substructure approach consists of three main sub-steps (see Figure 5.16):

1. **kinematic interaction**: the effect of a foundation with prescribed geometry and stiffness on the soil dynamics is analyzed to quantify any possible modifications to the input motion at the base of the structure in comparison to the free-field motion, resulting in the Foundation Input Motion (FIM);

2. **evaluation of the soil dynamic impedance functions**: the deformability and overall dynamic characteristics of the soil layers are analyzed to include the soil compliance at the base of the structural model;

3. **dynamic response of the structure**: inertial interaction, where the structural mass is considered, and its effects on the overall response of the structure, subjected to the FIM and on a compliant base, are determined.
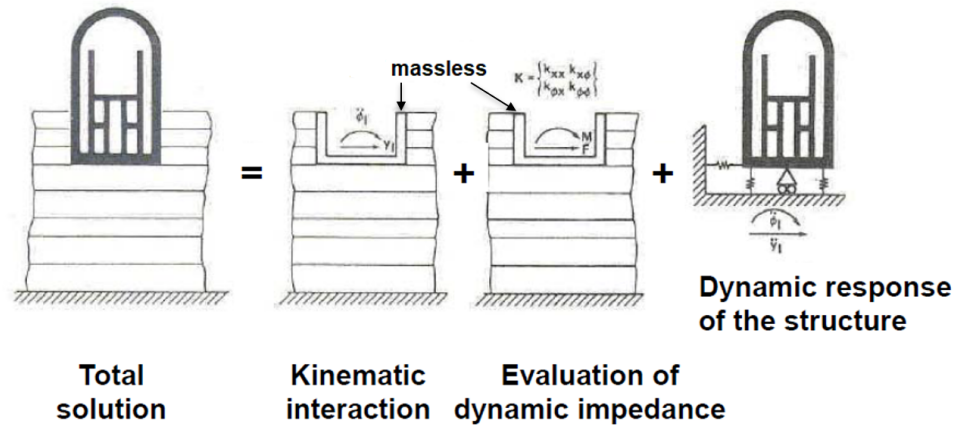
Figure 5.16: Sketch illustrating the substructure method and its sub-steps.

Dynamic Impedance Function

With reference to point (2) above, the dynamic impedance function ($\mathbf{K}$) is defined as the ratio between the force (or moment) $\mathbf{R}$ and the steady-state displacement (or rotation) $\mathbf{U}$ at the centroid of the base of the foundation assumed to be massless. It is a complex valued and frequency dependent function since, due to the presence of radiation and material damping, R is generally out of phase with U:

$$K(\omega) = k(\omega) + i\omega c(\omega) \tag{5.3}$$

169

The introduction of the dynamic impedance function allows the decoupling of the soil-foundation system from the superstructure system: under the assumption of linear elastic behaviour, the soil-foundation system could be represented, through the Lysmer's analogy, in an equivalent system of frequency dependent springs ($k(\omega)$) and dashpots ($c(\omega)$).

Gazetas (1991) provides the values of the dynamic impedance coefficients as a function of the soil's mechanics properties and of the foundation's geometry. In our case, each pier is assumed to be sustained by a square surface foundation (side dimension equal to 2B), therefore the elastic modulus of the equivalent translational (k_0) and rotational (k_r) springs are given by the following equations (Gazetas, 1991):

- **Translational stiffness**:

$$k_0 = k_{0y} = k_{0x} = \frac{9GB}{2 - \nu} \tag{5.4}$$

  where: G and ν are the shear modulus and Poisson's coefficient of the soil, respectively.

- **Rotational stiffness**:

$$k_r = k_{ry} = k_{rx} = \frac{3.6GB^3}{1 - \nu} \tag{5.5}$$

The equivalent translational (c_0) and rotational (c_r) dashpots instead are provided by Gazetas (1991) based on empirical curves.
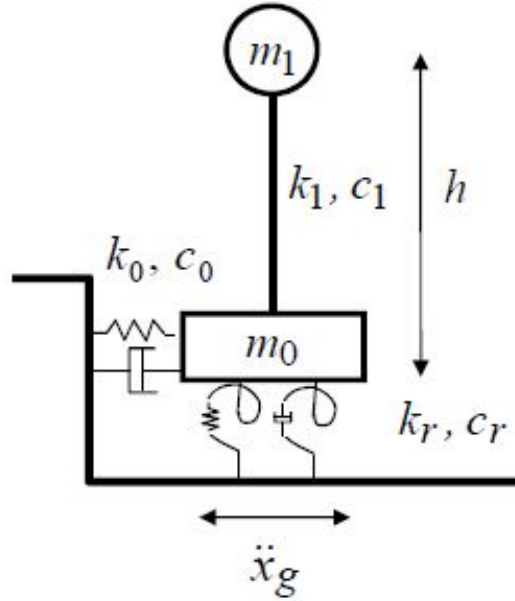
Figure 5.17: Equivalent 3DOF system.

Since the soil of the Groningen gas field area is characterized by shear wave velocity $V_{S,30} = 150$ m/s and mass density $\rho = 1800$ kg/m^3, the shear modulus of the soil is $G = \rho \cdot V_s^2 = 40.5$ Mpa. The properties of the equivalent spring and dashpots, implemented in the study herein, are summarized in Table 5.4 (all the coefficients are derived considering a Poisson's coefficient $\nu = 0.4$). Note that, as a simplifying hypothesis, we suppose that all the piers all the piers are supported by foundations with same dimensions (10 m x 10 m) whereas abutment foundations are characterized by a side dimension $2B = 20$ m.

	B (m)	k_y (N/m)	k_x (N/m)	k_{rx} (Nm/rad)	k_{ry} (Nm/rad)
Piers	5	1.14E+09	1.14E+09	3.04E+10	3.04E+10
Abutments	10	2.28E+09	2.28E+09	2.43E+11	2.43E+11

	B (m)	c_y	c_x	c_{rx}	c_{ry}
Piers	5	2.70E+07	2.70E+07	4.06E+08	4.06E+08
Abutments	10	1.08E+08	1.08E+08	6.50E+09	6.50E+09

Table 5.4: Dynamic stiffness and dashpot coefficients.

5.5.2 Impact of SSI on the bridge response

The substructure method is implemented in the SeismoStruct model: the base of each vertical bearing element (pier or abutment) is connected to the ground by means of elastic links and dashpots (with null dimensions). The elastic links and dashpots are characterized by elastic stiffnesses and damping coefficients, respectively, as defined in Table 5.4.

As first consequence, natural periods of vibration of the bridge structures increase with respect to the fixed base assumption (see Table 5.3) mostly in transverse direction, which, as expected, is stiffer compared to the longitudinal one. Table 5.5 reports the modal response properties of the structure evaluated through the eigenvalue analysis.

The period elongation is, physically, due to the generation of strains within the soil leading to an increasing the whole system flexibility. In this case study it implies beneficial effects: the response spectral acceleration is reduced (see Figure 5.9).

Mode	T (s)	f (Hz)	m_X (%)	m_Y (%)
1X	0.47	2.15	100	0.0
1Y	0.49	2.02	0.0	74.7
2Y	0.38	2.66	0.0	7.6
3Y	0.28	3.63	0.0	2.5
4Y	0.15	6.51	0.0	14.0

Table 5.5: Modal response properties. Modal periods (T), frequencies (f), and corresponding modal mass percentages in global coordinates (mi with i = X, Y), from eigenvalue analysis.

As for the fixed base assumption (see Figure 5.11), the response in longitudinal direction is dominated by the first mode and the SYN response is higher than the SV one. However, in this case the difference between SYN and SV turns out to be lower: SYN response is 18% and 37% higher than SV response at fundamental mode for edge-piers (P1 and P8) and central pier (P5), respectively.

Considering the transverse (Y) amplification response, it can be noted that:

- Under SYN input, the amplification functions show a different behaviour for the mid-span (P5) and end-span piers (P1 and P8). The fist mode is strongly amplified for pier P5 whereas the opposite occurs for piers P1 and P8 where

the magnification at is almost 3 times less than for P5.

Furthermore, the SYN motions in piers close-by the abutments tends to excite more higher vibration modes.

- SV ground motion provides different structural responses at the different piers. For P1 and P5, it constructively amplifies first mode with intensity similar to SYN motion whereas for piers P8, SV motion tends to amplify frequencies different from the modal ones.

Comparing amplification functions from fixed-base model (Figure 5.11) and SSI model (Figure 5.18), it appears clearly that the overall structural amplification is reduced due to the increased dissipation capacity of the soil-foundation-structure system: under fixed-base assumption, the only source if energy dissipation comes from the structure whereas in the SSI model the implementation of equivalent dash-pots at the supports allow to take into account also the radiation damping due to the propagation of waves into the soil.

Finally, the maximum absolute relative top displacement D^{max} has been chosen as engineering demand parameter to the aim of assessing the impact of SVEGM when fixed-based assumption or SSI interaction are considered.

Looking at Figure 5.19, it could be seen that:

- In longitudinal direction, it is confirmed that SV motion generates beneficial effects with respect to SYN reducing the structural demand.

- In Y direction, where the SVEGM effects become more relevant, the SSI tends to amplify the differences between SYN and SV motion for piers from P4 to P8 whereas for piers P1, P2 and P3 the opposite occurs. Furthermore, the model with fixed-base leads to results strongly different from SSI model for piers P6 and P7: the first one shows a beneficial effect of SV motion whereas, on the contrary, the second one highlight that SV motion increases the demand with respect to SYN one.

- As expected, the SSI effect produces a decreasing of the overall demand in both directions due to period elongation and damping ratio increasing (see Figure 5.19 bottom).

In the light of what has been observed, considering the effect of SSI, in very soft

soil condition, turns out to be important in order to evaluate correctly the actual dynamic behaviour of the bridge.

P1

P5

P8
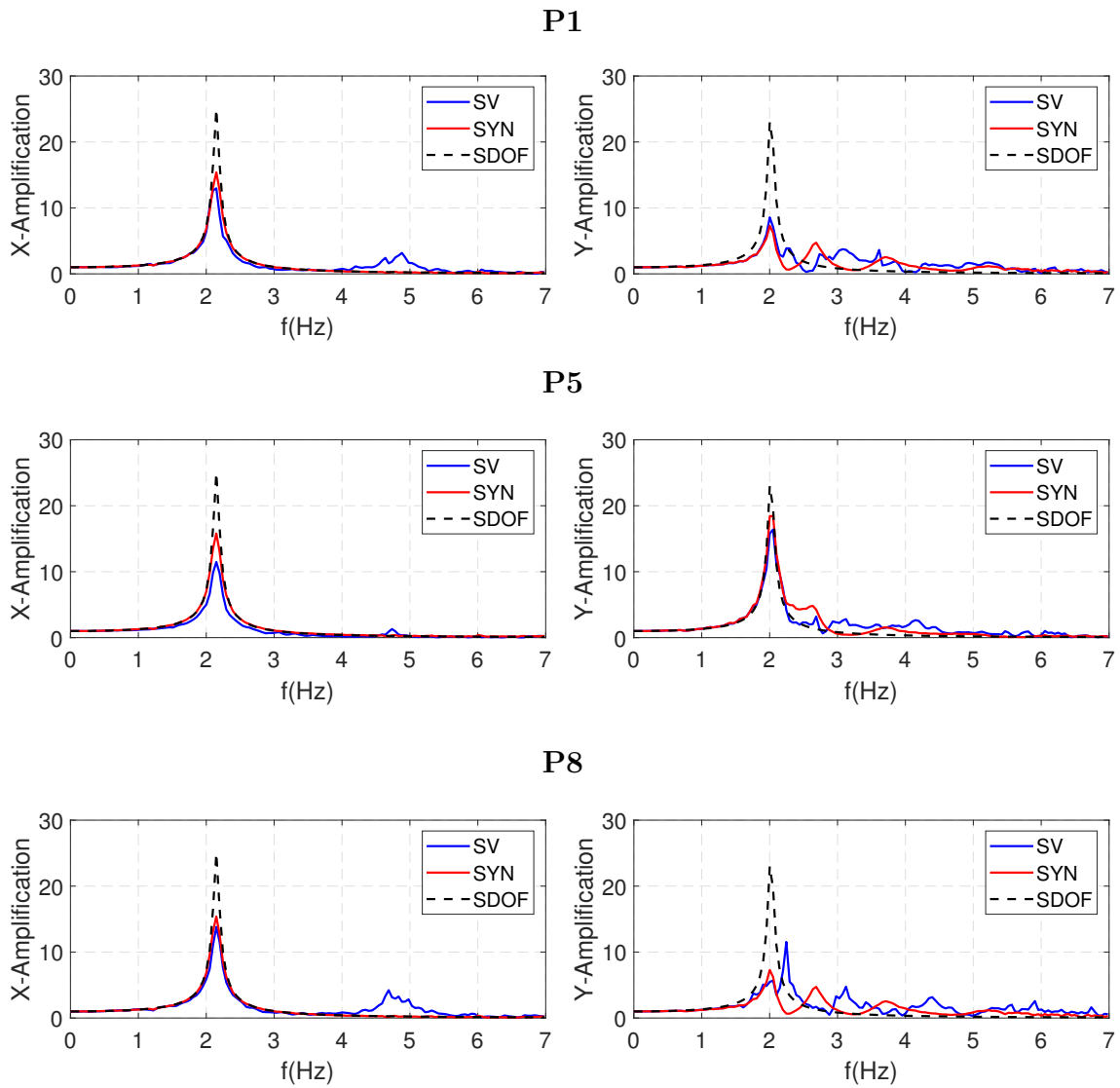
Figure 5.18: Deck amplification functions along longitudinal X (left) and transverse Y (right) direction for Piers P1, P5 and P8 under SYN-synchronous (red line) and SV-spatially variable (blue line) input. The theoretical SDOF amplification curve is also reported (black line).
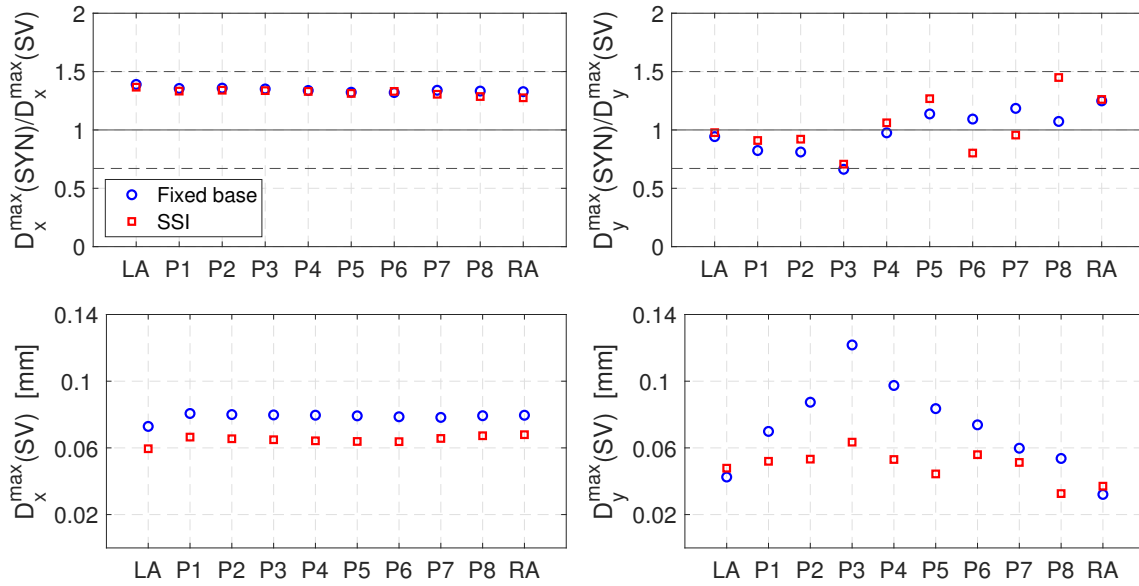
Figure 5.19: Ratio of maximum top pier displacement D^{max} (left: X direction ;
right: Y direction) obtained from SYN analysis over those from the corresponding
SV analyzes. The results from fixed-based model are reported in blue while the ones
from the SSI model in red. The absolute values of D_{max} from SV analyzes are shown
in the bottom panel.

Conclusions

The spatial variation of earthquake ground motions (SVEGM) denotes the differences in the seismic ground motion time histories (in both amplitude and phase) at various locations on the ground surface. The aspects related to the quantification of the SVEGM is crucial for the seismic analysis of the class of spatially extended civil engineering structures, such as bridges, pipelines, tunnel and dams. For these structures, characterized by significant spatial dimensions, comparable to those of the dominant wavelengths of ground motion, the assumption of a synchronous seismic excitation may provide unsafe estimates. For these reasons, in recent years, the modelling of the SVEGM and its influence on the response of lifeline systems, and, currently, design codes incorporate its effects in their provisions (NTC18, EC8).

The current state-of-the-art approaches for the seismic analysis of bridge structures are typically based on the use of artificial stochastic accelerograms satisfying a prescribed spatial coherency model or, in even more simplified approaches, accounting only for the time delay due to plane wave propagation with constant apparent propagation velocity. These artificial accelerograms are calibrated on a limited amount of data coming from different seismo-tectonic contexts and neglecting near-source conditions. As a more advanced alternative, earthquake ground motions recorded at spatial dense arrays or numerically simulated accelerograms can be used.

The available engineering models for SVEGM are calibrated on the basis of strong motion recordings at dense seismic arrays during past earthquakes and usually neglect the aspects related to the proximity to the seismic source. In spite of the increasing availability of strong motion records, observations at dense arrays are still very scarce especially in near-source conditions even on a worldwide scale and further studies are needed. Furthermore, recent studies have pointed out that the spatial coherency of earthquake ground motions is strongly region- and earthquake-specific so that a generic model, calibrated on a limited number of data coming from different regions and earthquakes worldwide, may be poorly representative of

the target site.

As a complementary tool to the analysis of earthquake recordings, numerical simulations of earthquake ground motion, based on 3D physical models of the seismic source, the propagation path from the source to the site and local geologic irregularities, can be used to simulate spatially variable ground motions when recorded data are lacking. Indeed, differently from ground motion records, the potential availability of numerous, repetitive simulations of ground motion, at arbitrarily dense arrays of receivers, from different realistic rupture scenarios and in different geo-morphological conditions, allows for the investigation of the effect of different physical factors, such as magnitude, source rupture features, local site conditions, source-to-site path, that may play an important role in the quantification of SVEGM at the site of interest.

Stimulated by these these considerations, the main objective of this thesis was to study the aspects related to the SVEGM in a rather comprehensive way with analyzes ranging from the evaluation of the spatial coherency of ground motions from available recordings (Chapter 3) and from 3D physics-based numerical simulations (Chapter 4), up to the assessment of the impact of an accurate modelling of spatially varying seismic input on the seismic response of bridge structures (Chapter 5). Starting from the theoretical framework regarding the stochastic estimation of SVEGM based on the definition of spatial coherency, the commonly used empirical and semi-empirical spatial coherency models, available in the literature, have been critically reviewed. After that, a suitable procedure has been proposed and validated to compute the spatial coherency of ground motion waveforms (both recordings and synthetics).

The analysis of ICEARRAY (Iceland), UPSAR array (California) and Italian dense arrays (L'Aquila and Mirandola) highlights some interesting insight:

- The rate of decay of coherency with frequency turns out to be more accentuated for low frequencies (up to 2 - 3Hz), while at higher frequencies coherency stabilize around constant values without reaching zero;

- From the regression of results based on Luco and Wong (1986) models, the coherency drop parameter α tends to be non-linearly dependent on distance: α turns out to decrease with increasing inter-station distance at a rate which tends to be higher at smaller distances (see Figures 3.40 and 3.41). This means that the rate of decay of coherency with frequency tends to decrease with increasing separation distance;

- A general agreement with literature coherency models is observed at low frequencies (up to 2 - 3Hz) whereas poor agreement appears at higher ones with a tendency for the models to overestimate the recorded coherency decay (see Figure 3.38).

Regarding physic-based numerical simulations, three different Italian case studies have been studied: Marsica, Emilia and Norcia. The capability of physic-based numerical simulations of accurately reproducing the ground motion at a specific site, although it is limited to the low frequency range, starting from its geological and seismological characterization, allows to study the dependence of the spatial coherency on physical parameters. Due to the variety of site conditions (each one of the three case studies have different peculiarities) and earthquake scenarios (scenarios with different magnitude, slip distribution, hypocenter location have been simulated), it was possible to shed light on the physical factors affecting the SVEGM:

- In near-fault regions, characterized by the absence of relevant buried geological irregularities, the fault-normal component tends to be more coherent than fault-parallel one owing to source due to the directivity effect (see Figures 4.31 and 4.32);

- Regarding normal focal mechanisms, the vertical component expresses lower coherency than horizontal components at arrays located on the hangingwall whereas the opposite occurs on footwall due to up-dip directivity effect (see Figures 4.31 and 4.33).

- Low magnitude earthquakes (point-sources) provide less coherent motion than medium-high earthquakes (finite-sources). No clear dependence, instead, appears among medium-high earthquakes (see Figure 4.34);

- Coherency decreases with decreasing source-to-site distance (see Figure 4.39);

- Coherency increases passing from soil to rock site condition (see Figure 4.40);

- Superficial hypocenters generate less coherent motion than deep ones (see Figure 4.41).

- In agreement to what observed from earthquake recordings, the parameter α of the Luco and Wong (1986) model appears to be non-linearly dependent with separation distance: α turns out to decrease with increasing inter-station

distance at a rate which tends to be higher at smaller distances. This non-linear dependence is more relevant for site on soil condition rather than on rock.

These considerations testify how complex and case specific are the mechanisms behind SVEGM, pointing out the need of models and tools capable of providing accurate and site-specific estimates of SVEGM, suitable for earthquake engineering applications. To this aim, owing to the growing computational power and to the development of efficient numerical algorithms, physics-based numerical simulations are expected to provide a valuable contribution in next future.

The potential of PBS to generate synthetic ground motions at arbitrary sites, based on realistic rupture scenarios and geo-morphological conditions, has been exploited to study the impact of a spatially variable motion on a bridge structure. An idealized 360-m long integral abutment bridge structure, located at the Groningen gas field area, was subjected to low intensity excitations (The M_L 3.4 Zeerijp earthquake of January 8, 2018) to evaluate whether an asynchronous seismic input is beneficial or detrimental in term of structural response. Furthermore, the sensitivity of the results on the hypothesises at the basis of the PBS model was analyzed. The most salient results can be summarized as follows:

- SVEGM turns out to affect both bridge principal directions: in the longitudinal direction, where the response is governed by a single vibration mode, it tends to excite less the fundamental frequency with consequent beneficial effect with respect a synchronous motion. In transversal direction, instead, SV motion tends to locally amplify or de-amplify structural demands, by factors up to 50% (see Figure 5.15), owing to the constructive or destructive interaction with vibration modes (as apparent from the bridge deck amplification function of Figure 5.11);

- The results in terms of structural response are strongly affected by the assumptions on the PBS model. Differences up to 200 % are observed passing from a simple one dimensional subsoil model to a more refined 3D one (see Figure 5.15). Note that, for design purposes, the simplest model (1D-Qf) provides values in favour of safety.

- In soft-soil condition, taking into account the soil structure interaction effects becomes relevant in order to assess correctly the structural response (see Figure 5.19).

Furthermore, results point out the relevance of a careful analysis of the relationship between the input excitation and higher vibration modes to get an accurate prediction of the impact of SVEGM and to identify the most affected structural elements.

Despite these conclusions are limited to only one integral abutment structural type and to a very low magnitude earthquake, they raise the point of a more in-depth evaluation of the impact of SVEGM, because the complexity of earthquake ground motion, especially in the proximity of the seismic source, may induce significant effects, even on a regular, 360-m long bridge on relatively homogeneous soft site ground conditions. For this reason, future researches should be addressed to couple PBS of strong earthquakes, in different regions, with bridge response, also in the non-linear range, and perform sensitivity analyzes with respect to the earthquake scenario and the structural configuration.

Appendix A

Smoothing of spectral densities

The smoothed spectral estimator of power and cross spectrum are defined as:

$$\bar{S}_{jj}(\omega) = \frac{1}{2\pi} \int_{-\infty}^{+\infty} w(\tau) R_{jj}(\tau) e^{-i\omega\tau} d\tau \tag{A.1}$$

$$\bar{S}_{jk}(\omega) = \frac{1}{2\pi} \int_{-\infty}^{+\infty} w(\tau) R_{jk}(\tau) e^{-i\omega\tau} d\tau \tag{A.2}$$

where $w(\tau)$ is the lag window.

Equivalently, the smoothed spectral densities can be obtained by smoothing the spectral densities with a window function $W(\omega)$ (Fourier transform of the lag window) directly in the frequency domain thought a convolution integral:

$$\bar{S}_{jj}(\omega) = \int_{-\infty}^{+\infty} W(u) S_{jj}(\omega - u) du \tag{A.3}$$

$$\bar{S}_{jk}(\omega) = \int_{-\infty}^{+\infty} W(u) S_{jk}(\omega - u) du \tag{A.4}$$

For discrete frequencies the previous equations become:

$$\bar{S}_{jj}^{M}(\omega_n) = \frac{2\pi}{T} \sum_{m=-M}^{+M} W(m\Delta\omega) S_{jj}(\omega_n + m\Delta\omega) \tag{A.5}$$

where $\Delta\omega$ is the frequency step, $\omega_n = n\Delta\omega$ is the discrete frequency, 2M+1 the number of frequencies over which the averaging is performed, and the superscript M

indicates the dependence of the estimate on the length of the smoothing window.

$$\bar{S}_{jk}^{M}(\omega_n) = \frac{2\pi}{T} \sum_{m=-M}^{+M} W(m\Delta\omega)\Lambda_j(\omega_n + m\Delta\omega)\Lambda_k(\omega_n + m\Delta\omega)$$
$$\cdot \exp(i[\phi_k(\omega_n + m\Delta\omega) - \phi_j(\omega_n + m\Delta\omega)]) \quad \text{(A.6)}$$

Equation A.6 derives from the definition of the Fourier transforms, $A_j(\omega)$ and $A_k(\omega)$ of time histories $a_j(t)$ and $a_k(t)$:

$$A_j(\omega) = \Lambda_j(\omega)\exp[i\phi_j(\omega)] \quad \text{(A.7)}$$

From the available smoothing windows, the Hamming window is most commonly used for smoothing the seismic spectral estimates. The expression of this function is given by (Zerva, 2009):

$$W(m) = \frac{0.54 - 0.46\cos\left(\dfrac{\pi(m+M)}{M}\right)}{1.08M} \quad \text{(A.8)}$$

Figure A.1 illustrated the graphical representation of Hamming Window function for M = 1, 3, 5, 9 and 11.
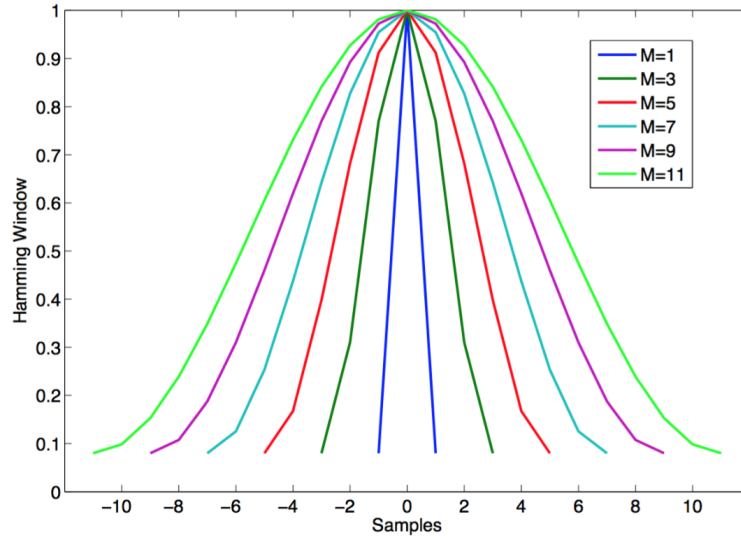
Figure A.1: Hamming windows for M = 1, 3, 5, 7, 9 and 11

In the selection of the frequency smoothing, there is a trade-off between the frequency resolution and the bias and uncertainty. On one hand, Smoothing over a small number of frequencies leads to high resolution in frequency but also leads to

large bias and large variability; on the other hand smoothing over a large number of frequencies gives poor resolution in frequency, but leads to small bias and small variability. An 11-point Hamming window is recommended by Abrahamson et al. (1991) for smoothing in frequency domain for time windows with less than approximately 2000 samples when the coherency estimates are to be used in structural analysis with damping coefficient of 5%.

Appendix B

Strong motion window evaluation

As explained in the previous sections, the assumption of stationarity of the stochastic process (i.e. the recorded signal) is fundamental in the definition of the coherency: it allows to consider a coherency function which depends only on the distance between two stations j and k, and does not depend on their locations; moreover, the notions of spectral densities can be used also because of that hypothesis.

Since earthquake ground motion signals are not stationary, strong motion windows of the signal are used for the evaluation of the spatial coherency (the signal within the strong motion windows is stationary Abrahamson et al. 1987).
The strong motion windows can be selected by computing the Arias Intensity (AI). It is a measure of the energy of the signal and it is estimated following the expression given by Abrahamson (2007):

$$AI(\tau) = \frac{\int_{T_p}^{\tau}(V_1^2(t) + V_2^2(t))dt}{\int_{T_p}^{T_p+25}(V_1^2(t) + V_2^2(t))dt} \tag{B.1}$$

where T_p is the arrival time of P-wave, i.e, the beginning of earthquake signals, and $V_1(t)$ and $V_2(t)$ are the both signal velocigrams in the horizontal component.

In addition to the requirements of stationarity, strong motion window should be selected to fulfill the resolution requirement. Coherency estimates are obtained at frequency points $f_p = p/N\Delta t$, $p = 1, \ldots, N/2 - 1$, where N is the number of sample points in the time series and Δt, the shorter the time segment analyzed, the lower is the resolution of the coherency estimates (Konakli et al., 2014). Thus, there is interest in considering as long a time segment as possible, without jeopardizing accuracy

of the estimates. For these reasons, the selection of the beginning and the end of the strong motion window depends on the case of study (earthquake signals derive from complex phenomena, therefore become difficult to define an unique rule). In general, they are considered to be the time when Arias Intensity reaches normalized value of 0.1 and 0.8. However, a visual inspection is then required in order to adjust the AI values in such a way that the requirements of stationarity and resolution are properly satisfied.

An analogue procedure was used by Abrahamson (2007) to estimate coherency from Piton Flat array recordings.

Bibliography

Abdel Raheem, S. E. (2014). Ground motion spatial variation effects on seismic performance of structural control of cable-stayed bridges. *Proceedings of the International Conference on Structural Dynamic , EURODYN*, 2014-Janua(1):1737–1744.

Abrahamson (2006). Program on Technology Innovation: Spatial Coherency Models for Soil-Structure Interaction. *EPRI, Palo Alto, CA, and U.S. Department of Energy, Germantown, MD: 2006. 1014101*, 3(3).

Abrahamson (2007). Program on Technology Innovation: Effects of Spatial Incoherence on Seismic Ground Motions. *Rpt. No. EPRI 1015110, Palo Alto, CA*.

Abrahamson, Schneider, and Stepp (1991). Empirical Spatial Coherency Functions for Application to Soil-Structure Interaction Analyses. *Earthquake Spectra*, 7:1–27.

Abrahamson, N. A., Darragh, R. B., Penzien, J., and Tsai, Y. B. (1987). Smart I Accelerograph Array (1980-1987): a Review.

AfifChaouch, K., Tiliouine, B., Hammoutene, M., Sigbjörnsson, R., and Rupakhety, R. (2016). Estimating ground motion incoherence through finite source simulation: a case study of the 1980 El-Asnam Earthquake. *Bulletin of Earthquake Engineering*, 14(4):1195–1217.

Akkar, S., Sandıkkaya, M. A., and Bommer, J. J. (2014). *Empirical Ground-Motion Models for Point- and Extended-Source Crustal Earthquake Scenarios*.

Ancheta, Stewart, and Abrahamson (2011). ENGINEERING CHARACTERIZATION OF EARTHQUAKE GROUND MOTION COHERENCY AND AMPLITUDE VARIABLITY. In *4th IASPEI / IAEE International Symposium: Effects*, number 1991, pages 1–12.

Bernard, P. and Herrero, A. (1994). Slip heterogeneity, body-wave spectra, and directivity of earthquake ruptures. *Annals of Geophysics*, 37(6).

Bernard, P., Herrero, A., and Berge, C. (1996). Modeling directivity of heterogeneous earthquake ruptures. *Bulletin of the Seismological Society of America*, 86(4):1149–1160.

Bigi, G. (1992). Structural Model of Italy 1:500,000.

Bindi, D., Massa, M., Luzi, L., Ameri, G., Pacor, F., Puglia, R., and Augliera, P. (2014). Pan-European ground-motion prediction equations for the average horizontal component of PGA, PGV, and 5%-damped PSA at spectral periods up to 3.0 s using the RESORCE dataset. *Bulletin of Earthquake Engineering*, 12(1):391–430.

Boccaletti, M., Corti, G., and Martelli, L. (2011). Recent and active tectonics of the external zone of the Northern Apennines (Italy). *International Journal of Earth Sciences*, 100(6):1331–1348.

Boissières, H. P. and Vanmarcke, E. H. (1995). Estimation of lags for a seismograph array: wave propagation and composite correlation. *Soil Dynamics and Earthquake Engineering*, 14(1):5–22.

Cauzzi, C., Faccioli, E., Vanini, M., and Bianchini, A. (2015). Updated predictive equations for broadband (0.01–10 s) horizontal response spectra and peak ground motions, based on a global dataset of digital acceleration records. *Bulletin of Earthquake Engineering*, 13(6):1587–1612.

Chen, Q. and Hong, N. (2019). Depth Coherency Analysis for Strong Seismic Motions from KiK-Net. *Journal of Earthquake Engineering*, 00(00):1–26.

Chioccarelli, E. and Iervolino, I. (2010). Near-source seismic demand and pulse-like records: A discussion for L'Aquila earthquake. *Earthquake Engineering and Structural Dynamics*.

Dabaghi, M. and Der Kiureghian, A. (2014). *UC Berkeley UC Berkeley Electronic Theses and Dissertations*. PhD thesis.

D'Amico, M., Felicetta, C., Schiappapietra, E., Pacor, F., Gallovič, F., Paolucci, R., Puglia, R., Lanzano, G., Sgobba, S., and Luzi, L. (2019). Fling effects from near-source strong-motion records: Insights from the 2016 M w 6.5 Norcia, Central Italy, Earthquake. *Seismological Research Letters*, 90(2 A):659–671.

Der Kiureghian, A. (1996). A coherency model for spatially varying ground motions. *Earthquake Engineering and Structural Dynamics*, 25(1):99–111.

Evangelista, L., Chiara, G., Landolfi, L., Paolucci, R., and Santo, A. (2017). Physics-based seismic input for engineering applications : a case study in the Aterno river valley , Central Italy. *Bulletin of Earthquake Engineering*, 15(7):2645–2671.

Faccioli, E., Maggio, F., Paolucci, R., and Quarteroni, A. (1997). 2D and 3D elastic wave propagation by a pseudo-spectral domain decomposition method. *Journal of Seismology*, 1(3):237–251.

Fletcher, J. B., Baker, L. M., Spudich, P., Goldstein, P., Sims, J. D., and Hellweg, M. (1992). The USGS Parkfield, California, dense seismograph array: UPSAR. *Bulletin - Seismological Society of America*, 82(2):1041–1070.

Fletcher, J. B., Spudich, P., and Baker, L. M. (2006). Rupture propagation of the 2004 Parkfield, California, earthquake from observations at the UPSAR. *Bulletin of the Seismological Society of America*, 96(4 B):129–142.

Gazetas, B. G. (1991). FORMULAS AND C H A R T S FOR IMPEDANCES O F. 117(9).

Halldórsson, B. and Sigbjörnsson, R. (2009). The Mw 6.3 Ölfus earthquake at 15:45 UTC on 29 May 2008 in South Iceland: ICEARRAY strong-motion recordings. *Soil Dynamics and Earthquake Engineering*, 29(6):1073–1083.

Harichandran, R. S. (1999). Spatial Variation of Earthquake Ground Motion. pages 1–21.

Harichandran, R. S. and Vanmarcke, E. H. (1986). Stochastic variation of earthquake ground motion in space and time. *Journal of Engineering Mechanics*, 113(8):1271–1273.

Imtiaz, A., Cornou, C., Bard, P.-Y., and Zerva, A. (2015). Spatial coherence of seismic ground motion and geometric structure of the sub-surface: an example in Argostoli, Greece. *9th Colloque National AFPS, 30 Nov - 2 Dec, Marne-La-Vallée, France*, page 12.

Imtiaz, A., Cornou, C., Bard, P. Y., and Zerva, A. (2018). Effects of site geometry on short-distance spatial coherency in Argostoli, Greece. *Bulletin of Earthquake Engineering*, 16(5):1801–1827.

Konakli, K. and Der Kiureghian, A. (2011). Stochastic Dynamic Analysis of Bridges Subjected to Spatially Varying Ground Motions. (August):282.

Konakli, K., Dreger, D., and Der Kiureghian, A. (2014). Coherency analysis of accelerograms recorded by the UPSAR array during the 2004 Parkfield earthquake. *EARTHQUAKE ENGINEERING & STRUCTURAL DYNAMICS*, (43):641–659.

Kramer, S. L. (1996). *Geotechnical Earthquake Engineering*. Prentice Hall.

Laib, A., Laouami, N., and Slimani, A. (2015). Modeling of soil heterogeneity and its effects on seismic response of multi-support structures. *Earthquake Engineering and Engineering Vibration*, 14(3):423–437.

Loh, C.-H. and Lin, S.-G. (1990). Directionality and simulation in spatial variation of seismic waves. *Engineering Structures*, 12(2):134–143.

Luco, J. E. and Wong, H. L. (1986). Response of a rigid foundation to a spatially random ground motion. Soil. *Soil Dyn. Earthqu. Engr.*, pages 891–908.

Lupoi, A., Franchin, P., Pinto, P. E., and Monti, G. (2005). Seismic design of bridges accounting for spatial variability of ground motion. *Earthquake Engineering and Structural Dynamics*, 34(4-5):327–348.

Ma, S., Custódio, S., Archuleta, R. J., and Liu, P. (2008). Dynamic modeling of the 2004 Mw 6.0 Parkfield, California, earthquake. *Journal of Geophysical Research: Solid Earth*, 113(2):1–16.

Mander, Priestley, and Park (1988). THEORETICAL STRESS-STRAIN MODEL FOR CONFINED CONCRETE. 114(8):1804–1826.

Mazzieri, Stupazzini, Guidotti, and Smerzini (2013). SPEED: SPectral Elements in Elastodynamics with Discontinuous Galerkin: a non-conforming approach for 3D multi-scale problems. *International*, (February):1102–1119.

Menegotto, M. and Pinto, P. E. (1973). Method of Analysis for Cyclically Loaded R. C. Plane Frames Including Changes in Geometry and Non-Elastic Behavior of Elements under Combined Normal Force and Bending. *proceedings of IABSE Symposium on Resistance and Ultimate Deformability of Structures Acted on by Well Defined Loads*, pages 15–22.

Monti, G., Nuti, C., and Pinto, P. E. (1996). NONLINEAR RESPONSE OF BRIDGES UNDER MULTISUPPORT EXCITATION. 122(October):1147–1159.

Novak, M. Š., Lazarević, D., and Atalić, J. (2015). Učinak prostorne promjenjivosti potresne pobude na seizmički odziv mostova. *Gradjevinar*, 67(10):943–957.

Özcebe, Smerzini, and Bhanu (2018). Insights into the Effect of Spatial Variability of Recorded Earthquake Ground Motion on the Response of a Bridge Structure. *Journal of Earthquake Engineering*, 24(6):920–946.

Özcebe, A. G., Smerzini, C., Paolucci, R., Pourshayegan, H., Plata, R. R., Lai, C. G., Zuccolo, E., Bozzoni, F., and Villani, M. (2019). On the comparison of 3d, 2d, and 1d numerical approaches to predict seismic site amplification: The case of norcia basin during the m6.5 2016 october 30 earthquake. *Earthquake Geotechnical Engineering for Protection and Development of Environment and Constructions- Proceedings of the 7th International Conference on Earthquake Geotechnical Engineering, 2019*, pages 4251–4258.

Paolucci, Evangelista, Mazzieri, and Schiappapietra (2016). The 3D numerical simulation of near-source ground motion during the Marsica earthquake, central Italy, 100 years later. *Soil Dynamics and Earthquake Engineering*, 91(June):39–52.

Paolucci, Gatti, F., Infantino, M., Smerzini, C., Özcebe, A. G., and Stupazzini, M. (2018). Broadband ground motions from 3D physics-based numerical simulations using artificial neural networks. *Bulletin of the Seismological Society of America*, 108(3):1272–1286.

Paolucci, Mazzieri, and Smerzini (2015). Anatomy of strong ground motion: Near-source records and three-dimensional physics-based numerical simulations of the Mw 6.0 2012 may 29 po plain earthquake, Italy. *Geophysical Journal International*, 203(3):2001–2020.

Paolucci, Smerzini, C., Mazzieri, Ozcebe, and Infantino, M. (2019). Development of advanced physics-based numerical approaches for earthquake ground motion prediction.

Paolucci, R., Mazzieri, Piunno, Smerzini, C., Vanini, M., and Özcebe (2020). Earthquake ground motion modeling of induced seismicity in the Groningen gas field.

Pourshayegan, H. (2019). 3D PHYSICS-BASED SIMULATIONS OF THE OCTOBER 30 2016 CENTRAL ITALY EARTHQUAKE.

Rahpeyma, S., Halldorsson, B., Olivera, C., Green, R. A., and Jonsson, S. (2016). Detailed site effect estimation in the presence of strong velocity reversals within

a small-aperture strong-motion array in Iceland. *Soil Dynamics and Earthquake Engineering*, 89:136–151.

Sandikkaya, M. A., Akkar, S., and Bard, P. Y. (2013). A nonlinear site-amplification model for the next pan-European ground-motion prediction equations. *Bulletin of the Seismological Society of America*, 103(1):19–32.

Sato, H., Fehler, M. C., and Maeda (2012). *Seismic wave propagations and scattering in the heterogeneous earth.* Springer Edition, second edi edition.

Saxena, V., Deodatis, G., and Shinozuka, M. (2000). Effect of spatial variation of earthquake ground motion on the nonlinear dynamic response of highway bridges. *Proceedings of the 12th World Conference on Earthquake Engineering*, pages 1–8.

Schneider, J. F., Stepp, J. C., and Abrahamson, N. A. (1992). The spatial variation of earthquake ground motion and effects of local site conditions.

Seismosoft (2020). SeismoStruct 2020 - a computer program for static and dynamic non-linear analysis of framed structures.

Sextos, A., Kappos, A. J., and Mergos, P. (2004). Effect of Soil-Structure Interaction and Spatial Variability of Ground Motion on Irregular Bridges- the Case of The Krystallopigi Bridge. (2298):15.

Sextos, A., Karakostas, C., Lekidis, V., and Papadopoulos, S. (2015). Multiple support seismic excitation of the Evripos bridge based on free-field and on-structure recordings. *Structure and Infrastructure Engineering*, 11(11):1510–1523.

Sextos, A. G. and Kappos, A. J. (2009). Evaluation of seismic response of bridges under asynchronous excitation and comparisons with Eurocode 8-2 provisions. *Bulletin of Earthquake Engineering*, 7(2):519–545.

Sextos, A. G., Kappos, A. J., and Pitilakis, K. D. (2003a). Inelastic dynamic analysis of RC bridges accounting for spatial variability of ground motion, site effects and soil-structure interaction phenomena. Part 2: Parametric study. *Earthquake Engineering and Structural Dynamics*, 32(4):629–652.

Sextos, A. G., Pitilakis, K. D., and Kappos, A. J. (2003b). Inelastic dynamic analysis of RC bridges accounting for spatial variability of ground motion, site effects and soil-structure interaction phenomena. Part 1: Methodology and analytical tools. *Earthquake Engineering and Structural Dynamics*, 32(4):607–627.

Smerzini, C., Lin, J., and Infantino, M. (2020). Spatial variability of earthquake ground motion: insights from 3D physics-based numerical simulations. pages 1–64.

Smerzini, C. and Villani, M. (2012). Broadband numerical simulations in complex near-field geological configurations: The case of the 2009 Mw 6.3 L'Aquila earthquake. *Bulletin of the Seismological Society of America*, 102(6):2436–2451.

Somerville, P. G., McLaren, J. P., Saikia, C. K., and Helmberger, D. V. (1988). Site-specific estimation of spatial incoherence of strong ground motion. *Geotechnical Special Publication*, pages 188—-202.

Somerville, P. G., Smith, N. F., Graves, R. W., and Abrahamson, N. A. (1997). Modification of empirical strong ground motion attenuation relations to include the amplitude and duration effects of rupture directivity. *Seismological Research Letters*, 68(1):199–222.

Spacone, E., Ciampi, V., and Filippou, F. C. (1996). Mixed formulation of nonlinear beam finite element. *Computers and Structures*, 58(1):71–83.

Svay (2017). *Modélisation de la variabilité spatiale du champ sismique pour les études d'interaction sol-structure*. PhD thesis.

Wang, G. Q., Tang, G. Q., Jackson, C. R., Zhou, X. Y., and Lin, Q. L. (2006). Strong ground motions observed at the UPSAR during the 2003 M 6.5 San Simeon and 2004 M 6.0 Parkfield, California, earthquakes. *Bulletin of the Seismological Society of America*, 96(4 B):159–182.

Wang, Y. R., Wen, R. Z., Ren, Y. F., and Wen, P. (2019). The Spatial Coherency of Ground Motions Based on Euroseistest Array. *Proceedings of the 2019 13th Symposium on Piezoelectrcity, Acoustic Waves, and Device Applications, SPAWDA 2019*, pages 1–5.

Zerva (2009). Stochastic Estimation of Spatial Variability. In *Spatial Variation of Seismic Ground Motions*, pages 9–64.

Zerva, A. and Harada (1997). Effect of surface layer stochasticity on seismic ground motion coherence and strain estimates. *Soil Dynamics and Earthquake Engineering*, 16(7-8):445–457.

Zerva, A. and Zervas, V. (2002). Spatial variation of seismic ground motions: An overview. *Applied Mechanics Reviews*, 55(3):271–296.

Zoubir, A. M. (2005). On confidence intervals for the coherence function. *ICASSP, IEEE International Conference on Acoustics, Speech and Signal Processing - Proceedings*, IV(April 2005).

ACKNOWLEDGMENT

Ho aspettato gli ultimi istanti disponibili, ma il momento tanto atteso è arrivato: i ringraziamenti.

Ringrazio la mia famiglia, Papà, Mamma e Gaia, tre capisaldi che, ognuno a suo modo, mi hanno accompagnato i questi anni in tutte le mie scelte cercando di fornirmi il massimo supporto possibile. Grazie Papi, tu sei davvero la mia roccia, il mio eroe, il mio riferimento sempre pronto a fare il possibile per facilitarmi la vita; tu hai fatto davvero tanto per me e spero che questo risultato possa, anche solo un minimo, renderti orgoglioso del tuo bocia. Grazie Nadi, tu sei la mia maestra: con il tuo supporto mi hai sempre spronato a superare i miei limiti, a mettermi in gioco e a non fermarmi mai, qualità che credo siano state a dir poco fondamentali in tutto il percorso di studio (e non solo). Grazie Ga, senza di te la mia vita non sarebbe stata mai la stessa, ti voglio tanto bene.

Inoltre, vorrei ringraziare vorrei ringraziare la professoressa Chiara Smerzini, relatore di questa tesi e fonte inesauribile di conoscenza. Il suo supporto è stato costante, ricco e fondamentale, ha saputo spronarmi nei momenti più intensi, dandomi la spinta per dare il 100%. La ammiro profondamente per il suo modo di lavorare, è stata e sarà un esempio. È stato un onore lavorare con lei.

Grazie Carla e Tarci, siete parte della mia famiglia non di sangue ma di cuore. Mi avete trattato come un figlio sin dai primi passi portandomi ovunque e riempiendomi di felicità. Grazie per avermi accolto per due anni a casa vostra, è stato a dir poco fondamentale per la riuscita di questo percorso. Non vi ringrazierò mai abbastanza, mi ritengo davvero fortunato ad aver incontrato persone come voi.

Grazie ai miei nonni. L'affetto e il sostegno che mi hanno dimostrato rendono questo traguardo ancora più prezioso. Grazie ai fratelli più che cugini Dado e Sofi, ne abbiamo passate tante insieme sugli sci e non: vi voglio bene! Grazie alle zie,

Claudia ed Elena, sempre presenti e pronte ad aiutare.

Una dedica speciale ai miei amici, che ogni giorno hanno condiviso con me gioie, sacrifici e successi, senza voltarmi mai le spalle. Grazie gruppo Manzite: Andy, Cesco, Dado, Gabri, Mele, Niki; le nostre serate leggendarie rimarranno nella storia, serate necessarie per staccare la spina nei momenti più duri. Vorrei ricordare il nostro motto: si può bere anche senza divertirsi!
Grazie a Pepsi capace di strapparmi sempre un sorriso.
Grazie anche a tutti i miei amici dell'università, gli unici che sanno veramente quanto si soffra a fare ingegneria: eravamo senza dubbio il miglior gruppo di sempre! Non vi scorderò mai.
Grazie a Fabio e Mattia, amici da una vita sin dalle prime gare di sci fino al corso maestri. Grazie per i momenti passati insieme sono indimenticabili (o quasi).

Infine, grazie a Benni (Benedetta è troppo serio). Dal primo giorno che ci siamo conosciuti è scattato qualcosa che non può essere descritto a parole, qualcosa che solo noi conosciamo, qualcosa di naturale, spontaneo e perfetto. Grazie per avermi supportato in questi anni, per avermi accompagnato in tutte le mie scelte e soprattutto per rendermi felice ogni volta con il tuo sorriso. Grazie perchè da quando ti ho conosciuto la mia vita è davvero migliore. Ti amo.

PS: spero di non aver dimenticato nessuno, ma, nel caso lo avessi fatto, ti metto qui. Grazie anche a te, persona di cui mi sono dimenticata il nome.